A Thesis Submitted for the Degree of PhD at the University of Warwick

Permanent WRAP URL:

http://wrap.warwick.ac.uk/161935

Inspection of Composite Aerospace Structures using Capacitive Imaging and Guided Waves

by

Silvio Amato

Submitted to the University of Warwick

for the degree of

Ph.D in Engineering

School of Engineering

June 2021

THE UNIVERSITY OF
WARWICK

Table of Contents

List of Figures

Chapter 1

Chapter 2

Chapter 3

Chapter 4

Chapter 5

Chapter 6

Chapter 7

List of Tables

Chapter 2

Chapter 3

Chapter 4

Chapter 5

Chapter 7

Acknowledgements

This research was funded by the European project NDTonAIR. My sincere thanks go to my compatriots Professor Marco Ricci and Dr. Stefano Laureti for their involvement in the NDTonAIR project, and their insights over the course of my PhD.

I would like to express my sincere gratitude to my two supervisors, Professor David Hutchins and Professor Steve Dixon, for their support throughout my PhD. For being able to play the roles of good cop and 'bad cop' by guiding me with their vast knowledge, and helping during the writing of my thesis. I can safely say that I have been extremely fortunate to have had two such supervisors.

In School of Engineering, I would like to thank Dr. Lee Davis for his forthright honesty, and assistance with every electronic device used during my research. Also, a special thank you to Dr. Richard Watson for helping me manufacture or buy a variety of the components used during my research. In the Physics department, thanks to Dr. Mark Potter for teaching me how to build EMATs, and Dr. Zhichao Li for patiently answering the most meaningless questions about PZFlex. In COTESA, thanks to Eng. Falk Stelzmann and Dr. Schulz for manufacturing the samples that were essential to the project.

I would also like to thank Nick Jaco and Sergey Gartsev for making my experience outside of university more enjoyable.

A huge thanks for support, patience and love must also go to Elena (my anchor), whose lovely words have sustained me through the most difficult moments of this journey. Last but not the least, I would like to thank my family: my parents and my brother for supporting me spiritually throughout this journey and my life in general.

Declaration

The research presented in this thesis is my original work, produced under the supervision of Prof. David Hutchins in School of Engineering and Prof. Steve Dixon in the Department of Physics at the University of Warwick, UK, between September 2017 and Jun 2021. No part of this work has been previously submitted to the University of Warwick, nor to any other academic institution for the purposes of obtaining a higher degree.

Publications arising from the research

[1] J. Vyas, E. Jasiuniene, R. Kažys, S. Amato, S. Dixon, D.A. Hutchins, ”The NDE of pultruded GRP composites using air-coupled ultrasound and EMAT-based guided wave inspection,” Review of Progress Quantitative Nondestructive Evaluation, 0, 1–3, 2019

[2] S. Amato, D. A. Hutchins, X. Yin, M. Ricci, S. Laureti, “Capacitive imaging using fused amplitude and phase information for improved defect detection,” NDT&E International, 2021 (Revised and Submitted – waiting for approval)

Summary

This thesis describes a possible new approach for the future of the NDT of aerospace materials by using both ultrasonic guided wave and capacitive imaging (CI) techniques. The two techniques complement each other and are selected depending upon the area inspected and the resolution required. Guided waves are used for long range defect detection, while capacitive imaging is used for localised characterisation.

The guided waves are generated by means of electromagnetic acoustic transducers (EMATs). These devices employ a coil, for inducing eddy currents, and a magnet (or an array of them), for generating a static magnetic field. The interaction of these two quantities produces ultrasonic guided waves based on the Lorentz force mechanism, but needs an electrically conductive surface to operate. In this thesis the conductive surface is provided by using thin, self- adhesive, removable metallic patches for both insulating and conducting samples. Conversely, the CI technique employs a pair of electrodes to establish a quasi-static electric field within the sample, and requires the sample to have a low (basically zero) electrical conductivity for allowing the field to probe it. Both techniques are non-contact and non-invasive nature.

Guided waves have been studied using periodic permanent magnet (PPM) EMATs, which here have been designed to generate shear horizontal waves, and predominantly the SH_0 mode is used in the thesis. In the aerospace field, the materials used are composites, whose electrical conductivity is often too low for efficient EMAT use, even when they contain carbon fibres. There is a notable exception, where a copper mesh for lightning strike protection is integrated into composite, as direct use of an EMAT on these samples is possible. For the cases where removable metallic patches are used, analytical models were designed to predict the forces and the generated wave within the sample. The predictions show good agreement with experimental measurements for the propagation of SH guided waves within different samples such a carbon fibre and glass fibre composites. Consequently, the methodology has been used for the detection of several types of defect, such as impact damage, delamination and lightning strikes. Furthermore, the production of images via a SAFT algorithm allows preliminary evaluations of the severity of the defects detected.

The CI technique has been investigated for various designs of CI probes using 2D and 3D finite element (FE) models in COMSOL. It is shown how conductivity affects performance, and the results from simulations of different probe designs has been compared to experiments in insulating materials, with good agreement. These results indicate that CI is a suitable NDT technique for samples such as glass fibre composites. Conventionally, the images from CI measurements are based on the amplitude of the received signal rather than phase, due to the higher signal-to-noise ratios that can be obtained with the amplitude measurement. In this work, an improved image processing method has been introduced. The method combines amplitude and phase information to form clearer images, and thus improving the evaluation of both sizing and location of defects.

The use of both techniques has been illustrated for the case of damage within pultruded glass fibre composites. It is shown that guided waves using EMATs and a removable copper patch can be used to detect defects at extended ranges, and that these can be characterised further at higher resolution using a localised inspection, the CI technique.

Abbreviations

AC : Alternating current.
ACU : Air-coupled ultrasonic.
BVID : Barely visible impact damage.
CFRP : Carbon fibre reinforced polymer.
CI : Capacitive imaging.
CMC : Ceramic matrix composite.
DC : Direct current.
ECT : Eddy current testing.
EMAT : Electromagnetic acoustic transducer.
ERT : Electrical resistance tomography.
ET : Electromagnetic testing.
FEM : Finite element model.
FFT : Fast Fourier transform.
GFRP : Glass fibre reinforced polymer.
LVI : Low velocity impact.
MFL : Magnetic flux leakage.
MMC : Metal matrix composite.
MPI : Magnetic particle inspection.
NDE : Non-destructive evaluation.
NDT : Non-destructive testing.
PCB : Printed circuit board.
PMC : Polymer matrix composite.
PPM : Periodic permanent magnet.
PSM : Phase shift migration.
RTM : Resin transfer moulding.
RX : Receiver.
SAFT : Synthetic aperture focusing technique.
SH : Shear horizontal.
SNR : Signal to noise ratio.
SV : Shear vertical.
ToF : Time of flight.
TX : Transmitter.
UD : Unidirectional.
VOI : Volume of influence.

Symbols

Latin:

$\vec{B}$: Magnetic flux density.

c : Elastic constant.

C_g : Group velocity.

C_p : Phase velocity.

c_{ijkl} : Elastic tensor.

$\vec{D}$: Electric displacement.

$\vec{E}$: Electric field.

e : Charge of an electron (section 2.2.3); Euler’s number (elsewhere).

E : Young’s modulus.

$\vec{F}$: Lorentz force.

f : Frequency.

G : Shear modulus.

$\vec{g}$: Gravitational acceleration.

$\vec{H}$: Magnetic field strength.

h : Height.

$\vec{I}$: Current.

i, j, k, l : Integer indices when used in index notation.

$\vec{J}$: Current density.

k : Wave number.

L : Distance.

$\vec{M}$: Magnetisation.

M_n : Normal component of the magnetisation.

m : Mass of an electron (Chapter 2); Mass (section 7.2.1).

$\vec{n}$: Unit vector normal to the surface S.

n_e : Electron density.

$\vec{P}$: Polarisation field.

$p(t, x, Z)$: Wavefield.

q : Electric charge.

R Amplitude.

$\vec{S}$: Displacement at the surface S.

t : Time.

U : Gravitational potential energy.

$\vec{v}$: Velocity of the charged particle.

$\overrightarrow{v_e}$: Mean electron velocity.

$\overrightarrow{v_i}$: Mena ion velocity.

V_x, V_y, V_z : Direction cosines.

x, y, z : Cartesian coordinates.

Z_i : Charge of an ion.

Greek:

Γ_{ij} : Christoffel matrix.
δ : Skin depth.
Δ : Data fusion output (eq. 6.1).
ε : Strain (section 4.2); permittivity (elsewhere).
ε_0 : Permittivity of free space.
ε_r : Relative permittivity.
$\boldsymbol{\varepsilon}$: Permittivity matrix.
$\boldsymbol{\varepsilon}_{eff}$: Effective permittivity matrix.
λ : Lamè parameter (section 4.2); wavelength (elsewhere).
μ_0 : Permeability of free space.
μ_r : Relative permeability.
μ : Lamè parameter (section 4.2).
$\vec{\xi}$: Displacement vector.
Ξ : Data fusion output (eq. 6.2).
ρ : Density (Chapter 4); charge density (elsewhere).
σ : Stress (section 4.2); electrical conductivity (elsewhere).
τ : Mean time between electron-ion collisions.
φ : Electric potential distribution.
Φ : Phase.
χ_e : Electric susceptibility.
ω : Angular frequency.

Miscellaneous:

∇ : Gradient operator.
$\nabla\cdot$: Divergence operator.
$\nabla\times$: Curl operator.

Chapter 1

Introduction

Non-destructive testing (NDT) covers a wide range of testing methods used to evaluate the properties of a material without causing damage [1]. The characterization of the material under test aims to localize and evaluate potential flaws that might cause catastrophic failure. These include fractures in aerospace components, rupture of pipelines and other less visible, but equally troubling, events [2]. A wide range of techniques are used in NDT [3,4]. The research described in this thesis is associated with an EU Interdisciplinary Training Network (ITN), involving the aerospace industry [5], where NDT plays a critical role. In this industry, development activities are defined by the research for the highest possible working safety (structural integrity) and economic efficiency.

The principal techniques used for inspecting aircraft are visual inspection (which is used for over 80 % of the inspections done), eddy current testing, ultrasonic testing and X-ray inspection [6-9]. Each method has its own pros and cons, and needs to be applied wisely, depending on several factors such as mechanical properties, component dimensions and geometry, type and position of defect, and point of access [10]. The inspections are based on the damage tolerance concept, which assumes that any component is faulty and defects are accepted if they do not exceed certain given dimensions [11].

1.1 Composites

In recent years, the use of composites has increased within the aerospace industry, as illustrated in figure 1.1.

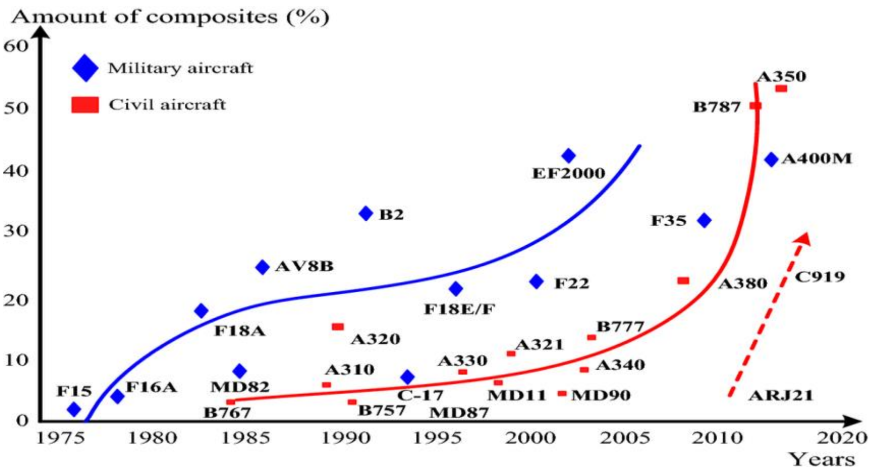

Figure 1.1 Increase in the use of composites during the last four decades (from [12]*).*

Composites are materials made by combining two or more components, usually fibres and a matrix, in order to take advantage of the features of each component. However, there are many other types of composites, including those containing honeycomb layers, which are used in aircraft. The enhancement that results is due to the following attributes that satisfy most of the following requirements for aerospace materials [13-18]:

- Light weight: the use of composite materials produces >30% weight reduction of aircraft structures, leading to considerable fuel savings. Moreover, lower fuel consumption will aid in reducing the emission of greenhouse gases
- High static strength: some components need to withstand extreme forces (e.g. wind shear)
- Good fatigue performance: the extended lifespan of aerospace structures relies on good fatigue performance
- High fracture toughness and damage tolerance: cracks and flaws within the structures should not grow quickly, preventing sudden failures
- High-impact energy: bird strikes, foreign objects, hail etc.
- Multi-functionality: examples include temperature change stability (ranging from freezing to high temperatures), resistance to lighting strikes, corrosion resistance
- Availability of affordable and easy designing and manufacturing techniques.

On the other hand, the use of composites also has some intrinsic weaknesses [19]:

- Poor resistance to out-of-plane tensile loads, which may lead to delamination of different plies
- Susceptibility to impact damage and high risk to internal damage, which may be barely or not visible
- Moisture absorption and consequentially reduction of temperature change stability
- Possible manufacturing defects.

Despite the weaknesses listed above, the benefits are extensive, and almost all aerospace manufacturers utilize large amount of composites. However, due to the immaturity of composite technology, a few difficulties still exist. Composites have a complex structure, with significant anisotropy and inhomogeneity, which leads to difficulties in detecting certain types of damage (especially impact damage); furthermore, such complexity requires complicated analysis tools to predict their behaviour under loading conditions when it is possible, and several expensive and time-consuming tests when it is not [19,20].

This research will concentrate on the inspection of Carbon Fibre Reinforced Polymer (CFRP) and Glass Fibre Reinforced Polymer (GFRP) composite materials used in aerospace in order to detect mainly two types of defects: impact damage and heat damage to the surface.

Impact damage can be categorized depending on the velocity of the impact: low velocity impact (LVI), intermediate velocity impact and ballistic impact. This PhD project deals specifically with LVI, which typically occurs at impact velocities below 10 m/s. When a composite specimen undergoes an impact, the material is subjected to large amounts of strain, depending on the magnitude of the impact, temperature and strain rates. In many cases, damage is not visible on the surface, though internal damage can negatively affect the residual strength and buckling load capacity [21]. The heterogeneity and anisotropy of composites lead to different modes of failure. In the majority of cases, these comprise: a dent on the impact side; delamination and/or debonding between plies; matrix cracking; fibre breakage and buckling due to bending; and, under severe conditions, penetration. Figure 1.2 depicts a schematic representation of these defects.

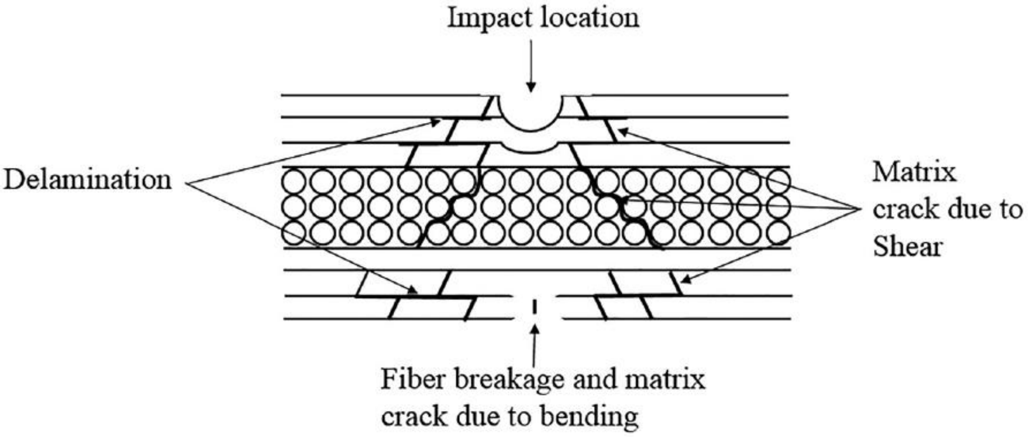

Figure 1.2 Schematic representation of impact damage of composite laminate (from [22]*).*

Aside from mechanical impact damage, another type of defect from heating of the surface can occur, due to lightning strikes. This event is a natural electric discharge and occurs, on average, about once each year to a typical operational commercial aircraft [23] and exhibits three features: a bright flash, a loud noise and, in some cases, minor damage [24]. Due to the lower electrical conductivity of composites (fibres may be conductive, though the matrix is a good dielectric), it is necessary to adopt countermeasures to allow the lightning current flow throughout the aircraft skin without causing damages to the structure, which could cause catastrophic failure [24]. The solution commonly used is a metallic mesh (copper or aluminium), bonded few plies below the outer surface, which permits the lightning currents to dissipate along the airframe, protecting the inside of the aircraft [25]. Usually, the most severe damage appears as burn marks or burn holes, which occur at the entry and exit points of a lightning strike, where the energy density is highest, as figure 1.3 depicts:

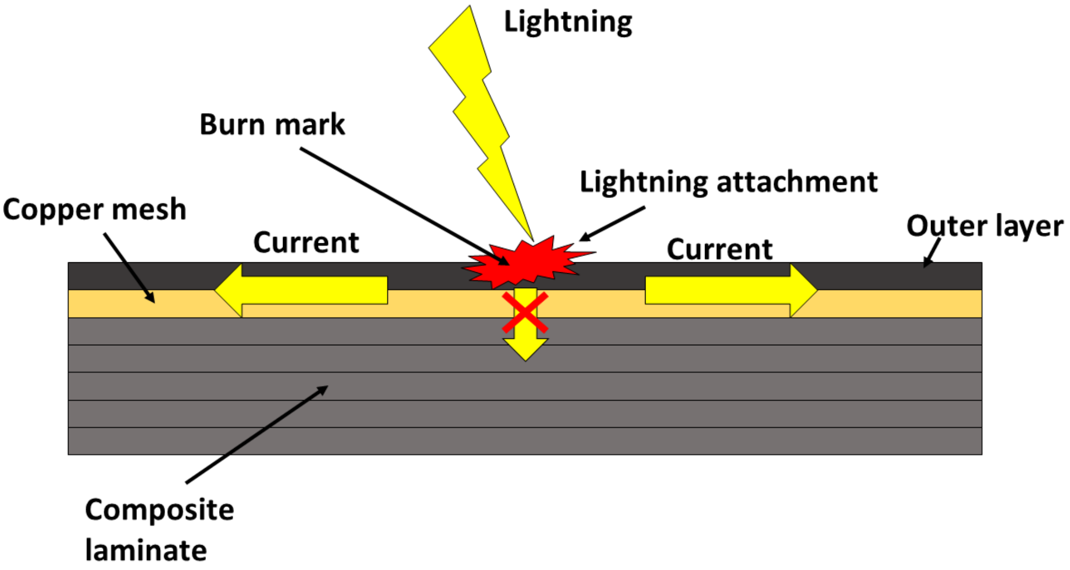

Figure 1.3 Schematic diagram of a lightning strike (after [26]*).*

1.2 The techniques used in this thesis

The experimental testing methods used in this thesis have been performed using two main techniques, depending on resolution and scan area required. These are ultrasonic guided-wave inspection for large areas [27], and capacitive imaging for small areas [28].

Ultrasonic guided waves have been of increased interest over the past decade, as the range of applications for which they are used has increased. In contrast to conventional ultrasonic testing, which uses bulk waves (longitudinal and shear waves), guided waves can accomplish inspection over a greater distance, due to the use of the structure itself as a waveguide. Hence, unlike bulk waves, the structure can be inspected from a single probe position [29], providing time and cost savings during the inspection [30].

Depending on the shape and dimensions of the component under test, several types of guided wave mode can exist. For the purpose of this research, which will investigate samples in the form of large areas of wing structure, Shear Horizontal (SH) guided waves are the most relevant. The term "horizontal" is due to the fact that particle vibrations within an SH mode are polarised in a plane that is parallel to the specimen surface, as illustrated in figure 1.4.

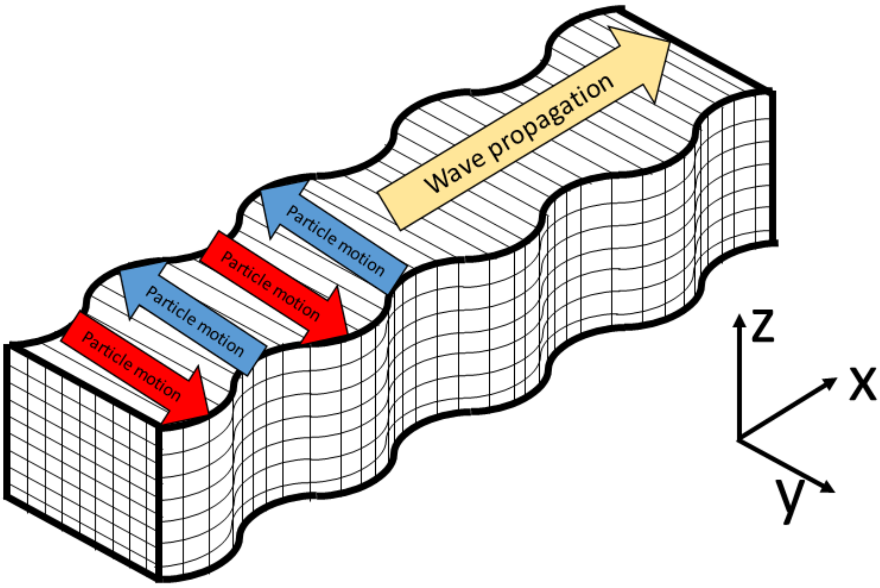

Figure 1.4 SH wave mode propagation. The blue and red arrows represent the direction of the particle motion (along the y axis). The yellow arrow indicates the direction of propagation of the wave (along the x axis).

Having vibration polarisation parallel to a boundary, means that the reflecting wave does not show mode conversion for a uniformly thick sample (independent of the incident angle), and the amplitude is also not affected (although there is a π phase shift) [31,32]. In principle, a sample can support multiple modes: symmetric and anti-symmetric. These modes are labelled in increasing orders (SH_0, SH_1, SH_2…), and apart from the zero-order mode (SH_0), each has a cut-off frequency below which they do not propagate. Moreover, for isotropic and homogenous plates the SH_0 does not exhibit velocity dispersion, unlike the other higher order modes which are dispersive, as shown in figure 1.5. Thus, the frequency-thickness product does not affect the propagation velocity of the SH_0 mode.

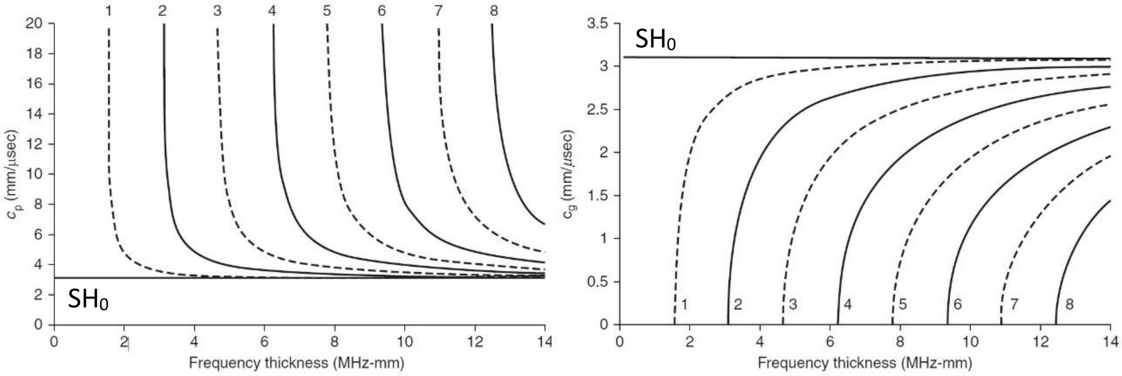

Figure 1.5 SH mode phase and group velocity dispersion curves for an aluminium layer (from [31]*).*

In previous research, SH guided waves had not received much attention, due to experimental wave generation difficulties if piezoelectric transducers are used [33]. This is the reason that the transducers used for generating such waves have primarily been EMATs (Electromagnetic acoustic transducers), but piezoelectric transducers have also been used [34]. An EMAT consists of two principle parts, these being the coil and the magnet, and the generation of elastic waves occurs via an electromagnetic mechanism. More details will be given in Chapter 2.

The second method, used in this research to inspect small areas at a higher resolution than the EMATs, employs a pair of co-planar electrodes (driving and sensing electrodes), which can be thought of as an unfolded parallel capacitor, as shown in figure 1.6 [35,36]. The CI technique has been used to inspect small areas at higher resolution than the EMATs. The enhanced resolution is provided by the size of electrodes comparable to defects, and the distribution of the electric field lines (due to the geometry of the electrodes). Further details will be given in Chapter 5.

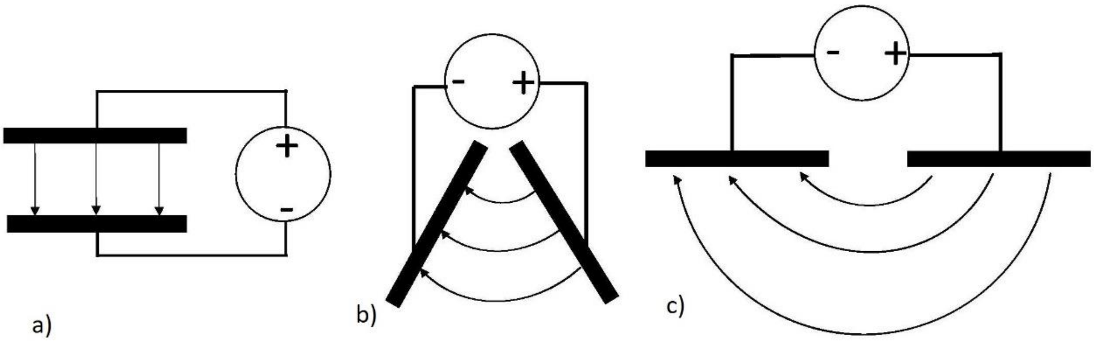

Figure 1.6 Schematic diagram of the electric field distribution as electrodes change from being in a conventional parallel-plate capacitor geometry (a) to become coplanar in (c).

Considering the co-planar probe of figure 1.6(c), an electric field distribution will be generated within the sample when an AC potential exists between the driving and the sensing electrodes is established. The sample itself and the presence of any defects will affect the resultant field, as shown in figure 1.7. The field on the sensing electrode will then result in a change in the charge induced, and this can be detected and used to plot changes in the sample condition. Figure 1.7 is only representative of the working principles not taking in account the electronics of the system. In Chapter 5 the electronics will be fully described.

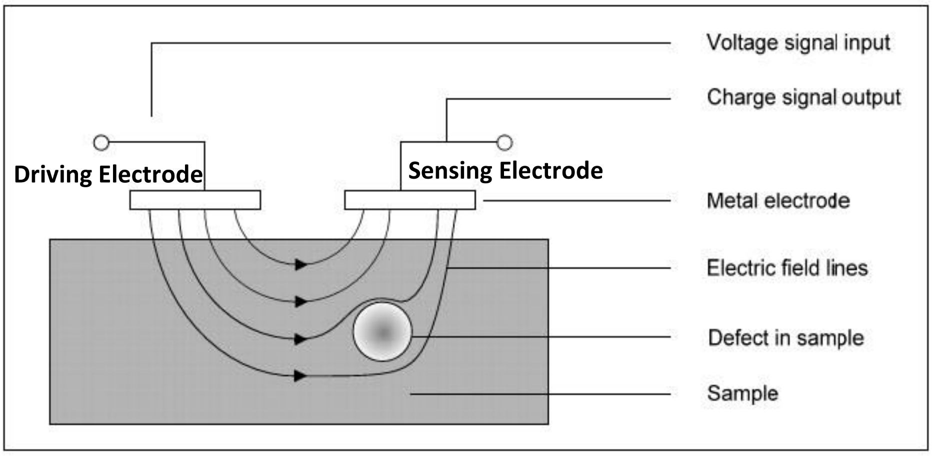

Figure 1.7 Schematic diagram of the capacitive imaging (after [37]*).*

Depending on the material (insulator or conductor), the behaviour of the probing electric field will vary. If the specimen is a dielectric material or has very low electrical conductivity, the electric field will have a certain volume of influence (VOI), the region of the sample under the probe which plays a significant role in the measurement. The presence of defects will alter the electric field, and change the quantity of induced charges on the sensing electrode, as stated above and illustrated in figure 1.7.

1.3 Objectives of the research and outline of the thesis

The objective of the work in this thesis is to design a possible new approach for future NDT of aerospace materials, by introducing reliable methods for guaranteeing the high safety levels required in this field. This will be achieved by applying ultrasonic guided wave and capacitive imaging techniques in different ways: guided waves for long range defect detection and capacitive imaging for more detailed localized characterization. This is reflected in the following thesis structure:

Chapter 2 gives a general review of EMATs, which will be used for the generation of guided waves. This begins with a basic physical description of how such devices can generate and detect ultrasonic guided waves. This is followed by an explanation of the operation of several typical EMAT designs for mode selection, including the periodic EMAT used in this work. The solution adopted to overcome the lower conductivity of the material inspected is also described, involving the use of removable, thin metal patches.

Chapter 3 provides an extensive description of the methodology used to model the propagation of SH guided waves within composite components for the purpose of predicting and comparing actual measurements. Firstly, Finite Element (FE) models are designed in COMSOL in order to calculate the eddy currents and the magnetic fields of a periodic EMAT within a thin metallic patch. Subsequently, the calculation of the Lorentz forces in MATLAB is described. Finally, the use of the resultant forces for generating guided waves within specimens actually tested.

In Chapter 4, a series experiments in different materials are described which illustrate the use of EMATs for testing non-conductive samples by means of removable metallic patches. Firstly, the relationship between ultrasound and mechanical properties is considered. A preliminary measurement is conducted on an aluminium sample for verifying the laboratory instrumentation. Subsequently, the potential of the approach is illustrated by testing a series of non-conductive and low conductivity samples.

Chapter 5 describes the fundamentals of the CI technique, design principles for CI probes and a preliminary measurement. A brief review of the physical principles, the quasi-static approximation, electrical properties of samples and a classification of the modes of operation is given. The design principles are thus introduced and two type of CI probes, symmetric and concentric, are described. Subsequently, 2D and 3D FE models are presented for assessing the performance of the probes. Finally, a preliminary measurement is compared to the results of the analytical model.

In Chapter 6, the CI technique is used for inspecting several GFRP plates having an impact damage. The standard results obtained by using either amplitude or phase are compared to a novel approach which combines these two features.

In Chapter 7, the methodology described in Chapter 4 is used for testing various composite samples affected by several types of defect. Furthermore, an imaging technique is briefly described and used for imaging defects detected by PPM EMATs for preliminary evaluations. Finally, a comparison between the guided wave and Capacitive Imaging techniques is provided, illustrating the advantages of using both for characterising defects.

Finally, Chapter 8 draws conclusions from this research, and suggests further work and application which have arisen from the finding of this thesis.

References Chapter 1

[1] L. Cartz, Nondestructive Testing, Milwaukee WI USA: ASM International, 1995.

[2] "NDT Resource Center," [Online]. Available: https://www.nde-ed.org/AboutNDT/aboutndt.htm.

[3] E.D. Bray, D. McBride, "Nondestrucitve testing techniques," Wiley, 1992, p. 798.

[4] B. Raj, T. Jayakumar, M. Thavasiumuthu, Practical Non-destructive Testing, Abigton: Woodhead Publishing Limited, 2002.

[5] "NDTonAIR," [Online]. Available: http://www.ndtonair.eu/.

[6] "NDT Resource Center," [Online]. Available: https://www.nde-ed.org/AboutNDT/SelectedApplications/AircraftInspection/Aircraft%20Inspection.htm.

[7] G. Yang, A. Tamburrino, L. Udpa, S. S. Udpa, Z. Zeng, Y. Deng, P. Que, "Pulsed Eddy-Current Based GIant Magnetoresistive System for the inspection of aircraft structures," *IEEE Transactions on Magnetics,* vol. 46, no. 3, pp. 910-917, 2010.

[8] A. Sophian, G.Y. Tian, D. Taylor, J. Rudlin, "Design of a pulsed eddy current sensor for detection of defects in aircraft lap-joints," *Sensor and Actuators,* vol. 101, no. 1-2, pp. 92-98, 2002.

[9] W.J. Staszewski, C. Boller, G.R. Tomlinson, Health Monitoring of Aerospace Structures, Chichester: Wiley, 2004.

[10] S. Gholizadeh, "A review of non-destructive testing methods of composite materials," *Procedia Structural Integrity,* vol. 1, pp. 50-57, 2016.

[11] H.-J. Schmidt, B. Schmidt-Brandecker, G. Tober, "Design of Modern Aircraft Structure and the Role of NDI," in *7th ECNDT,* Copenhagen, 1998.

[12] L. Zhang, X. Wang, J. Pei, Y. Zhou, " Review of automated fibre placement and its prospects for advanced composites," *Journal of Materials Science,* vol. 55, no. 17, pp. 7121-7155, 2020.

[13] R. Alderliesten, "Designing for damage tolerance in aerospace: a hybrid technology," *Materials & Design,* vol. 66, pp. 421-428, 2015.

[14] K. Koski, A. Siljander, M. Bäckström, S. Liukkonen, J. Juntunen, M. Sarkimo, K. Lahdenperä, J. Tikka, R. Lahtinen, "Fatigue, residual strength and non-destructive tests of an aging aircraft's wing detail," *International Journal of Fatigue,* vol. 31, no. 6, pp. 1089-1094, 2009.

[15] Z. Huda, P. Edi, "Materials selection in design of structures and engines of supersonic aircrafts: A review," *Materials & Design,* vol. 46, pp. 552-560, 2013.

[16] A. P. Mouritz, Introduction to aerospace materials, Reston, VA: American Institute of Aeronautics and Astronautics, 2012.

[17] M. Nurhaniza, M. K. A. Ariffin, A. Ali, F. Mustapha, A.W. Noraini, "Finite element analysis of composites materials for aerospace applications," *IOP Conference Series: Materials Science and Engineering*, vol. 11, p. 012010, 2010.

[18] C. Pevitt, F. Alam, "Static Computational Fluid Dynamics simulations around a specialised delta wing," *Computer & Fluids,* vol. 100, pp. 155-164, 2014.

[19] P. D. Mangalgir, "Composite materials for aerospace applications," *Bulletin of Materials Science,* vol. 22, no. 3, pp. 657-664, 1999.

[20] S. Rana, R. Fangueiro, "Advanced composites in aerospace engineering," in *Advanced Composite Materials for Aerospace Engineering,* Woodhead Publishing, 2016, pp. 1-14.

[21] U. Vaidya, "Impact response of laminated and sandwich composites," in *Impact engineering of composite structures,* Wien, Springer, 2011, pp. 97-191.

[22] A. Tabiei, W. Zhang, "Composite Laminate Delamination Simulation and Experiment: A Review of Recent Development," *Applied Mechanics Reviews,* vol. 70, no. 3, 2018.

[23] A. Larsson, P. Lalande, A. Bondiou-Clergerie, A. Delannoy, "The lightning swept stroke along an aircraft in flight. Part I: thermodynamic and electric properties of lightning arc channels," *Journal of Physics D: Applied Physics,* vol. 33, no. 15, pp. 1866-1875, 14 August 2000.

[24] M.A. Uman, V.A. Rakov, "The interaction of lighting with airborne vehicles," *Progress in aerospace sciences,* vol. 39, no. 1, pp. 61-81, 2003.

[25] M. Gagné, D. Therriault, "Lightning strike protection of composites," *Progress in aerospace sciences,* vol. 64, pp. 1-16, 2014.

[26] J. Han, H. Zhang, M. Chen, D. Wang, Q. Liu, Q. Wu, Z. Zhang, "The combination of carbon nanotube buckypaper and insulating adhesive for lightning strike protection of the carbon fiber/epoxy laminates," *Carbon,* vol. 94, pp. 101-113, 2015.

[27] R.P. Dalton, P. Cawley, and M.J.S. Lowe, "The Potential of Guided Waves for Monitoring Large Areas of Metallic Aircraft Fuselage Structure," *Journal of Nondestructive Evaluation,* vol. 20, no. 1, pp. 29-46, 2001.

[28] X. Yin, D. A. Hutchins, "Non-destructive evaluation of composite materials using a capacitive imaging technique," *Composites Part B: Engineering,* vol. 43, no. 3, pp. 1282-1292, 2012.

[29] J. L. Rose, "Ultrasonic Guided Waves in Structural Health Monitoring," *Key Engineering Materials,* Vols. 270-273, pp. 14-21, 2004.

[30] J. Rose, Ultrasonic guided waves in solid media, New York: Cambridge university press, 2014.

[31] J. Rose, "Waves in Plates & Horizontal Shear," in *Ultrasonic Waves in Solid Media,* New York, Cambridge University Press, 2004, pp. 112 - 245 - 246.

[32] P.A. Pether, S.E. Burrows, S. Dixon, "Shear (SH) ultrasound wave propagation around smooth corners," *Ultrasonics,* vol. 54, no. 4, pp. 997-1004, 2014.

[33] J. Rose, Ultrasonic guided waves in solid media, New York: Cambridge university p, 2014.

[34] W. Zhou, H. Li, F. Yuan, "Guided wave generation, sensing and damage detection using in-plane shear piezoelectric wafers," *Smart Materials and Structures,* vol. 23, no. 1, p. 015014, 2014.

[35] G. Diamond, D. A. Hutchins, K. K. Leong, T. H. Gan, "Electrostatic Capacitive Imaging: A new NDE Technique," *AIP Conference Proceedings,* vol. 894, no. 1, pp. 689-694, 2007.

[36] X. Yin, D.A. Hutchins, G.G. Diamond, P. Purnell, "Non-destructive evaluation of concrete using a capacitive imaging technique: Preliminary modelling and experiments," *Cement and Concrete Research,* vol. 40, no. 12, pp. 1734-1743, 2010.

[37] D. A. Hutchins X. Yin, "Non-destructive evaluation of composite materials using capacitive imaging technique," *Composites,* vol. 43, no. 3, pp. 1282-1292, 2012.

Chapter 2

Electromagnetic Acoustic Transducers (EMATs)

2.1 Introduction

The following chapter describes the basic operation principles of EMATs, showing their advantages and limitations and introducing some EMAT designs. In general, EMATs are devices which are basically made of a coil to induce dynamic electromagnetic fields at the surface of a conductive material, and a magnet or a series of them to provide a DC biasing magnetic field, as shown in figure 2.1. This is compared to a typical piezoelectric device which, as shown in the figure, requires some form of couplant to couple it to the surface of the sample.

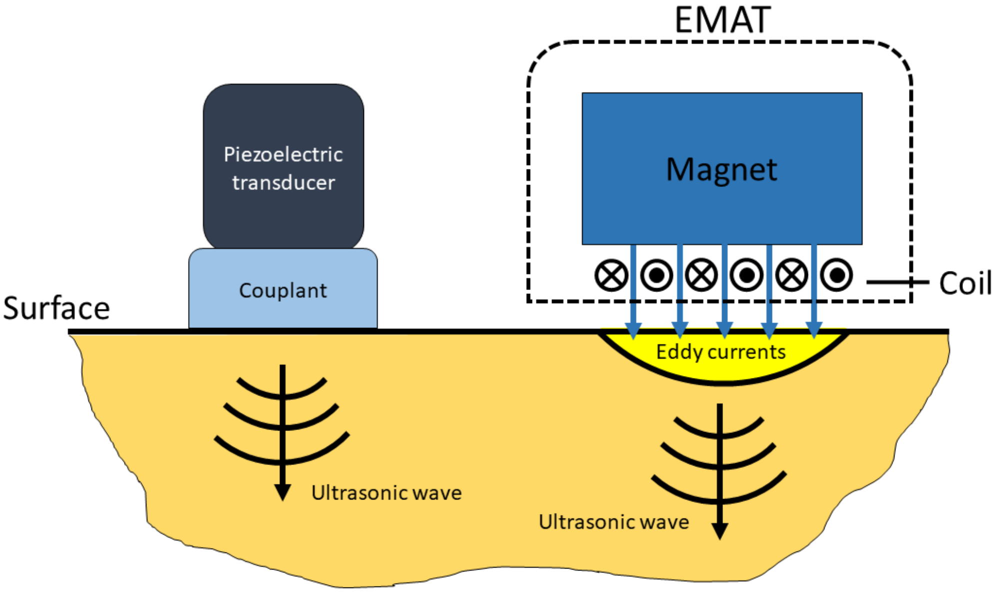

Figure 2.1 Scheme of an EMAT compared to a piezoelectric UT.

The interaction between induced eddy currents and the static magnetic field generates elastic waves within the sample (which needs to be conductive). It is possible to generate different wave modes, depending on the geometry of the coil and the configuration of the magnets. Figure 2.2 shows the most common coil designs.

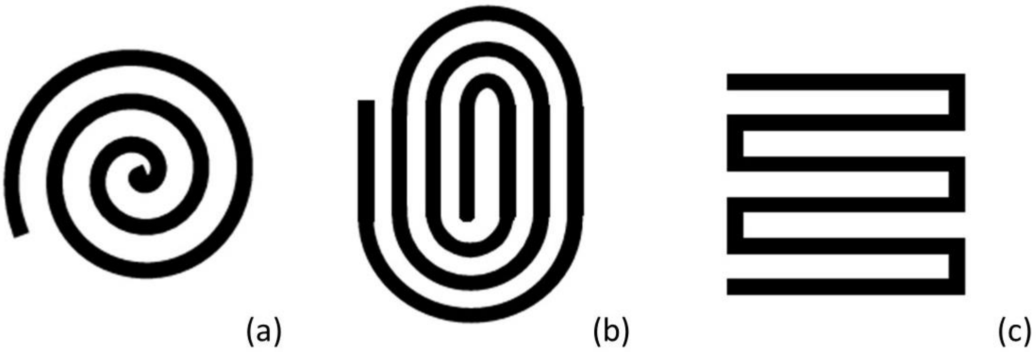

Figure 2.2 Coil designs: (a) spiral, (b) racetrack and (c) meander coil.

Many authors have advanced theoretical and numerical models to describe the transduction mechanisms. It is difficult to establish who the “inventor” of EMATs was [1]. The physical principles governing their operation were known since the studies of Maxwell on fundamental electromagnetism including what was later identified as the Lorentz force in 1861 [2] (a more detailed explanation of Maxwell’s equations and EMAT governing equations will be given in the next paragraph). Over a century later, due to the development of technology, the first EMATs were designed for NDE purposes. Seemingly, according to [1], the studies of Grimes and Buchsbaum [3] on helicons (low-frequency electromagnetic waves) reported in the early sixties gave the kick-off. Afterwards, in the late sixties, Gaerttnear et al. examined ultrasound generation due to magnetic body forces [4]. At the beginning of the following decade, Dobbs [5] began to investigate electromagnetic mechanisms for generating ultrasonic waves. In conclusion he stated that the forces were due to the Lorentz effect and proposed the use of such a phenomenon for NDE.

In the same period, Thompson [6] illustrated the generation of Rayleigh and Lamb waves in metal plates by mean of a meander coil EMAT. He also introduced an analytical model incorporating the Lorentz force mechanism and studied the effect of the lift-off on the generated signal. Later, Thompson focused on the study of magnetostriction: he dealt with the efficiency of this mechanism on different ferromagnetic materials in 1977 [7].

One year later, Thompson [8] provided some insight of the equations governing EMAT operation, including a further generation effect, the magnetization force, which was demonstrated to be less effective compared to the other mechanisms. He and Vasile proposed a new kind of EMAT: the periodic permanent magnet EMAT [9]. Such a transducer is capable of generating shear horizontal (SH) waves in plates, a task that traditional piezoelectric transducers struggle to achieve.

In 1976, Kawashima [10] introduced a major improvement in the modelling of spiral coil EMATs, applied to non-ferromagnetic metals. He designed the coil as the superposition of several circular loops, lying on parallel planes to the sample surface, at a certain distance. This assumption allowed him to use the model proposed by Dodd and Deeds [11] in order to model eddy current probes. This solves the electrodynamics equations in steady-state conditions, by mean of a magnetic vector potential formulation, taking an axisymmetric geometry. The analytical solution is in the form of an integral of Bessel functions, which can be easily calculated numerically. This relationship and the measurements of the magnetic flux density were used by Kawashima to predict the Lorentz forces. The further hypothesis used was that the forces could be treated as surface forces rather than body ones, as they are confined within the electromagnetic skin depth, which is much smaller than the wavelength of the elastic waves. Kawashima's model, unlike the previous ones, was the first one to give useful equations for the actual design of the device: practical parameters, such as the dimensions of the coil and the number of turns, which are directly tied to the generation and reception efficiencies of the transducer. A crucial role was played by the widespread development of numerical methods, such as the finite element method and the finite difference method, in the formulation of realistic EMAT models. Kawashima also demonstrated that EMATs are velocity sensors, proving it for a pancake coil [12] and later generalised to any type of coil. This will be explained in more detail in Section 2.2.5. In the nineties, Ludwig and colleagues introduced a 2-dimensional FE code, including all the generation mechanisms, with an arbitrary transient excitation [13-18]. In the model, an inhomogeneous magnetic field was included. This permitted the investigation of more complex systems, for instance a variable lift-off coil, fed by a tone-burst excitation current. Hsu et al. later proposed a solution for the inspection of non-conducting composite materials [19]. The study describes the application of EMATs on non-conducting materials by adhering a removable aluminium foil tape on the surface.

In recent years, Dixon and collaborators [20], introduced enhancements in the design of EMATs. Their studies were more mainly focused on the Lorentz force mechanism, concentrating on the dynamic magnetic field produced by the driving current in the coil. In a study on Rayleigh wave generation, FE models of the Lorentz force mechanism were used to depict the orientation of the bias field which can be selected such that the Lorentz forces due to the static and dynamic magnetic fields constructively interfere, enhancing signal amplitude [20,21]. Furthermore, they took after previous studies which showed the possibility of generating acoustic waves without the presence of a permanent magnet, or electromagnet, by using the self-generated magnetic field interacting with induced eddy current [5,7] , proving the enhancements of adding a ferrite back-plate [22]. Dixon and co-workers exploited a plate of magnetite iron oxide above the coil to enhance the induced magnetic flux density [22,23]. In other analytical research [24], the presence of two conductive layers was evaluated: the sample and an electrically conductive screen between the coil and the magnet, to reduce ultrasonic generation in the magnet. The impedance of the coil is affected by the extra conductive layer because eddy currents are induced in both the conductive media. This means that the original Dodd and Deeds model had to be adjusted in order to compute the correct impedance of the coil.

The analysis of previous research shows that even if the use of EMAT is widespread on conductive materials, little research has been carried out for implementing such devices on non-conducting materials. This is one of the main contributions of this thesis and is described in detail in this and subsequent chapters.

The following sections describe the basic principles of operation of EMATs, including mechanisms that contribute to the coupling, advantages and disadvantages of their application, types of EMATs, and their use on non-conducting samples.

2.2 Governing equations

2.2.1 Maxwell's equations and constitutive relations

EMATs generate and detect ultrasound usually in metals via an electromagnetic coupling which does not need direct contact between the sample and the transducer. The acoustic energy is produced into the sample by coupling the electrical energy through three mechanisms: the Lorentz [4,6,25,26], magnetization and magnetostriction mechanisms. The latter two can be included in one macro-group named magneto-elastic mechanisms [1,8]. In order to give an overview of the electromagnetic interaction between the device and an electrically conductive specimen, an introduction of the Maxwell's equations is required, as listed in the following expressions.

$$\nabla \cdot \vec{D} = \rho, \tag{2.1}$$

$$\nabla \cdot \vec{B} = 0, \tag{2.2}$$

$$\nabla \times \vec{E} = -\frac{\partial \vec{B}}{\partial t}, \tag{2.3}$$

$$\nabla \times \vec{H} = \vec{J} + \frac{\partial \vec{D}}{\partial t}. \tag{2.4}$$

Here $\vec{D}$ is the electric displacement, ρ is the charge density, $\vec{B}$ is the magnetic flux density, $\vec{E}$ is the electric field, $\vec{H}$ is the magnetic field strength and $\vec{J}$ is the current density. The following constitutive relations [27] also accompany Maxwell's equations:

- Between the magnetic flux density ($\vec{B}$) and the magnetic field ($\vec{H}$)

$$\vec{B} = \mu_0(\vec{H} + \vec{M}) \tag{2.5}$$

where $\vec{M}$ is the magnetisation, which represents how a material reacts to an applied magnetic field, and μ_0 is the permeability of free space. If the relation between $\vec{M}$ and $\vec{H}$ is known for the material in which the field is present, the equation can often be simplified. If the assumption of an isotropic and homogeneous material is made, the equation can be further simplified to:

$$\vec{B} = \mu_0 \mu_r \vec{H} \tag{2.6}$$

where μ_r is the relative permeability.

- Between the electric displacement ($\vec{D}$) and the electric field ($\vec{E}$)

$$\vec{D} = \varepsilon_0 \vec{E} + \vec{P} \tag{2.7}$$

where ε_0 is the permittivity of the free space, and $\vec{P}$ is the polarisation field. The equation describes how a material reacts at the presence of an electric field. Once again, this can be reduced if the relation between $\vec{P}$ and $\vec{E}$ is known and if the material is isotropic and homogeneous the equation can be approximated to:

$$\vec{D} = \varepsilon_0 \varepsilon_r \vec{E} \tag{2.8}$$

where ε_r is the relative permittivity.

- The current density within a sample ($\vec{J}$) and the electric field:

$$\vec{J} = \sigma \vec{E} \tag{2.9}$$

where σ is the material electrical conductivity. This equation plays a crucial role in generating elastic waves within a specimen. In section 2.5 the importance of this equation will be described.

2.2.2 Skin depth

In order to couple an EMAT electromagnetically to a conducting sample the first step is to feed an alternating current ($\overrightarrow{I_c}$) into its coil. The dynamic magnetic field ($\overrightarrow{B_d}$) due to the driving current probes the sample surface and is linked to the induced electric field ($\vec{E}$) at the perimeter of the sample, as stated in Faraday's law (equation 2.3). The electric field induces an eddy current (also called image current) within the sample surface. In turn, this current will produce a magnetic field and oppose the penetration of the electromagnetic wave deeper into the specimen. In order to better explain this phenomenon, an expression representing an electromagnetic wave propagating in a conducting sample needs to be derived by following this procedure [27]:

$$\nabla \times \vec{E} = -\frac{\partial \vec{B}}{\partial t}, \tag{2.10}$$

$$\nabla \times (\nabla \times \vec{E}) = -\frac{\partial (\nabla \times \vec{B})}{\partial t}. \tag{2.11}$$

The function $\nabla \times (\nabla \times \vec{E})$ can be substituted using a vector identity:

$$\nabla \times \left(\nabla \times \vec{E}\right) = -\nabla^2 \vec{E} + \nabla(\nabla \cdot \vec{E}) \tag{2.12}$$

furthermore, if the net charge density in the sample is assumed to be zero $(\nabla \cdot \vec{E} = 0)$, hence the vector identity further reduces $(\nabla \times \left(\nabla \times \vec{E}\right) = -\nabla^2 \vec{E})$, simplifying equation 2.11 to:

$$\nabla^2 \vec{E} = \frac{\partial (\nabla \times \vec{B})}{\partial t}. \tag{2.13}$$

The right hand side of this expression can be conveyed in terms of the electric field as:

$$\nabla^2 \vec{E} = \mu_0 \mu_r \sigma \frac{\partial \vec{E}}{\partial t} + \mu_0 \mu_r \varepsilon_0 \varepsilon_r \frac{\partial^2 \vec{E}}{\partial t^2}. \tag{2.14}$$

Since EMATs are normally used at frequencies lower than 100 MHz [1], the second term in the right hand side of the previous equation can be neglected. Thus, equation 2.14 takes the form:

$$\nabla^2 \vec{E} = \mu_0 \mu_r \sigma \frac{\partial \vec{E}}{\partial t}. \tag{2.15}$$

A solution to this is:

$$\vec{E} = \overrightarrow{E_0} e^{j(\omega t - z/\delta)} e^{-z/\delta} \tag{2.16}$$

where ω is the angular frequency of the electromagnetic field in the wire or sample, z is the depth into the material from the surface, and δ is the skin depth (or depth of penetration) [27,28], which can be expressed as:

$$\delta = \sqrt{\frac{2}{\mu_0 \mu_r \sigma \omega}}. \tag{2.17}$$

This quantity measures how quickly the electric field is attenuated in the specimen. From this expression it can be seen that when $z = \delta$ the magnitude of the electric field has diminished by $1/e$ of its surface value ($\overrightarrow{E_0}$).

It is worth noting that if the thickness of the sample is much greater than the skin depth, increasing the frequency of the driving alternating currents, this volume phenomenon can be approximated as a surface phenomenon, even though, in reality, coils produce current profiles not only along the thickness direction. This assumption will be carried on over the whole body work as the thin metallic foil, where the eddy currents are induced, is attached at the surface of a thick insulator, as depicted in figure 2.3. The ratio between the sample thickness (within the range of mm, at least 1 mm) and the metallic foil thickness (0.065 mm), where the eddy currents are induced, is over 10 times. The foil thickness has been selected to minimise the length of travel for maximising the transfer of the elastic waves into the sample.

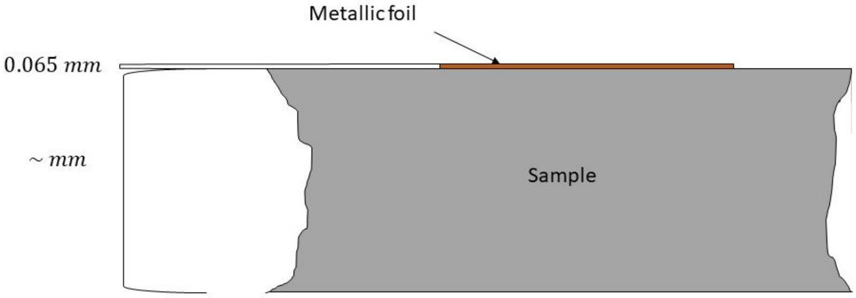

Figure 2.3 Schematic diagram showing the metallic foil attached at the surface of sample.

2.2.3 Generation – Lorentz force mechanism

A charged particle in a medium under the presence of an electric and magnetic field experiences a force $\vec{F}$, called the Lorentz force [29]:

$$\vec{F} = q(\vec{E} + \vec{v} \times \vec{B}) \tag{2.18}$$

where q is the electric charge, $\vec{E}$ is the electric field, $\vec{v}$ is the velocity of the charged particle and $\vec{B}$ is the magnetic flux density. Macroscopically, when a sensor is place close to the surface, an eddy current density $\vec{J}$ is induced in it. Lorentz forces then arise in the presence of $\vec{B}$. If the medium is electrically neutral, the Lorentz force is reduced to:

$$\vec{F} = q\vec{v} \times \vec{B} = \vec{J} \times \vec{B}. \tag{2.19}$$

In this equation the magnetic field is the superposition of all sources of magnetic field: the static magnetic field $\overrightarrow{B_s}$ supplied by the EMAT itself (precisely the magnet) and the dynamic magnetic field $\overrightarrow{B_d}$ produced by current flowing in the coil. As shown in figure 2.4, the two magnetic fields act differently on the sample.

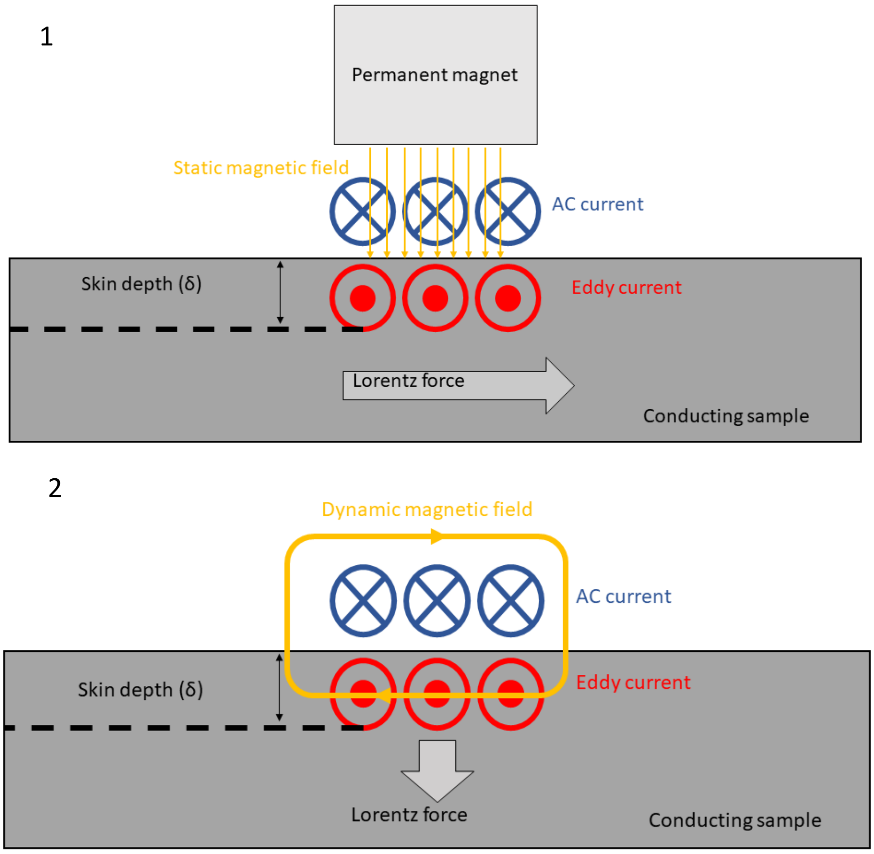

Figure 2.4 Diagram showing the Lorentz force arising from the interaction between a static magnetic field (1) and dynamic magnetic field (2) with eddy currents induced in the near-surface of the sample.

Generally the Lorentz force is predominant due to the static magnetic field, especially if the driving current is below 100 A in the EMAT coil. For higher currents the force generated by the dynamic field is still relatively small [22,23], but not negligible [30].

As it will explained in detail later in this section, the electrons transfer the Lorentz force experienced to the ions which oscillating cause a vibration. The oscillation is at right angles to both the eddy currents and the external magnetic field, as equation 2.19 shows. Integrating the current density along the depth of the sample (z) is possible to retrieve the total induced current for a unit surface area. Exploiting equation 2.9 and the expression for the electric field (equation 2.16) this gives:

$$I = \int_0^\infty J dz = \frac{J_0}{\sqrt{\omega\mu\sigma}} e^{j(\omega t - \pi/4)} \tag{2.20}$$

where $J_0 = \sigma E_0$. Hence the Lorentz force in the sample is proportional to the driving current oscillating at the same frequency as the current flowing in the EMAT coil, but with a phase delay of $\pi/4$, when only the external magnetic field is considered. On the other hand, when only the self-field is taken in account, the dynamic magnetic field ($\overrightarrow{B_d}$) oscillates proportionally to the driving AC as well as J_e. Therefore the force on the ions is proportional to I^2, instead of I. This causes a doubling in frequency of the ion oscillations and so the ultrasound generated by the self-field.

Microscopically, the electric field $\vec{E}$ induced by the driving current applies a Coulomb force $-e\vec{E}$ on the electrons of the specimen and accelerates them to an average velocity $-eE\tau/m$; due to the presence of a static magnetic flux density $\vec{B}$ the electrons are also subjected to the Lorentz force $e\overrightarrow{v_e} \times \vec{B}$. In the previous equation, e represents the charge of the electron and $\overrightarrow{v_e}$ its mean velocity [1]. Due to the different time scale between the interaction electron-ion and the oscillation of the applied AC current ($T \gg \tau$, where T is the period of the AC pulse), the inertial forces of the electrons can be ignored for harmonic oscillation much slower than the mean frequency of electron-ion collision $1/\tau$, the equation describing the motion reduces to:

$$\frac{n_e(m\overrightarrow{v_e})}{\tau} = -n_e e(\vec{E} + \overrightarrow{v_e} \times \vec{B}) \tag{2.21}$$

where n_e represents the number density of electrons and m the electron mass. The momentum of the electrons is exchanged with the ions of the metal through collisions, and force acting on the positive charges can be written as:

$$\vec{F} = NZ_i\left(\vec{E} + \vec{v_i} \times \vec{B}\right) + \frac{n_e(m\vec{v_e})}{\tau} \tag{2.22}$$

where N is the number density, Z_i is the charge of ions and $\vec{v_i}$ is their velocity. By substituting equation 2.21 in 2.22 it can be seen that [1]:

$$\vec{F} = -n_e e\vec{v_e} \times \vec{B} \tag{2.23}$$

considering that, $NZ_e = n_e e$ and the velocity of the ions is much lower than that of the electrons, therefore it will be neglected. Hence comparing the general equation for the Lorentz force (equation 2.19) with equation 2.23, we can deduce that $-n_e e\vec{v_e}$ is the eddy current density, $\vec{\jmath}$.

In conclusion, when the presence of an eddy current in the metallic sample has been defined, and under the effect of a magnetic field $\vec{B}$, the Lorentz force in equation 2.23 can cause an ultrasonic wave to travel in the medium, moreover, as already mentioned, this force can be treated as a surface force for ultrasonic wavelength much greater than the skin depth.

2.2.4 Generation – Magneto-elastic mechanisms

The Lorentz mechanism explained in the previous section will always act when an EMAT is applied on a conducting sample. The mentioned mechanism is present also within ferromagnetic materials, though two more mechanisms have to be considered: magnetization force and magnetostriction [31].

When ferromagnetic materials are subjected to an external magnetic field ($\vec{H}$) the magnetisation force ($\vec{M}$) occurs. According to Hirao and Ogi [1], after the correction given by Ribichini et co. [32], the force acting in the sample and on its surface can be expressed as:

$$\vec{F} = \int_V \nabla^*\left(\vec{M} \cdot \vec{H}\right)dv + \frac{1}{2}\mu_0 \int_S \vec{n}M_n^2 dS \tag{2.24}$$

Where ∇^* is nabla operating only on the magnetic field, $\vec{n}$ is a unit vector normal to the surface of the sample, and M_n is the normal component of the magnetisation at the surface. On the right hand side of the expression the first term is known as the magnetisation force, while the second one occurs due to a sudden change of the electromagnetic fields at the surface and dissipates inside the sample.

Magnetostriction, on the other hand, occurs because ferromagnetic domains tend to align along the direction of an external magnetic field, provoking a net mechanical strain [33]. In case the magnetic field has a component varying in time this strain can be utilized to generate ultrasonic waves [7,8]. The ultrasound transduction efficiency from the latter mechanism strongly relies on the physical material properties such as elastic constants and electromagnetic properties; it is also dependent on the bias magnetic field and on the change of all these factors by cause of temperature variations. As shown in figure 2.5, the contribution of magnetostriction to the transduction efficiency is predominant at lower bias fields, though at high fields the Lorentz contribution dominates over magnetostriction [6].

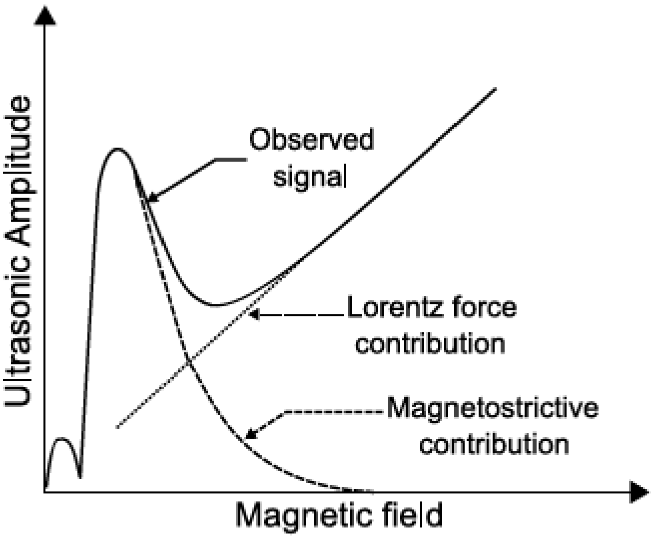

Figure 2.5 Schematic dependence of transduction efficiency due to Lorentz force and magnetostriction mechanisms in iron (from [34]).

The two magneto-elastic mechanisms mentioned above will not be considered further within the rest of the thesis as the ultrasonic generation is due predominantly to the Lorentz contribution in non-magnetic materials.

2.2.5 Detection – Velocity sensor

As the ultrasonic wave travels through a conducting sample, atoms move in the lattice normal to the direction of propagation, both ions and electrons will move in unison. In presence of a static magnetic field parallel to the wave propagation when this motion occurs, both atoms experience a Lorentz force. The ion acceleration due to this force is irrelevant when compared to the of the electrons, thus only electrons generate an eddy current; which, in turn, will induce an image current on the EMAT coil as depicted in section 2.2.3 for the generation process.

A key remark in the detection process is that EMATs are particle velocity sensors [10], which can be shown by following the procedure exploited by Dixon et al. [35]. The displacement occurring due to an ultrasonic wave travelling up to the material surface can be expressed as:

$$\vec{S}(t,z) = \overrightarrow{S_0} e^{i(\omega t - kz)} \tag{2.25}$$

where ω is the angular frequency of the ultrasonic wave, k is the wave number, t is the time and z is the direction of propagation. At the surface, the displacement is obtained by the superposition of the wave travelling up to the surface and the reflection travelling away, see figure 2.6, as described below:

$$\vec{\xi} = \overrightarrow{S_0} e^{i\omega t} e^{ikz} e^{-ikz} = \overrightarrow{S_0} e^{i\omega t}(2\cos(kz)) \tag{2.26}$$

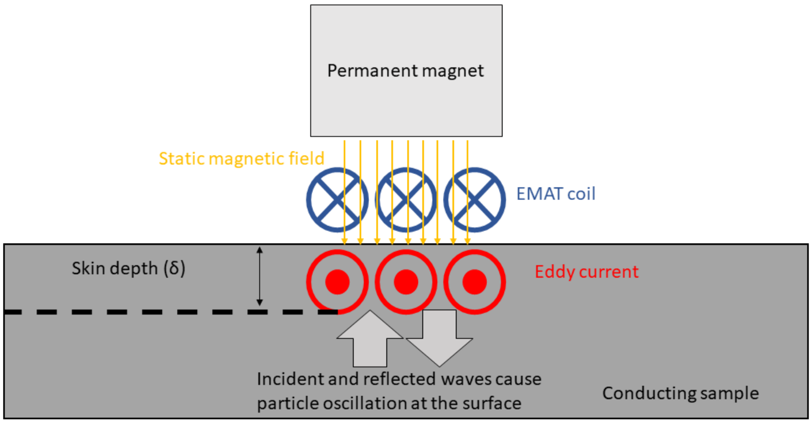

Figure 2.6 EMAT detection mechanism. The interaction between the particle displacement and the magnetic field induces eddy current in the near-surface of the sample which are detected by the EMAT coil.

Since the induction of the electric field due to the acoustic wave is proportional to the product of the rate of displacement variation ($\frac{\partial \vec{\xi}}{\partial t}$) and the static magnetic field ($\vec{B}$), the current density at the surface ($\vec{J}(z)$) can be expressed as:

$$\vec{J}(z) = \sigma \frac{\partial \vec{\xi}}{\partial t} \vec{B} = i\omega\sigma \overrightarrow{S_0} e^{i\omega t}(2\cos(kz)) \tag{2.27}$$

Since the image current is restricted within the skin depth (δ) for a certain frequency, this means that $z \leq \delta$. Furthermore, the skin depth is typically much smaller than the ultrasonic wavelength ($k\delta \ll 1 \Longrightarrow \cos(k\delta) \approx 1$), as a result the current density at the surface can be approximated to:

$$\vec{j}(z) \approx i\omega\sigma 2\overrightarrow{S_0}(t,0)e^{i\omega t} \approx 2\sigma \frac{\partial(\overrightarrow{S_0}(t,0))}{\partial t} \tag{2.28}$$

which shows that $\vec{j}(z)$ being proportional to the first time derivative of displacement (i.e. velocity), hence EMATs are actually velocity sensors.

2.3 Typical EMAT designs

2.3.1 Bulk-wave EMAT

Figure 2.7 depicts the configuration of a bulk-wave EMAT, which is able to generate and detect longitudinal waves and shear waves with a polarisation parallel to the specimen surface [1].

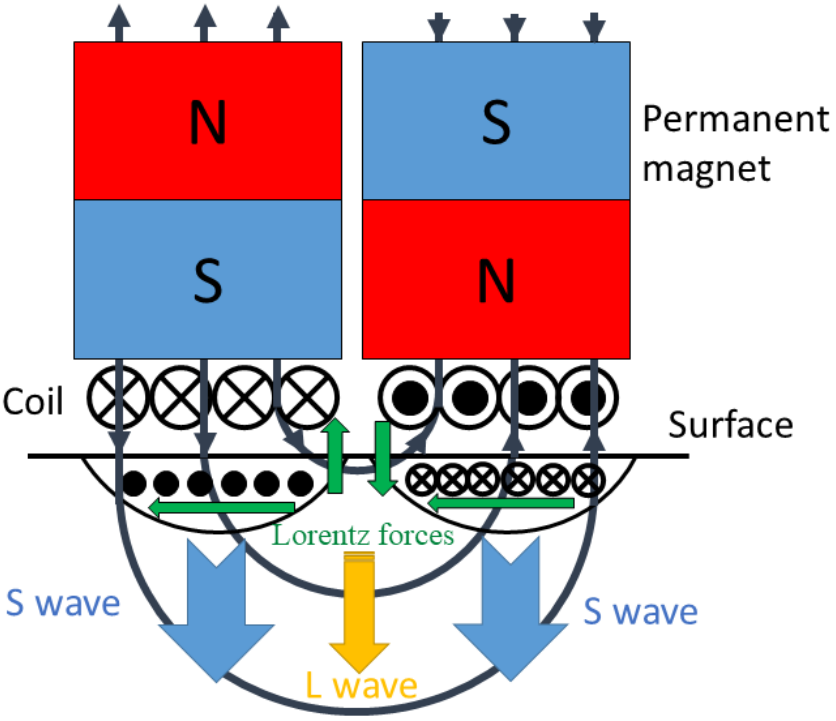

Figure 2.7 Generation mechanism by Lorentz force of a bulk-wave EMAT (from [7]).

The static magnetic field (typically 1.35 T) provided by the permanent magnet is oriented normally to the surface under the unidirectional coil elements and tangentially at the centre and edges of the coil elements. The resultant force ($\vec{F}$) is parallel to the surface. In these cases, such an EMAT will be referred to as shear wave EMAT.

On the other hand, figure 2.8 depicts another bulk-wave EMAT.

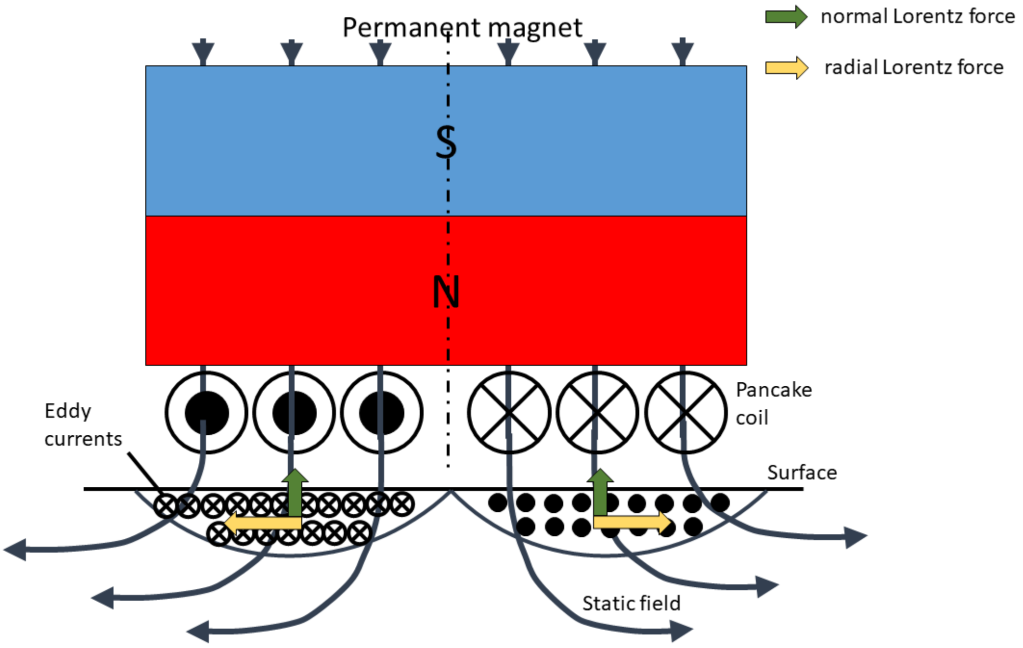

Figure 2.8 Lorentz force mechanism of dual-mode EMAT (after [8]).

This consists of a single cylindrical permanent magnet and a flat pancake coil. The magnet provides a static magnetic field having radial and normal components, which interact with the eddy currents generating Lorentz forces along the normal and radial directions, respectively.

For ferromagnetic material, magnetostriction forces will be present. Such forces generate simultaneously a longitudinal wave and radially-polarised shear wave propagating in the thickness direction, for this feature this is called dual-mode EMAT [36]. If the metal presents orthorhombic anisotropy, the shear waves decompose into two polarisations along the two principal directions producing the split resonance peaks. This kind of EMAT is typically used for in-plane measurements in rolled steel sheets [38] and the birefringent acoustoelastic stress measurement [39].

2.3.2 Meander line EMAT

This type of EMAT is used for generating Rayleigh and Lamb waves, and angled shear and longitudinal waves (travelling obliquely into the specimen) [1], its configuration is depicted in figure 2.9.

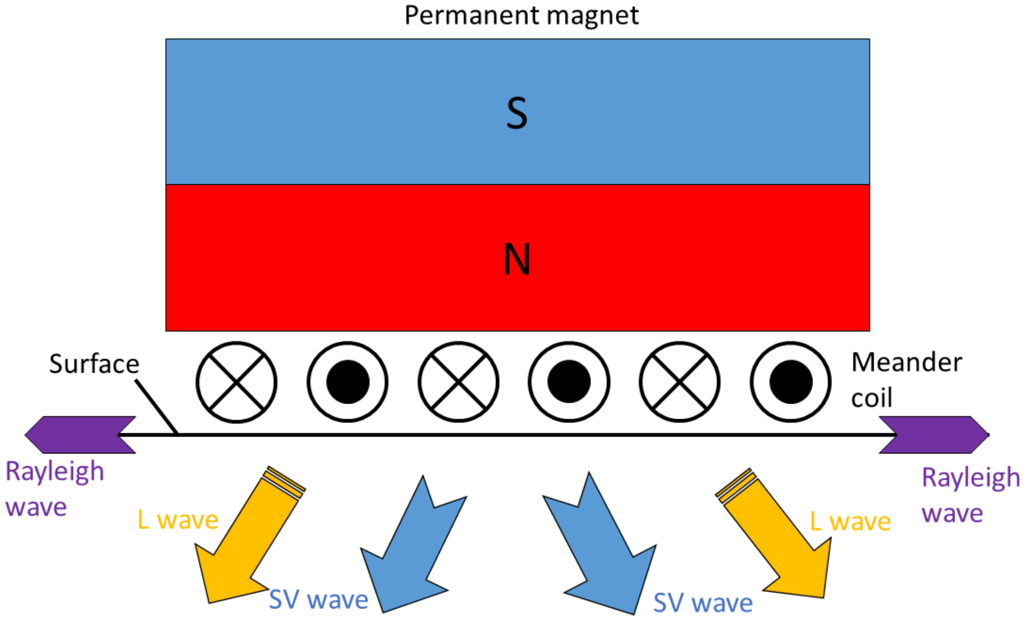

Figure 2.9 Ultrasonic waves generated by a permanent magnet and meander coil (after [9]).

The disadvantage of this EMAT is the difficulty of the mode identification in the received echoes. A normal biasing field and the coil (see figure 2.8) gives rise to Lorentz and magnetostriction forces parallel to the surface, whose directions alternate accordingly to the meander-line coil. The generation frequency is given by the meander-line period, which can be designed by manufacturing the coil by a printed circuit technique. Thus, it is possible to adjust the generation frequency by modifying the periodicity of the coil. Depending on the thickness of the sample, the device can generate Rayleigh waves (on thick samples) and Lamb waves (on thinner samples). In order to have the maximum transfer efficiency of Lamb waves, the wavelength needs to be tuned to the thickness of the sample [7], otherwise the generation would be corrupted by destructive interferences arising due to an excitation frequency which does not match the periodicity of the meander coil, its nominal wavelength. For generating SH waves the coil interacts with the tangential biasing magnetic field [41]. One drawback is the necessity of a very large biasing magnetic field when the static magnetic field is adopted along the straight lines of the meander-line coil.

2.3.3 Periodic Permanent Magnet (PPM) EMAT

PPM-EMATs are devices that generate shear waves that are polarised parallel to the surface of the specimen [9,41,42]. The shear waves propagate not only along the surface but also into the material [43]. The EMAT has been often adopted for measurements with the surface (Rayleigh) waves or Shear Horizontal (SH) waves in a plate. Such waves are attractive for NDT purposes and are generally not easily excited with traditional piezoelectric transducers. A classical configuration of this type of EMAT is illustrated in figure 2.10.

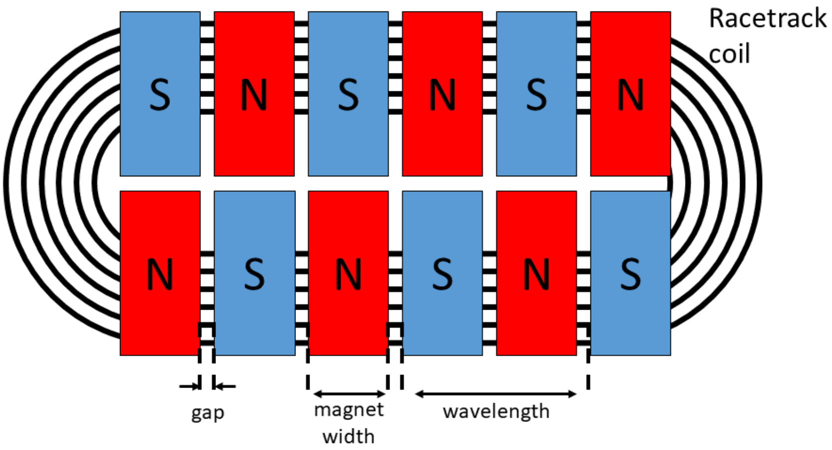

Figure 2.10 A PPM EMAT for emission and reception of SH waves (after [10]).

PPM EMATs' coils usually have a racetrack shaped coil in front of the PPM array, arranged in such a way that north and south (N/S) poles alternate periodically, as shown in figure 2.8 . Due the alternating polarity of the permanent magnets the tangential Lorentz and magnetostriction forces varies according to magnet array [1,9,45,46]. The maximum transfer efficiency occurs when the device is fed by a driving current chosen accordingly to the spacing of magnets (its nominal wavelength). The periodically alternating polarity sets the primary wavelength of the ultrasound generated. Therefore, in order to excite higher frequency SH waves, the width of the magnets needs to be decreased so the wavelength. Nonetheless, the efficiency drastically drops with reduced magnet thickness; thus, a limitation of this EMAT is its operation frequency, usually only up to ~1 MHz.

2.4 Advantages and limitations of EMATs

As explained in the previous sections, generation and reception occurs through an electromagnetic mechanism which does not require the devices to be in contact with the sample and, therefore, the use of any couplant (gel or water) is not necessary. The efficiency of the transduction decreases exponentially with the distance (lift-off) between the sensor and the specimen, confining the practical gap to a few millimetres. Nonetheless, this small separation is enough to have a relevant advantage over piezoelectric transducers in some applications, and indeed EMATs can be used in hot and hazardous environments such as sheet steel production [47,48]. Since contact is not necessary, easing the operation and reducing the need for surface treatment; furthermore, there is no need to take account of the variability given by the couplant, so that highly reproducible measurements can be attained. A further advantage of using EMATs over piezoelectric is the wide selection of ultrasonic modes that can be excited. The design of the geometry of the coil and the magnet, and their relative position plays a fundamental role in order to generate and detect a particular wave [1,49-51], as stated in the previous section.

On the other hand, the contactless nature of EMATs has some disadvantages: first of all, traditional piezoelectric transducers are still more efficient compared to electromagnetic transducers. Careful design and special electronics are necessary in order to enhance an otherwise rather poor signal-to-noise ratio [45]. Another issue with EMATs is that their performance is strictly dependent on the electromagnetic properties of the sample: a sensor working perfectly on one metal can give low-quality signals when adopted on another material. In addition, the operation principles of EMATs (fully explained in the previous sections) rely on the good electrical properties of specimens in order to generate and detect ultrasonic waves. Table 2.1 summarises the advantages and limitations of such devices.

Table 2. 1 Outline of the advantages and limitations of EMATs.

Advantages	**Limitations**
• No contact • Couplant-free • Multiple mode generation • High temperature inspection • High speed inspection • Reproducibility	• Low signal-to-noise ratio • Special equipment required • Material-dependent • Applicable “only” on good conductors or highly magnetostrictive metals

2.5 The use of a metallic foil

It is common belief to state that EMATs cannot be used on non-conducting or low electrical conductivity materials. However previous researches have already hinted [52] and demonstrated [19] the possibility of inspecting such materials by means of an easily applied and readily removable metallic foils for allowing the Lorentz force transduction. The latest research [19] has proved that SH waves can be excited and received in a variety of composites. However, no specific SH mode was carefully selected. The research in this thesis demonstrates the possibility of inspecting non-conducting engineering materials, specifically composites, with SH_0 wave mode generated by PPM EMATs. As already mentioned, the generation and reception mechanisms rely on the electrical conductivity (σ) of the sample under test. Typically σ in metals is in the order of $10^7\ (\Omega m)^{-1}$, whereas carbon fibre composites have at least up to 3 order of magnitude less conductivity, see table 2.2.

Table 2.2 Comparison electrical conductivity.

Material	**Electrical Conductivity**
Copper	$3.77\ \times 10^7\ (\Omega m)^{-1}$
Aluminium	$5.95\ \times 10^7\ (\Omega m)^{-1}$
Carbon Fibre Composite	$6.25\ \times 10^4\ (\Omega m)^{-1}$

Beyond the lower electrical conductivity composites are particular material in which fibres, which can be conductive (i.e. carbon fibres), are embedded in a matrix, which is dielectric (i.e. epoxy resin). For this feature, inducing eddy current is really difficult.

The removable metallic foil, a patch, is simply attached on the surface of the sample through a non-damaging and easily removable adhesive layer. The adhesive layer acts as a couplant between the metallic surface, whereby Lorentz forces arise within the patch due to a static magnetic field interacting with eddy currents induced by the coil; the resulting strains are then transmitted to the sample by mechanical coupling via the adhesive layer. The use of the metallic foil to electromagnetically generate ultrasound in non-conductive materials can be compared to the use of CHOTs (Cheap optical transducers) which are activated optically by laser-generated ultrasound [53]. These 2D structures can be printed or attached onto the surface. Unlike the metallic foils used in this thesis, the geometry of the driving (g-CHOT) and receiving (d-CHOT) CHOTs are different in order to enhance their operation of, respectively, the generation and detection of the wave mode [54].

Throughout my work the patches were provided by cutting a metallic tape commercially available. Normally the size of the patch used was enough for covering the entire active surface of the transducer, i.e. 5x5 cm. The chosen metallic tapes are made of copper and aluminium, and their features are listed in table 2.3.

Table 2.3 Metallic tapes.

Item name	Material	Width and length	Thickness
Advance Tapes AT525 Non-conductive Copper Tape	Copper	50 mm x 33 m	0.065 mm
3M 1436 Conductive Aluminium Tape	Aluminium	50 mm x 50 m	0.075 mm

During the experiments the use of aluminium tape was revealed to be unpractical because its adhesive layer was thicker than the metallic one making difficult the removal of the tape. For this reason, all experiments which will be presented are made by means of copper tape. The effect of the patch size has been studied and it will be reported later.

The patches are to be placed onto the surface of non-conducting materials in order to allow the electromagnetic mechanism to generate and detect waves with EMATs. Once the measurement is complete, the patches can be easily removed without damaging the sample, a necessary property for the technique to be considered as non-destructive. Rarely the metallic tape can leave a little residual glue on the sample, whenever that happens it can be easily removed by cleansing the surface with simple water. Figure 2.11 depicts the set-up adopted for inspecting non-conducting materials.

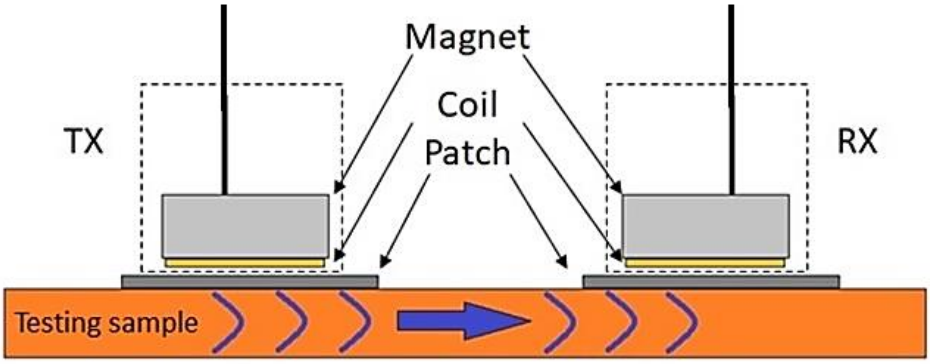

Figure 2.11 Diagram of the set-up adopted for inspection.

2.6 Conclusions

This chapter gave a brief introduction of the past research into EMAT operation, highlighting the extensive work applied to conducting or magnetic materials. A review of the operation principles of EMATs was presented by analysing the physical principles that allow such devices to generate and detect ultrasonic waves. Special attention was given to the Lorentz force mechanism which has been the only mechanism considered as the sample tested were not magnetic. The concept of a metallic foil patch for use on non-conducting samples was then introduced. The detailed mechanisms that operate within such patches have not been studied extensively in the literature, in terms of how the eddy current is generated within the patch, and how the Lorentz force created then results in the creation of a guided wave. This concept will be studied further in the following chapters.

References Chapter 2

[1] M. Hirao, H. Ogi, EMATs for science and industry: noncontacting ultrasonic mesurements, Boston: Kluwer Academic Publishers, 2003.

[2] J. C. Maxwell, On physical lines of force, London, 1862.

[3] C. C. Grimes, S. J. Buchsbaum, "Interaction Between Helicon Waves and Sound Waves in Potassium," *Physical Review Letters*, vol. 12, no. 13, pp. 357-360, 1964.

[4] M. R. Gaerttner, W. D. Wallace, B. W. Maxfield, "Experiments Relating to the Theory of Magnetic Direct Generation of Ultrasound in Metals," *Physical Review,* vol. 184, no. 3, pp. 702-704, 1969.

[5] E. R. Dobbs, "Electromagnetic generation of ultrasonic waves," in *Physical Acoustic: Principles and Method - volume 10*, New York, Academic Press, 1973, pp. 127-191.

[6] R. Thompson, "A Model for the Electromagnetic Generation and Detection of Rayleigh and Lamb Waves," *IEEE Transactions on Sonics and Ultrasonics,* vol. 20, no. 4, pp. 340-346, 1973.

[7] R. B. Thompson, "Mechanisms of electromagnetic generation and detection of ultrasonic Lamb waves in iron-nickel alloy polycrystals," *Journal of Applied Physics,* vol. 48, no. 12, pp. 4942-4950, 1977.

[8] R. B. Thompson, "A model for the electromagnetic generation of ultrasonic guided waves in ferromagnetic metal polycrystals," *IEEE Transactions on Sonics and Ultrasonics,* vol. 25, no. 1, pp. 7-15, 1978.

[9] R. B. T. C. F. Vasile, "Excitation of horizontally polarized shear elastic waves by electromagnetic transducers with periodic permanent magnets," *Journal of Applied Physics,* vol. 50, no. 4, pp. 2583-2588, 1979.

[10] K. Kawashima, "Theory and numerical calculation of the acoustic field produced in metal by an electromagnetic ultrasonic transducer," *The Journal of the Acoustical Society of America,* vol. 60, no. 5, pp. 1089-1099, 1976.

[11] W. E. D. C. V. Dodd, "Analytical Solutions to Eddy-Current Probe-Coil Problems," *Journal of Applied Physics,* vol. 39, no. 6, pp. 2829-2838, 1968.

[12] K. Kawashima, "Quantitative Calculation and Measurement of Longitudinal and Transverse Ultrasonic Wave Pulses in Solid," *IEEE Transactions on Sonics and Ultrasonics,* vol. 31, no. 2, pp. 83-93, 1984.

[13] D. M. a. W. L. R. Ludwing, "A comparative study of analytical and numerical transient force excitations on an elastic half-space," *IEEE Transactions on Ultrasonics, Ferroelectrics and Frequency Control,* vol. 36, no. 3, pp. 342-350, 1989.

[14] R. Ludwing and X. W. Dai, "Numerical and analytical modeling of pulsed eddy currents in a conducting half-space," *IEEE Transactions on Magnetics,* vol. 26, no. 1, pp. 299-307, 1990.

[15] R. Ludwing and X. W. Dai, "Numerical simulation of electromagnetic acoustic transducer in the time domain," *Journal of Applied Physics,* vol. 69, no. 1, pp. 89-98, 1991.

[16] R. Ludwig, "Numerical implementation and model predictions of a unified conservation law description of the electromagnetic acoustic transduction process," *IEEE Transactions on Ultrasonics, Ferroelectrics and Frequency Control,* vol. 39, no. 4, pp. 481-488, 1992.

[17] R. Ludwig, "Theoretical basis for a unified conservation law description of the electromagnetic acoustic transduction process," *IEEE Transactions on Ultrasonics, Ferroelectrics and Frequency Control,* vol. 39, no. 4, pp. 476-480, 1992.

[18] R. Ludwig, Z. You, and R. Palanisamy, "Numerical simulations of an electromagnetic acoustic transducer-receiver system for ndt applications," *IEEE Transactions on Magnetics,* vol. 29, no. 3, pp. 2081-2089, 1993.

[19] D. K. Hsu, K. Im and I. Yang, "Applications of Electromagnetic Acoustic Transducers in the NDE of Non-Conducting Composite Materials," *KSME International Journal,* vol. 13, no. 5, pp. 403-413, 1999.

[20] S. Dixon and S. B. Palmer, "Wideband low frequency generation and detection of Lamb and Rayleigh waves using electromagnetic acoustic transducers (EMATs)," *Ultrasonics,* vol. 42, no. 10, pp. 1129-1136, 2004.

[21] X. Jian, S. Dixon, R. S. Edwards and J. Reed, "Coupling mechanism of electromagnetic acoustical transducers for ultrasonic generation," *The Journal of the Acoustical Society of America,* vol. 119, no. 5, pp. 2693-2701, 2006.

[22] X. Jian and S. Dixon, "Enhancement of EMAT and eddy current using a ferrite back-plate," *Sensors and Actuators A: Physical,* vol. 136, no. 1, pp. 132-136, 2007.

[23] S. Dixon and X. Jian, "Eddy current generation enhancement using ferrite for electromagnetic acoustic transduction," *Applied Physics Letters,* vol. 89, no. 19, p. 193503, 2006.

[24] X. Jian, S. Dixon and S. B. Palmer, "In-plane and out-of-plane particle velocity measurement using electromagnetic acoustical transducers," *IEEE Ultrasonic symposium*, pp. 1276-1279, 2005.

[25] W.P Mason and R. N. Thurston, Physical acoustic: Principles and methods - volume 10, New York: Academic Press, 1973.

[26] W. P Mason and R. N. Thurston, Physical acoustic: Principles and methods - volume 14, New York: Academic Press, 1979.

[27] I. S. Grant and W. R. Phillips, Electromagnetism, John Wiley & Sons, 1991.

[28] H. A. Wheeler, "Formulas for the skin effect," *Proceedings of the IRE,* vol. 30, no. 9, pp. 412-424, 1942.

[29] D. S. Jones, The theory of electromagnetism, Pergamon Press, 1964.

[30] Y. Fan, The analysis of surface defects using the ultrasonic Rayleigh surface, University of Warwick, 2008.

[31] H. Ogi, "Field dependence of coupling efficiency between electromagnetic field and ultrasonic bulk waves," *ournal of Applied Physics,* vol. 82, no. 3, pp. 3940-3949, 1997.

[32] R. Ribichini, P. B. Nagy and H. Ogi, "The impact of magnetostriction on the transduction of normal bias field EMATs," *NDT&E International,* vol. 51, pp. 8-15, 2012.

[33] D. Jiles, Introduction to magnetism and magnetic materials, Chapman & Hall, 1991.

[34] R. B. Thompson, "A model for the electromagnetic generation of ultrasonic guided waves in ferromagnetic metal polycrystals," *IEEE Transactions on Sonics and Ultrasonics*, vol. 25, no. 1, pp. 7-15, 1978.

[35] S. Dixon, C. Edwards and S. B. Palmer, "High-accuracy non-contact ultrasonic thickness gauging of aluminium sheet using electromagnetic acoustic transducer," *Ultrasonics*, vol. 39, no. 6, pp. 445-453, 2001.

[36] M. Hirao and H. Ogi, "Bulk-Wave EMATs," in *Electromagnetic acoustic transducers - Noncontacting ultrasonic measurements using EMATs*, Springer, 2016, p. 40.

[37] M. Hirao and H. Ogi, "Bulk-wave EMATs," in *Electromagnetic acoustic transducers - noncontacting ultrasonic measurements using EMATs,* Springer, 2016, p. 41.

[38] S. Dixon, C. Edwards and S.B. Palmer, "Texture measurements of metal sheets using wideband electromagnetic acoustic transducers," *Journal of Physics D: Applied Physics,* vol. 35, no. 8, pp. 816-824, 2002.

[39] M. Hirao, H. Ogi and H. Fukuoka, "Advanced Ultrasonic Method for Measuring Rail Axial Stresses with Electromagnetic Acoustic Transducer," *Research in Nondestructive Evaluation,* vol. 5, no. 1, pp. 211-223, 1994.

[40] G. L. Workman, K. Doron and P. O. Moore, "Non Destructive Testing Handbook Ultrasonic Testing," *American Society for nondestructive testing,* 2007.

[41] H. Ogi, E. Goda and M. Hirao, "Increase of Efficiency of Magnetostriction SH-Wave Electromagnetic Acoustic Transducer by Angled Bias Field: Piezomagnetic Theory and Measurement," *Japanese Journal of Applied Physics,* vol. 42, no. Part 1, No 5B, pp. 3020-3024, 2003.

[42] M. Hirao and H. Ogi, "An SH-wave EMAT technique for gas pipeline inspection," *NDT & E International,* vol. 32, no. 3, pp. 127-132, 1999.

[43] W. P. Mason, R. N. Thurston and A. D. Pierce, Ultrasonic Measurement Methods, Academic Press, 1990.

[44] P.A Petcher, S.E. Burrows and S.Dixon, "Shear horizontal (SH) ultrasound wave propagation around smooth corners," *Ultrasonics,* vol. 54, no. 4, p. 998, 2014.

[45] M. G. Silk, Ultrasonic transducers for nondestructive testing, Bristol: A. Hilger, 1984.

[46] Y. Ohtsuka, M. Higashi, M. Nishikawa, "Fundamental experiment for inspection of cooling pipes in operation by using ultrasonic technique," *Fusion Engineering and Design,* vol. 81, no. 8-14, pp. 1583-1587, 2006.

[47] R. B. Thompson, S. S. Lee, and J. F. Smith, "Angular dependence of ultrasonic wave propagation in a stressed, orthorhombic continuum: theory and application to the measurement of stress and texture," *The Journal of the Acoustical Society of America,* vol. 80, no. 3, pp. 921-931, 1986.

[48] S. Dixon and M. D. G. Potter, "Ultrasonic texture measurement of sheet metals: An integrated system combining lamb and shear wave techniques," *Nondestructive Testng and Evaluation,* vol. 20, no. 4, pp. 201-210, 2005.

[49] B. W. Maxfield and C. M. Fortunko, "The design and the use of electromagnetic acoustic wave transducers (emats)," *Materials Evaluation,* vol. 41, pp. 1399-1408, 1983.

[50] R. B. Thompson, "Physical principles of measurements with EMAT transducers," in *Ultrasonic Measruement Methods,* New York, Academic Press, 1990, pp. 157-200.

[51] H. Kwun, C. M. Teller, "Magnetostrictive generation and detection of longitudinal, torsional, and flexural waves in a steel rod," *The Journal of the Acoustical Society of America,* vol. 96, no. 2, pp. 1202-1204, 1994.

[52] T.L. Szabo, H.M. Frost, "SAW Electromagnetic Transducer Design for Nondestructive Evaluation Applications," *IEEE Transactions on Sonics and Ultrasonics,* vol. 23, no. 5, pp. 323-328, 1976.

[53] T. Stratoudaki, J. A. Hernandez, M. Clark, M.G. Somekh, "Cheap optical transducers (CHOTs) for narrowband ultrasonic applications," *Measurement Science and Technology,* vol. 18, no. 3, pp. 843-851, 2007.

[54] T. Stratoudaki, M. Clark, M. Somekh, A. Arca, "CHeap Optical Transducers (CHOTs) for generation and detection of longitudinal waves," *IEEE International Ultrasonics Symposium, IUS,* pp. 961-964, 2012.

Chapter 3

FE Modelling of EMATs using metallic patches

3.1 Introduction

It was seen in Chapter 2 that the use of a thin metallic patch has not been fully investigated for use with EMATs. This chapter introduces the method adopted to study this problem for an EMAT source. The method used can be divided into three steps [1-3]:

1. Calculation of the magnetic flux density and current density within the metallic patch (COMSOL)
2. Calculation of the Lorentz forces in the patch (Matlab)
3. Prediction of wave propagation within the sample (PZFlex)

The output of the last step can then be compared to actual measurements for validating the results acquired.

The finite element method (FEM) is employed widely in all engineering fields in order to provide accurate predictions in cases where the geometry is complicated [4,5]. It can be adopted for modelling a large variety of applications including structural mechanics, fluid dynamics, ultrasound propagation and electromagnetic induction – as in this case. The FEM can be summarised as follow: a real system is converted into a series of small regions, named elements, with simple geometries. The elements are then reconnected at discrete points, named nodes. The governing equations are applied to each element and the unknown values at the nodes can be achieved. The behaviour over the whole domain can be determined by connecting the elements together through the nodes.

3.2 COMSOL

COMSOL Multiphysics is the commercial FEM software chosen for solving the electromagnetic equations that govern the generation via EMAT of guided waves.

As explained in Chapters 1 and 2, the Lorentz force mechanism is based on the interaction between magnetic flux density and eddy currents. The former are derived from a static magnetic model which computes the $\vec{B}$ field generated by a series of permanent magnets, arranged with alternating polarity placed above the sample (in this case a metallic patch). The latter, on the other hand, needs a dynamic electromagnetic model, which evaluates the eddy current density $\vec{J}$ induced in the sample by a current flowing in a racetrack coil. In this section the procedure utilised for computing these quantities will be explained. The probe considered and modelled here is a ppm EMAT, having a 10 mm nominal wavelength as depicted in figure 3.1.

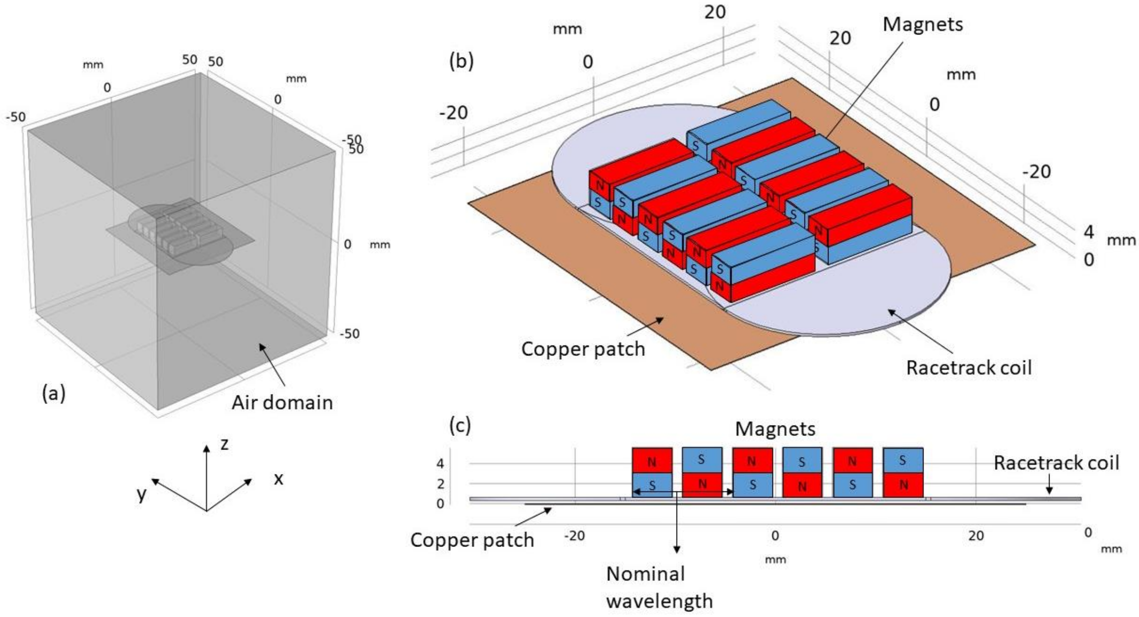

Figure 3.1 Design of fundamental components of a ppm EMAT on a metallic patch in COMSOL: (a) Whole domain; (b) magnet arrangement and racetrack coil on top of the copper patch; (c) Side view of magnets, racetrack coil and copper patch.

Due to the complexity and the computational demand for calculating simultaneously the static magnetic field and the eddy currents on the patch, the two distinct phenomena are treated separately. In the next sections, each one will be explained.

3.2.1 Calculation of magnetic flux density

As permanent magnets are used, the calculation of the magnetic flux density is performed by adopting a stationary model: the intensity of the magnetic field does not vary in time. This model follows Gauss' law for magnetic field (equation 2.2). A cubic domain filled with air is designed for simulating the surrounding environment. The dimensions of the cube are 100 x 100 x 100 mm, centred at the origin (0,0,0) of the (X,Y,Z) system. All dimensions presented in this body work are in mm. Inside the main domain, the metallic patch is modelled according to the real dimensions. The metallic patch is a thin foil of dimensions 50 x 50 mm and 0.065 mm thickness, centred at (0,0,-0.0325) in order to have its surface at z = 0, just for simplicity, as depicted in figure 3.2.

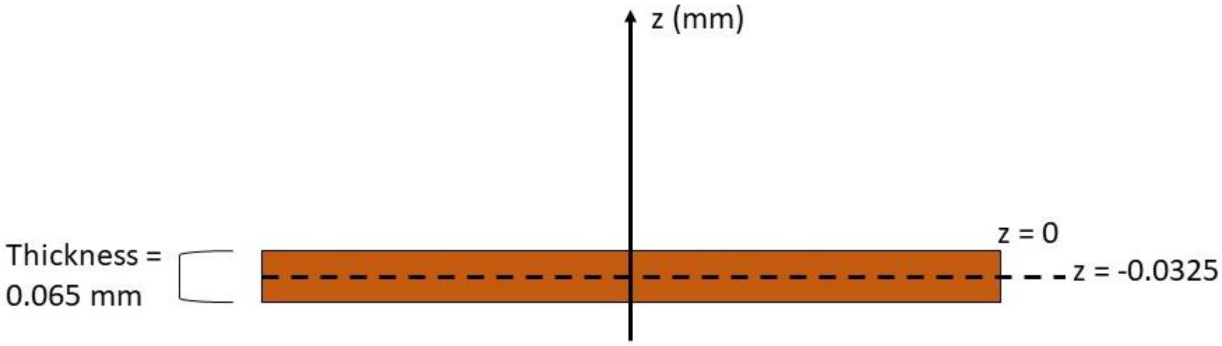

Figure 3.2 Side view of the metallic patch.

Then one magnet is introduced, its dimensions are 13 x 4 x 5 mm, as shown in figure 3.3. The lift-off of the magnets is established, taking into account the presence of the coil, even though it is not present at this stage. The coordinates of the magnet are (7.5,-12.7,-3.115).

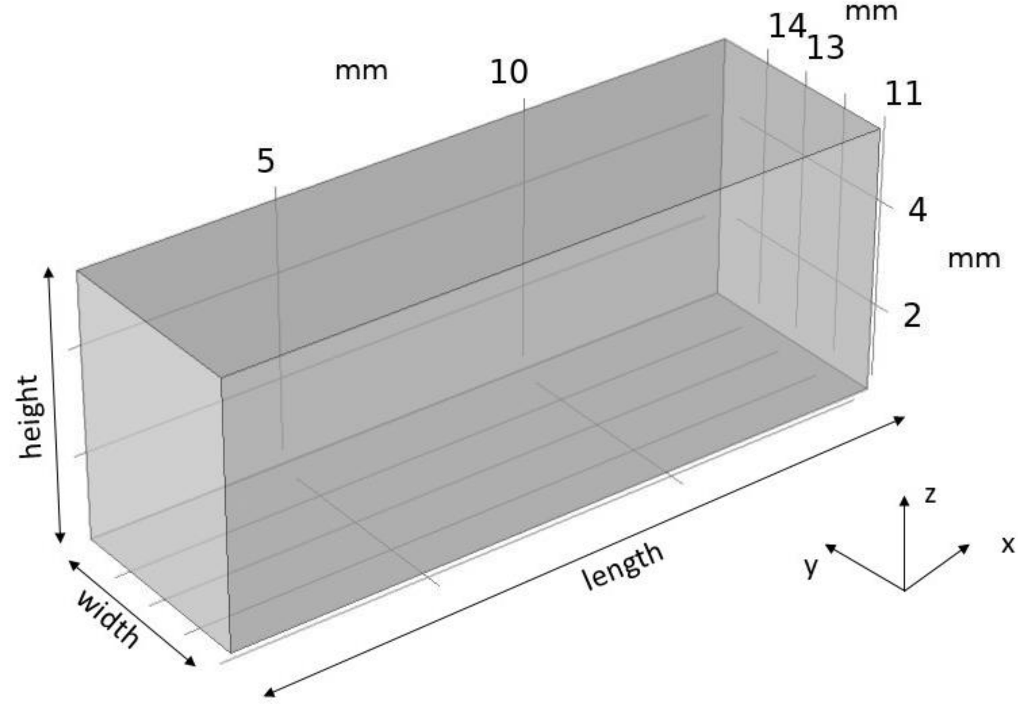

Figure 3.3 Design of a magnet in COMSOL.

The magnet arrangement is designed by using two COMSOL features: “array” and “mirror”. The “array” function allows the creation of one row. The separation between magnets is set to be 5 mm, so that the nominal wavelength is 10 mm [6], which is the value used in most of the measurements using ppm EMATs in this thesis. The “mirror” function creates the second geometrically symmetric row, as depicted in figure 3.4. The material of the patch is selected to be copper, as is used in the actual measurements, while the material of the magnets is neodymium iron boron (NdFeB).

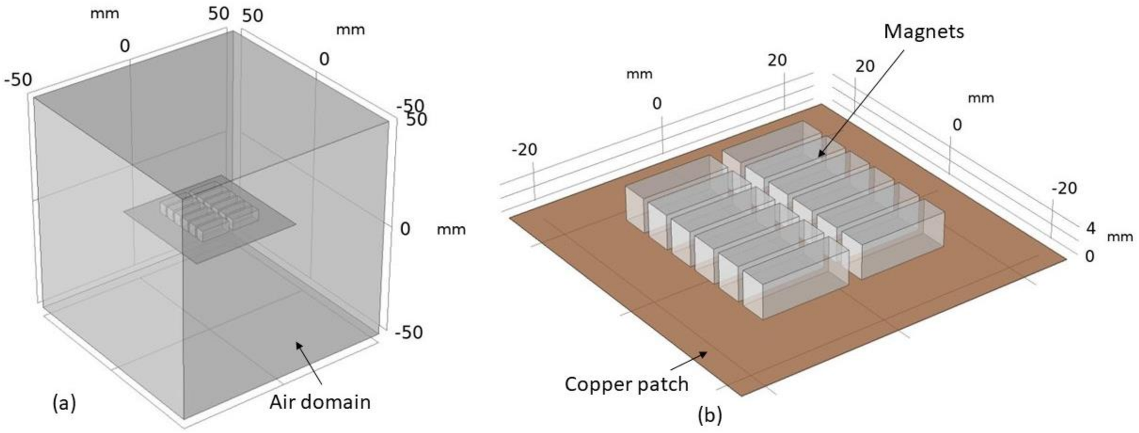

Figure 3.4 Design of magnet arrangement of a ppm EMAT on a metallic patch in COMSOL: (a) Whole domain; (b) magnet arrangement on top of the copper patch.

In COMSOL, the physics interface describes specific mechanisms for solving the relevant equations. The physics interface adopted for simulating this phenomenon is "Magnetic Fields, No Currents (mfnc)" [7]. Inside this physics interface, it is possible to provide the characteristics of the magnetic flux density: strength and direction. The strength is the same for all magnets, namely 1.35 T. However, as the direction of the magnets is alternating, it is necessary to use two physics interfaces, one for the magnetic field going upward and the other downward, as depicted in figure 3.5.

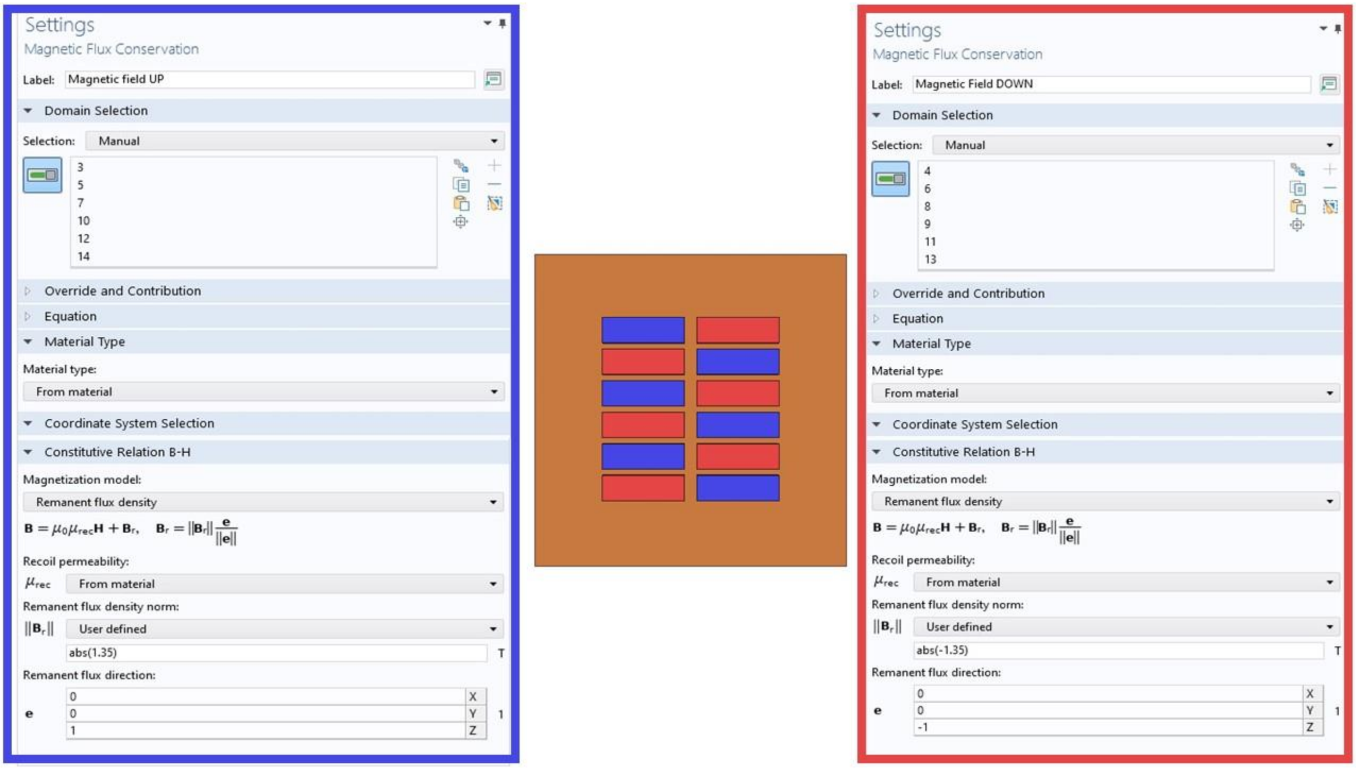

Settings
Magnetic Flux Conservation
Label: Magnetic field UP
Domain Selection
Selection: Manual
3
5
7
10
12
14
Override and Contribution
Equation
Material Type
Material type: From material
Coordinate System Selection
Constitutive Relation B-H
Magnetization model: Remanent flux density
$\mathbf{B} = \mu_0\mu_{\mathrm{rec}}\mathbf{H} + \mathbf{B}_r, \quad \mathbf{B}_r = \|\mathbf{B}_r\|\frac{\mathbf{e}}{\|\mathbf{e}\|}$
Recoil permeability: μ_{rec} From material
Remanent flux density norm: $\|\mathbf{B}_r\|$ User defined
abs(1.35) T
Remanent flux direction:
$\mathbf{e}$ 0 X, 0 Y, 1 Z, 1

Settings
Magnetic Flux Conservation
Label: Magnetic Field DOWN
Domain Selection
Selection: Manual
4
6
8
9
11
13
Override and Contribution
Equation
Material Type
Material type: From material
Coordinate System Selection
Constitutive Relation B-H
Magnetization model: Remanent flux density
$\mathbf{B} = \mu_0\mu_{\mathrm{rec}}\mathbf{H} + \mathbf{B}_r, \quad \mathbf{B}_r = \|\mathbf{B}_r\|\frac{\mathbf{e}}{\|\mathbf{e}\|}$
Recoil permeability: μ_{rec} From material
Remanent flux density norm: $\|\mathbf{B}_r\|$ User defined
abs(-1.35) T
Remanent flux direction:
$\mathbf{e}$ 0 X, 0 Y, -1 Z, 1

Figure 3.5 Magnetic flux density setting tabs.

The mesh adopted is controlled by the physics interface itself, and the element size is set to be "Extra fine" in order to achieve the higher level of accuracy with respect to the computational demand. The whole domain meshed is shown in figure 3.6.

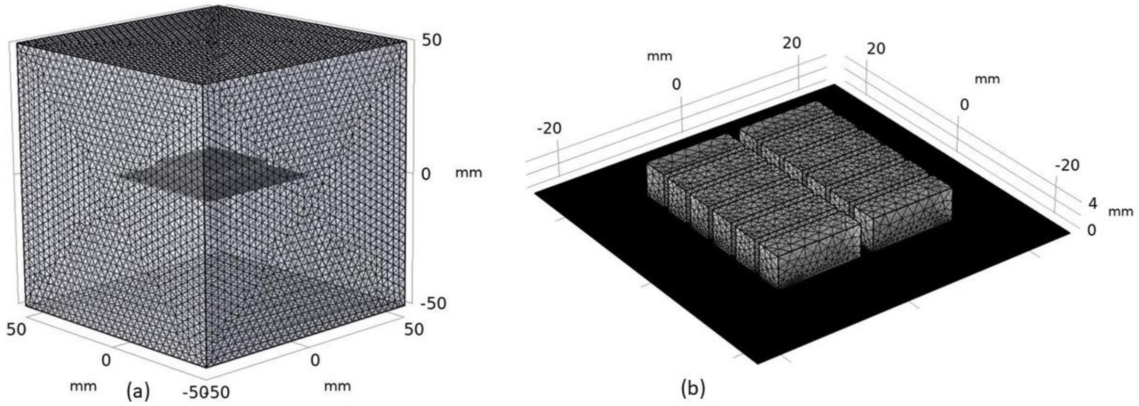

Figure 3.6 3D model: (a) FE meshing of the whole domain; (b) FE meshing of the magnet arrangement on top of the copper mesh.

As explained earlier, the study used for solving, and hence calculating, the magnetic flux density acting on the patch is set to be stationary as the strength of $\vec{B}$ does not vary in time. The outcome of the simulation is presented in figure 3.7.

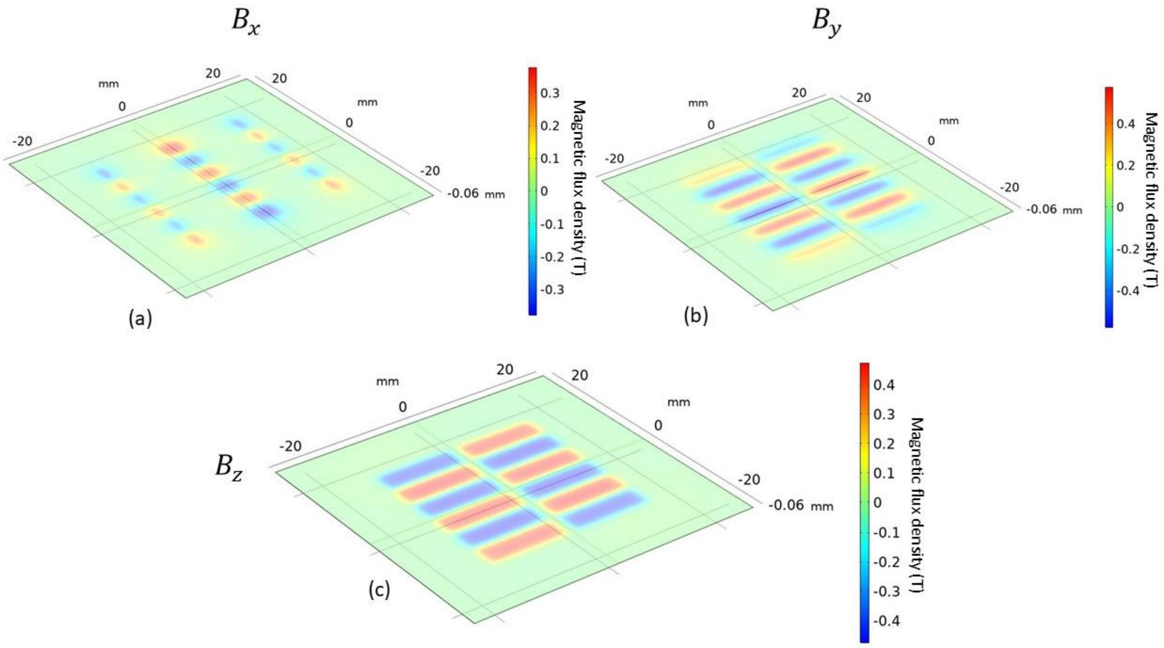

Figure 3.7 Plot of x(a), y(b), z(c) components of the magnetic flux density acting on the metallic patch.

The data are then extracted and imported into Matlab, where the Lorentz force is calculated. The extraction occurs by creating a point grid only at the surface of the patch, although it has a thickness of 0.315 mm. The reason will be explained in the following section, where the skin depth plays an important role. As the surface is 50 x 50 mm (i.e. the patch size) and the step between each point is 0.5 mm, the grid consists of 101x101 points, as depicted in figure 3.8.

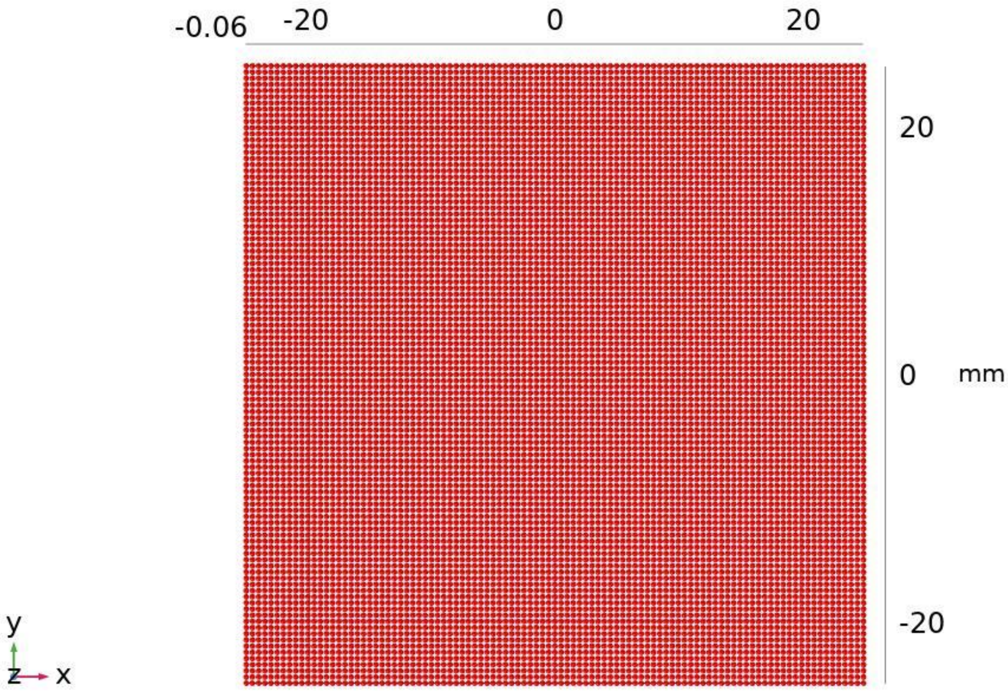

Figure 3.8 Point grid on the surface of the metallic patch.

Once the point grid has been created, a point evaluation of the magnetic flux density components (B_x, B_y and B_z) in each point of the grid is then calculated. In other words, we launch three evaluations – one per each component – on the grid. The result is then stored in an array and exported as a text file. The use of this data will be explained in section 3.3.

3.2.2 Calculation of current density

The calculation of the current density, unlike the previous section, is performed by using a time-dependent model, as the driving current flowing in the coil generates a dynamic (time varying) magnetic field, which, in turn, induces eddy currents within the skin depth of the sample. The geometry of the model is as follows: a block filled with air acts as the surrounding environment, its dimensions are 100 x 100 x 50 mm and it is centred at the origin of the (X, Y, Z) system. Inside the air domain, the metallic patch is designed as already described in the previous section. The racetrack coil, is modelled in a plane at 0.3 mm from the surface of the patch, as it is in reality. The racetrack coil can be thought as the union of two ellipses linked by a rectangle, as depicted in figure 3.9. The resultant shape is extruded with a 0.315 mm, which is the diameter of the coil adopted for the transmitter.

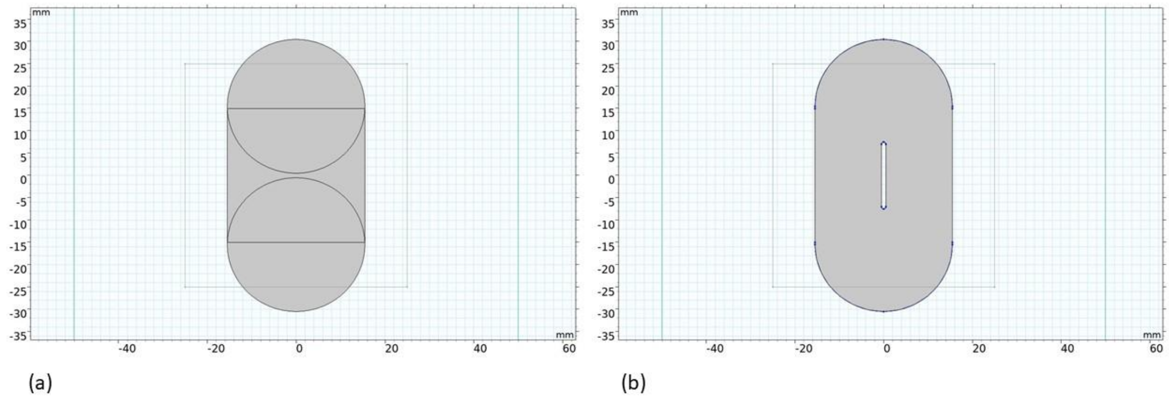

Figure 3.9 Steps for designing a racetrack coil in COMSOL: (a) the geometric shapes combining the coil; (b) final outcome.

In figure 3.10, the resultant geometry of the model is presented. However, it is possible to use the symmetry of the system to reduce the size by one-half, so as to reduce the computational time. The resultant geometry of the model is presented in figure 3.11.

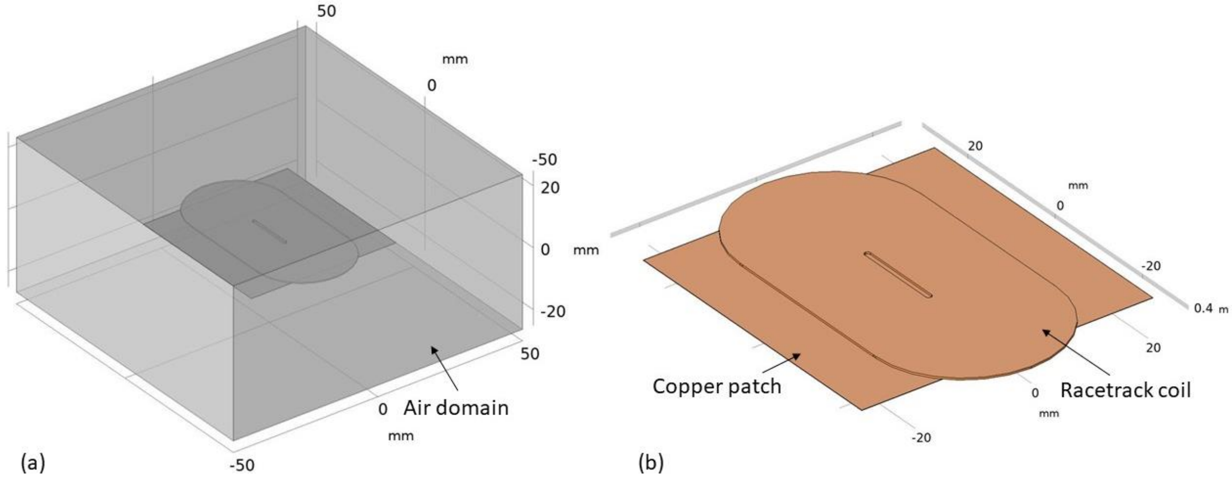

Figure 3.10 Design of racetrack coil on a metallic patch in COMSOL: (a) Whole domain; (b) racetrack on top of the copper patch, they both share the same colour because are made of copper.

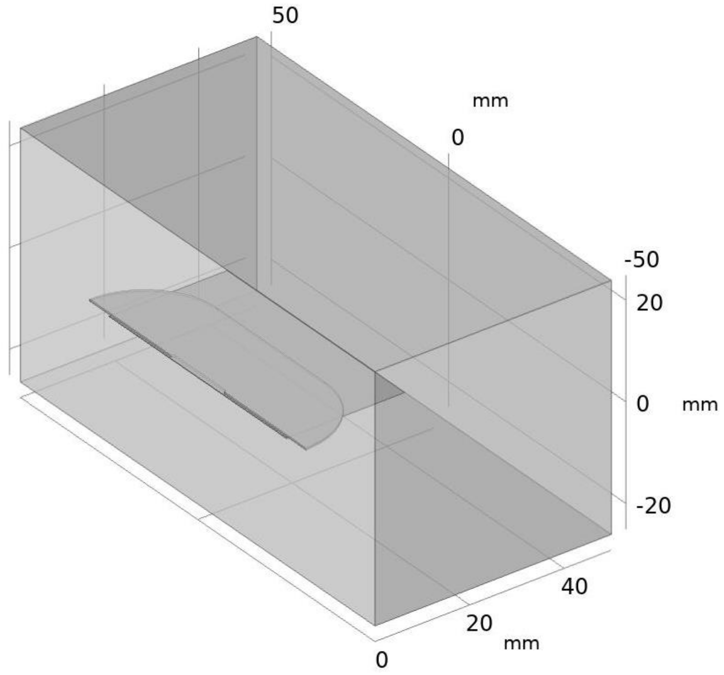

Figure 3.11 Resultant geometry of the 3D model.

The physics interface chosen for this simulation is “Magnetic Fields (mf)”, which can be employed to compute magnetic fields and induced current distributions in and around coils [7]. The half racetrack coil is modelled by using the node “Coil”, where the coil is modelled as “Homogenised multi-turn”. This setting models a wire tightly wound in a racetrack-shaped (the shape of the domain) and separated by an electrical conductor, so that the current flows only in the direction of the wires and is negligible in the other directions, as in the actual coil. The driving current used within the coil is a sine wave with a certain number of cycles, windowed with a Gaussian function and padded by the addition of zeros after the signal, as shown in figure 3.12. The signal is zero-padded because in an actual measurement, the driving current is modulated with a pulse 100 ms, whose width coincides to the length of windowed sine wave.

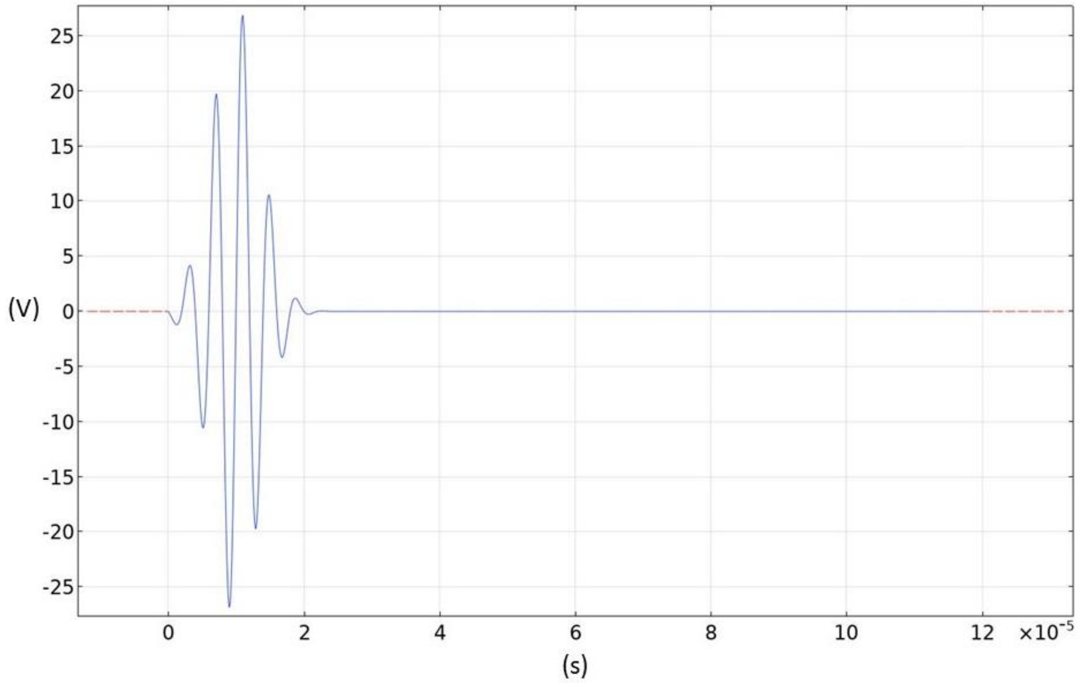

Figure 3.12 Example of piecewise function as driving current made in COMSOL.

The node “Coil” requires both an input and an output boundary to be set. The user selects the direction of the current flowing within the coil, as depicted in figure 3.13.

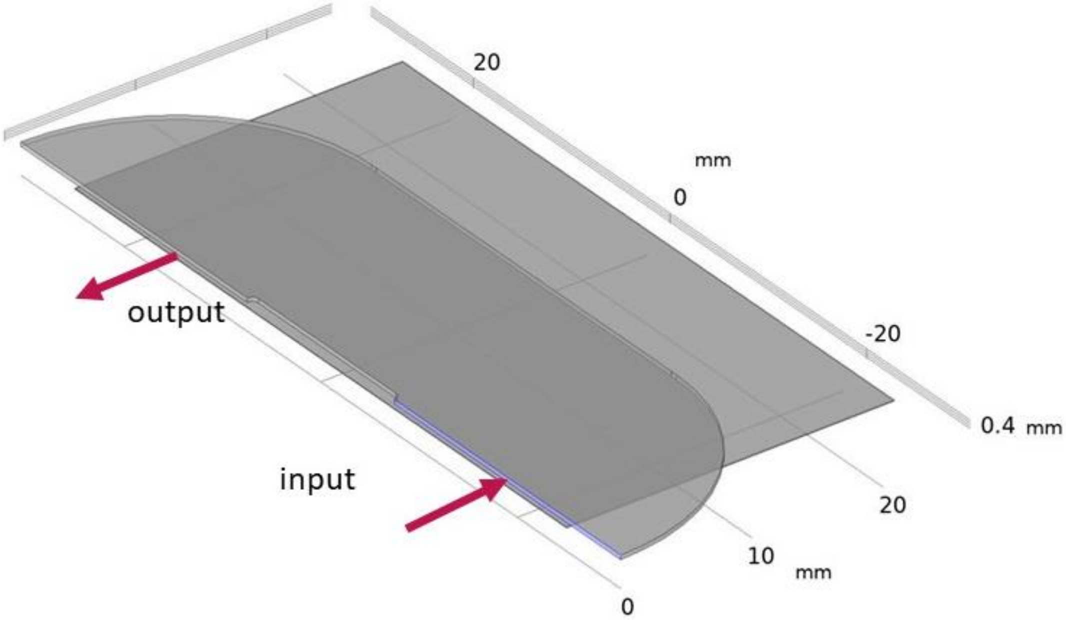

Figure 3.13 Direction of current flowing in the coil.

In order to exploit the symmetry described above, a magnetic insulation boundary condition is applied at the plane of symmetry. This condition means that the magnetic field is zero in the normal direction to the plane. As a consequence, the current can only flow in the normal direction through the boundary, as depicted in figure 3.14.

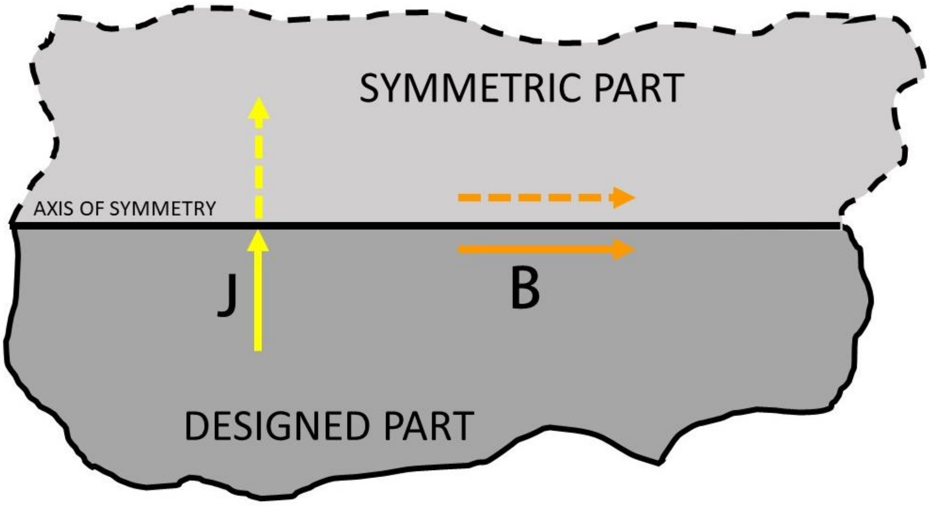

Figure 3.14 Magnetic insulation boundary condition (after [11]).

Unlike the simulation previously presented (section 3.2.1), where the mesh is controlled by the physics interface, in this case a user-controlled mesh has been selected, so that the computation time can be reduced. The mesh of the metal patch is denser than that of the surrounding environment, as the data we want to obtain is the current density induced on the metal patch. Figure 3.15 shows the entire meshed domain.

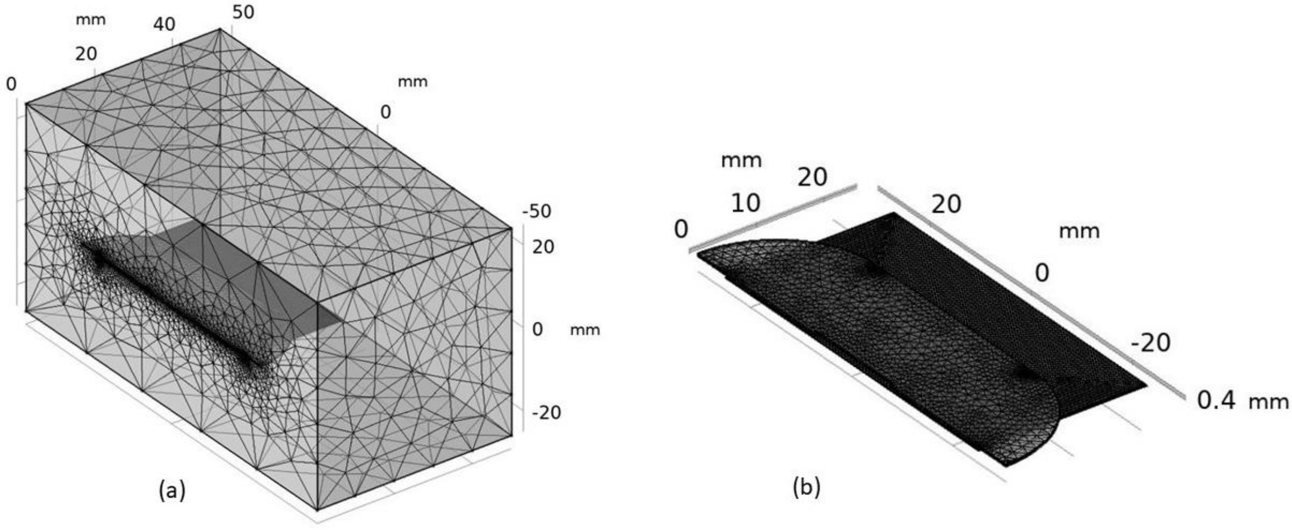

Figure 3.15 3D model: (a) FE meshing of the whole domain; (b) FE meshing of the racetrack coil on top of the copper mesh.

Once the simulation has finished, we anti-symmetrically mirror the domain in which we are interested (the metal patch), as shown in figure 3.16.

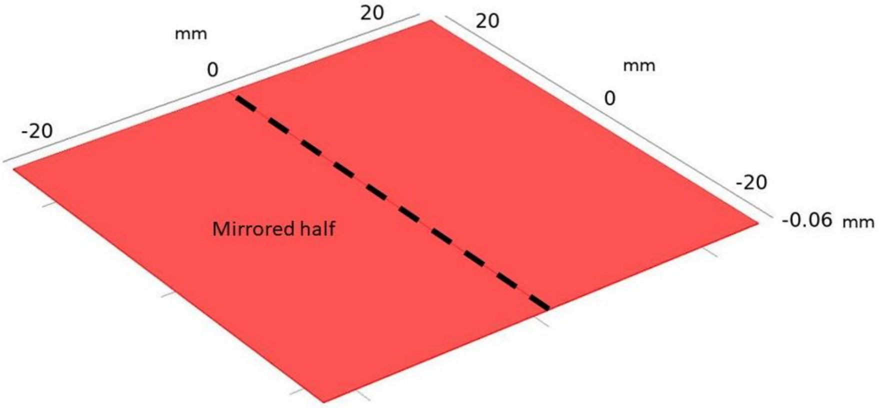

Figure 3.16 Metallic patch anti-symmetrically mirrored.

As mentioned above, the property of interest from this analytical model is the current density $\vec{J}$. Figure 3.17 shows one frame (a single time step) of the absolute magnitude of the current density. Similar to the magnetic flux density, the components of the current density (J_x, J_y, J_z) will be extracted by the procedure described already. As an approximation, although the induced current is present within the skin depth (see section 2.2.2) [8], data are extracted only at the surface of the sample.

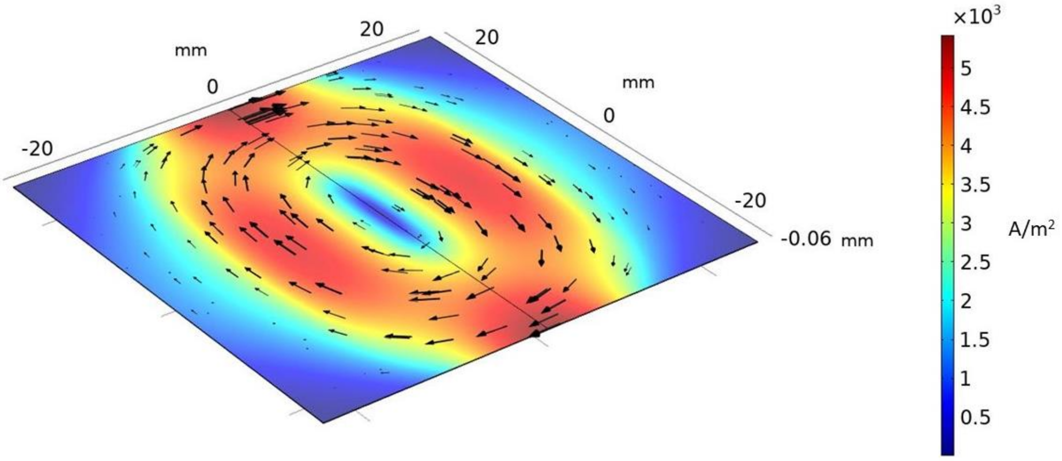

Figure 3.17 Frame of the output: absolute magnitude and direction (depicted by the black arrows) of the current density.

3.3 MATLAB for Lorentz force calculation

Within the Matlab program, the Lorentz force is calculated using the following equation:

$$\vec{F} = \vec{J}(t) \times \vec{B}. \tag{2.19}$$

The calculation is performed in Matlab because the variables ($\vec{J}$ and $\vec{B}$) are solved in two different models. The terms of the cross product can be expressed using their components:

$$\vec{J}(t) = \begin{pmatrix} J_x(t) \\ J_y(t) \\ J_z(t) \end{pmatrix} \tag{3.1}$$

$$\vec{B} = \begin{pmatrix} B_x \\ B_y \\ B_z \end{pmatrix} \tag{3.2}$$

and consequently equation 2.19 can take the following form:

$$\vec{F} = \begin{pmatrix} J_x(t) \\ J_y(t) \\ J_z(t) \end{pmatrix} \times \begin{pmatrix} B_x \\ B_y \\ B_z \end{pmatrix}. \tag{3.3}$$

Equation 3.4 can be solved by applying Sarrus's law [9] to give:

$$\vec{F} = \begin{pmatrix} J_x(t) \\ J_y(t) \\ J_z(t) \end{pmatrix} \times \begin{pmatrix} B_x \\ B_y \\ B_z \end{pmatrix} = \begin{vmatrix} \vec{\imath} & \vec{\jmath} & \vec{k} \\ J_x(t) & J_y(t) & J_z(t) \\ B_x & B_y & B_z \end{vmatrix}, \tag{3.4}$$

where $\vec{\imath}$, $\vec{\jmath}$, $\vec{k}$ are the standard unit vectors. One calculates the Lorentz force by solving the determinant of the 3 x 3 matrix, as shown by the following expression:

$$\begin{aligned} \vec{F}(t) &= \begin{vmatrix} \vec{\imath} & \vec{\jmath} & \vec{k} \\ J_x(t) & J_y(t) & J_{z(t)} \\ B_x & B_y & B_z \end{vmatrix} \\ &= \begin{vmatrix} J_y(t) & J_z(t) \\ B_y & B_z \end{vmatrix} \vec{\imath} - \begin{vmatrix} J_x(t) & J_z(t) \\ B_x & B_z \end{vmatrix} \vec{\jmath} + \begin{vmatrix} J_x(t) & J_y(t) \\ B_x & B_y \end{vmatrix} \vec{k} \end{aligned} \tag{3.5}$$

where the x, y and z components of $\vec{F}$ are:

$$F_x(t) = \begin{vmatrix} J_y(t) & J_z(t) \\ B_y & B_z \end{vmatrix} \vec{\imath}; \tag{3.6}$$

$$F_y(t) = - \begin{vmatrix} J_x(t) & J_z(t) \\ B_x & B_z \end{vmatrix} \vec{\jmath}; \tag{3.7}$$

$$F_z(t) = \begin{vmatrix} J_x(t) & J_y(t) \\ B_x & B_y \end{vmatrix} \vec{k}. \tag{3.8}$$

The next step is to calculate the magnitude and the direction cosines [10] of the force for each time step. The magnitude can be easily calculated by the expression:

$$\|F(t)\| = \sqrt{F_x(t)^2 + F_y(t)^2 + F_z(t)^2}, \tag{3.9}$$

whereas the direction cosines are obtained using

$$V_x(t) = {F_x(t)} \Big/ {\sqrt{F_x(t)^2 + F_y(t)^2 + F_z(t)^2}}. \tag{3.10}$$

$$V_y(t) = {F_y(t)} \Big/ {\sqrt{F_x(t)^2 + F_y(t)^2 + F_z(t)^2}}. \tag{3.11}$$

$$V_z(t) = {F_z(t)} \Big/ {\sqrt{F_x(t)^2 + F_y(t)^2 + F_z(t)^2}}. \tag{3.12}$$

Once the direction cosines have been obtained, it is possible to derive the actual waveform of the Lorentz force for each point, as shown in figure 3.18(a). The values previously obtained from the expression 3.9 are in absolute values.

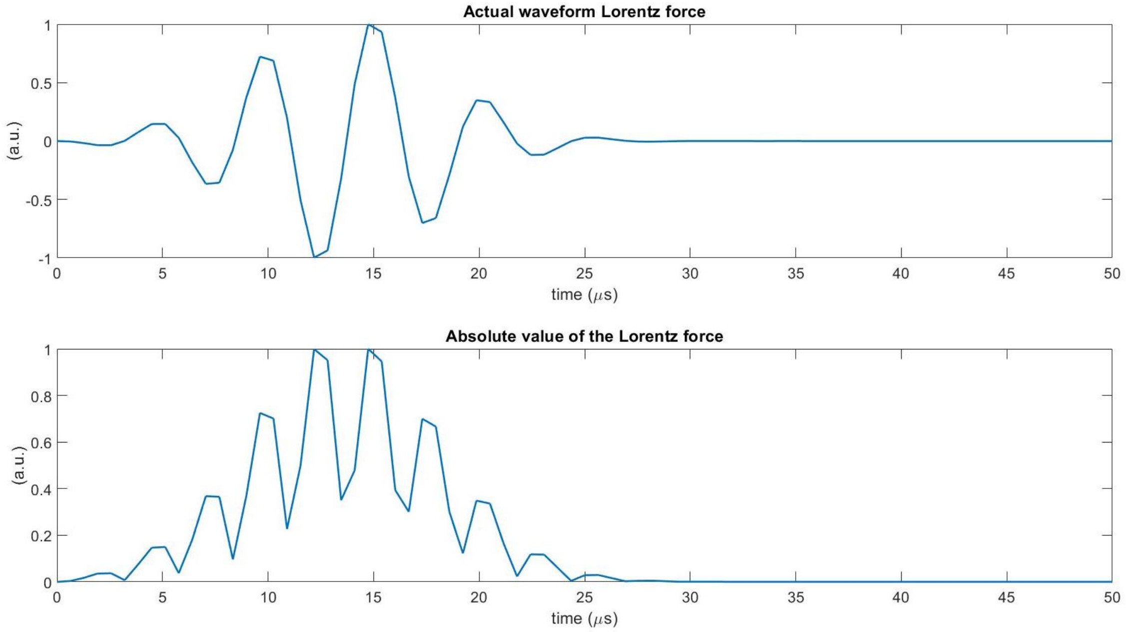

Figure 3.18 (a) Actual waveform of the Lorentz, (b) its absolute value.

The waveform obtained at each point will be then used as load input for the next, and last, step of the three-step method, which will be explained in the next section.

3.4 PZFlex for ultrasonic waveform calculation

The commercial software package PZFlex is used to analyse and validate the propagation of the ultrasonic waves generated by the PPM-EMAT on composite samples. The choice of this software is due to its explicit time-domain approach, which provides a rapid analysis of broadband wave propagation problems. Hence, time-domain finite element models were implemented considering the geometry of the sample, its material properties, and specific boundary conditions, such as absorbing boundaries to prevent unwanted echo signals.

The first step to build the model is to define the geometry and material properties of the sample. The former can be easily defined by measuring the dimensions (length, width and thickness) of the sample, plus the relative position of the source with respect to the edges. The latter requires the information provided by the manufacturing company (for example, the material properties of a ply and stacking sequence for a carbon fibre composite material), which is then used in combination with an additional MATLAB-based software "Dispersion calculator" [11]. This software has been developed at the Centre for Lightweight Production Technology (ZLP) of the German Aerospace Centre (DLR) in Augsburg, Germany. It is an interactive software for computing dispersion curves of guided waves in both isotropic and anisotropic materials. A broader explanation of material properties and guided waves relation will be given in Chapter 4.

Once the geometry of the model and the relevant material properties have been defined, the further step is to import and apply the load previously calculated at the chosen position. PZFlex works similarly to COMSOL where the model is broken into elements. Considering the nominal wavelength of the transducer adopted is 10 mm, one can set the size of the element (0.5 mm, calculated using 20 elements per wavelength [12,13] that ensures the model converges to an accurate solution. The pressure load is applied at the surface (upper side) resulting in the generation of ultrasonic waves. The upper and bottom sides of the 3D model are set to be free boundaries, that is the nodes are not subjected to external forces so they can move freely. The other sides are usually set to be absorbing boundary, in order to eliminate any unwanted reflections. Figure 3.19 depicts the boundary conditions usually adopted in this body work.

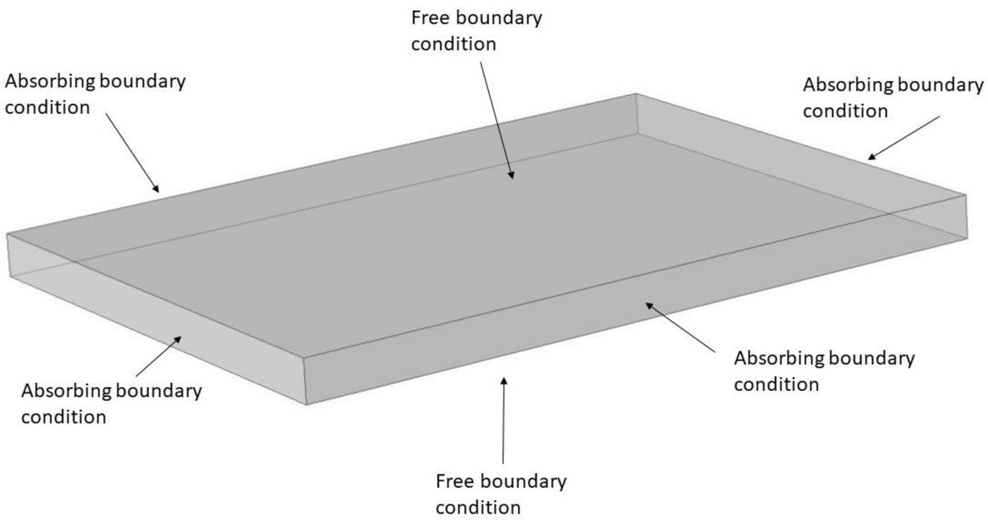

Figure 3. 19 Schematic of the boundary conditions. The load is applied at the top surface.

The software is a time-domain solver which generates its results as a set of time histories, which will be compared to actual measurements. The quantity extracted is the velocity along the direction of particle motion, in this body work this direction is along the y axis. The velocity is used because, as mentioned in the previous chapter (section 2.2.5), EMATs are effectively velocity sensors.

In the next section, an example will be presented and compared with the results of an actual measurement in order to validate and show the reliability of the 3-step model here presented.

3.5 Example model of a CFRP plate

The measurement which will be modelled, is as follows: the sample is a quasi-isotropic CFRP plate whose dimensions are 480 x 350 x 2.8 mm. COTESA [14] (the manufacturing company) provided the material plies and stacking sequence. The materials adopted are:

1. CFRP prepreg (W3T-282-42’’-F593-44-1067)
2. GFRP prepreg (M21-56%-1080-1100), at the outer layer (upper surface).

The nomenclature used for naming the materials means:

1. W3T282 (carbon fabric type), 42” (width in mm), F593 (resin type), 44 (% resin content), 1067 (width in mm)
2. M21 (resin type), 56 % (resin content), 1080 (reinforcement reference) and 1100 (width in mm).

These materials are stacked as presented in figure 3.20.

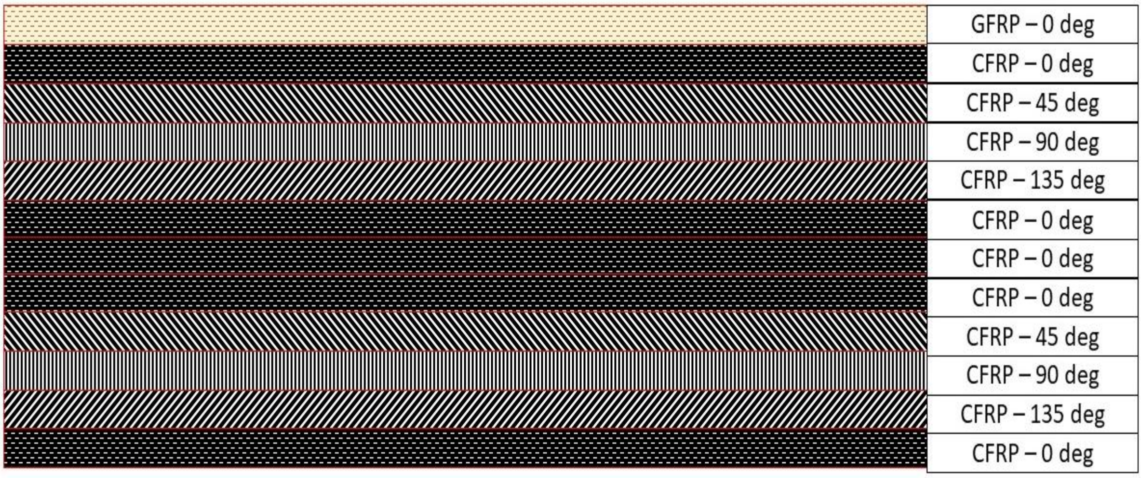

Figure 3.20 Schematic diagram of the sample viewed from a side

The density of the resultant material is 1.46 g/cm^3. The next step is to calculate the stiffness matrix of the sample, which for this material is shown in table 3.1, and import it into the PZFlex model. It can be seen that the lower half of the stiffness matrix is black because the matrix is symmetrical. A more detailed explanation will be given in the next chapter.

Table 3.1 Stiffness matrix of the quasi-isotropic CFRP sample.

48.10 (GPa)	15.07	15.07	0	0	0
15.07	47.27	14.87	0	0	0
15.07	15.07	47.27	0	0	0
0	0	0	16.2	0	0
0	0	0	0	10.86	0
0	0	0	0	0	10.86

The measurement consists of generating SH_0 waves and detecting them at 16, 18 and 20 cm distances from the generation point. As figure 3.21 shows, the source was centred at (16, 17.5, 2.8) cm in a (X,Y,Z) system whose origin is at the top right corner.

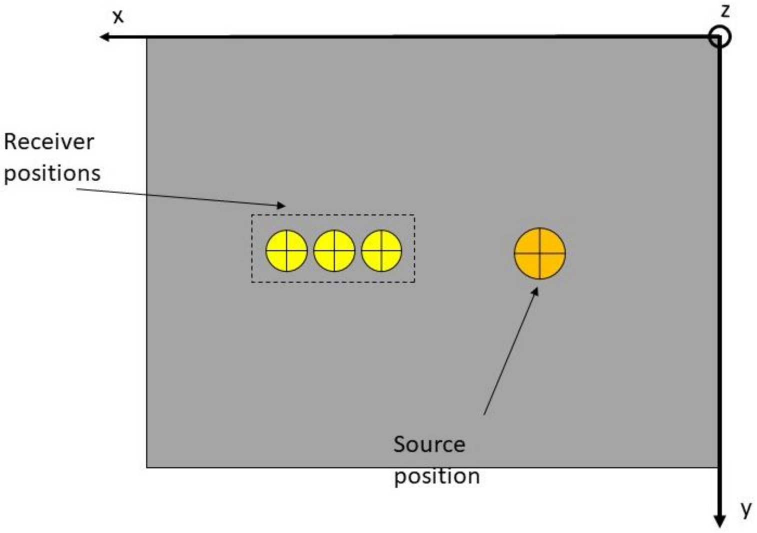

Figure 3.21 Schematic diagram of the measurement/simulation.

In order to excite the desired SH_0 mode, the driving current is an 8-cycle sine wave, whose frequency is 250 kHz, windowed with a Gaussian function, as depicted in figure 3.22.

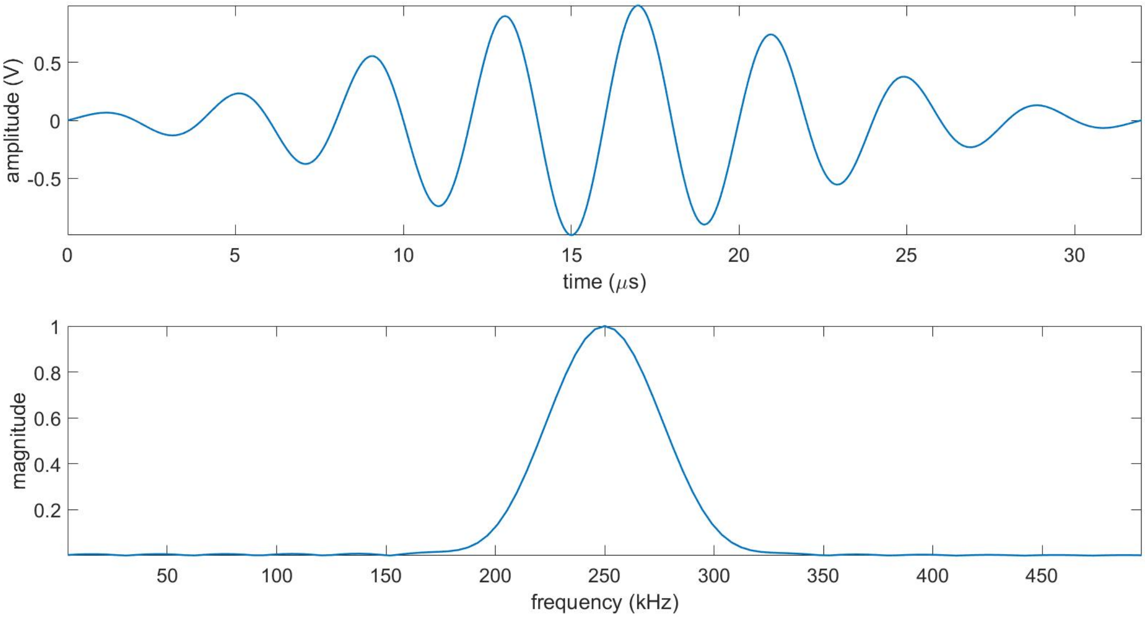

Figure 3.22 Driving current for exciting SH_0 within the quasi-isotropic CFRP sample and its frequency spectrum.

A series of images showing the velocity magnitude and all its components in the composite plate are shown in figure 3.23. The figures 3.23(a-d) show the waves propagating within the sample from above, while 3.23 (e) is from the side.

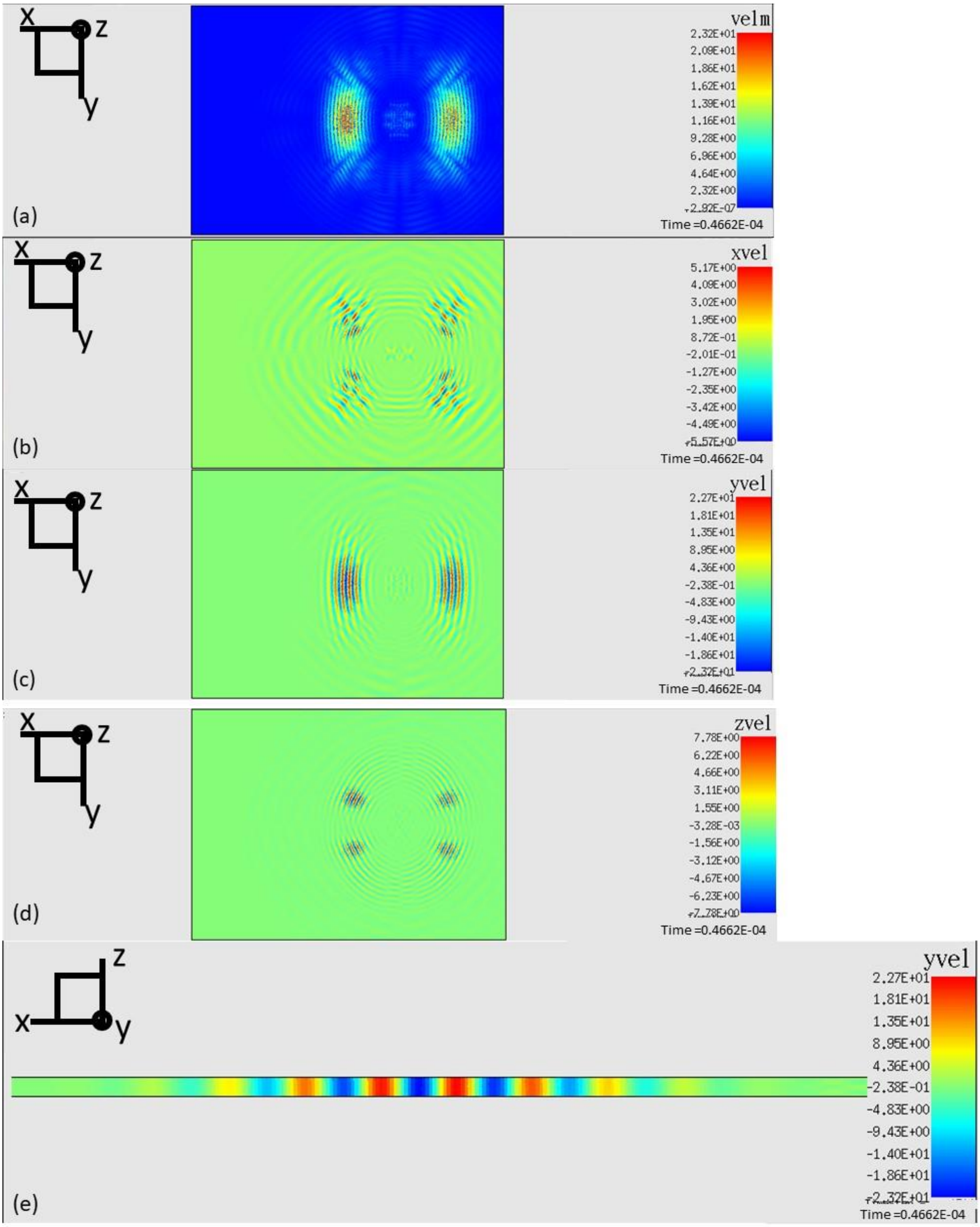

Figure 3.23 Wave propagation within the sample modelled (quasi-isotropic CFRP plate): (a) velocity magnitude; (b) x velocity component; (c) y velocity component; (d) z velocity component; (e) y velocity component. (a-d) from above; (e) from a side.

In addition, waveforms are produced from the simulation. The outputs of the model are shown in figure 3.24. These results will be then compared in the next Chapter to show the excellent correlation with the experimental results.

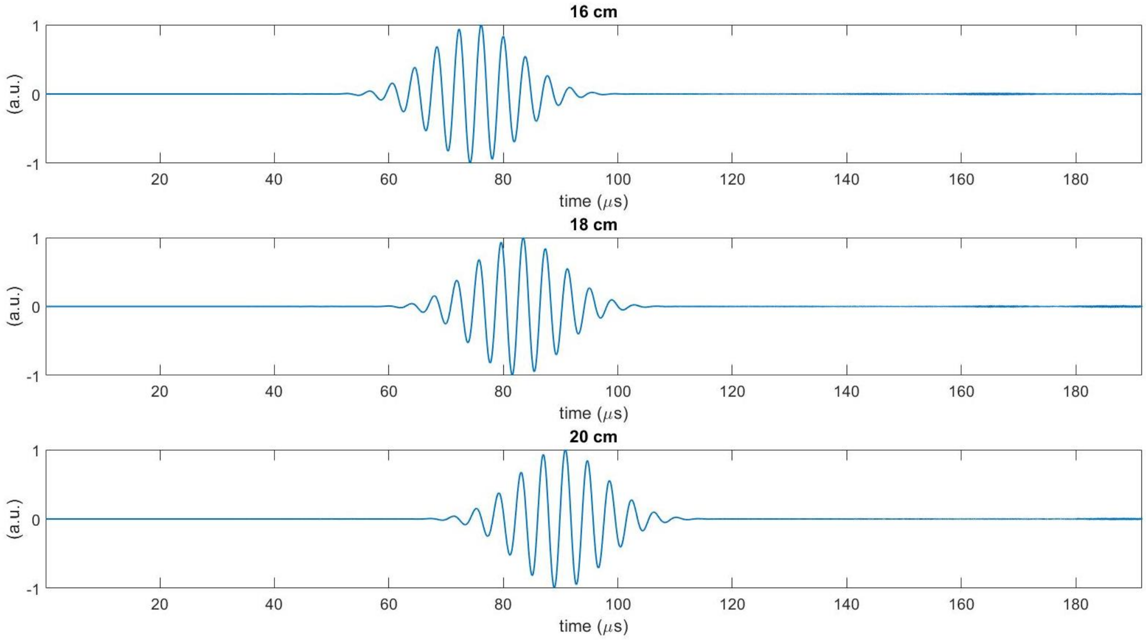

Figure 3.24 Waveforms representing the outcome of the simulation recorded at different positions: 16, 18 and 20 cm.

3.6 Conclusions

This chapter has presented a three-step method, by which a better understanding and prediction of the propagation of guided waves generated by a PPM EMAT can be achieved.

The method followed these steps:

1- Calculation of the magnetic field flux and current density.

These two quantities can be calculated within two models, produced in COMSOL. The need to use two models is due to two reasons. The first is the need to reduce the computational time, while the second is due to the use of two different physics interfaces: one without current ("Magnetic Fields, No Currents") and another with ("Magnetic Fields"). For both models, a grid of points is formed, and at each point the components of the calculated quantities ($\vec{B}$ or $\vec{J}$, depending on the model) are saved. These are then imported into MATLAB.

2- Calculation of the Lorentz force

The cross-product between $\vec{B}$ and $\vec{J}$ takes a matrix form, as the direction of the resulting force must also be known. By calculating the determinant of a 3x3 matrix (Sarrus' rule), we obtain the x, y and z components of the force. The components, in turn, are used to calculate the magnitude and direction cosines of the resulting force. These forces are then imported into

PZFlex, and are used to generate the desired guided wave, depending on the driving frequency used in the previous step.

3- Guided wave propagation within the sample under investigation

After determining the geometry of the problem, material of the sample and its mechanical properties, boundary conditions and where to apply the previously calculated forces, a simulation can be generated. Since EMATs are actually velocity sensors, the quantity recorded is the y (in-plane) component of the velocity, which represent the SH guided waves.

This method shows the possibility of validating and predicting measurements with SH guided waves generated by PPM EMAT on composite materials.

References Chapter 3

[1] K. Kawashima, "Theory and numerical calculation of the acoustic fiel produced in metal by an electromagnetic ultrasonic transducer," *The Journal of the Acoustical Society of America,* vol. 60, no. 5, pp. 1089-1099, 1976.

[2] R. Thompson, "A model for the electromagnetic generation of ultrasonic guided waves in ferromagnetic metal polycrystals," *IEEE Transactions on Sonics and Ultrasonics,* vol. 25, no. 1, pp. 7-15, 1978.

[3] R. Ludwig and X.W. Dai, "Numerical simulation of electromagnetic acoustic transducer in the time domain," *Journal of Applied Physics,* vol. 69, no. 1, pp. 89-98, 1991.

[4] J. Whiteley, Finite Element Methods, Cham: Springer, 2017.

[5] A. Morris, A practical guide to reliable finite element modellng, Chicester: John Wiley & Sons, 2008.

[6] P.A. Petcher, S.E. Burrows, S. Dixon, "Shear Horizontal (SH) ultrasound wave propagation around smooth corners," *Ultrasonics,* vol. 54, no. 4, pp. 997-1004, 2014.

[7] COMSOL, "COMSOL," 2018. [Online]. Available: https://doc.comsol.com/5.4/doc/com.comsol.help.acdc/ACDCModuleUsersGuide.pdf. [Accessed 18 12 2020].

[8] H. Wheeler, "Formulas for the Skin Effect," *Proceedings of the IRE,* vol. 30, no. 9, pp. 412-424, 1942.

[9] P. Finck, in *Elements d'algebre,* Strasbourg, 1846, p. 95.

[10] H.C. Ohanian and J.T. Market, "The position vector; components of a vector," in *Physics for engineerings and scientists*, New York, W.W Nortono & Co., 2007, p. 77.

[11] A. Huber, "DLR.de," Center for Lightweigth Production Technology, November 2018. [Online]. Available: https://www.dlr.de/zlp/en/desktopdefault.aspx/tabid-14332/24874_read-61142/. [Accessed 18 December 2020].

[12] F. Moser, L.J. Jacobs, J. Qu, "Modelin elastic wave propagation in waveguides with the finite element method," *NDT&E international,* vol. 32, no. 4, pp. 225-234, 1999.

[13] D. Alleyne, P. Cawley, "A two-dimensional Fourier transform method for the measurement of propagating multimode signals," *The Journal of the Acoustical Society of America,* vol. 89, no. 3, pp. 1159-1168, 1991.

[14] "COTESA COMPOSITES," COTESA, 2002. [Online]. Available: https://www.cotesa.de/index_en.html. [Accessed 21 12 2020].

[15] J. Millman, in *Microelectronics*, New York, McGraw-Hill, 1987, pp. 496-497.

Chapter 4

Experimental validation in different materials

4.1 Introduction

In the previous chapters, the fundamental concepts needed to understand the operation of EMATs, and the analytical model adopted to compare the experimental results, have been discussed. This chapter describes how one can use guided waves generated and detected by EMATs on composite samples (both insulating and partially conductive) through the use of a removable metallic tape attached to a sample surface, placed under both transmitting and receiving probes. Firstly, the relationship between ultrasonic wave propagation and the mechanical properties of the sample will be addressed in order to introduce concepts such as a stiffness matrix, which is used to describe the elastic properties of composites. Subsequently, the instrumentation used for the experiments will be introduced. Results are first shown for an aluminium, conductive isotropic material, sample, where EMATs can be used without the metallic tape, in order to test the laboratory set-up and the analysis process. A glass plate, representing an electrically-insulating isotropic medium, is then tested with EMATs using the metallic tape. The removable patch method is then used on composite materials with a low conductivity, illustrating the potential of the approach in CFRP and pultruded GFRP plates.

This Chapter starts with brief details of acoustic wave propagation in solids, before experiments are described in metal, glass and composite plates. These experiments demonstrate the operation of the patches in each case. It is also shown that the model described in Chapter 3 gives a good prediction of the type of signals that can be generated in the different materials studied.

4.2 Acoustic wave propagation in solids

Ultrasonic signals are acoustic waves propagating at frequencies above 20 kHz and can exist in solid, liquid and gaseous media [1-4]. In order to mathematically express these vibrations it is necessary to understand the material deformation and the internal restoring forces that lead to oscillatory motions. In the case of elastic solids [5-7], this expression is obtained by the relationship between stress (σ) and strain (ε) in the specimen, and using rectangular Cartesian coordinates (x, y, z axes), these conditions can be depicted in the form of tensors as:

$$\sigma_{ij} = \begin{pmatrix} \sigma_{xx} & \sigma_{xy} & \sigma_{xz} \\ \sigma_{yx} & \sigma_{yy} & \sigma_{yz} \\ \sigma_{zx} & \sigma_{zy} & \sigma_{zz} \end{pmatrix} \tag{4.13}$$

$$\varepsilon_{ij} = \begin{pmatrix} \varepsilon_{xx} & \varepsilon_{xy} & \varepsilon_{xz} \\ \varepsilon_{yx} & \varepsilon_{yy} & \varepsilon_{yz} \\ \varepsilon_{zx} & \varepsilon_{zy} & \varepsilon_{zz} \end{pmatrix} \tag{4.14}$$

As the tensors are symmetric, each component can be defined by one subscript rather than two, and it is possible to write them as a six-element column matrix rather than a nine-element matrix [8], which can be expressed as:

$$\sigma = \begin{pmatrix} \sigma_1 & \frac{1}{2}\sigma_6 & \frac{1}{2}\sigma_5 \\ \frac{1}{2}\sigma_6 & \sigma_2 & \frac{1}{2}\sigma_4 \\ \frac{1}{2}\sigma_5 & \frac{1}{2}\sigma_4 & \sigma_3 \end{pmatrix} = \begin{pmatrix} \sigma_1 \\ \sigma_2 \\ \sigma_3 \\ \sigma_4 \\ \sigma_5 \\ \sigma_6 \end{pmatrix} \tag{4.15}$$

$$\varepsilon = \begin{pmatrix} \varepsilon_1 & \frac{1}{2}\varepsilon_6 & \frac{1}{2}\varepsilon_5 \\ \frac{1}{2}\varepsilon_6 & \varepsilon_2 & \frac{1}{2}\varepsilon_4 \\ \frac{1}{2}\varepsilon_5 & \frac{1}{2}\varepsilon_4 & \varepsilon_3 \end{pmatrix} = \begin{pmatrix} \varepsilon_1 \\ \varepsilon_2 \\ \varepsilon_3 \\ \varepsilon_4 \\ \varepsilon_5 \\ \varepsilon_6 \end{pmatrix} \tag{4.16}$$

In the case of small deformations (or within the linear elastic limit), it is observed that the strain in a deformed body is linearly proportional to the applied stress (Hook's law) [9], which can be expressed as:

$$\sigma_{ij} = c_{ijkl}\varepsilon_{kl} \tag{4.17}$$

where c_{ijkl} is a 4th rank elasticity tensor with 81 components. This can be reduced to 36 (2nd rank tensor) components in the case where the stress symmetry condition is satisfied, as it is depicted in equation (4.6):

$$\begin{pmatrix}\sigma_1\\ \sigma_2\\ \sigma_3\\ \sigma_4\\ \sigma_5\\ \sigma_6\end{pmatrix} = \begin{pmatrix} c_{11} & c_{12} & c_{13} & c_{14} & c_{15} & c_{16}\\ c_{21} & c_{22} & c_{23} & c_{24} & c_{25} & c_{26}\\ c_{31} & c_{32} & c_{33} & c_{34} & c_{35} & c_{36}\\ c_{41} & c_{42} & c_{43} & c_{44} & c_{45} & c_{46}\\ c_{51} & c_{52} & c_{53} & c_{54} & c_{55} & c_{56}\\ c_{61} & c_{62} & c_{63} & c_{64} & c_{65} & c_{66}\end{pmatrix} \cdot \begin{pmatrix}\varepsilon_1\\ \varepsilon_2\\ \varepsilon_3\\ \varepsilon_4\\ \varepsilon_5\\ \varepsilon_6\end{pmatrix} \tag{4.18}$$

The number of independent elastic stiffness constants necessary to describe a body varies with respect to its structure, so for particular cases certain constants in the matrix can be zero, or equal in magnitude. The simplest material can be isotropic, and provided that the general elastic isotropy condition is matched ($c_{12} = c_{11} - 2c_{44}$), then it is possible to show that the stiffness matrix for this case can be reduced to [8]:

$$\begin{pmatrix} c_{11} & c_{12} & c_{12} & 0 & 0 & 0\\ c_{12} & c_{11} & c_{12} & 0 & 0 & 0\\ c_{12} & c_{12} & c_{11} & 0 & 0 & 0\\ 0 & 0 & 0 & c_{44} & 0 & 0\\ 0 & 0 & 0 & 0 & c_{44} & 0\\ 0 & 0 & 0 & 0 & 0 & c_{44}\end{pmatrix} \tag{4.19}$$

Therefore, it can be stated that an isotropic medium has only two independent elastic constants (c_{11} and c_{44}); which are often taken to be the Lamè parameters (λ and μ), and are defined by:

$$\lambda = c_{12} \tag{4.20}$$

$$\mu = c_{44} \tag{4.21}$$

Composites are generally made by stacking single plies (or laminae) of continuous fibres in different orientation to achieve the desired strength and stiffness properties [10]. Unidirectional (UD) fabric is the simplest arrangement, where the fibres are oriented along one direction only, as shown in figure 4.1. This kind of anisotropic medium, which has a preferred direction and is isotropic in the plane orthogonal to this direction, is defined as transversely isotropic.

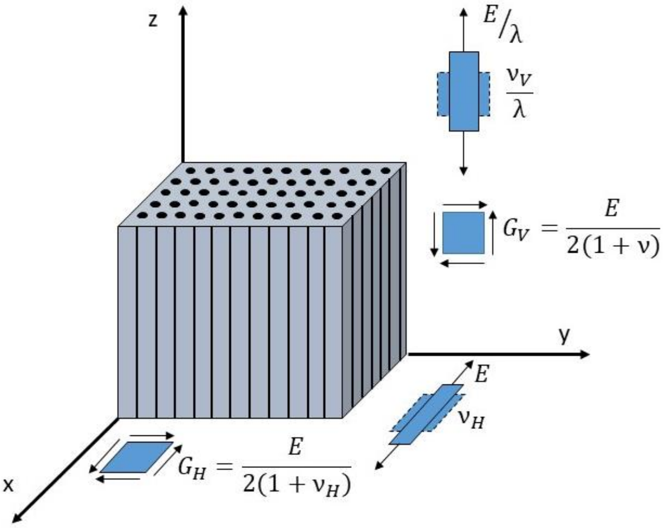

Figure 4.1 Example of transversely isotropic material. Given E, the modulus of the medium in the plane xy, $E/_\lambda$ *is the elasticity modulus in the z direction;* G_V *is the shear modulus for shear in the z direction;* G_H *is the shear modulus in the plane xy (after [11]).*

A transversely isotropic medium can be totally defined by five independent elastic constants, and thus its stiffness matrix is:

$$\begin{pmatrix} c_{11} & c_{12} & c_{13} & 0 & 0 & 0 \\ c_{12} & c_{11} & c_{13} & 0 & 0 & 0 \\ c_{13} & c_{13} & c_{33} & 0 & 0 & 0 \\ 0 & 0 & 0 & c_{44} & 0 & 0 \\ 0 & 0 & 0 & 0 & c_{44} & 0 \\ 0 & 0 & 0 & 0 & 0 & \frac{1}{2}(c_{11}-c_{12}) \end{pmatrix} \tag{4.22}$$

In aerospace and many other composites, laminae tend to be stacked in order to make quasi-isotropic laminates. These laminates have properties which are reasonably uniform (although not totally so) in the plane of the sample, even though they are not an optimal composite design in strength-to-weight or stiffness-to-weight ratios [12]. A more detailed explanation of such materials will be given later in this chapter.

Now considering acoustic propagation in such media, an approach for describing the propagation of uniform plane wave in a freely vibrating medium is by using the Christoffel equation [13]:

$$k^2\Gamma_{ij}v_j - \rho\omega^2 v_i = 0, \tag{4.23}$$

where Γ_{ij} is the Christoffel matrix, k is the wave number, ρ is the density, ω is the angular frequency, and v is the phase velocity. Such an equation in full tensor form becomes:

$$k^2 \begin{bmatrix} \Gamma_{11} & \Gamma_{21} & \Gamma_{31} \\ \Gamma_{12} & \Gamma_{22} & \Gamma_{32} \\ \Gamma_{13} & \Gamma_{23} & \Gamma_{33} \end{bmatrix} \begin{bmatrix} v_x \\ v_y \\ v_z \end{bmatrix} - \rho\omega^2 \begin{bmatrix} v_x \\ v_y \\ v_z \end{bmatrix} = 0 \tag{4.24}$$

For simplicity, the case of an isotropic medium will be considered. Given its stiffness matrix (equation (4.7)), the Christoffel matrix becomes a purely diagonal matrix, turning the above equation into:

$$k^2 \begin{bmatrix} c_{44} & 0 & 0 \\ 0 & c_{44} & 0 \\ 0 & 0 & c_{11} \end{bmatrix} \begin{bmatrix} v_x \\ v_y \\ v_z \end{bmatrix} - \rho\omega^2 \begin{bmatrix} v_x \\ v_y \\ v_z \end{bmatrix} = 0. \tag{4.25}$$

This describes a wave solution dependent on wave propagation and polarisation direction.

From equation (4.13) it is possible to determine the phase velocity for shear and longitudinal waves, resulting in three independent equations:

$$k^2 c_{44} v_x = \rho\omega^2 v_x \tag{4.26}$$

$$k^2 c_{44} v_y = \rho\omega^2 v_y \tag{4.27}$$

$$k^2 c_{11} v_z = \rho\omega^2 v_z \tag{4.28}$$

Longitudinal waves occur when the particle motion is along the direction of propagation of the wave, whilst shear waves occur when the particle motion is perpendicular to the direction of propagation, as depicted in figure 4.2.

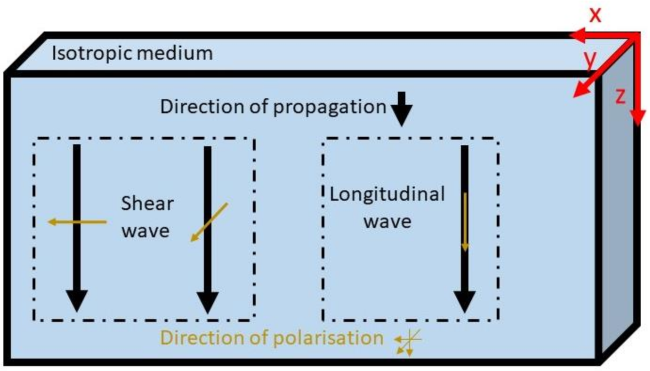

Figure 4.2 Schematic diagram of longitudinal and shear waves in an isotropic medium. For shear waves the direction of polarisation (brown arrow) is perpendicular to the direction of propagation (black arrow). While, for longitudinal waves the two directions are parallel.

In accordance to equations (4.14-16) the x-polarised (z-propagating) and y-polarised (z-propagating) shear wave solutions, must both satisfy:

$$k^2 c_{44} = \rho\omega^2 \tag{4.29}$$

and the longitudinal wave solution must satisfy:

$$k^2 c_{11} = \rho\omega^2 \tag{4.30}$$

hence, the phase velocity ($v = {}^{\omega}/_{k}$) which is independent of direction for this sort of medium (isotropic), has two values. For the two shear waves this is:

$$v_s = \sqrt{\frac{c_{44}}{\rho}} \tag{4.31}$$

and for the longitudinal wave:

$$v_l = \sqrt{\frac{c_{11}}{\rho}} \tag{4.32}$$

4.3 Laboratory set-up

The measurement set-up used for performing measurements with EMATs on both conductive and insulating samples is displayed in figure 4.3.

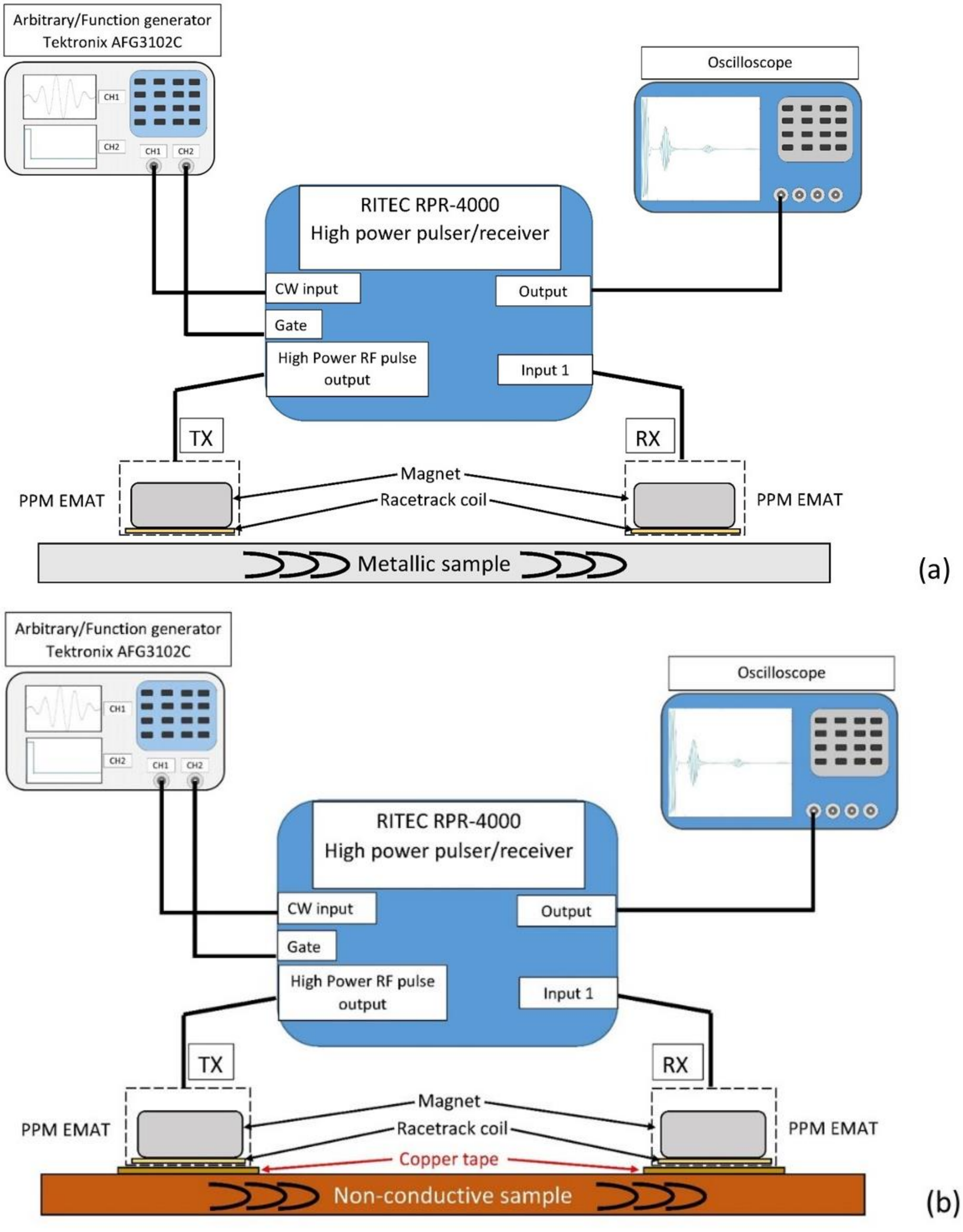

Figure 4.3 Diagram of the laboratory set-up for inspecting both conductive (a) and insulating (b) sample.

A driving waveform, previously created in MATLAB, is loaded into the arbitrary function generator AFG3102C. Then, the voltage waveform is input into the RITEC RPR-4000, which drives a current waveform with the same temporal profile to the transmitting PPM EMAT, whose nominal wavelength is 10 mm. In the case of conductive samples, such as aluminium, the generation of elastic waves occurs directly within the specimen. For the insulating or low electrical conductivity samples, the elastic waves are produced within the metallic layer of a copper tape patch, attached under both source and receiver, and are transferred by the adhesive layer into the sample. These waves then propagate along the sample and are detected by the receiver PPM EMAT that has the same nominal wavelength as the generating EMAT. The acquired signal goes back to the receiver section of the RITEC where it is then amplified. From the RITEC, the amplified, detected signal is input to the oscilloscope, where can be displayed.

In theory, the arbitrary function generator is not essential, since the RITEC can already generate tonebursts for driving current to the generation EMAT [14]. The driving current generated by the RITEC is a rectangular windowed sinusoid, and so in order to reduce the spectral leakage [15], the arbitrary function generator was used. Figure 4.4 shows two examples of such waveforms with different windowing functions, one generated by the RITEC (4.4(a)) and the temporal profile of waveform (4.4(b)) actually used for experiments, each shown with the resultant frequency spectra.

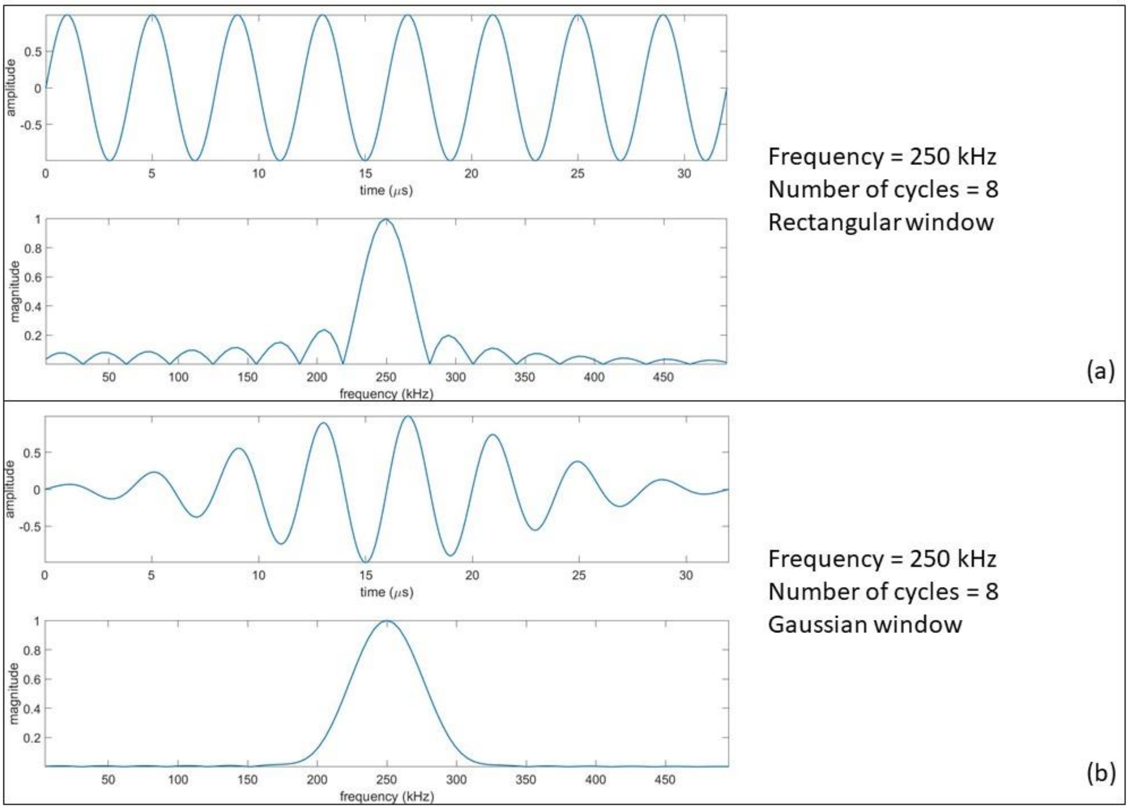

Figure 4.4 Comparison between two sinusoids windowed with a rectangular window (a) and a Gaussian window (b).

4.4 Aluminium test sample

An aluminium sample has been used as benchmark for validating the equipment used for all following measurements. The aim was to demonstrate the equipment operation for generating a specific SH guided wave mode, the SH_0 mode, in a conducting sample without the need for a removable conductive patch [16-19]. As stated in Chapter 2, EMATs are usually used for inspecting conducting materials, and not conventionally used for composites with low conductivity [20]. Hence, in this case, as the sample is conductive, the use of copper patches is unnecessary. Therefore, the measurements have not been conducted using the laboratory set-up shown in figure 4.3(a). The benchmark specimen was a 3 mm thick aluminium plate, whose dimensions are 420 x 300 mm. Several measurements have been taken varying the distance between source and receiver. The probes were placed at 20, 21, 22 and 23 cm far apart, as figure 4.5 shows.

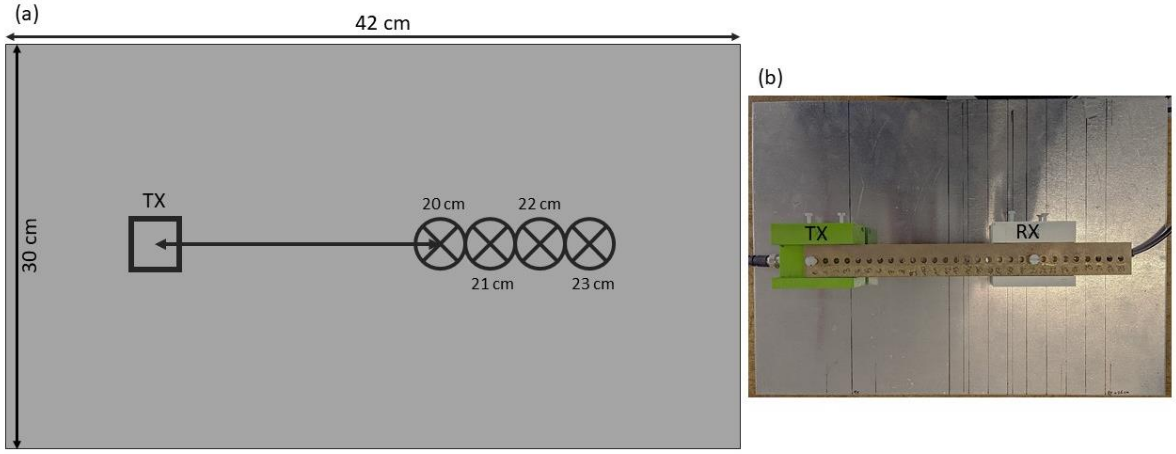

Figure 4.5 (a) sketch of the probe set-up; (b) photo of the probes in place.

It is worth remembering that ppm EMATs restrict the wavelength to a certain value given by the distance between the two same magnetic poles [21], see section 2.2.6.3. Therefore, the mode selection occurs by carefully choosing the driving frequency. In order to establish which mode is efficiently excited at a particular frequency, examination of the dispersion curve is necessary. The dispersion curve related to the benchmark specimen are calculated in “Dispersion calculator”, as explained in the previous chapter, and displayed in figure 4.6.

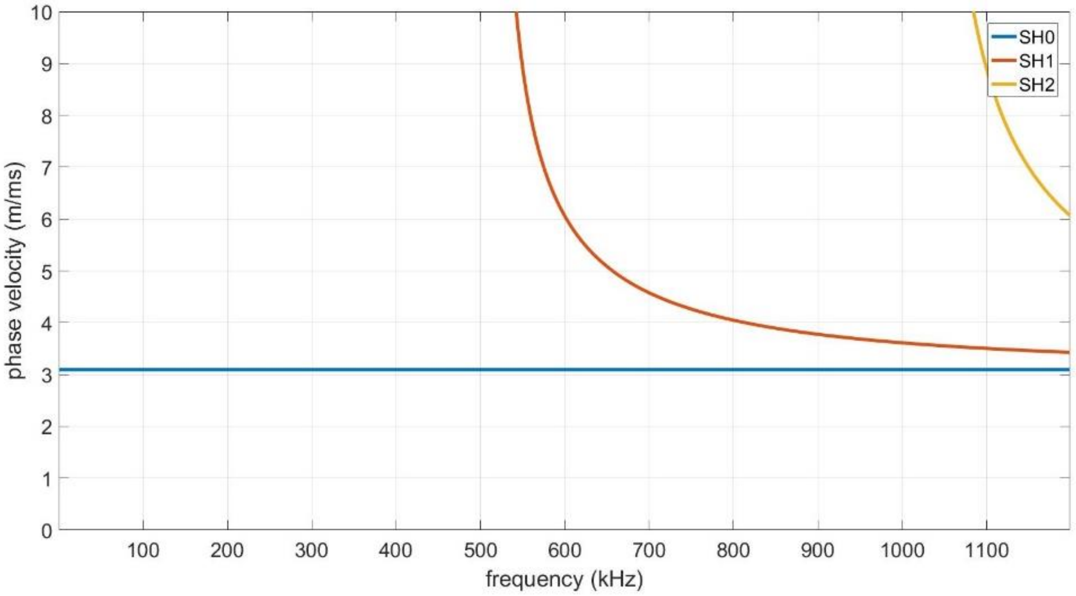

Figure 4.6 Dispersion curve for SH waves of aluminium plate 3mm thick.

Once the dispersion curve has been calculated, it is necessary to include the wavelength information of the source. It is commonly assumed that PPM EMATs will generate waves with a wavelength equal to the magnets periodicity. In reality, though, the transducer has a spatial bandwidth within certain modes can be generated. From the 3D model, explained in Chapter 3, the spatial bandwidth of the probe is retrieved, as figure 4.7 shows. It can be noted that the spectrum curve is centred at 10 mm, which corresponds to the nominal wavelength of both PPM EMATs (source and receiver). The spatial bandwidth, measured at half of the peak height, is confined within 8 and 12 mm.

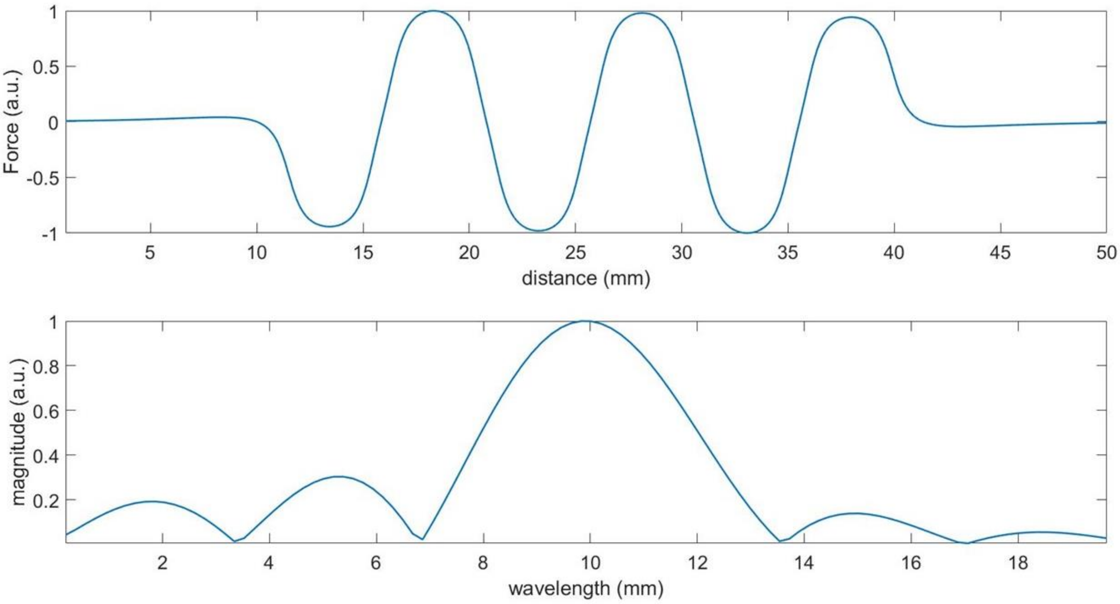

Figure 4.7 Approximate spatial distribution of Lorentz force from a 10 mm periodicity PPM and its spectrum.

As the relationship between velocity, wavelength and frequency is known via $v = \lambda \times f$, it is possible to draw three lines that intersect the dispersion curve, the gradient of which is the nominal wavelength λ, and the upper and lower boundaries of the bandwidth, as figure 4.8 depicts. Thus, in this example, SH_1 mode can be excited by feeding the generator with driving waveforms at frequencies between 576 and 648 kHz.

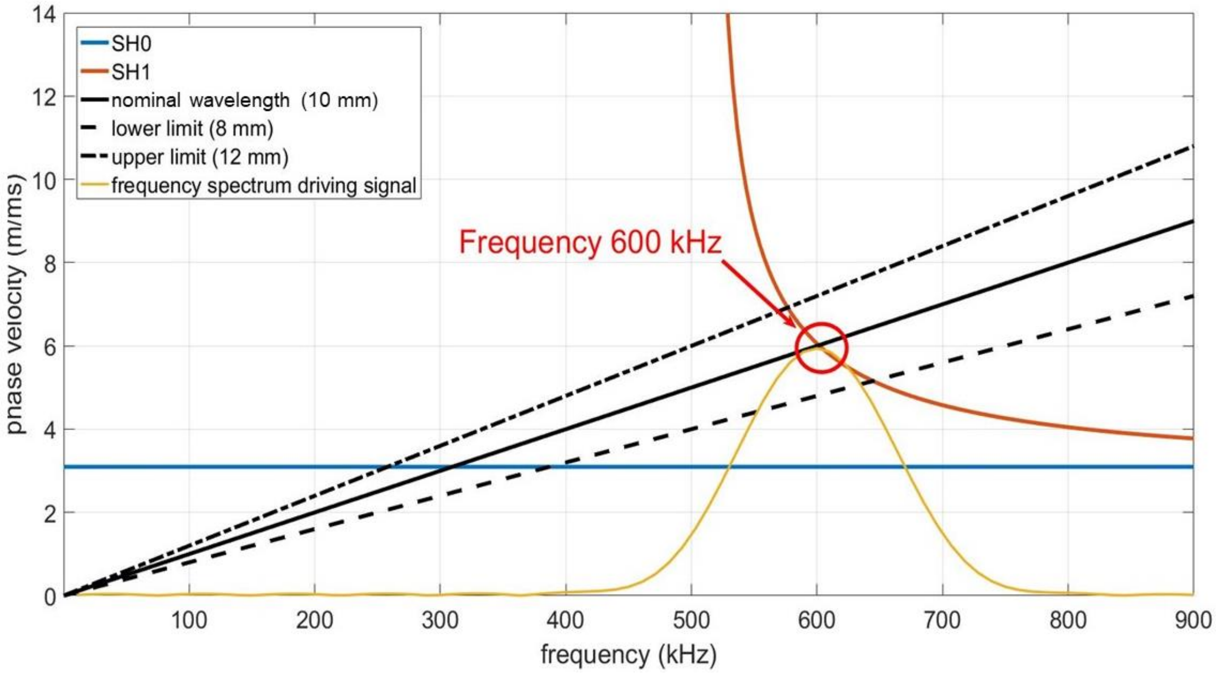

Figure 4.8 Dispersion curve for SH waves in aluminium plate 3mm thick, one solid line of which gradient is the nominal wavelength, two dashed lines of which gradient is the lower (8 mm) and upper (12 mm) limit of the spatial bandwidth and the frequency magnitude spectrum of an 8-cycle toneburst.

Hence, driving an 8-cycle toneburst at a frequency of 600 kHz, within the operating frequency range, ensures that SH_1 mode is generated. In many cases, the assumption of the single wavelength is sufficient to provide reasonably accurate measurements. So the following figures will only show the intersection of the "wavelength" line with the desired wave mode.

The mode selected for the purpose of the measurement was the SH_0 mode, which is represented by the blue horizontal line. The working frequency sought can be retrieved from the intersection of the wavelength line with the SH_0 curve mode, as depicted in figure 4.9. Hence, the generation of the SH_0 can occur by exciting the source at a frequency of approximately 300 kHz.

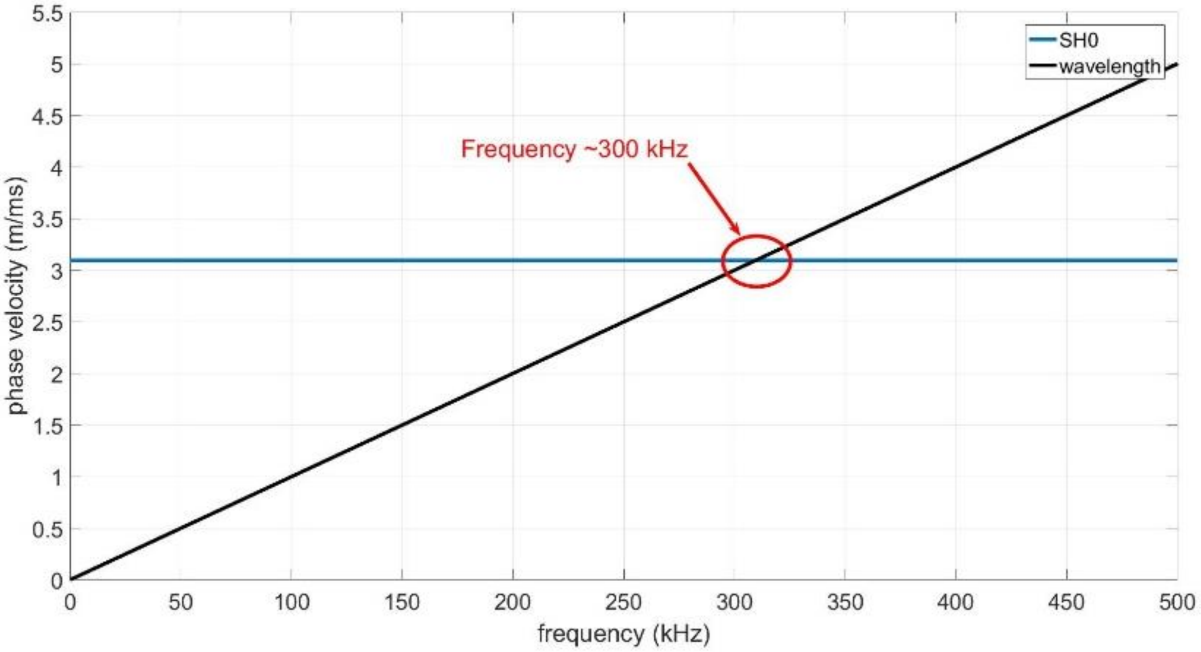

Figure 4.9 Intersection between wavelength gradient and SH wave relative mode.

Once the working frequency is known, it is possible to design the driving waveform in MATLAB. So, the driving current was a 5-cycle sine wave at 300 kHz, windowed with a Gaussian function, as shown in figure 4.10.

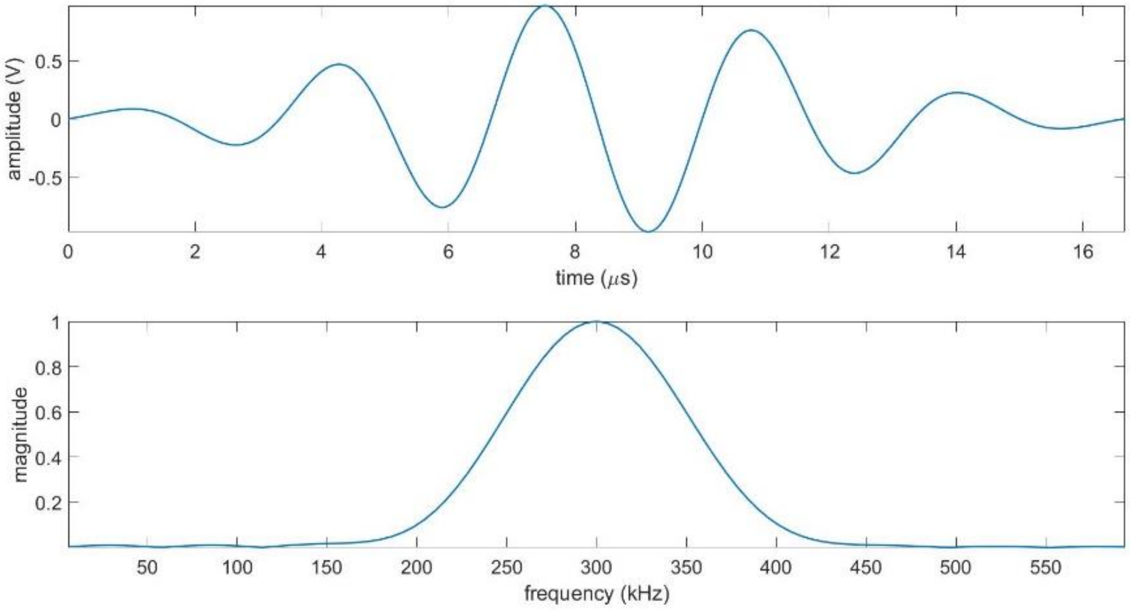

Figure 4.10 Driving current for exciting SH$_0$ within a 3 mm thick aluminium plate and its frequency spectrum.

Each acquired signal was bandpass-filtered in order to remove signals at any unwanted frequency. The bandpass filter was a Butterworth filter whose lower and upper frequency were selected from the bandwidth of the driving current measured at -6 dB: 245 kHz and 354 kHz, respectively. The bandpass filter was applied by using the MATLAB function *filtfilt* which performs a zero-phase digital filtering in order to remove the phase shift [22]. The signals recorded at four different propagation distances are depicted in figure 4.11.

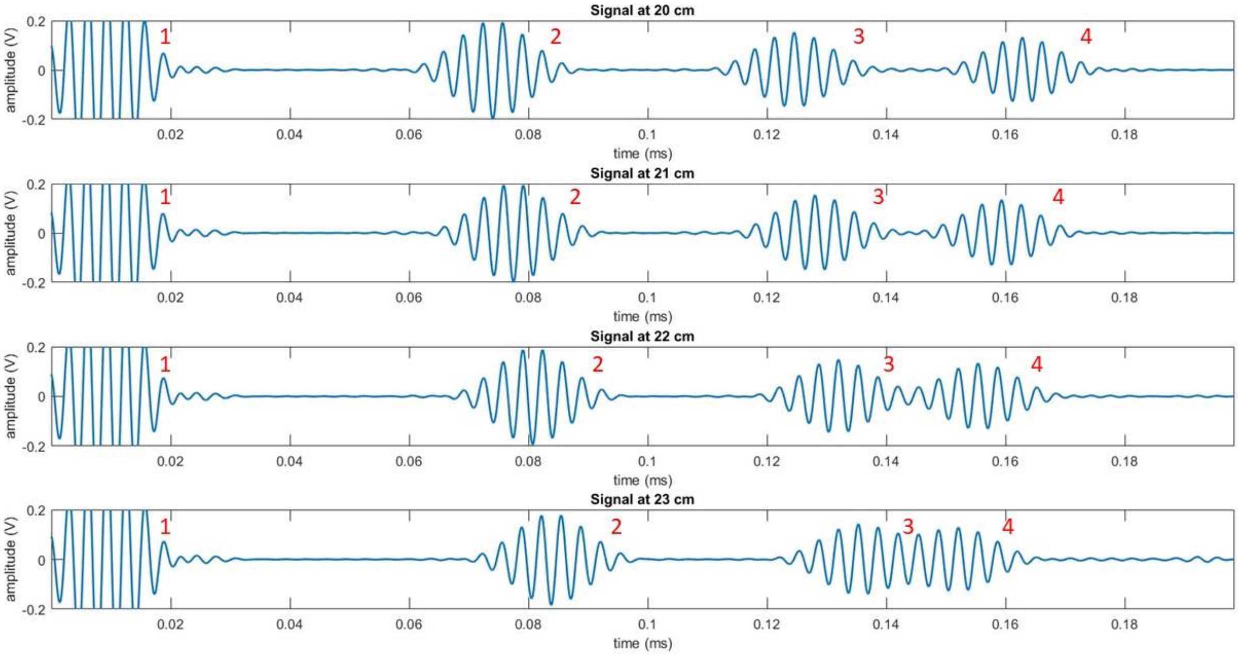

Figure 4.11 Recorded signals at 20, 21, 22 and 23 cm in a 3 mm thick aluminium plate.

From the above figure, it can be noted the presence of four separate arrivals (numbered 1-4). The first (number 1) is electrical pick-up. Number 2 is the direct signal (source to receiver) whose delay increases with distance. Numbers 3 and 4 are reflections from sample edges, and indeed as the receiver is moved away from the generator the two reflections overlap.

In order to check the properties of the excited mode (a 300 kHz SH_0 mode), each direct signal has been analysed in the frequency domain via a magnitude FFT performed in MATLAB. The signals and their relative spectra are depicted in figure 4.12.

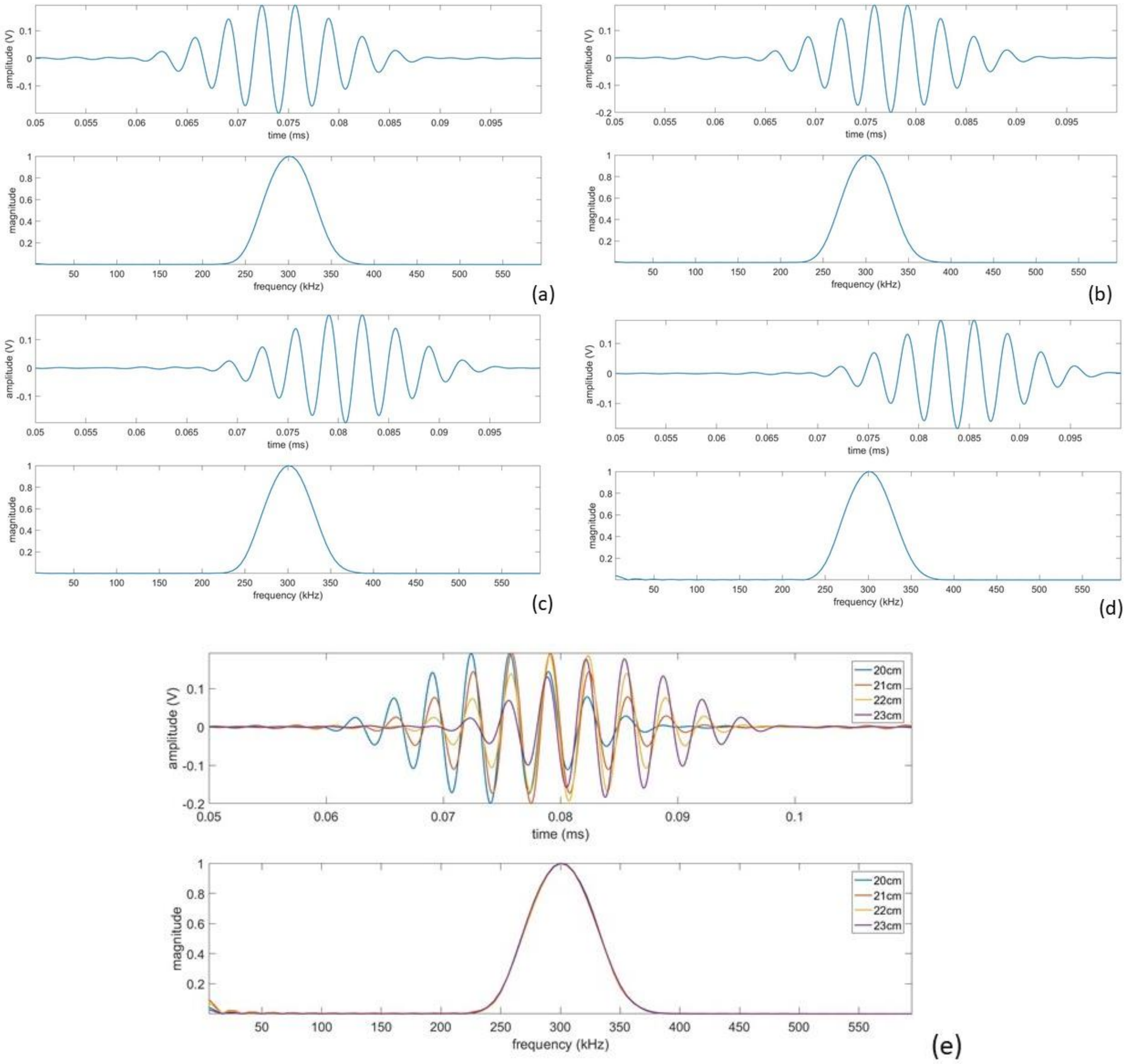

Figure 4.12 Waveform and its FFT spectrum of the signal at (a) 20, (b)21, (c)22, (d)23 cm.(e) Comparison of all signals and their frequency spectra.

The next step in the analysis, in order to demonstrate the reliability of the method, is to measure the phase and group velocity of the travelling wave. The method adopted uses the phase information carried by the wave for retrieving the propagation velocities [23]. The phase velocity is determined by using the equation:

$$c_p = \frac{2\pi f L}{(\Phi_1 - \Phi_2) + 2\pi f \tau_s} \tag{4.33}$$

where f is the carrier frequency (i.e. the driving frequency of 300 kHz), L is the distance between the two signals selected, $(\Phi_1 - \Phi_2)$ is the phase difference between the two signals and τ_s is the arrival time difference between them. The phase difference is calculated by taking the central frequency of the received signals, which is the peak frequency in the frequency domain, and evaluating their relative phase values at that frequency. τ_s is calculated by cross-correlating the two signals determining the time difference between them. The group velocity, on the other hand, is evaluated by applying the following equation:

$$c_g = \frac{2\pi f L}{{d\Phi}/{df} - \tau_s} \tag{4.34}$$

where ${d\Phi}/{df}$ is the frequency derivative of the phase.

The method, whenever applied, will be done by using the closest and the furthest signals recorded. In this the case, the reference distance (L) is 3 cm. The two signals taken in account, at 20 and 23 cm, are depicted in figure 4.13.

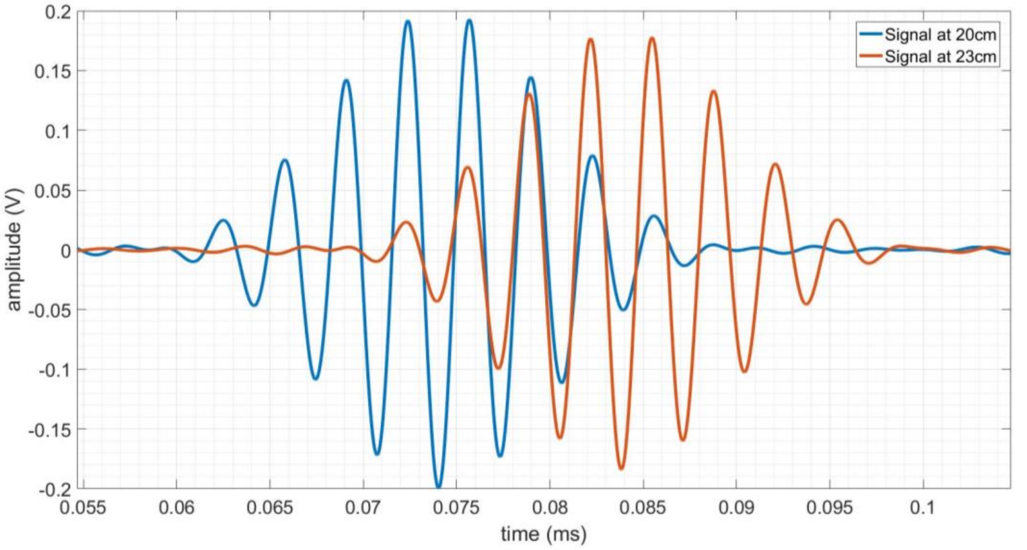

Figure 4.13 Detail of the signals acquired at 20 and 23 cm in a 3 mm thick aluminium plate.

Then, these two signals are converted into the frequency domain. It is worth briefly explaining the way in which MATLAB calculates magnitude and phase [22]:

- The magnitude is calculated by using the function *abs(x)* which provides the real part of the frequency content of the signal
- The phase is calculated by using two function concatenated *unwrap(angle(x))*. The inner function, *angle*, returns the phase angle in the within $-\pi$ and $+\pi$. While the outer function, *unwrap*, unwraps the radian phase angle in a linear array adding a multiple of $\pm 2\pi$ whenever the difference between two adjacent angles is greater than or equal to pi radians.

Even though *unwrap* works well in several circumstances, erroneous phase jumps may occur regardless of the presence of noise [24,25]. Therefore, in order to reduce possible error due to the algorithm, the phase is unwrapped and measured within the bandwidth of the frequency spectrum. The magnitude and phase of the signals is shown in figure 4.14.

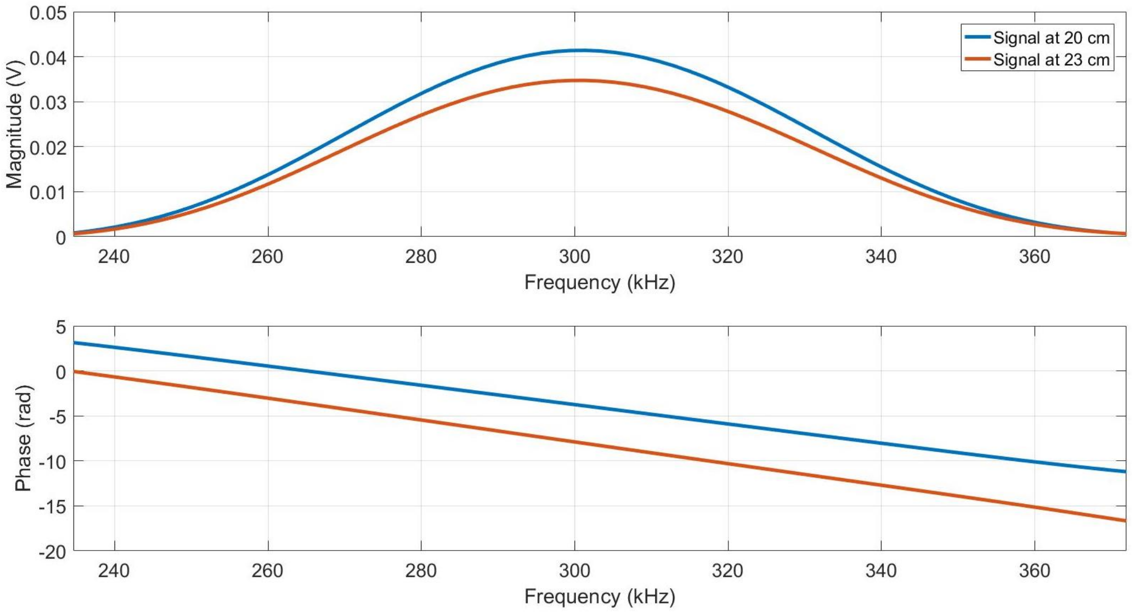

Figure 4.14 Magnitude and phase of the signals received at 20 and 23 cm.

The phase values, Φ_1 and Φ_2, are calculated by measuring the peak frequency and extracting the phase information at that frequency, *i.e.* $\Phi(f)$ where f is the peak frequency. The phase and group velocity can then be plotted with respect to the frequency using equations (4.21) and (4.22), as shown in figure 4.15.

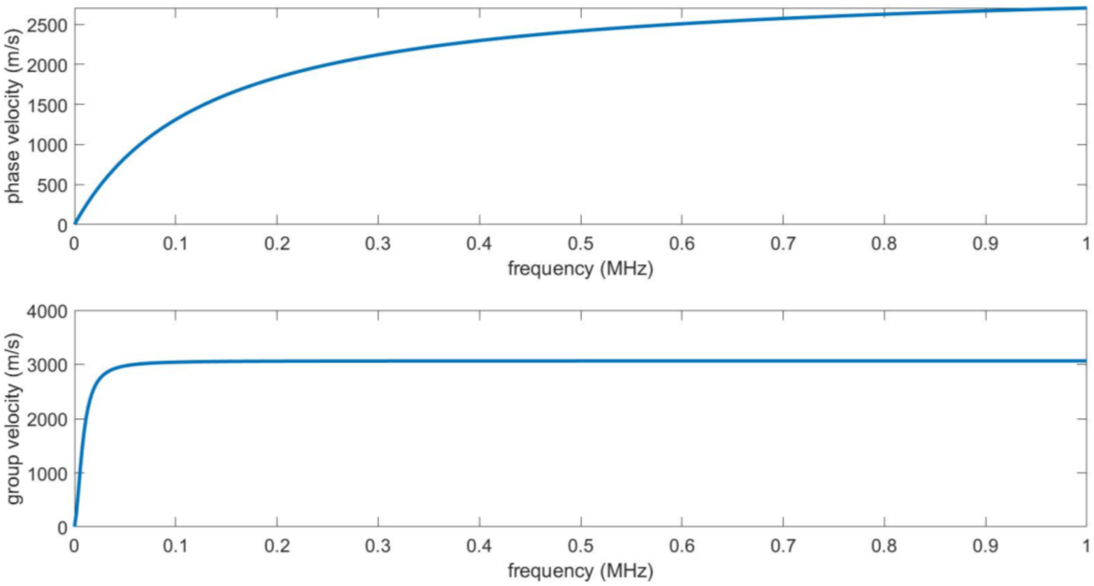

Figure 4.15 Phase and group velocities of SH_0 waves propagating in a 3mm thick aluminium plate.

It can be seen that the two graphs are different, even though the mode studied is an SH0 mode, where the phase and group velocity curves should correspond to the driving frequency of 300 kHz. In fact, it can be seen that the phase velocity is 2,500 ± 30 m/s while the group velocity is 3,060 ± 30 m/s, as shown in figure 4.16.

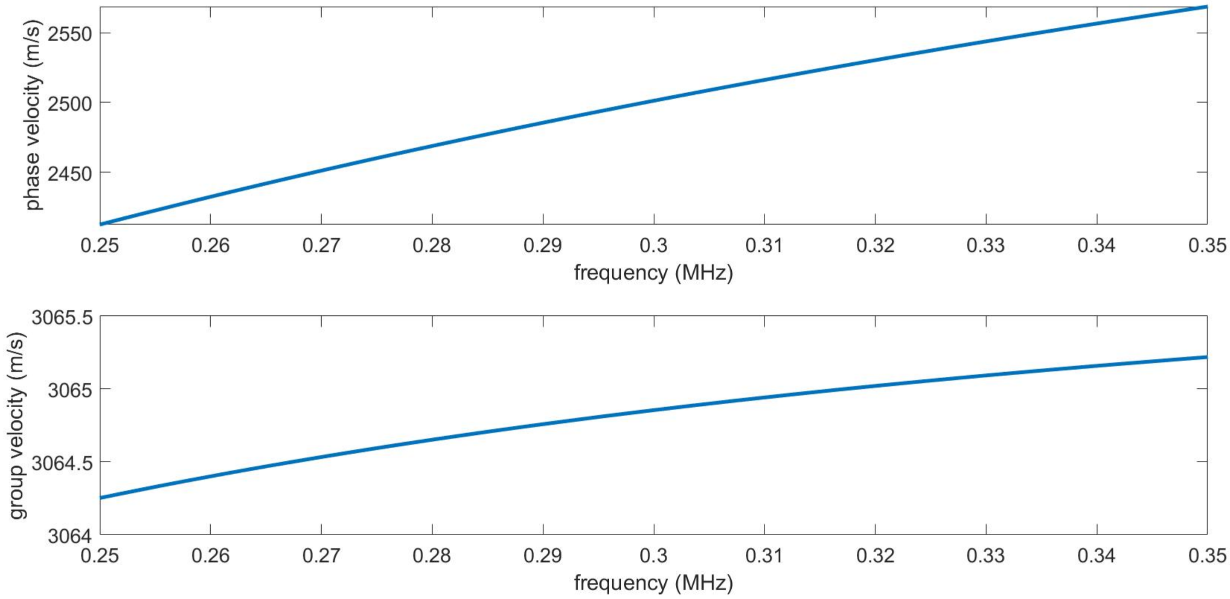

Figure 4.16 Detail of phase and group velocities of SH_0 waves propagating in a 3mm thick aluminium plate.

This discrepancy is due to the abovementioned reason: the *unwrap* algorithm. The calculation of the phase velocity is done using the phase difference, so any erroneous jumps can affect the terms of the difference making the final result not as reliable as the group velocity calculation, as in this case. The group velocity, in fact, is calculated using the derivative of the phase, making the calculation more robust as the phase gradient is not affected by the variation of single values. For the purposes of analysis, the phase velocity graphs will still be shown as the group velocity calculation passes through the phase calculation.

The next analyses will be carried out by following a similar procedure in order to show the possibility of exciting and analysing SH_0 wave mode within composite samples.

4.5 Glass sample

In the previous case, as the sample was an aluminium plate, metallic patches were not needed. The next sample described is a glass sheet, the kind used for windows, and so copper patches are necessary. This material is perfectly suited for the purpose of demonstrating the possibility of using EMATs in combination with copper tape, to generate and receive SH guided waves.

Glass is an isotropic, electrically insulating material [26]. Such characteristics make the specimen ideal for testing the system and the method, which were previously adopted on an aluminium sample, that was almost isotropic (mildly anisotropic in reality) and conductive. The sample is a 3 mm thick glass plate square-shaped, whose side is 400 mm long. The test consisted of taking 5 measurements moving the receiver at 18, 19, 20, 21 and 22 cm from the fixed position transmitter, as figure 4.17 shows.

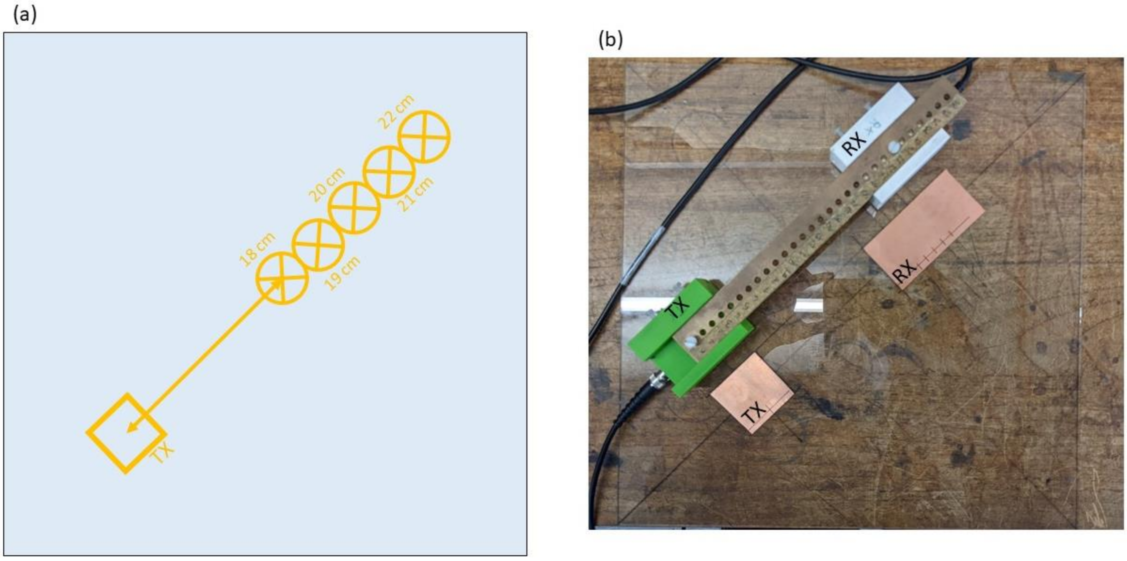

Figure 4.17 (a) sketch of the measurement geometry; (b) photo of the glass plate above a wooden surface, showing the transmitting (TX) and receiving (RX) probes and the two copper tape patches.

As above, the dispersion curve relevant to the specimen are calculated, and the nominal wavelength is drawn within the plot, in order to establish the working frequency as depicted in figure 4.18.

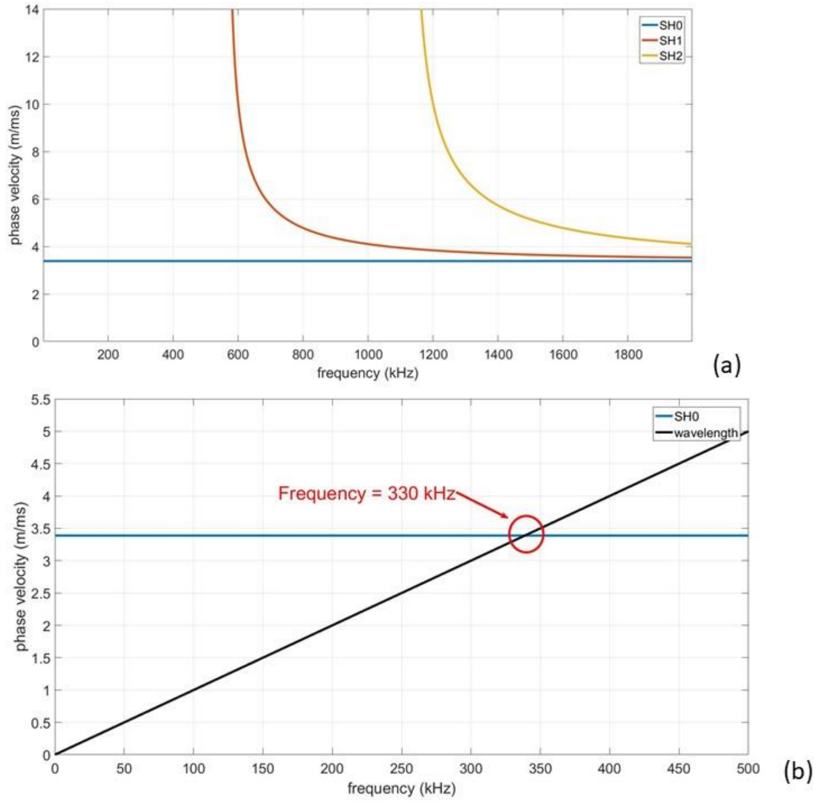

Figure 4.18 (a) Dispersion curve for SH waves in glass plate 3mm thick and a line of which gradient is the wavelength; (b) detail of (a) which shows the intersection between wavelength gradient and SH wave relative mode.

The driving current was an 8-cycle sine wave signal at a frequency of 330 kHz with a Gaussian window. As before, once recorded, the signals were then bandpass-filtered between the lower and upper frequency of the driving current bandwidth measured at -6 dB: 292 kHz and 368 kHz, respectively. The recorded signals are displayed below in figure 4.19.

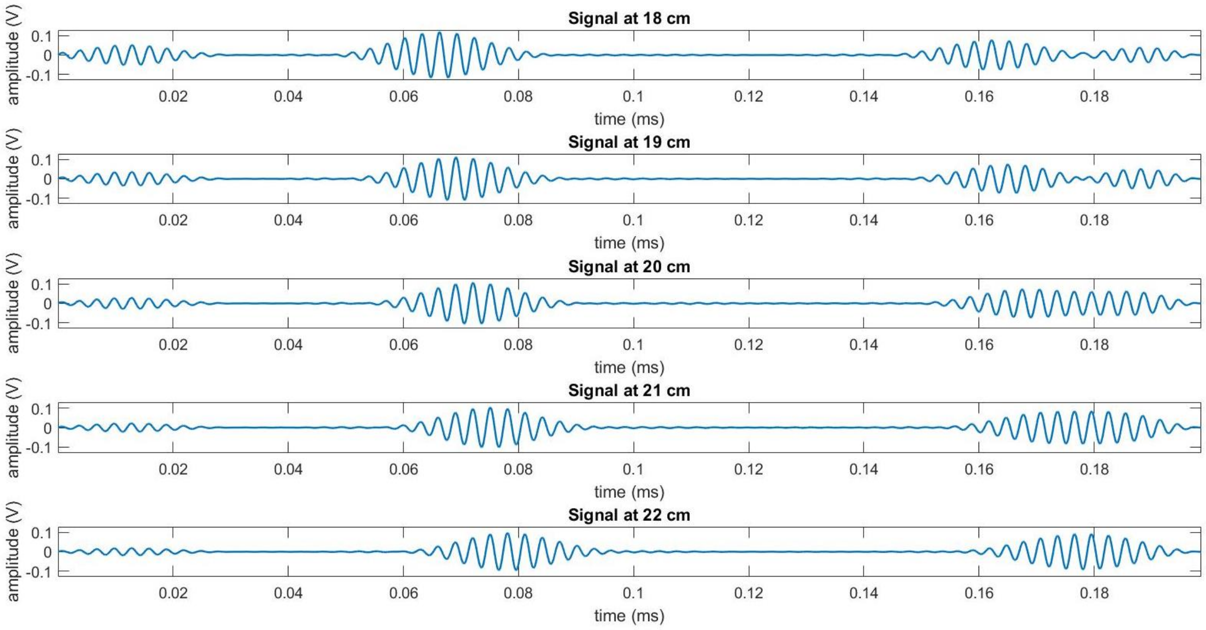

Figure 4.19 Received signals at 18, 19, 20, 21 and 22 cm in a 3mm thick glass plate.

The signals were then studied in the frequency-domain. As figure 4.20 shows the frequency peaks are all centred around 330 kHz. Moreover, the frequency spectra do not present any distortion, a fundamental feature as the waves generated are SH_0, where no dispersion would be expected.

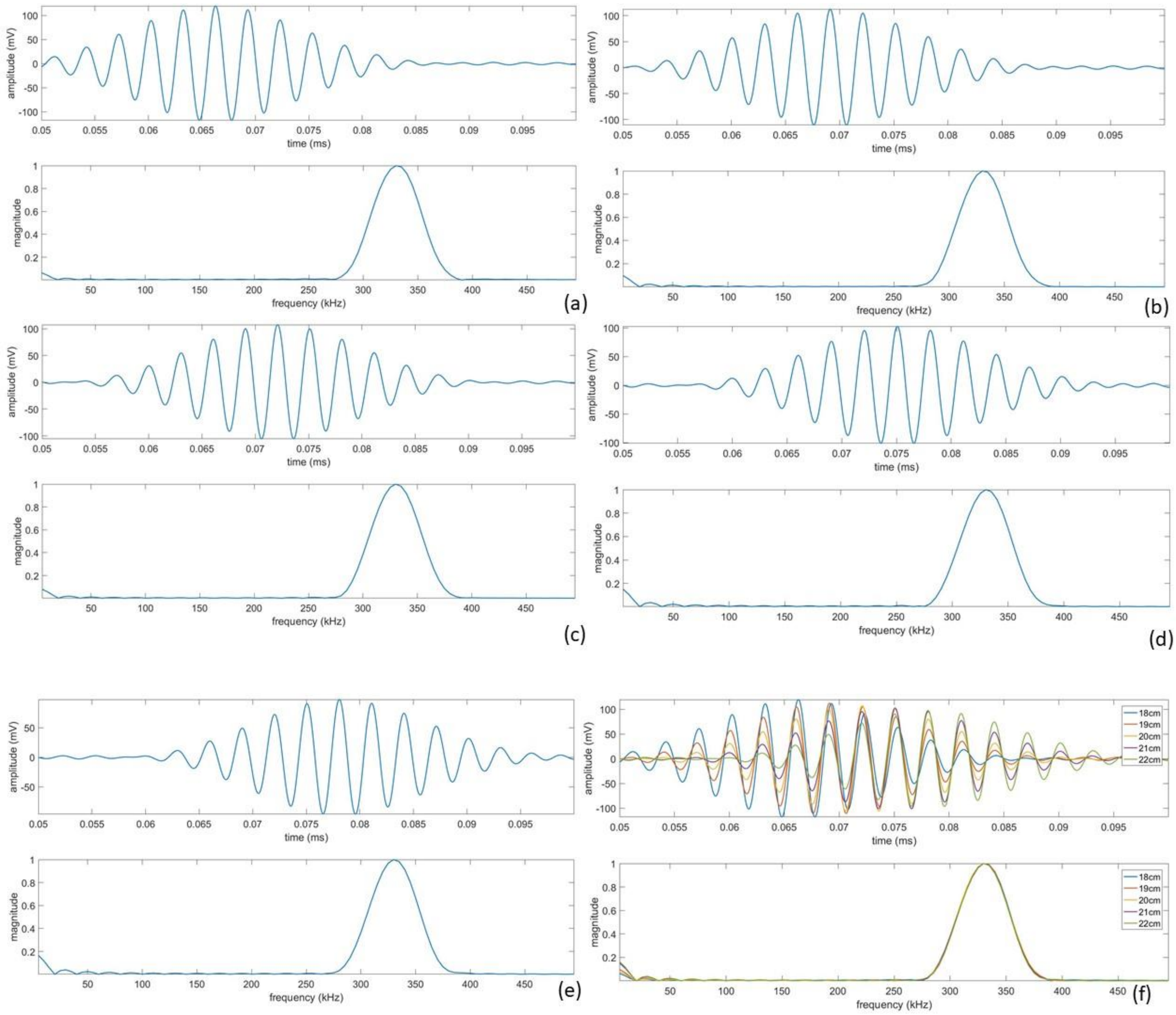

Figure 4.20 Waveform and its FFT spectrum of the signal at (a) 18, (b)19, (c)20, (d)21 cm, (e)22 cm. (f) Comparison of all signals and their frequency spectra.

As explained before, the next step was to measure phase and group velocities of the wave, using equations (4.21) and (4.22), as depicted in figure 4.21. In figure 4.21(a) the received signals at 18 and 22 cm are shown, their relative magnitude and phase are depicted in 4.21(b) and the resultant phase and group velocities are shown in 4.21(c-d).

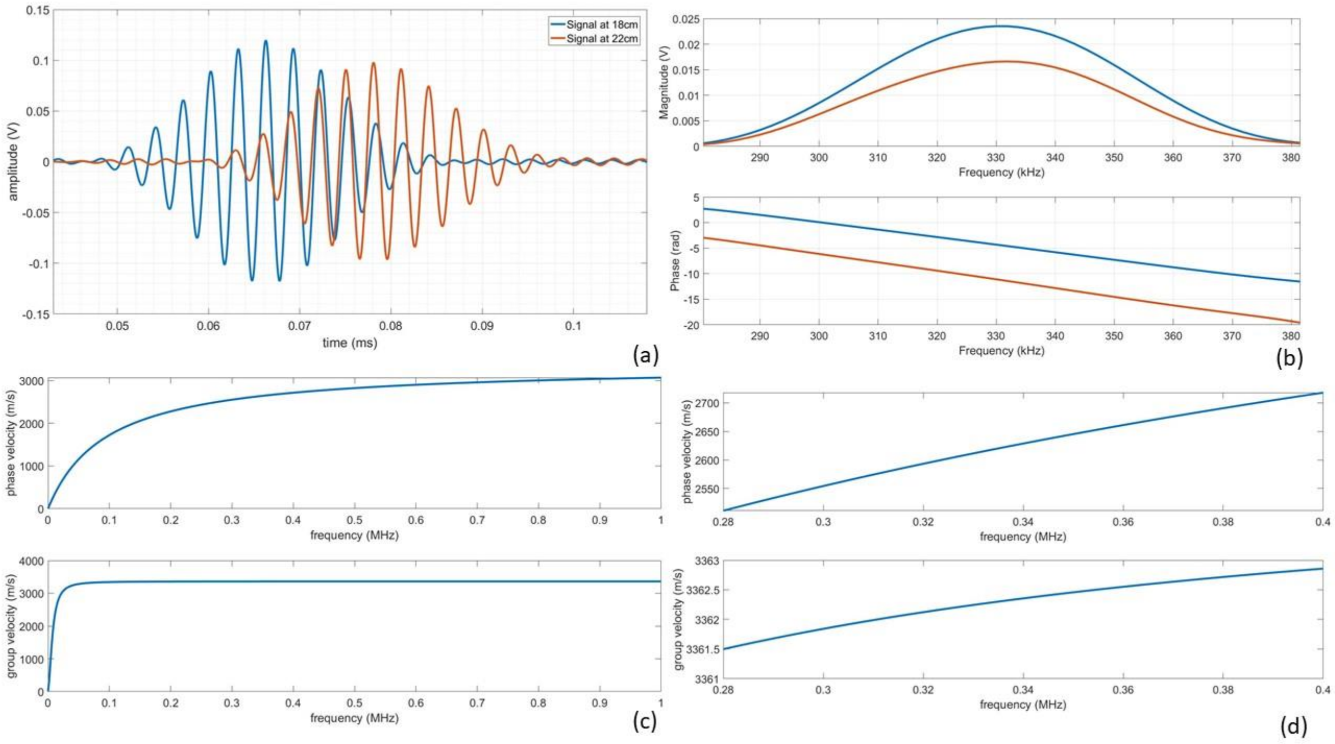

Figure 4.21 (a) Signals received at 18 and 22 cm; (b) their magnitude and phase; (c) phase and group velocities of SH_0 waves propagating in a 3mm glass plate; (d) detail of phase and group velocities.

As mentioned before, the calculation of the phase velocity is affected by the *unwrap* function, yielding a phase velocity of 2,630 ± 30 m/s, calculated at 330 kHz. The group velocity is in line with the predicted group velocity being equal to 3,360 ± 30 m/s.

This test demonstrates the validity of the method for generating SH waves in a non-conductive medium, using EMATs by means of copper tape where eddy currents are induced within the copper layer, and the subsequent generation of elastic waves transferred into the sample through the adhesive layer.

4.6 Composite samples

4.6.1 Typical composite structures

In the few last decades, the use of composite materials in aerospace manufacturing has grown rapidly, due to their important characteristics [27]. Composites are materials realised by a combination of at least two elements, which results in better mechanical properties than those of the components taken individually. Composite materials are manufactured by using a reinforcing phase and a continuous phase. The reinforcing phase (or reinforcement) provides strength and stiffness, while the continuous phase (or matrix) preserves the orientation, ensures the safety (against abrasion or corrosion) of fibres and moreover transmits loads between fibres.

The matrix can be either a polymer (such as epoxy resin), metal or a ceramic, from which it is possible to classify composites into polymer matrix composite (PMC), metal matrix composite (MMC) and ceramic matrix composite (CMC) [28]. A further classification of resins is as either thermoplastic or thermoset. The properties of the resultant material are directly affected by:

- Properties of the resin (i.e. matrix);
- Properties of the fibre (i.e. reinforcement);
- Ratio resin/fibre (fibre volume up to 70%);
- Geometry and orientation.

The reinforcement is either continuous-fibre or discontinuous-fibre (or particulate) [10], where the typical fibre materials are either carbon or glass. Particulate composites are materials where reinforcing particles, evenly distributed [29], are suspended in a matrix [30]. Such composites have isotropic structure and properties, due to the random orientation of the particles [29]. An example of discontinuous reinforcements are chopped fibres and random mat [10].

The continuous-fibre composites are characterised by fibres, whose length is much greater than its diameter, also suspending in a matrix. These composites generally have a preferred orientation, unlike particulate composites, and include unidirectional and woven cloth. Figure 4.22 shows different categories of reinforcement.

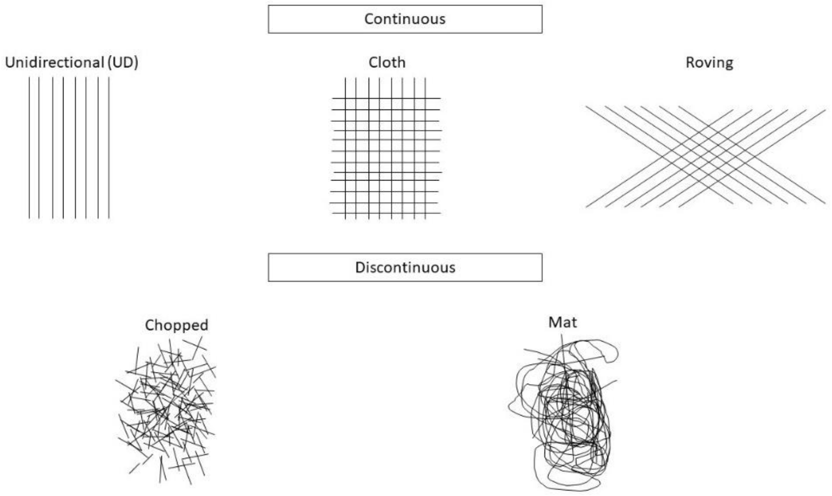

Figure 4.22 Type of reinforcement (after [10]).

The end properties of a composite part produced from the abovementioned combination is not only a function of the individual properties of matrix and fibre, but is also dependent on the way the components are processed, that is the manufacturing process. The different manufacturing methods can be classified as direct processes (like resin transfer moulding – RTM, pultrusion, contact moulding), which use separate fibres and resin brought at the point of moulding; or indirect (e.g. vacuum bag/autoclave moulding, compression moulding) processes where fibres are pre-impregnated with resin (prepreg) [31]. Ideally, a fabrication process should have [32]:

- High productivity;
- Minimum material cost;
- Maximum geometrical flexibility;
- Maximum property flexibility;
- Minimum finishing requirements;
- Reliable and high quality manufacture.

4.6.2 Composite manufacturing methods

For the work in this thesis samples produced in autoclave and by pultrusion were used, [33] so these two manufacturing methods will be discussed in more detail below.

4.6.2.1 Autoclave-based methods

Before describing this process, it is necessary to digress and introduce an important term, although it has been used previously: "prepreg". The term prepreg refers to pre-impregnated fibres. In general, a prepreg appears as a thin sheet or lamina of unidirectional (or possibly woven) fibre/polymer composite, protected on both sides with easily removable separators, as shown in figure 4.23. Thus prepregs represent an intermediate stage in the fabrication of a polymeric composite component, and the resin inside is actually partially cured.

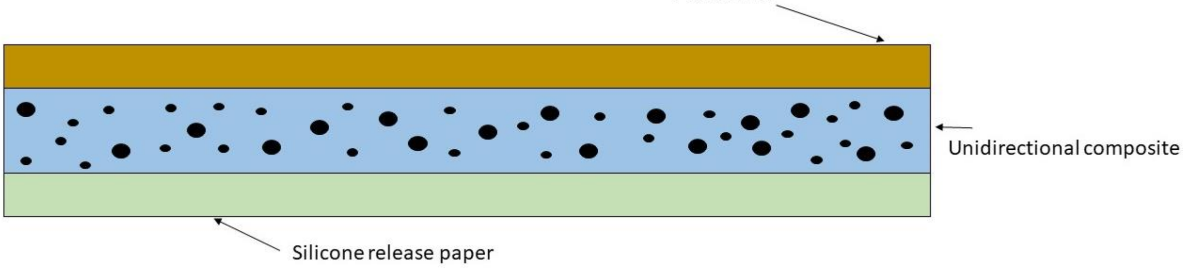

Figure 4.23 Sketch of a prepreg (after [10]).

Autoclave-based processing of PMCs produces a very high quality product, which is why aerospace components are made by this process. An autoclave is a closed vessel where processes occur under the simultaneous application of high temperature and pressure. The combination of these two factors (heat and pressure) consolidates the laminae, removes the entrapped air and cures the polymeric matrix. Thus, the involved phenomena in autoclave processing of composites are: chemical reaction, flow of the resin and heat transfer. The setup in an autoclave consists of a bag containing prepregs stacked in desired orientations, as depicted in figure 4.24.

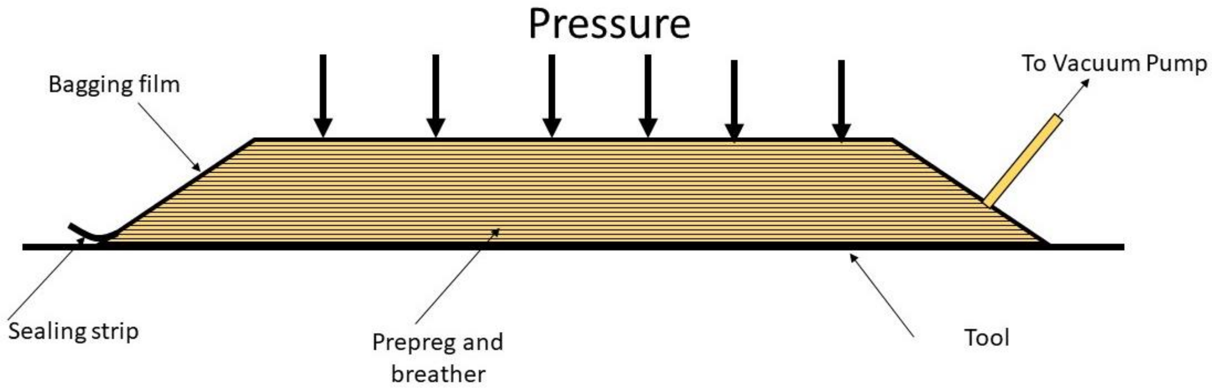

Figure 4.24 Set-up in an autoclave (after [10]).

The bag is a thin and flexible membrane made of rubber, which divide the layup sequence from the gas used to compress. The pressure difference across the bag walls achieves densification and curing. Vacuum can be used, in which case the contents of the bag are removed and air pressure consolidates the composite. The orientation sequence of plies in the laminate (which is still mostly done by hand) is previously determined from the theory of elasticity in order to achieve appropriate magnitudes and directions of stress, and to prevent unwanted twisting and/or torsion.

4.6.2.2 Pultrusion

In this process, continuous sections of PMCs with fibres oriented mostly axially are fabricated. Figure 4.25 depicts a schematic diagram of this process.

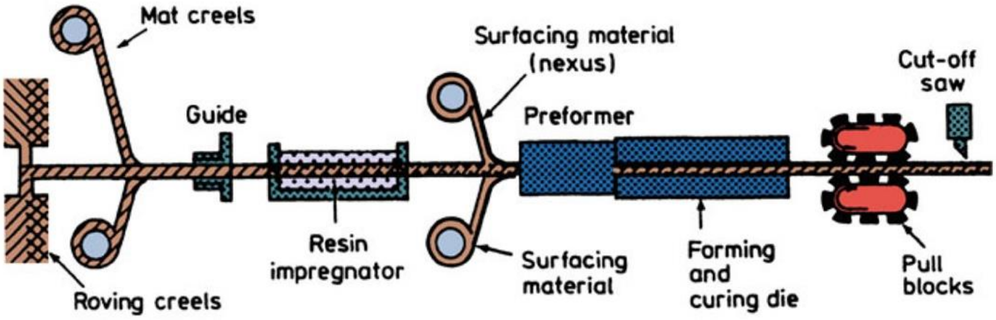

Figure 4.25 Sketch of the pultrusion process (from [10]).

As noted, the pultrusion process involves pulling the necessary raw materials which are, commonly, in form of continuous fibre tows. Mat or biaxial fabric may be added to them in order to provide some transverse strength. Next, they pass through a resin bath containing a resin. After this, the impregnated fibres go through a series of wipers which remove any excess polymer and then enter the heated die. The heated die has the shape of the component to be produced. At this step, the resin is cured in the die and the composite is pulled out. Different forms of reinforcement can be used. Other forms of materials include chopped strand mat consisting of short fibres which can be bonded or stitched to a carrier material, generally a unidirectional tape. The addition of such forms provides reinforcement at 0°, 90°, or an arbitrary angle to the loading direction.

4.6.3 Tests on CFRP specimens

All CFRP samples were manufactured by COTESA GmbH (a German company, where the author had a 3 month secondment). The specimens were produced by autoclave-methods and the samples were analysed following the procedure explained above.

4.6.3.1 UD sample

The first specimen tested was a 3 mm thick unidirectional CFRP plate, whose dimensions were 350 x 550 mm. The specimen was made from 16 unidirectional prepreg plies. The prepreg was used to manufacture the composite specimen. From the specifics given by the manufacture the stiffness matrix could be retrieved, which is shown below in table 4.1.

Table 4.4 Stiffness matrix for the unidirectional CFRP plate.

168.59 (GPa)	3.82	3.82	0	0	0
3.82	9.84	3.82	0	0	0
3.82	3.82	9.84	0	0	0
0	0	0	3.01	0	0
0	0	0	0	4.98	0
0	0	0	0	0	4.98

As before once known, the mechanical properties of the sample the dispersion curves can be calculated by using the software “Dispersion calculator”. The dispersion curves are drawn and, then, the nominal wavelength of the source is plotted among them in order to establish the frequency required to excite the SH_0 mode, as shown in figure 4.26.

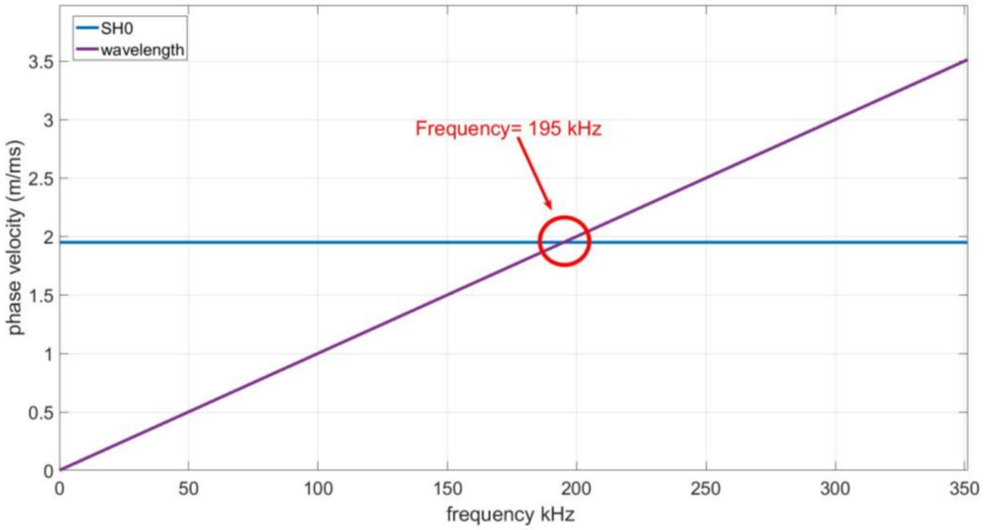

Figure 4.26 (a) Dispersion curve for SH waves in a 3mm thick UD CFRP plate together with a line of whose gradient is that of the chosen wavelength.; (b) intersection between wavelength gradient and SH wave relative mode.

From the intersection between the wavelength and the curve depicting the desired mode (SH_0), the working frequency is equal to 195 kHz. Knowing the working frequency, the driving waveform was then created in MATLAB. The driving current was a 10-cycle sine wave with a Gaussian window. In this case, the measurement consisted of taking 4 measurements along the direction of the fibre, and placing the receiver at 20, 22, 24 and 26 cm from the source, as figure 4.27 shows.

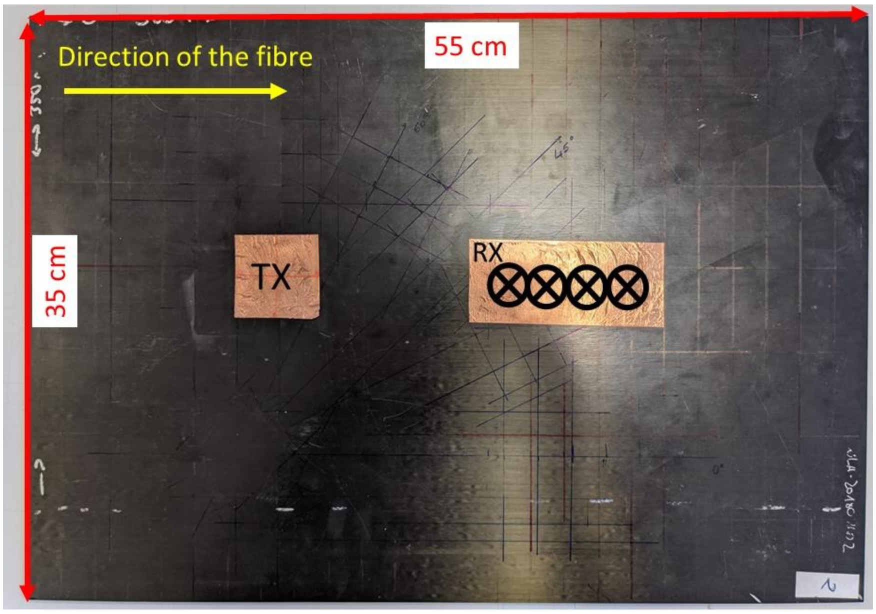

Figure 4.27 Photo of the UD sample, showing the copper tape patches and the direction of the fibre.

Once acquired, the signals were bandpass-filtered adopting the same type of filter described previously. In this case, the lower and upper frequencies of the driving current bandwidth measured at -6dB and, hence, the high- and low-pass frequencies were 177 kHz and 213 kHz, respectively. The received signals are shown below in figure 4.28.

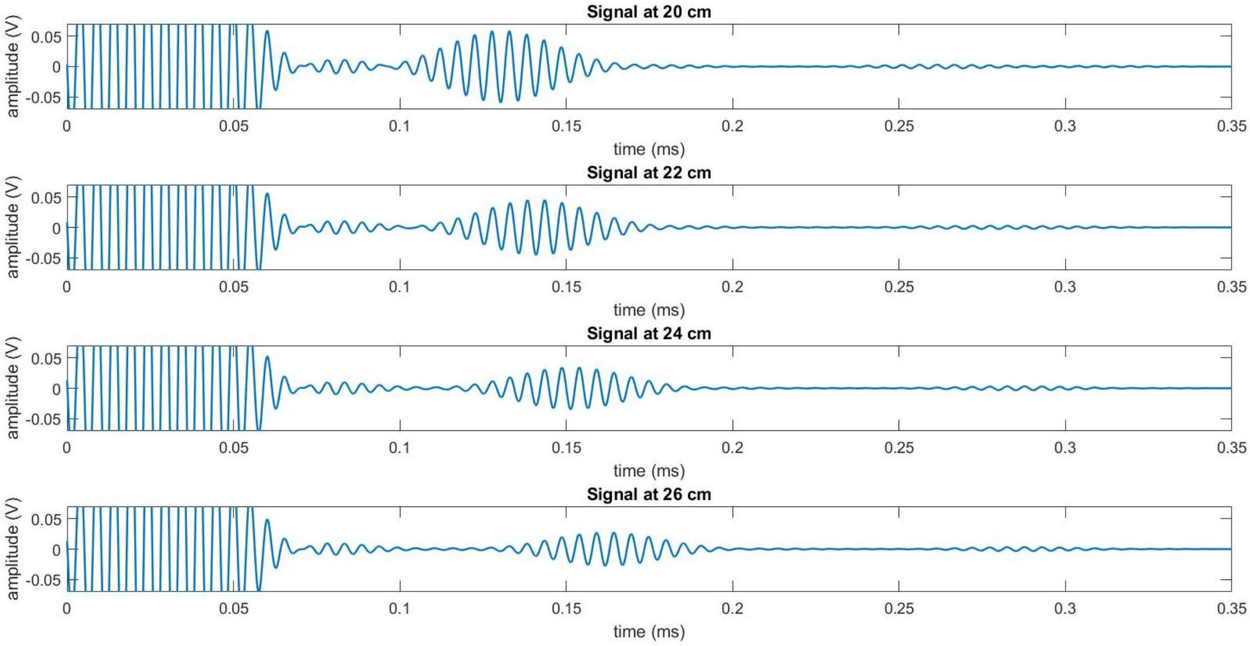

Figure 4.28 Received signals at 20, 22, 24 and 26 cm in a 3 mm thick UD CFRP plate.

The next step was to study the signals in the frequency-domain. As figure 4.29 shows the frequency peaks are all centred around 195 kHz, within the excitation bandwidth.

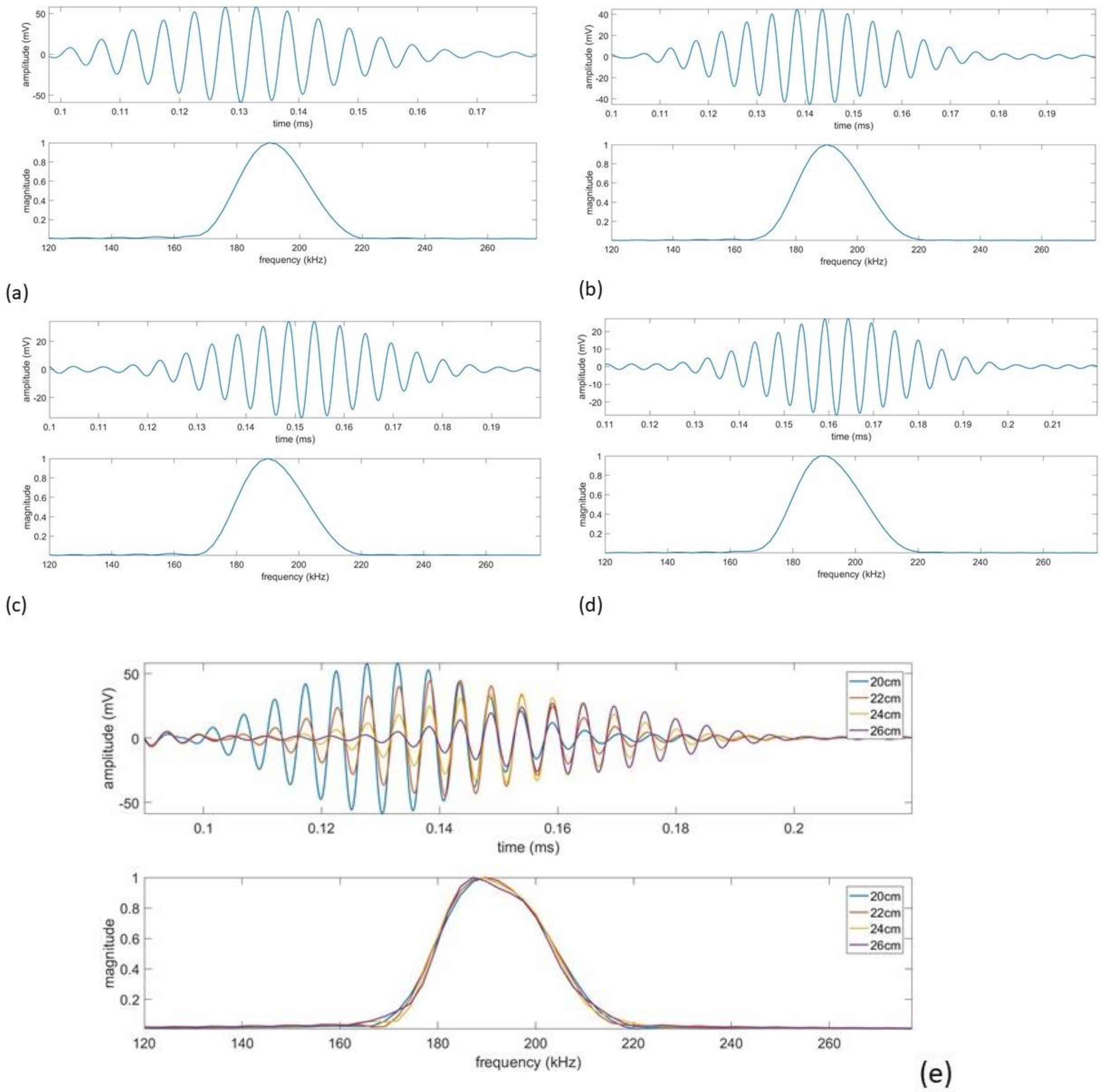

Figure 4.29 Waveform and its FFT spectrum of the signal at (a) 20, (b)22, (c)24, (d)26 cm.(e) Comparison of all signals and their frequency spectra.

The following step in the analysis was to measure phase and group velocities of the wave travelling using equation (4.21) and (4.22), as depicted in figure 4.30.

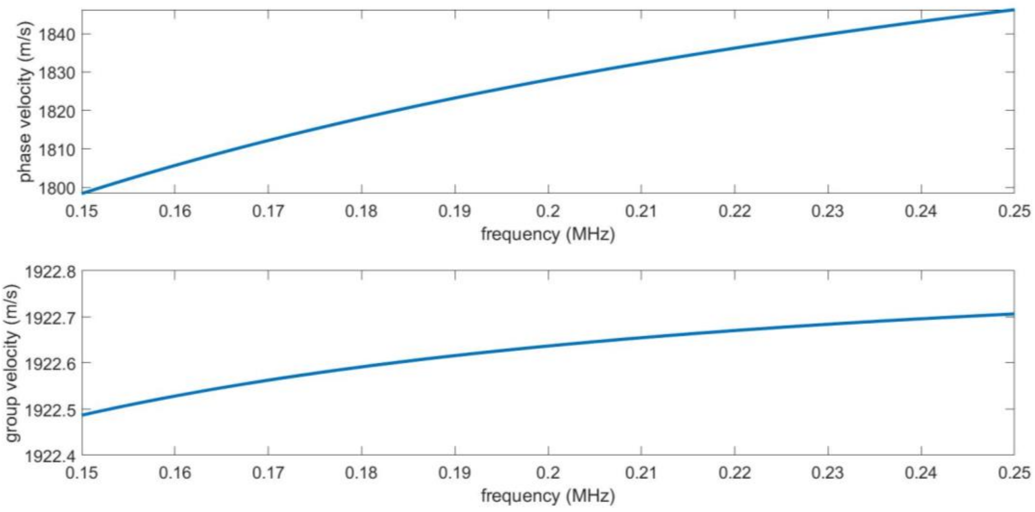

Figure 4. 30 Phase and group velocities of SH_0 waves propagating in a 3mm UD CFRP plate for frequencies between 150 and 250 kHz.

From the analysis, the values of phase and group velocity at the frequency peak (195 kHz) are, 1,820 ± 30 m/s and 1,920 ± 30 m/s respectively. As expected, the phase velocity is not as reliable as the group velocity, due to the phase unwrap process as mentioned previously. The group velocity is in line with the expected value, as a further demonstration of the possibility of exciting an SH_0 within a composite sample via EMATs and a patch.

4.6.3.2 Quasi-isotropic sample

The last type of CFRP specimen tested was a quasi-isotropic plate, already introduced in section 3.5. The dimensions of the sample are 480 x 350 x 2.8 mm. The stiffness matrix of the sample was shown earlier in Table 3.1. The relevant dispersion curves are displayed and, as before, from the intersection of the wavelength with the desired mode’s curve the working frequency is retrieved. Figure 4.31 depicts the selection of the frequency.

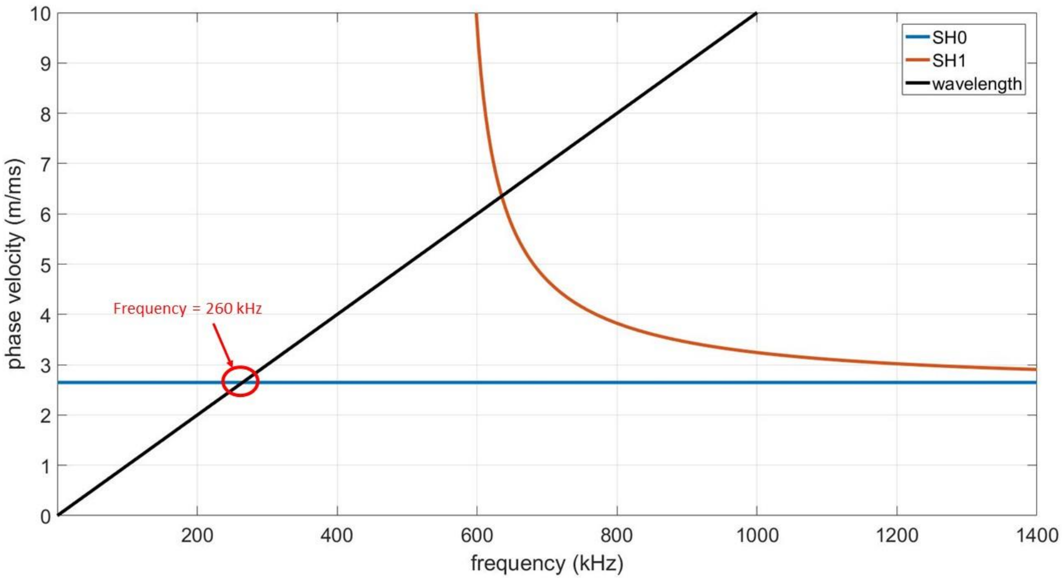

Figure 4.31 (a) Dispersion curve for SH waves in a 2.8 mm thick quasi-isotropic CFRP plate, whose stiffness matrix is described in table 3.1, and a line of which gradient is the wavelength.

The driving current was designed in MATLAB, and consisted of an 8-cycle sine wave signal at a frequency of 250 kHz, windowed with a Gaussian function. Although figure 4.35 indicates 260 kHz to be the correct value to generate the SH_0 mode, it was experimentally observed that a current at 250 kHz showed a slightly higher SH_0 wave amplitude. The measurement consisted of taking 3 measurements along the 0° direction of the fibre, by placing the receiver at 16, 18 and 20 cm from the source. The acquired signals were bandpass-filtered as described before. The lower and upper frequencies of the filter were 220 and 280 kHz, respectively, and the results are shown in figure 4.32.

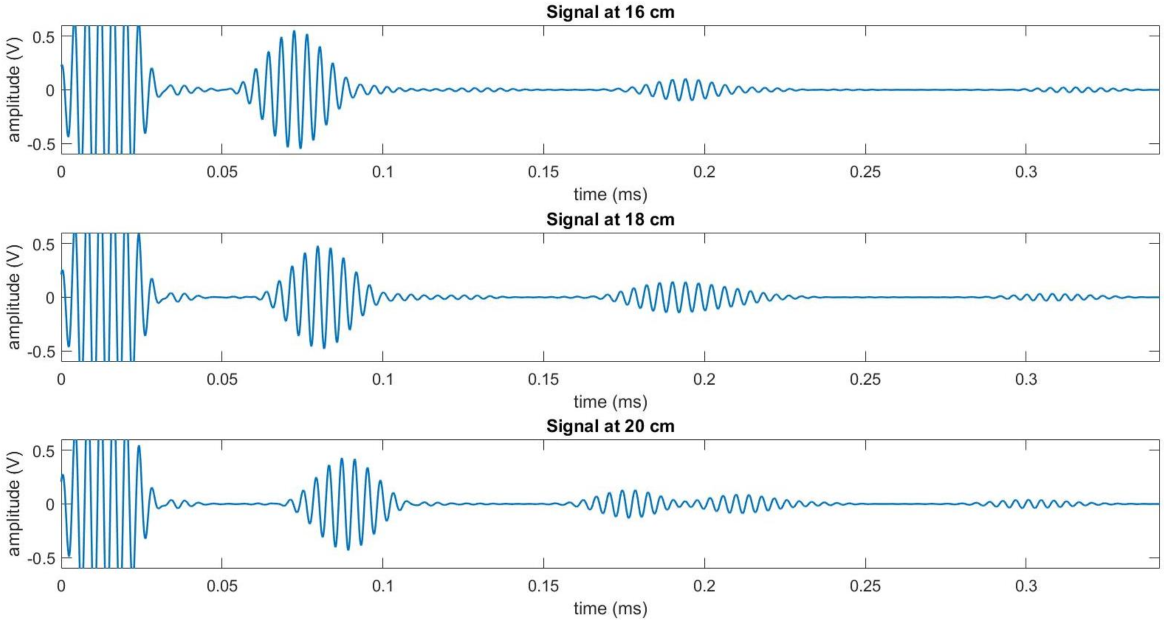

Figure 4.32 Received signals at 16, 18 and 20 cm in a 2.8 mm thick quasi-isotropic CFRP plate.

The frequency spectra of the signals are shown in figure 4.33. The frequency peaks are centred at 250 kHz. Figure 4.33(d) displays the frequency spectra comparison of all received signals, where it can be noted that the spectra perfectly overlap, not showing any significant distortion.

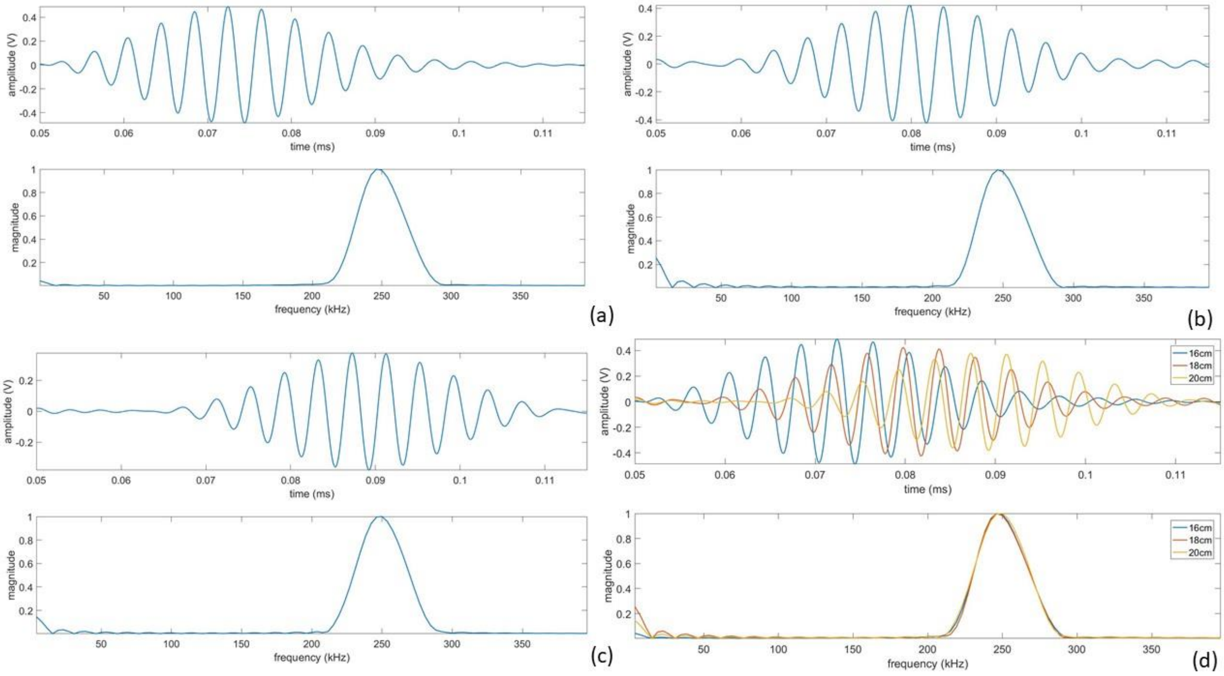

Figure 4.33 Waveform and its FFT magnitude spectrum of the signal at (a)16, (b)18 and (c)20 cm.(d) Comparison of all signals and their frequency spectra.

The calculation of phase and group velocity was performed on the signals received at 16 and 20 cm, as displayed in figure 4.34.

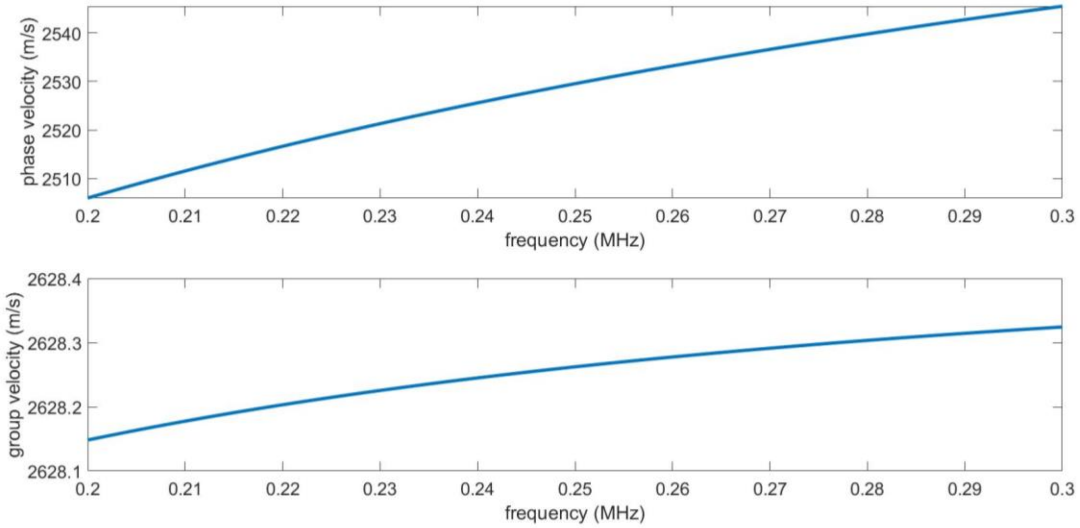

Figure 4.34 Detail of phase and group velocity of SH_0 wave propagating in a 2.8 mm thick quasi-isotropic CFRP plate between 200 and 300 kHz.

The analysis at 250 kHz, gave a phase velocity of 2,530 ± 30 m/s and a group velocity of 2,630 ± 30 m/s, the latter result being in line with the expected value of the group velocity.

A further test was used to demonstrate the isotropy of the sample by measuring the group velocity at different angles, using the same analysis as described previously [23]. The first set of measurements consisted of taking 3 measurements per each angle, from 0° to 90° every 5°. Even though the sample is quasi-isotropic, the slowness presented an odd behaviour between 30° and 60°. For this reason, further investigations have been conducted in order to understand the phenomenon. The test following the same procedure as before, 3 measures taken per each angle, only between 30° and 60° with an angle step of 2°. The set-up of the experiment is shown in figure 4.35.

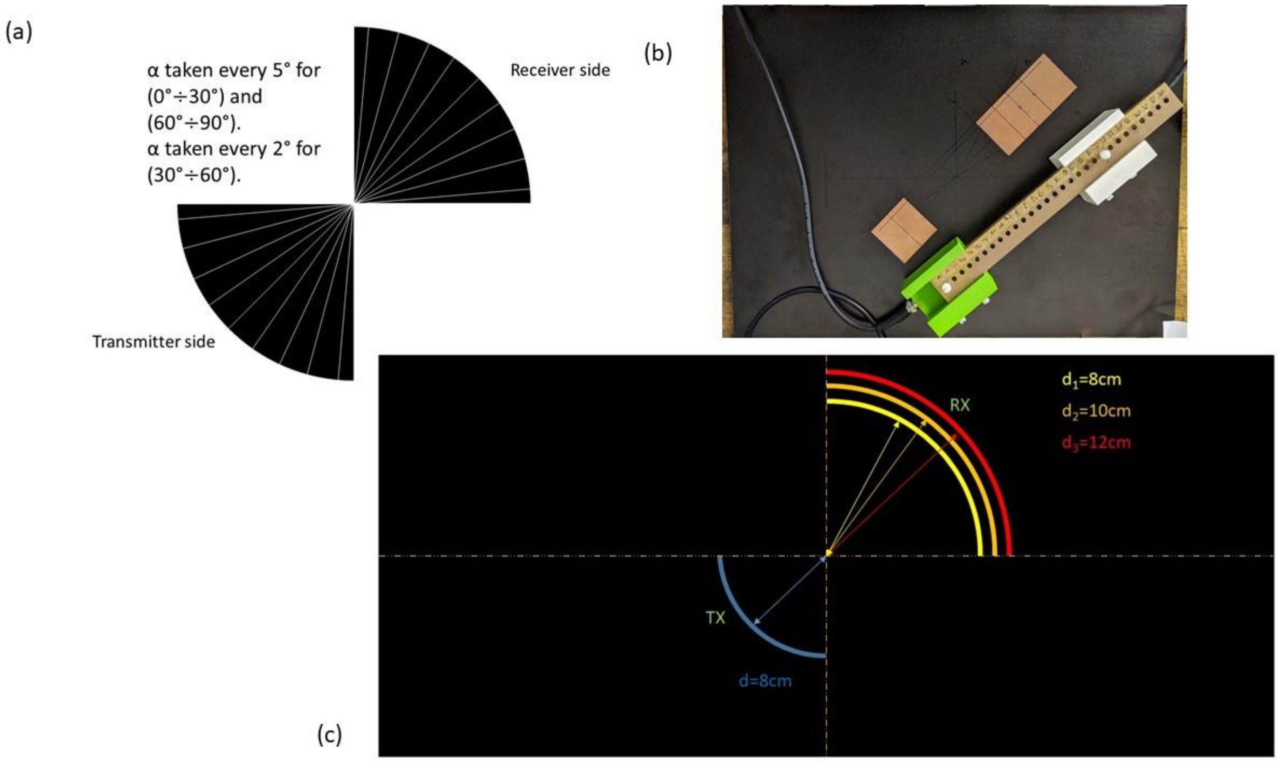

Figure 4. 35 (a) Sketch of the measurement set-up; (b) photo of the sample, probes and copper tape. (c) Diagram of the measurement set-up highlighting the relative distances of transmitter and receiver with respect to the centre of the sample. The receivers were place at 16, 18 and 20 cm from the source.

The results have been plotted using MATLAB to draw a resultant slowness surface of the sample, as shown in figure 4.36. The slowness surface is a plot of the inverse of the velocity ($^1/_{c_g}$) versus the direction (angle) of the measurement.

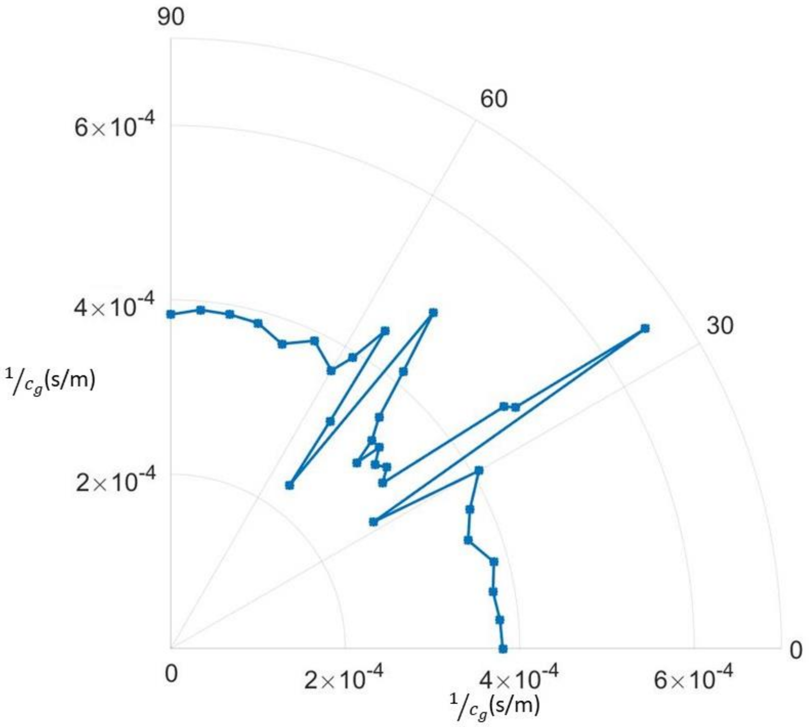

Figure 4.36 Resultant slowness surface for SH_0 wave in a quasi-isotropic CFRP plate.

Also the resultant slowness surface shows the anisotropic feature between 30° and 60°, which may due to the direction and magnitude between the energy flow and the wave vector [34].

The same analysis for retrieving the slowness surface has been performed on a quasi-isotropic CFRP sample, having a copper mesh two plies down the outer surface of the specimen. Its stacking sequence is depicted in figure 4.37. The copper mesh is adopted in aerospace as lightning protection [35].

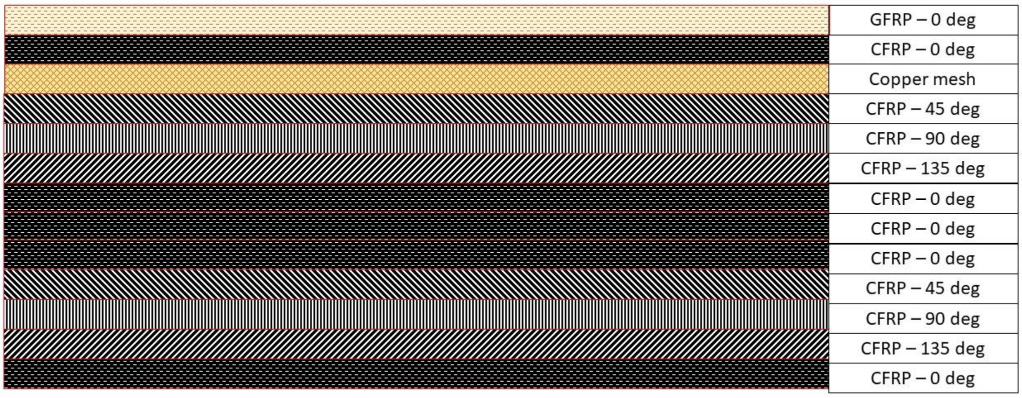

Figure 4.37 Stacking sequence quasi-isotropic CFRP sample with copper mesh.

The aim of this test was to check if the copper mesh within the sample would affect the "isotropy" of the sample. The resultant slowness surface has been calculated and plotted with the one in figure 4.36 for comparison, as depicted in figure 4.38.

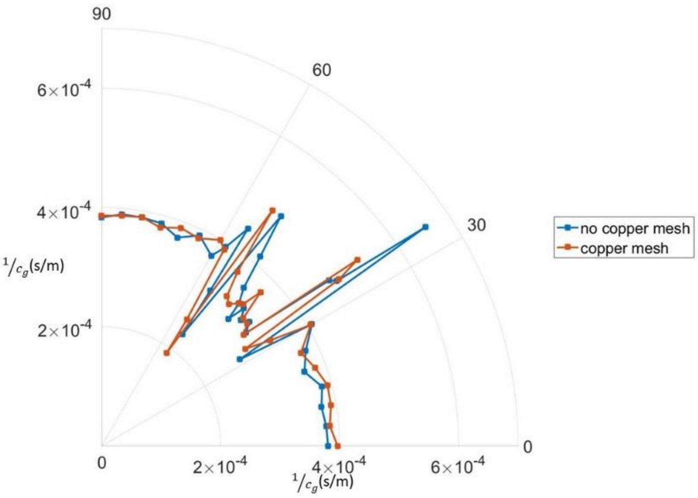

Figure 4.38 Comparison between the slowness surfaces of quasi-isotropic CFRP plate without (blue line) and with (red line) copper mesh protection.

The results show how the copper mesh does not heavily affect the resultant slowness surface. Both slowness surfaces present that abovementioned anisotropic feature.

4.6.3.3 Comparison to model prediction

In this section the waveforms obtained in Section 3.5 were compared to the measurements explained in the previous section (see Section 4.6.3.2). Figure 4.44 illustrates this comparison between the analytical results and the experimental ones. It can be noted an excellent correlation between them. Nonetheless, it is worth mentioning that the consistent delay (0.35 μs) between the experimental and simulated results is due to a signal propagation time delay through the electronics [15].

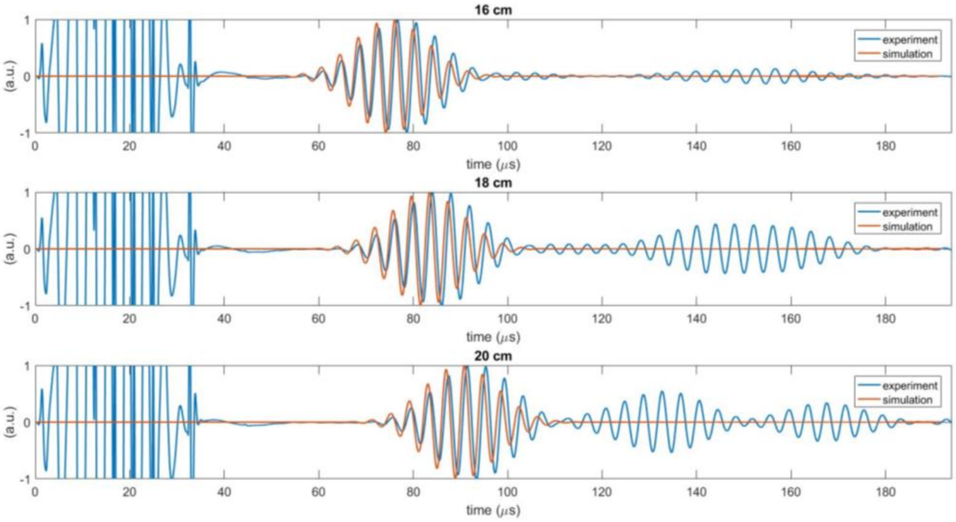

Figure 4.39 Waveforms comparison. The red lines represent the outcome of the simulation, while the blue lines are from an actual measurement (at the front the electrical pick-up can be noted, plus there are also reflections coming after the direct signal).

4.6.4 Pultruded GFRP sample

The pultruded GFRP sample (series 500) – specifically fibreglass reinforcement and thermosetting polymer - made by EXTREN® was also tested. The specimen was manufactured by pultrusion, and unlike the previous ones is electrically insulating. The dimensions of the sample were 600 x 400 x 3 mm. The mechanical properties of the sample can be considered approximately isotropic as it contains chopped fibres that are randomly/evenly distributed. The parameters required for the calculation are: the engineering constants, which can be retrieved by measuring the longitudinal and shear wave speed, and the density, which can be calculated knowing volume and weight. The dispersion curves are calculated and then drawn with the nominal wavelength of the source in order to retrieve the working frequency, as shown in figure 4.39.

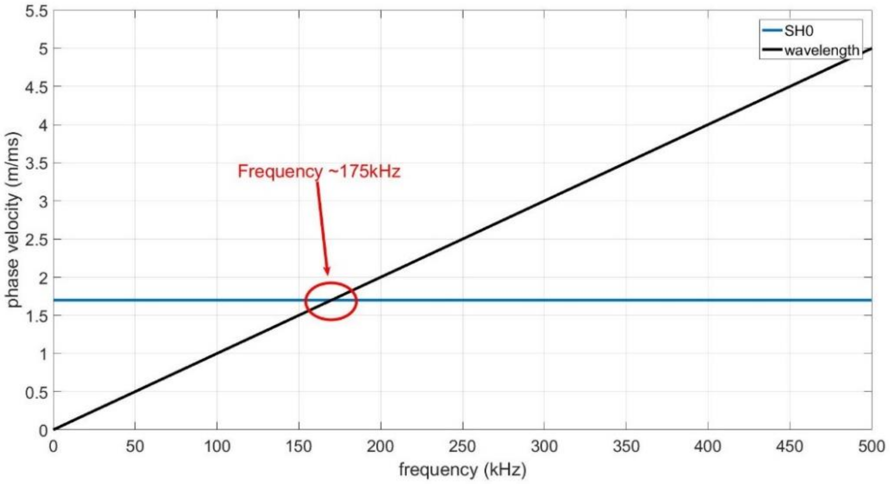

Figure 4.40 Intersection between wavelength gradient and the fundamental SH wave in a pultruded GFRP plate 3mm thick.

The driving current was a 5-cycle sine wave signal at a frequency of 175 kHz, windowed with a Gaussian window. The measurement consists of taking 5 measures with the receiver placed at 19, 20, 21, 22 and 23 cm from the source, as depicted in figure 4.40.

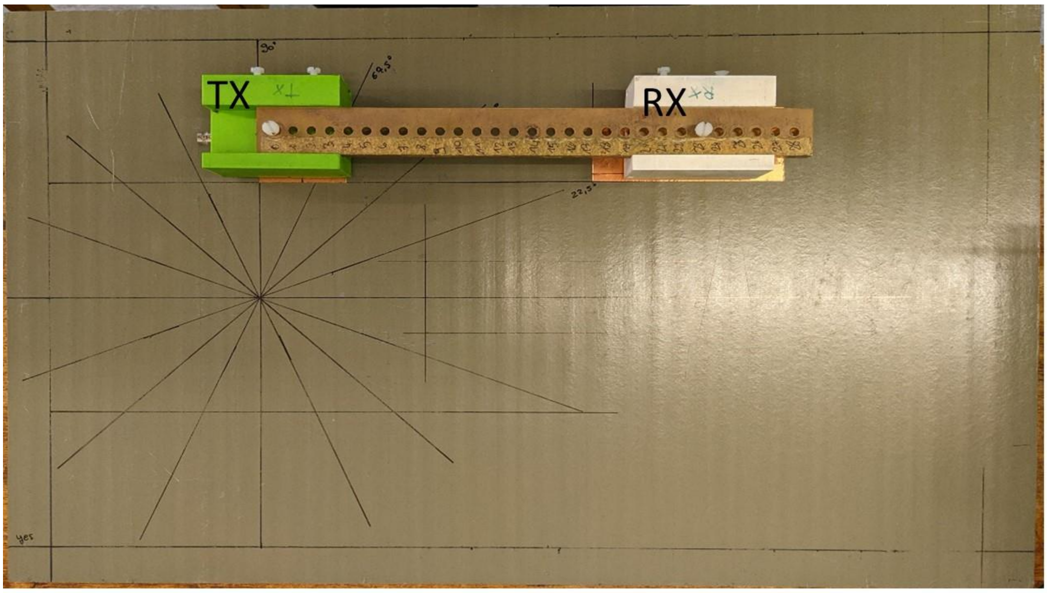

Figure 4.41 Photo of the ppm EMATs above the GFRP plate. The transducers are inside plastic cases, which are connected by a brass ruler for keeping them in place.

As in the previous measurements, the recorded signals were bandpass-filtered between 143 and 207 kHz, and the resultant signals are shown in figure 4.41.

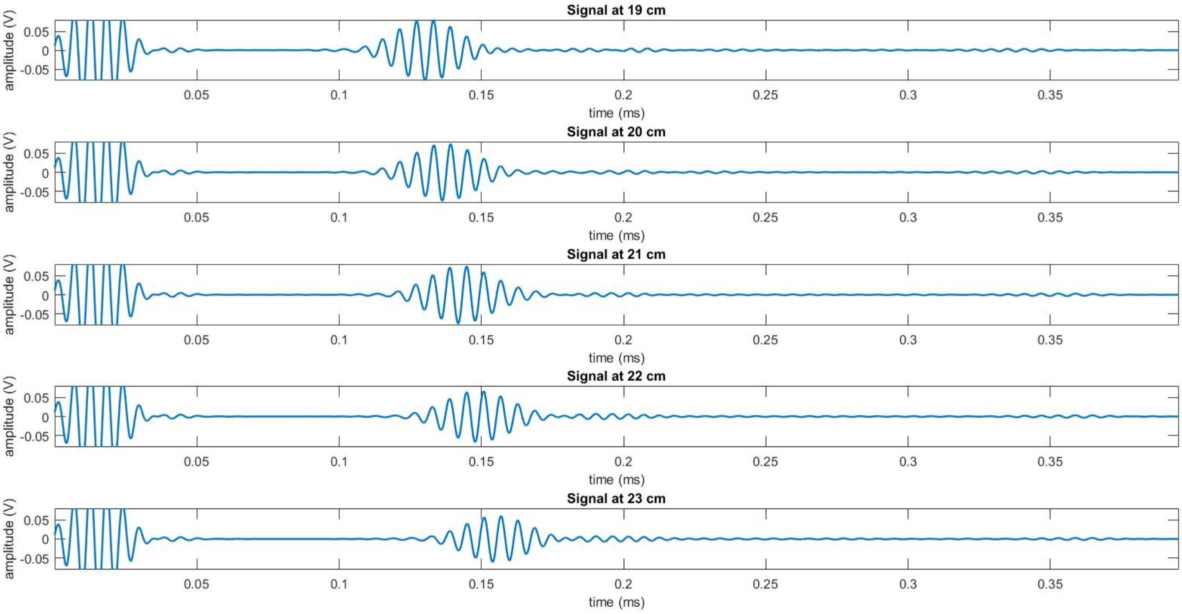

Figure 4.42 Received signal at 19, 20, 21, 22 and 23 cm in a 3 mm thick pultruded GFRP plate.

The dominant frequency of the ultrasonic pulses shown in figure 4.41 is approximately 165 kHz, as shown in the FFT magnitude plots of figure 4.42. Note that there is still some significant bandwidth to these ultrasonic pulses, with the half height peak width extending from 100 kHz to 185 kHz.

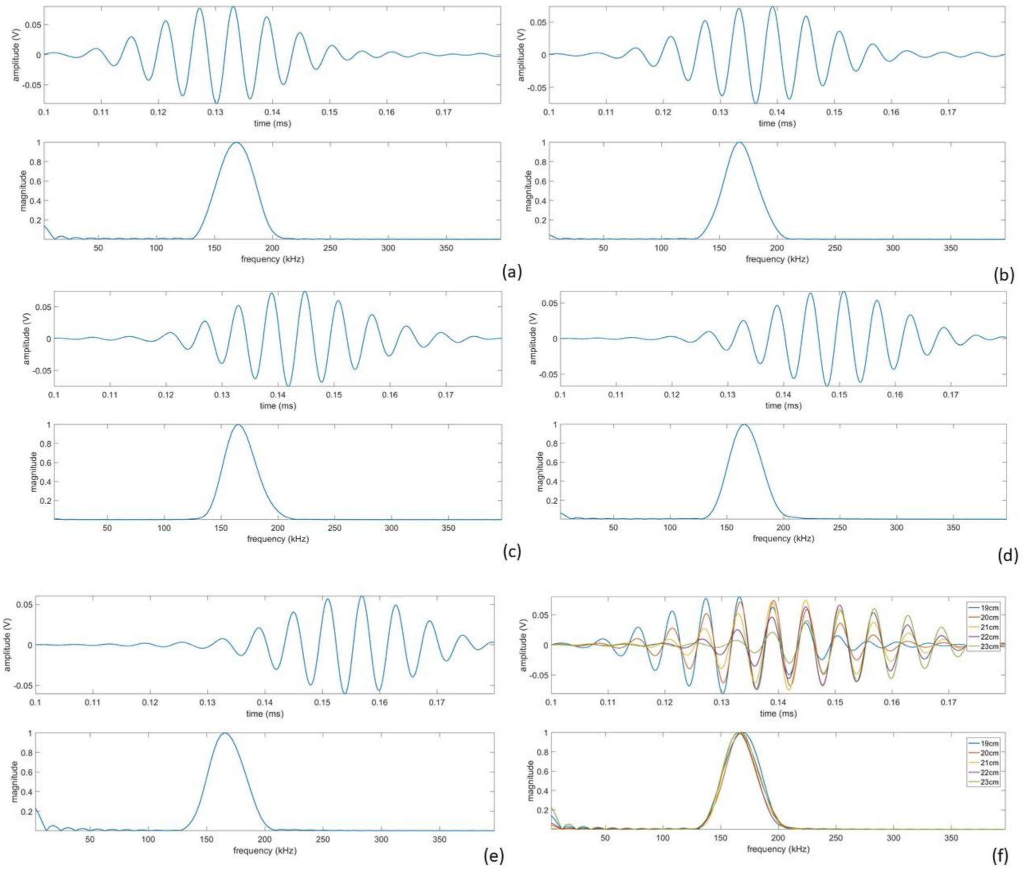

Figure 4.43 Waveform and its FFT spectrum of the signal at (a) 19, (b)20, (c)21, (d)22 and (e) 23 cm.(f) Comparison of all signals and their frequency spectra.

The calculation of phase and group velocity was performed by taking into account the signals received at 19 and 23 cm, as depicted in figure 4.43.

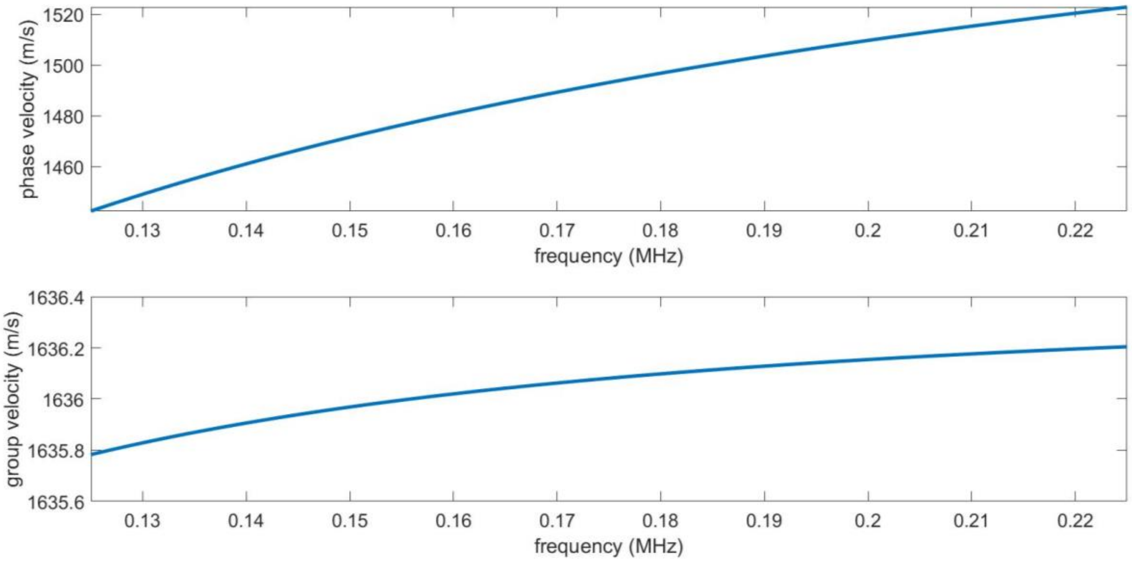

Figure 4. 44 Detail of phase and group velocity of SH_0 wave propagating in a 3 mm thick pultruded GFRP plate between 125 and 225 kHz.

The analysis revealed that, at the dominant frequency peak (175 kHz), the phase velocity was 1,500 ± 30 m/s and the group velocity 1,630 ± 30 m/s. The latter result is close with the expected value of the group velocity (1700 m/s) showing the possibility of using EMATs for exciting SH_0 wave mode within a non-conductive GFRP sample, by means of copper tape stuck on the surface.

4.7 Conclusions

This chapter contains a brief introduction of ultrasonics to provide the reader with a general background of ultrasonic waves and mechanical properties, and to introduce concepts such as the stiffness matrix, which is fundamental to the inspection of composites. The main aim was to demonstrate the possibility of generating and receiving the SH_0 guided wave mode within composite plates (both partially conductive and insulating), by means of a removable metallic tape stuck on surface of the specimen tested. The metallic patch acted as a medium within which eddy currents could exist. The interaction between the currents and the static magnetic field, which gives rise to the Lorentz forces, occurs within the patch, and the resultant motion is transferred to the specimen through the adhesive layer. The experimental set-up and the analysis has been demonstrated first on an aluminium sample, that has predictable behaviour for EMAT inspections, and then on a glass plate, isotropic and insulating medium, by using the metallic tape. Then, tests have been performed on both pultruded GFRP and CFRP plates (the latter with different stacking sequences). The results demonstrate that the metallic patch approach can be used in the testing of composite materials with EMATs.

References Chapter 4

[1] R.B. Lindsay, Acoustics: historical and philosophical development, Dowden, Hutchinson & Ross, 1973.
[2] K. Graff, "Ultrasonics: Historical Aspects," in *Ultrasonics Symposium*, 1977.
[3] G.A. Georgiou, T.B. Wolldrige, "The basic principles, capabilities and limitations of ultrasonic NDT - Part 2," *Insight*, vol. 42, no. 11, pp. 708-712, 2000.
[4] R.E. Green, "Non-contact ultrasonic techniques," *Ultrasonics*, vol. 42, pp. 9-16, 2004.
[5] A. Love, A treatise on the mathematical theory of elasticity, Cambridge University Press, 1927.
[6] W. Mason, "Physical Acoustics and the Properties of Solids," *Journal of the Acoustical Society of America*, vol. 28, no. 6, pp. 1197-1206, 1956.
[7] J. Achenbach, Wave propagation in elastic solids, North-Holland, 1973.
[8] B. Auld, Acoustic fields and waves in solids, Krieger publishing Co., 1990.
[9] J. Rose, Ultrasonic wave in solid media, Cambridge University Press, 1999.

[10] F. Campbell, Structural Composite Materials, ASM International, 2010.

[11] V. L. Popov, M. Heß, E. Willert, "Transversely isotropic problems," in *Handbook of contact mechanics,* Springer-Verlag Berlin Heidelberg, 2019, p. 205.

[12] V.L. Popov, M. Heß, E. Willert, Handbook of Contact Mechanics, Berlin: Springer.

[13] J. Rose, "The Christoffel equation for anisotropic media," in *Ultrasonics waves in solid media*, Cambridge University Press, 1999, pp. 27-30.

[14] RitecInc, "RitecInc," [Online]. Available: http://www.ritecinc.com/docs/RPR-4000_OPMAN.pdf. [Accessed 20 01 2021].

[15] F. Harris, "On the use of windows for harmonic analysis with the discrete fourier transform," *Proceedings of the IEEE,* vol. 66, no. 1, pp. 51-83, 1978.

[16] H. Frost, "Electromagnetic–Ultrasound Transducers: Principles, Practice, and Applications," *Physical Acoustics,* vol. 14, pp. 179-275, 1979.

[17] D. N. Alleyne, P.Cawley, "Optimization of lamb wave inspection techniques," *NDT and E International,* vol. 25, no. 1, pp. 11-22, 1992.

[18] P. A. Petcher, S. Dixon, "Mode mixing in shear horizontal ultrasonic guided waves," *Nondestructive Testing and Evaluation,* vol. 32, no. 2, pp. 113-132, 2017.

[19] P. A. Petcher, S.E. Burrows, S. Dixon, "Shear horizontal (SH) ultrasound wave propagation around smooth corners," *Ultrasonics*, vol. 54, no. 4, pp. 997-1004, 2014.

[20] H. Mei, R. James, V. Giurgiutiu, "Damage detection in laminated composites using pure SH guided wave excited by angle beam transducer," in *Health Monitoring of Structural and Biological Systems XIV*, 2020.

[21] H. Ogi, M. Hirao, "An SH-wave EMAT technique for gas pipeline inspection," *NDT and E International,* vol. 3, no. 127-132, p. 32, 1999.

[22] Mathworks, "Mathworks," Mathworks, [Online]. Available: https://uk.mathworks.com/help/signal/ug/practical-introduction-to-frequency-domain-analysis.html;jsessionid=4a147464c2667013f6509c62a37b. [Accessed 2021 01 30].

[23] W. Sachse, Y. Pao, "On the determination of phase and group velocities of dispersive waves in solids," *Journal of Applied Physics,* vol. 49, no. 8, pp. 4320-4327, 1978.

[24] R. Cusack, J. M. Huntley, H. T. Goldrein, "Improved noise-immune phase-unwrapping algorithm," *Applied Optics,* vol. 34, no. 5, p. 781, 1995.

[25] M. R. Cook, K. L. Gee, S. D. Sommerfeldt, T. B. Neilsen, "Coherence-based phase unwrapping for broadband signals," *The Journal of the Acoustical Society of America,* vol. 141, no. 5, pp. 3914-3914, 2017.

[26] N. Bansal, R. Doremus, Handbook of Glass Properties, Orlando: Academic Press, 1986.

[27] X. Yi, S. Du, L. Zhang, Composite Materials Engineering, Volume 1, Beijing: Chemical Industry Press, 2018.

[28] A. Bekal, A. M. Hebbale, M.S. Srinath, "Review on Material Processing Through Microwave Energy," *IOP Conference Series: Materials Science and Engineering,* vol. 376, p. 012079, 2018.

[29] I.D. Marinescu, W.B. Rowe, B. Dimitrov, I. Inasaki, Tribology of Abrasive Machining Processes, William Andrew, 2004.

[30] G. Staab, Laminar composites, Butterworth-Heinemann, 1999.

[31] J.W. Kaczmar, K. Pietrzak, W. Wlosinski, "The production and application of metal matrix composite materials," *Journal of Materials Processing Technology,* vol. 106, no. 1-3, pp. 58-67, 2000.

[32] K. Potter, Introduction to Composite Products, Springer Netherlands, 1996.

[33] K. Chawla, Composite Materials, Springer Nature Switzerland, 2019.

[34] S. H. Rhee, J. K. Lee and J.J. Lee, "The group velocity variation of Lamb wave in fiber reinforced composite plate," *Ultrasonics*, vol. 47, no. 1-4, pp. 55-63, 2007.

[35] T.M. Dhanya, C.S. Yerramalli, "Lightning strike effect on carbon fiber reinforced composites – effect of copper mesh protection," *Material today communications,* vol. 16, pp. 124-134, 2018.

Chapter 5

Capacitive Imaging

5.1 Introduction

The previous chapters considered the use of a metallic patch to allow ultrasonic guided waves to be generated and detected by an EMAT. These could then be used in NDE experiments, to be described later in the thesis, for materials such as CFRP and GFRP composites of interest in the aerospace industry. It should be noted that there are other techniques that exploit electromagnetic mechanisms for inspecting samples. These methods are based on the relationship between physical, electrical and magnetic properties (e.g. electrical conductivity, electrical permittivity and magnetic permeability). By evaluating the electrical and magnetic property changes, discontinuities or variations of material property within the specimen can be detected, but typically operate at conducting surfaces. The aim here is to investigate another non-contact technique that could be used for non-conducting samples such as CFRP structures. Guided waves could be used to identify the presence of a defect, but at a low resolution, over large distances – i.e.as part of a large area scan. An electromagnetic technique that could then be used to provide greater detail of the defect (e.g. in CFRP) would be very valuable.

Among the electromagnetic testing (ET) methods, the most widely used is eddy current testing (ECT). ECT relies on the principles of electromagnetic induction (as is also the case for EMATs). This method permits crack detection in wide variety of conductive materials, either ferromagnetic (i.e. steel) or non-ferromagnetic (i.e. copper, aluminium) [1]. Due to the widespread use of composites, ECT has also been employed on composite materials [2]. Other ET methods are magnetic particle inspection (MPI) and magnetic flux leakage (MFL). Unlike ECT, these tests can be applied only on ferromagnetic materials. MPI and MFL differ in the kind of detectable defect: the former can only detect surface and near surface discontinuities [3], while the latter can also detect far-surface flaws (i.e. shrinkage cavities) [4]. All of the above require a conductive sample.

Other than the techniques mentioned above, there are also capacitive methods which use capacitive coupling between an active electrode pair and a sample, through an electric field interaction. Historically, these methods have not been widely used for NDE as they cannot be used within the structure of a conducting material. However, with the increasing adoption of non-conducting materials (i.e. polymers and composites) in the manufacture of engineering components, the applications for which these methods may be suitable has been extending. It is worth mentioning that among the composite samples, those made with carbon fibre, whose fibre are conductive, it is not possible to detect internal discontinuities (such as delamination), unless their presence affects the surface, like dents or bumps. Before finding appropriate applications, most capacitive sensors have been used for measurements which are not considered routinely, for example dielectric constant characterisation. The most commonly-used sensors are planar fringing field sensors (also named dielectrometry sensors [5]). They need access to only one side of a sample due to their co-planar nature, and can measure electrical properties (such as dielectric permittivity and electrical conductivity) of the sample close to the sensor surface [6-8]. This approach has been used for imaging a variety of materials and structures, from insulators to metallic conductors [9].

The next sections explain the concepts of the capacitive imaging (CI) technique used in this thesis by approaching the physics behind it (Maxwell equations) and the quasi-static approximation made. This is followed by the design principles of the CI sensors, and examples of different sensor designs. The chapter concludes with FEM models of CI performance and a comparison to a simple experiment.

5.2 Capacitive imaging fundamentals

The basic design of a CI probe consists of two or more electrodes set as a co-planar capacitor. This particular design of the electrodes can be thought of as the unfolding of a parallel capacitor into the same plane, as figure 5.1 shows. The electric field distribution is generated on both sides of the electrode, though only the side facing the sample will vary affecting the measurement, as it will be explained later in this section. Thus, for simplicity, electric field lines are drawn only for the side facing towards the sample.

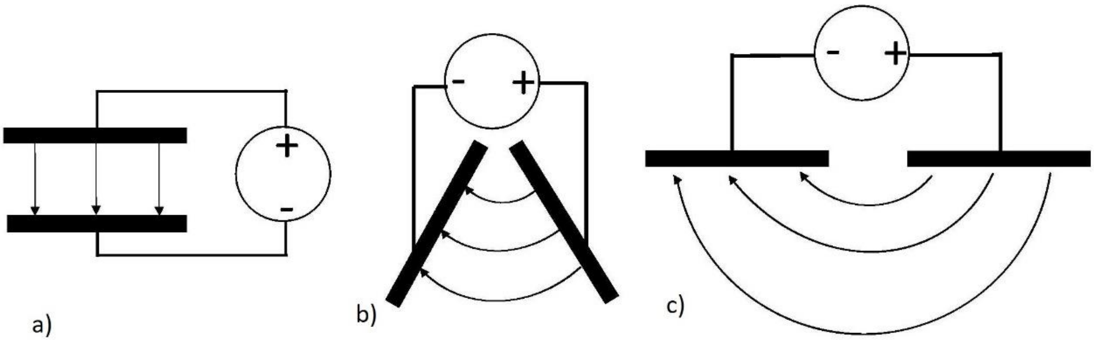

Figure 5.1 Schematic diagram of the electric field distribution as electrodes change from being in a conventional parallel-plate capacitor geometry (a) to become co-planar (c).

The co-planar probe is placed at a fixed distance away from, and parallel to, the surface of the sample under test. A voltage drive waveform (such as sinusoidal signal at a particular frequency) is input across the electrodes. Once applied, the driving signal to the source electrode an electric field is established, with field lines penetrating into the specimen. Charge can then be induced on the sensing electrode [9]. The presence of the object to be analysed affects the resultant electric field pattern, and moreover, any property change within the test material (like discontinuities) also have an effect on the electric field distribution, as depicted in figure 5.2. The electric field variations at the sensing electrode will then result in a change in the charge induced on the receiver electrode, and this can be detected and used to plot changes in the sample condition as the electrode pair is moved over the surface.

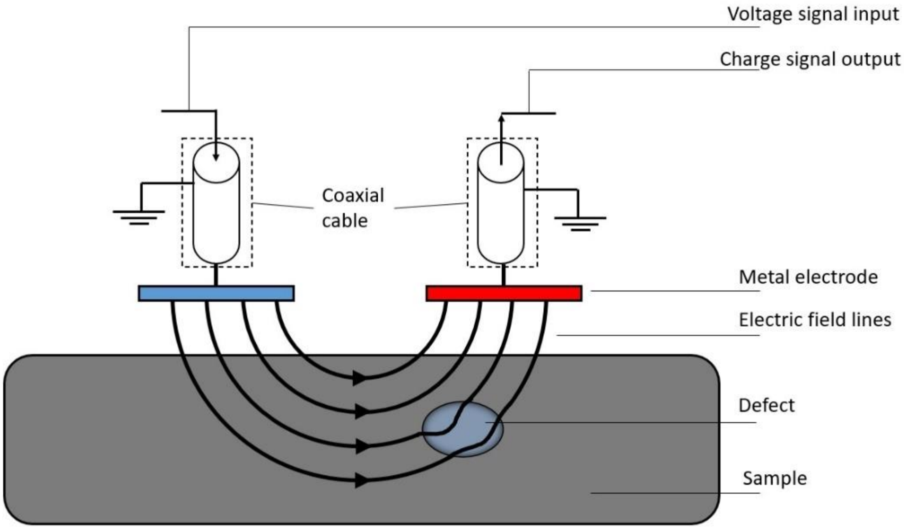

Figure 5.2 Schematic diagram of the capacitive imaging approach.

Depending on the material (insulator or conductor), the behaviour of the probing electric field varies. If the specimen is a dielectric material or has very low electrical conductivity, the electric field will have a certain volume of influence (VOI), this being the part of the sample under the probe which plays a significant role in measurement. The presence of discontinuities will alter the electric field, and change the quantity of induced charge on the sensing electrode, as stated above and shown in figure 5.3(a).

If the sample is a conductor, the electric field will not penetrate a significant distance into the structure due to the high conductivity, creating an equipotential surface. Hence, only surface characteristics (for instance: pitting, crack, corrosion etc.) will vary the pattern of the local electric field, as depicted in figure 5.3(b). It is worth noting that the CI technique is a non-contact application and the separation between the active surface of the probe and the surface sample can be in a range of millimetres. Therefore, surface treatments are often not necessary. The lift-off is chosen accordingly to the geometry of the probe (i.e. shape and size of electrodes) and the dimensions of the sample (i.e. the thickness), so that as many field lines as possible can probe the sample.

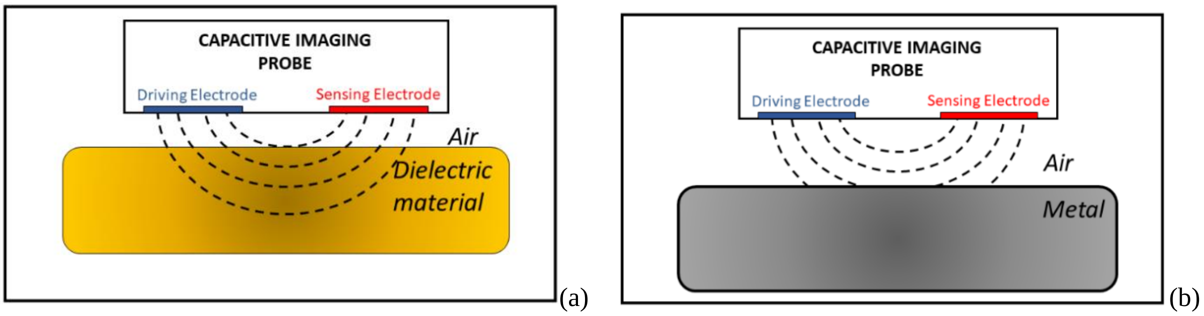

Figure 5.3 The schematic diagrams of the sensing mechanisms for (a) a non-conducting specimen and (b) a conducting specimen.

As figure 5.4 depicts, a typical probe for this method consists of a co-planar triangular imaging electrodes, plus grounded guard electrodes (which are employed in order to shield the two electrodes electrically from each other). The electrodes are constructed by etching a printed circuit board (PCB) substrate, which is coated in copper on its back surface, to reduce noise interference and to raise the radiated electric field magnitude towards the sample surface [10], and placed within a plastic box. Later in this chapter a more detailed explanation of these features will be given.

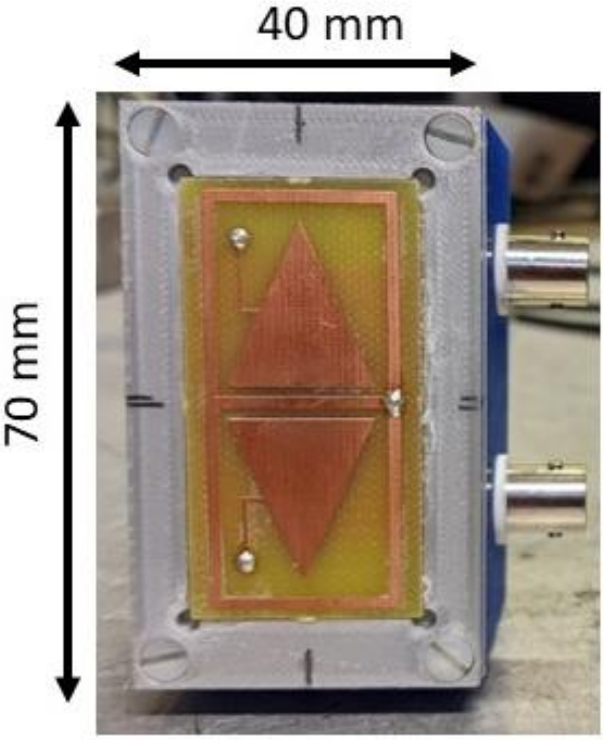

Figure 5.4 Photograph of a pair of triangular electrodes, mounted in a plastic container.

5.3 Maxwell equations and the quasi-static approximation

As explained in chapter 2, electromagnetic mechanisms such as capacitive coupling are described by Maxwell's equations (equations 2.1 - 2.4) and the constitutive relations (equations 2.6, 2.8 and 2.9). However, under certain conditions, it is possible to simply the previous equations by making an approximation which ignores magnetic fields, without significant loss of accuracy. Systems in which such an approximation is reasonable are identified as quasi-static systems. In electrodynamics, quasi-static refers to regimes where the electromagnetic wavelength is much greater than the sample size [11,12]. In the CI technique, the frequency range is typically between 10 kHz and 1 MHz. Thus, the corresponding wavelengths are in the range of 300 m and 30 km, which is considerably greater than the dimensions of the system. Hence, the CI technique sits comfortably in the quasi-static regime. In this regime, the electric field and magnetic field can be assumed to be decoupled and, in addition, the latter can be ignored as it changes so slowly. Therefore, Maxwell's equations can be simplified and they will assume this notation:

$$\nabla \cdot \vec{D} = \rho, \tag{5.1}$$

$$\nabla \cdot \vec{B} = 0, \tag{5.2}$$

$$\nabla \times \vec{E} \approx 0, \tag{5.3}$$

$$\nabla \times \vec{H} \approx 0. \tag{5.4}$$

These simplifications signify that the electric field $\vec{E}$ generated by a given charge density distribution ρ is irrotational (equation 5.3), and the magnetic field intensity $\vec{H}$ is approximated to zero (equation 5.4). Additionally, the electric field $\vec{E}$ can be expressed as the gradient of the electric potential of voltage (φ):

$$\vec{E} = -\nabla \varphi \tag{5.5}$$

Thus, the CI system analysis can be treated as an electrostatic analysis and the question can be reduced to the estimation of the electric field generated by different charge distribution (probe geometries) within various sample material. This exploits Poisson's equation, namely:

$$\nabla(\varepsilon_0 \varepsilon \nabla \varphi) = \rho \tag{5.6}$$

In the majority of CI applications, the samples are dielectric so there is no free charge in the volume where the probing field is present. Therefore, the previous equation can be simplified, as the charge density (ρ) equals to zero, and can be rewritten as:

$$\nabla(\varepsilon_0 \varepsilon \nabla \varphi) = 0 \tag{5.7}$$

Hence, the electric potential distribution (φ) can be predicted by solving equation (5.7).

Further details will be given in Section 5.8.

5.4 Dielectric and conducting materials

The knowledge of how the electrical properties, like conductivity and permittivity, affect the measured signal is essential for using the CI technique correctly. In the case of good conductors, as mentioned above, the quasi-static electric field will not probe the sample terminating at the surface, and the electrical properties (mostly conductivity) do not have relevant effect on the detected signal. On the other hand, for insulating materials and poor electrical conductors, the electric field probes the sample sub surface, and the electrical properties (permittivity) have important effects on the received signal and need to be clarified.

When a dielectric material is subjected to an external electric field, as the amount of free charge is very small, effectively zero (i.e. equation 5.7), the material will be electrically polarised, and the inner `structure (atoms or molecules) develops an electric dipole that provides an electric field which is inclined to oppose the applied field. In case of a linear and isotropic material, the polarisation field $\vec{P}$ is linked to the external electric field intensity $\vec{E}$ as follows:

$$\vec{P} = \varepsilon_0 \chi_e \vec{E} \tag{5.8}$$

where χ_e is the electric susceptibility of the material. Then the electric displacement ($\vec{D}$) is tied to the polarisation field ($\vec{P}$) by the constitutive relation (equation 2.7) as follows:

$$\vec{D} = \varepsilon_0 \vec{E} + \vec{P} = \varepsilon_0 (1 + \chi_e) \vec{E} = \varepsilon_0 \varepsilon \vec{E} \tag{5.9}$$

Therefore ε, the static relative permittivity of the material, can be expressed as follows:

$$\varepsilon = (1 + \chi_e). \tag{5.10}$$

For anisotropic materials this quantity (ε) is a tensor which is called the permittivity matrix, somewhat similar to the stiffness matrix in mechanics [13]. It is worth mentioning that the constitutive relation of equation 5.9 is for the static case. For a time-varying electric field, the polarisation is frequency-dependent and the frequency domain response of a dielectric material can be expressed in terms of the complex permittivity **ε** as:

$$\boldsymbol{\varepsilon} = \varepsilon' - \mathrm{j}\varepsilon'' \tag{5.11}$$

where ε', the real part, is commonly named permittivity which describes the ability of a material to preserve an electrical field, and ε'', the imaginary part, is the loss factor representing the losses in the material (such as relaxation, resonant effect, or loss by ionic conduction). As all materials have a finite, even though very small, conductivity (σ), a more general expression can be written for describing the effective permittivity $\boldsymbol{\varepsilon}_{eff}$:

$$\boldsymbol{\varepsilon}_{eff} = \varepsilon' - \mathrm{j}\left(\varepsilon'' + \frac{\sigma}{\omega \varepsilon_0}\right). \tag{5.12}$$

From equation above (5.12), it can be noted that the dielectric response of an insulating material is frequency-dependent (ω is the angular frequency). Even though several mechanisms are related with phenomenon and it is a field of study itself [14-16], in this particular study such phenomena are not applicable, as in the quasi-static regime ε'' equals zero hence $\varepsilon' = \varepsilon$ (static relative permittivity). Therefore equation 5.12 can be written as:

$$\boldsymbol{\varepsilon}_{eff} = \boldsymbol{\varepsilon} = \varepsilon' - \mathrm{j}\frac{\sigma}{\omega\varepsilon_0}. \quad (5.13)$$

For insulating materials the electrical conductivity values are typically very small, the static relative permittivity (ε) is a good approximation for characterising such materials, an assumption made throughout this thesis.

It is important to mention that composite materials can be considered for simplicity either conducting (i.e. CFRP) or dielectric (i.e. GFRP). The electrical conductivity of CFRP, as mentioned previously, is due to the carbon fibres which present a conductivity of $6.25 \times 10^4\ \mathrm{S/m}$ for a diameter of 7.5 μm [17], which shield the sample from the electric field.

5.5 Modes of operation

The sample properties determine the CI configuration, as demonstrated below in this section.

5.5.1 Non-conducting specimen not grounded

The first case of a non-conducting specimen which is not grounded [18] is shown in figure 5.5.

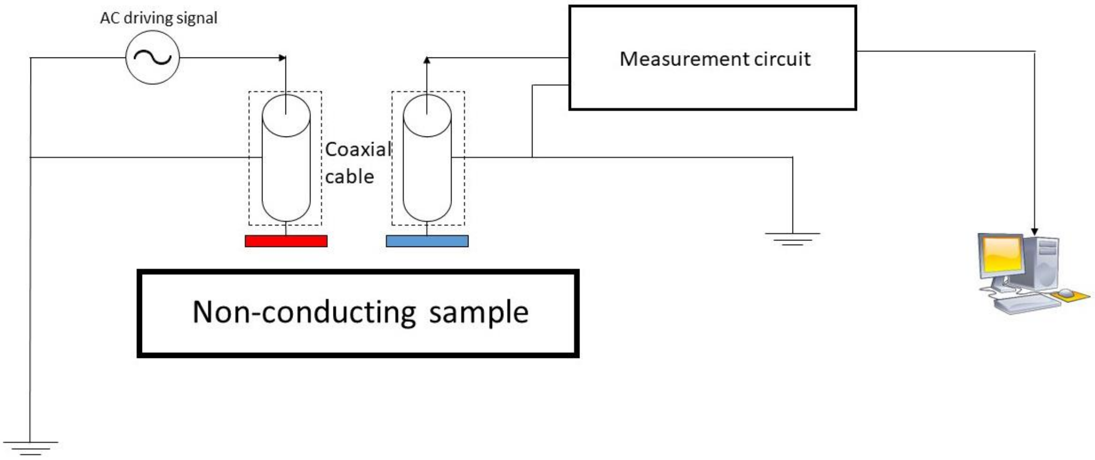

Figure 5.5 Schematic diagram of the CI probe testing a non-conducting specimen.

When a CI probe is placed in proximity of the surface sample, the sample itself and the air gap between probe and surface specimen will act as the dielectric material between the two electrodes of the equivalent variable capacitor, as depicted in figure 5.6. Permittivity changes within the volume tested by the probing field (such as variation of the lift-off, a dent on the surface, a discontinuity under the surface or other type of defects) will affect the value of the capacitance measured.

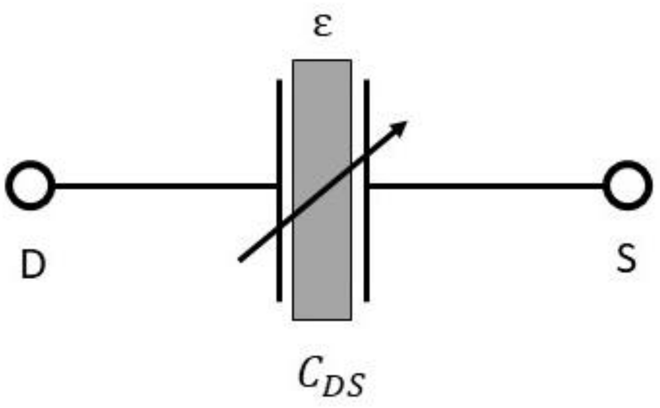

Figure 5.6 Equivalent circuit of the CI probe testing a non-conducting specimen.

5.5.2 Non-conducting specimen on a grounded substrate

In the case of a non-conducting specimen on a grounded substrate [18], the situation is as shown in figure 5.7.

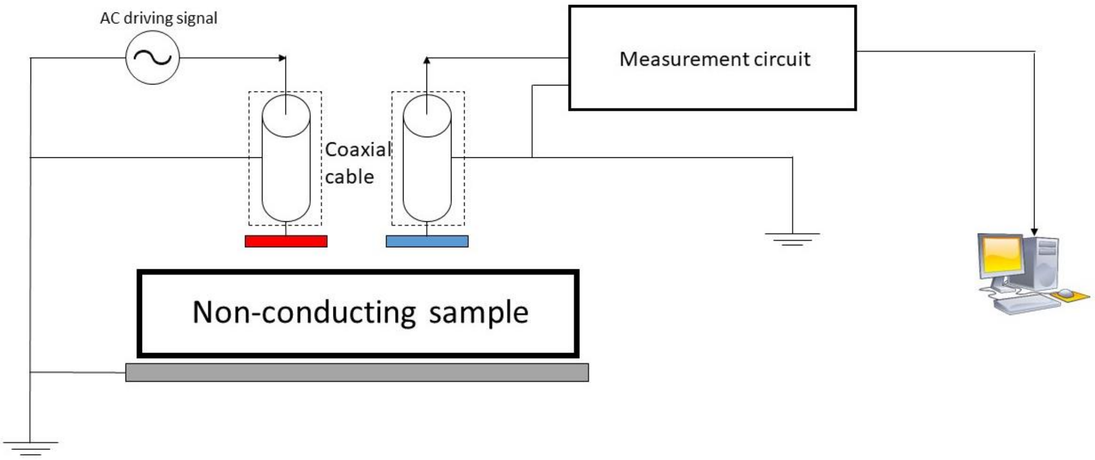

Figure 5.7 Schematic diagram of the CI probe testing a non-conducting specimen on a grounded substrate.

If the sample is not too thick for the grounded substrate to have an effect, the grounded substrate will operate as a third parallel-placed counter electrode, as figure 5.8 depicts. Each electrode will interact to the grounded substrate as it acts as an additional parallel-plate capacitor, expressed as C_{DG} and C_{SG}. These two capacitors, which are parallel plate capacitors, will not be affected by the position of the sample and the possible defects (if the lift-off is maintained constant). Nonetheless, the capacitance between the CI probe electrodes (C_{DS}) will still be affected by the lift-off distance and the presence (and its relative position) of possible defects.

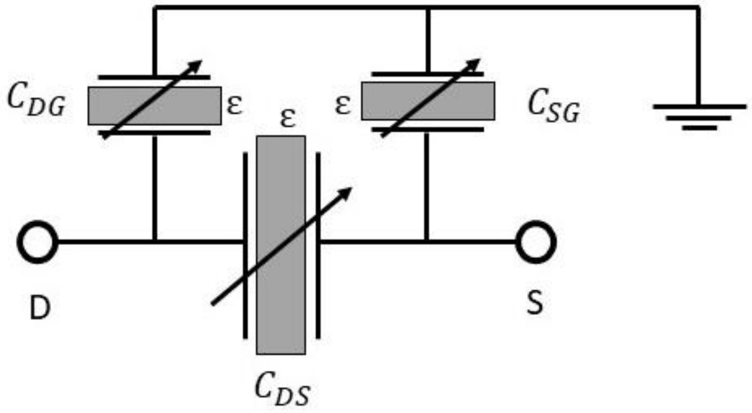

Figure 5.8 Equivalent circuit of the CI probe testing a non-conducting specimen on a grounded substrate.

5.5.3 Grounded conducting specimen

The case of a grounded conducting specimen [19] is depicted in figure 5.9.

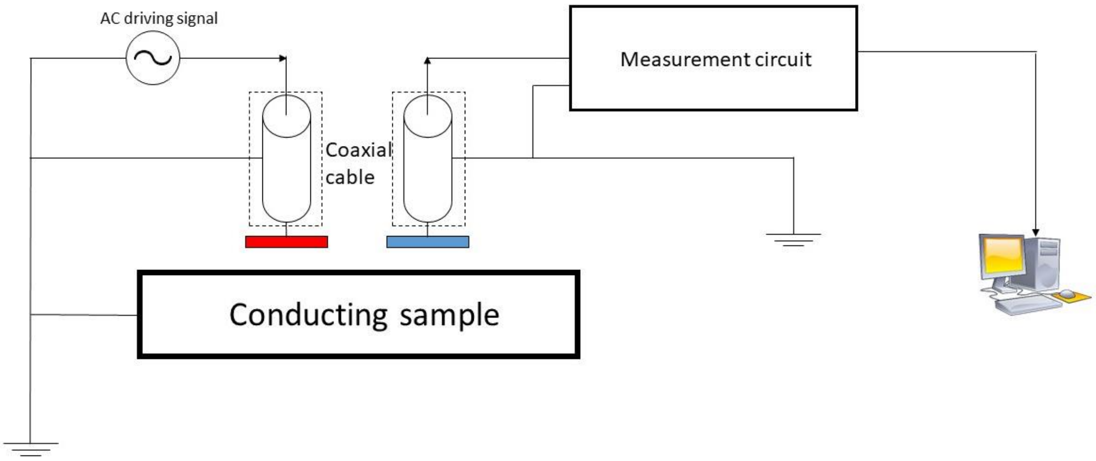

Figure 5.9 Schematic diagram of the CI probe testing a grounded conducting specimen.

When a CI probe is placed in proximity of the surface sample, the grounded specimen surface will operate as a third, parallel counter electrode and each electrode will interact at the surface of the sample creating two additional parallel-plate capacitors, expressed as C_{DG} and C_{SG}. Figure 5.10 depicts the equivalent circuit. Any variation of lift-off between the electrodes and the sample surface (even variation due to surface features) will affect the capacitances. For the capacitance established between the two electrodes due to the shielding effect (C_{DS}) [20], more electric field lines from the source electrode will end on the grounded conducting surface rather than reach the sensing electrode as the grounded surface approaches the probe,. Hence, C_{DS} is affected by the distance between the CI probe and the grounded surface (lift-off).

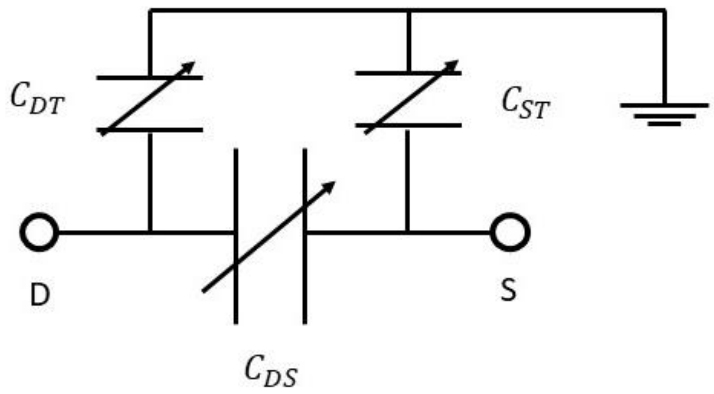

Figure 5.10 Equivalent circuit of the CI probe testing a grounded conducting specimen.

5.5.4 Floating conducting specimen

The case of a floating (i.e. non-grounded) conducting sample [19] is presented in this section and depicted in figure 5.11.

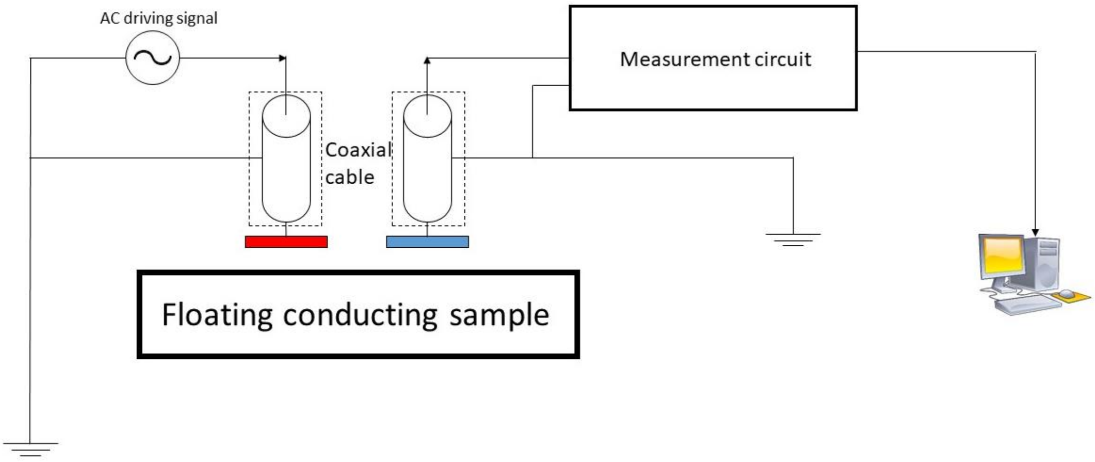

Figure 5.11 Schematic diagram of the CI probe testing a floating conducting specimen.

When a CI probe is close to the conducting and electrically floating surface, each electrode will interact with the sample surface creating two parallel-plate capacitors, as figure 5.12 shows. Comparing the two equivalent circuits (figure 5.10 and figure 5.12), the shielding effect of the floating surface can be viewed as the shield effect of a grounded surface paired with the variable parasitic capacitor (expressed as C_{TG}) from the floating surface to ground.

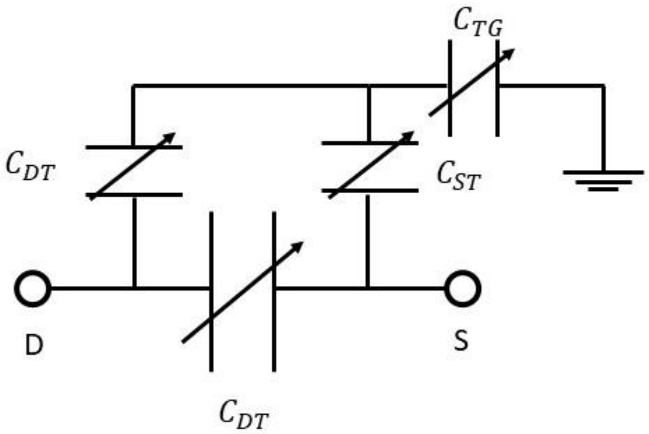

Figure 5.12 Equivalent circuit of the CI probe testing a floating conducting specimen.

5.6 Design principles

5.6.1 Depth of penetration

As the term indicates, the depth of penetration is a measure of how deep the electric field can penetrate into the sample. In these applications, the penetration depth is ruled by two factors: the permittivity of the material and the electrode geometry. The higher the permittivity of the sample material the quicker the electric field decays within the specimen. However, the primary factor for determining penetration depth for a given material is the electrode geometry.

5.6.2 Measurement sensitivity

The measurement sensitivity is described as the ratio between the output change and the change of targeting parameter. For conventional capacitive sensors (designed for measuring sample electric properties), the absolute value of the measurement sensitivity is sufficient as the whole sample under test is considered to be homogenous. For imaging applications, due to the non-uniformity of the electric field and consequently the dependency of this parameter on position, the distribution of sensitivity is of interest. An estimation of the sensitivity distribution can be given by using the slope of the curve shown in figure 5.13, and it can be noted that the sensitivity decreases with increased distance.

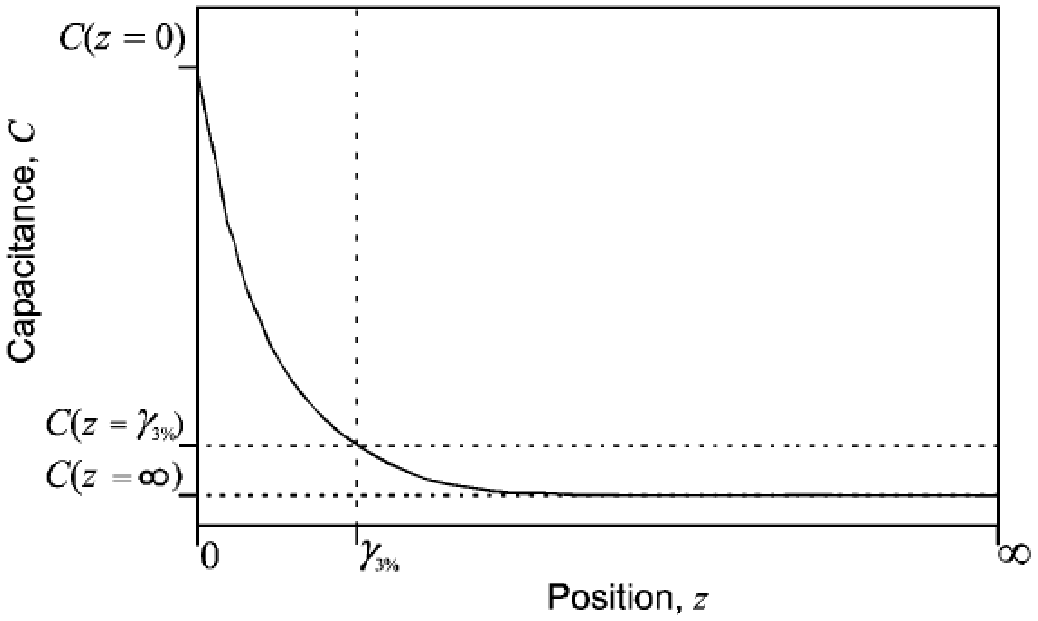

Figure 5.13 Evaluation of the penetration depth of a planar capacitive sensor, where $\gamma_{3\%}$ *is the effective penetration depth (from [10]).*

The measurement sensitivity distribution depicts how well each region in the sensing area is supplying to the measured charge signal on the sensing electrode, and it can be useful to work out the VOI and the imaging ability of the sensor. This distribution is determined by the distribution of the electric field from the CI probe, which is mainly controlled by the geometry of the probe. In general, for a particular capacitive sensor, a change in the local electric property, such as the presence of a defect, will provoke a greater signal change if it is positioned in a place where the electric lines are more densely spaced (usually near the probe surface) as it will alter more electric lines. It is worth mentioning that the imaginary electric field lines generated by the driving electrode can terminate at ground, infinity and the sensing electrodes. Only those which terminate at the sensing electrode participate in the measurement. Hence, the sensitivity is higher at a place where the electric lines, terminating at the sensing electrode, are more densely spaced. Later in this chapter, the sensitivity distribution prediction will be discussed in detail.

5.6.3 SNR and Imaging resolution

The CI technique employs the fringing electric field from the planar electrodes, and therefore the capacitive coupling between the electrodes (driving and sensing) is relatively weak. As a consequence, the very low signal on the sensing electrode can be perturbed by noise. The probe design can be used to improve the SNR in order to increase the signal level (the use of bigger size electrode and smaller electrode separation) and to reduce the noise level (the use of grounded back plane and guard electrodes).

The imaging resolution refers to the smallest detectable feature from a scan. For NDE applications, the CI probe requires a reasonable spatial resolution to produce an image which defines shape and size of a defect. For a 2D X-Y scan, each pixel of the image corresponds to the measurement from a scan position, and the intensity of the pixel is a result on the local electric properties averaging over a certain volume (VOI), which is also determined by the geometry of the probe. In general, lower resolution is due to a bigger electrode separation as the probe samples a bigger volume, for a fixed electrode size and shape. It is worth noting that the electric properties (conductivity and permittivity) affect the imaging resolution of a given CI probe, because the probing electric field acts differently with a conductive or insulating sample.

5.7 Examples of electrodes

In previous studies two types of probes have been tested in order to demonstrate the general relationship between the design variables and the probe performance, namely symmetric probes and concentric ones.

5.7.1 Symmetric electrodes

The simplest design for a symmetric capacitive probe consists of a pair of rectangular metal plates acting as the positive and negative electrodes of the capacitor. Their performance can be improved by accurately considering several design factors, which are listed and discussed as follows:

1) Separation between electrodes:

The separation of a given shape of electrodes is a crucial factor in regulating the penetration depth. Figure 5.14(a) depicts a pair of square electrodes with a separation equal to d_1 between their centres, and figure 5.14(b) another pair with an augmented separation d_2 ($>d_1$). Figures 5.14(c) and 5.14(d) show the cross-sectional views of the probe. The electric field lines (indicated as dashed lines) are those lines effectively taking part in the measurements. It can be noted that the design with a larger separation has worse signal strength, as the field lines cover a larger volume of solid material. This design improves the penetration depth, useful for detecting deeper features, although the associated electric field strength decreases. This reduction of the electric field is due to the greater distance travelled by the electric field lines to reach the sensing electrode. Vice versa, if the separation is smaller (as depicted in Figure 5.14(a)), the coupling between the electrodes is stronger, hence the electric field strength is improved, though the penetration depth is smaller.

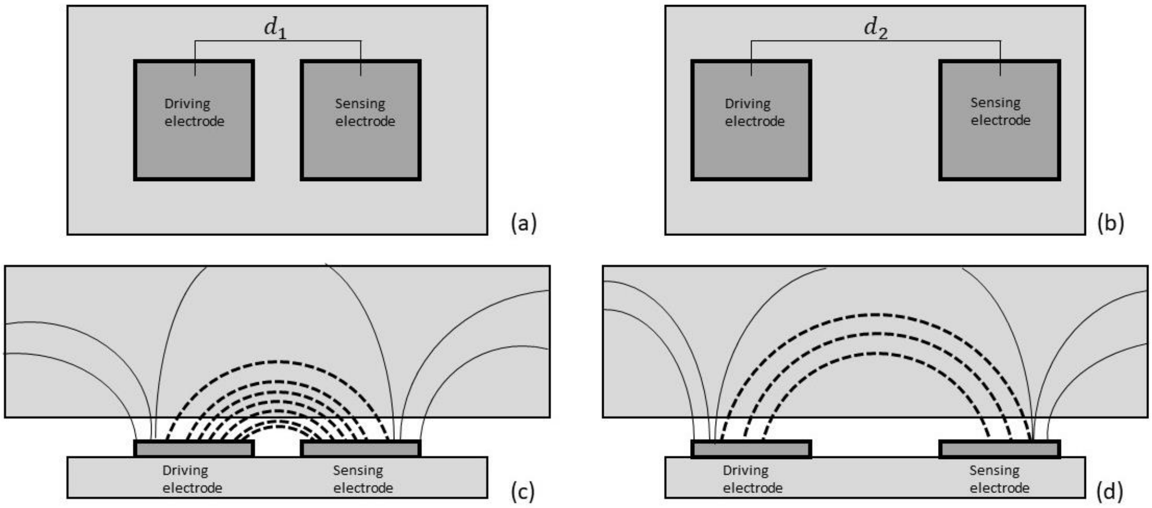

Figure 5.14 Schematic diagram for CI probes with different electrode separations. (a) Separation d1, (b) separation d2, (c) cross-section of the probe (separation d1) and (d) cross-section of the probe (separation d2).

2) Guard electrode:

The application of a voltage to the driving electrode of a CI probe generates an electric field emanating from all surfaces of the electrode, also from the side edges even though the electrode is usually very thin. The electric field lines developed from the driving electrode are generally denser near the probe surface thus such devices are too sensitive to very small surface features, which may be unwanted (like surface roughness and dirt). Plus, if the thickness of the sample is small compared to the probe size, the actual regions of measurement will be outside the specimen. Such factors are difficult to control in practical tests, so that the outcomes may become unreliable [21].

Guard electrodes are adopted to reduce these disadvantages as well as focus the electric field and cancel noise from undesired sources (e.g. environmental electromagnetic field) by applying the same voltage of the sensing electrode (0 V) thus the electric field is confined into the volume of the sensing electrode. In CI applications the guard electrodes are held at a “ground” potential. Figure 5.15(a) shows a top view of a CI probe with a symmetric pair of co-rectangular shaped planar electrodes, while figure 5.15(b) shows the same CI probe with grounded electrodes (represented as darker areas surrounding and between the electrodes).

Figure 5.15(c) and 5.15(d) depict (from a cross-sectional view) the schematic electric field lines generated across the electrodes. The effective electric lines, those effectively "participating" in the measurement, are drawn as dashed lines.

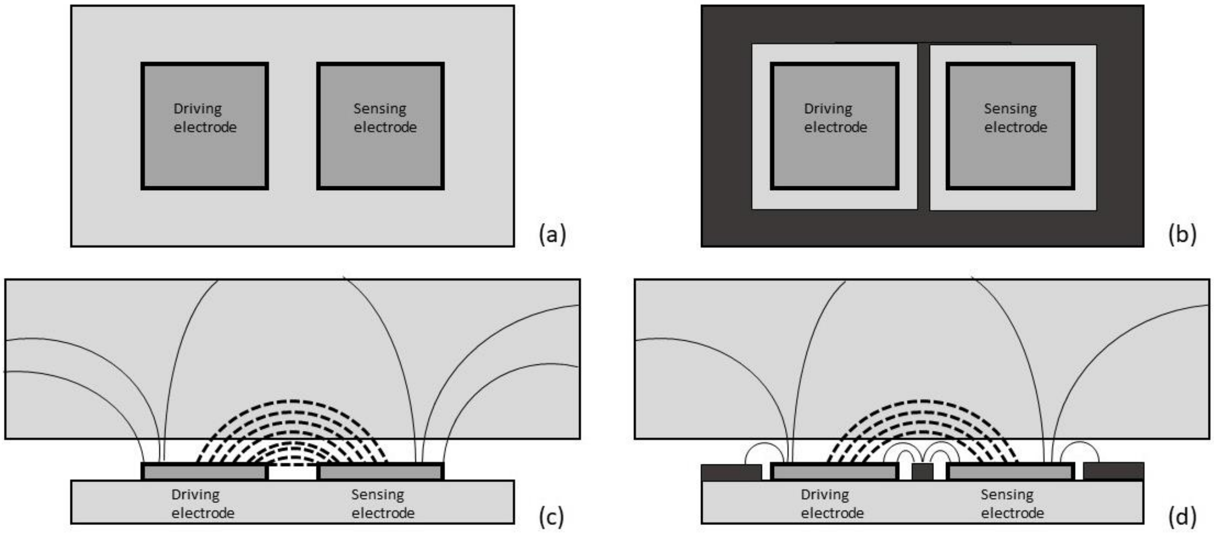

Figure 5.15 Schematic diagram for CI probes with and without guard electrodes. (a) Top view CI probe without guard electrode, (b) top view CI probe with guard electrodes, (c) cross-section of CI probe without guard electrodes and (d) cross-section of CI probe with guard electrodes. The dashed lines represent the electric field lines actually participating in a measurement.

As already mentioned, the fringing electric field originated from the driving electrode travels through the air gap penetrates into the specimen and terminates on the sensing electrode. In the absence of guard electrodes, some of the electric field lines would travel directly from the driving electrode to the sensing electrode and being more densely-packed within the air gap, which makes the probe very sensitive to the small lift-off distance, see figure 5.15(c). To counteract this effect, the inner guard electrodes is mounted between the electrodes, in order to block the direct path of the electric field line and push more field lines toward the specimen, as depicted in figure 5.15(d). Despite the fact that the grounded guard electrode between and surrounding the driving and sensing electrodes will diminish the signal strength, as some charges are lost in the parasitic coupling between driving/sensing electrode and the grounded guard electrode, it will increase the penetration depth making the probe less influenced to changes in small lift-off variations. This is a disadvantage for displacement/distance measurement but a benefit for imaging purposes.

Furthermore, the surrounding guard electrodes counteract the effect mentioned earlier - if the thickness of the specimen is small compared to the probe size, some electric lines will probe through the sample and appear from the far side, as shown in figure 5.15(c) (solid lines). Even though these lines are not located in the high sensitivity region, they might introduce errors in measurements. The counteraction is obtained by attracting some of the outer electric lines which makes the probe less sensitive to the sample thickness, see figure 5.15(d).

3) Choice of electrode shape:

Conventional capacitive sensors usually mount two rectangular shape electrodes [22] or two sets of interdigital electrodes. As mentioned before, the separation between the centroids of the two electrodes establishes the penetration depth of those sensors [23]. In order to augment the penetration depth, the separation between adjacent electrodes can be increased, although the coupling is then weaker and the image resolution lower.

Triangular electrodes can be exploited to balance these trade-offs (penetration depth and image resolution), and can be arranged in two orientations: back-to-back and point-to-point, as shown in figure 5.16(a) and figure 5.16(b) respectively.

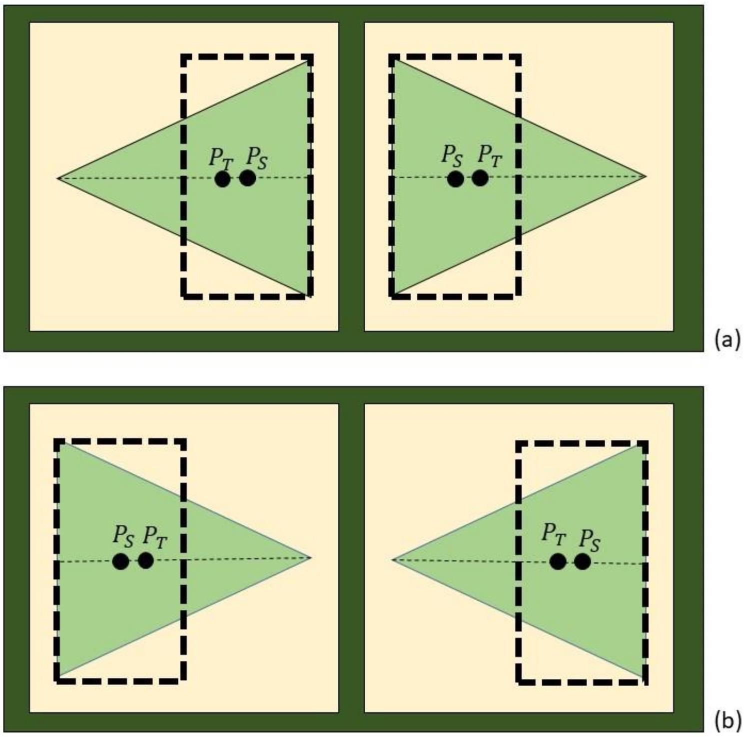

Figure 5.16 Diagram of two triangular electrode probes: (a) back-to-back and (b) point-to-point.

In Figure 5.16, both electrode orientations are compared to rectangular electrodes of the same area in order to demonstrate that the centroids P_T for the triangular electrodes are further apart (for back-to-back triangular electrodes) and more closely-spaced (for point-to-point electrodes) than the equivalent rectangular electrodes. In the former case, the penetration depth will be greater when imaging bulk features in non-conductive samples. In the latter one, the coupling between the electrodes will be stronger which is good for surface feature imaging.

Each arrangement has its own characteristics, and can be used in different situations. Figure 5.17 shows a simulation of the electric field distribution in air when scanning a probe along the dotted line and in a plane perpendicular to the page. It can be noted that for a back-to-back triangular probe, the electric field (figure 5.17(a)) is converging towards the middle of the probe, while for a point-to-point triangular probe, figure 5.17(b), the electric field is diverging toward the side of the probe. In figure 5.18, it can be better seen the distribution of the electric field lines for the two geometries in a 3D space. Therefore, it can be stated that the volume of influence of a back-to-back triangular probe is smaller than that of a point-to-point triangular probe in absence of a sample as shown in figure 5.19. It is worth noting that the electric field maps (figure 5.17) are in the form of equipotential lines from the measured electric potential (voltage). Even though the figures show that the electric field lines are more dense under the driving electrode, this does not imply that targeting features under the driving electrodes is a more effective measurement, as only some field lines will actually terminate on the sensing electrode.

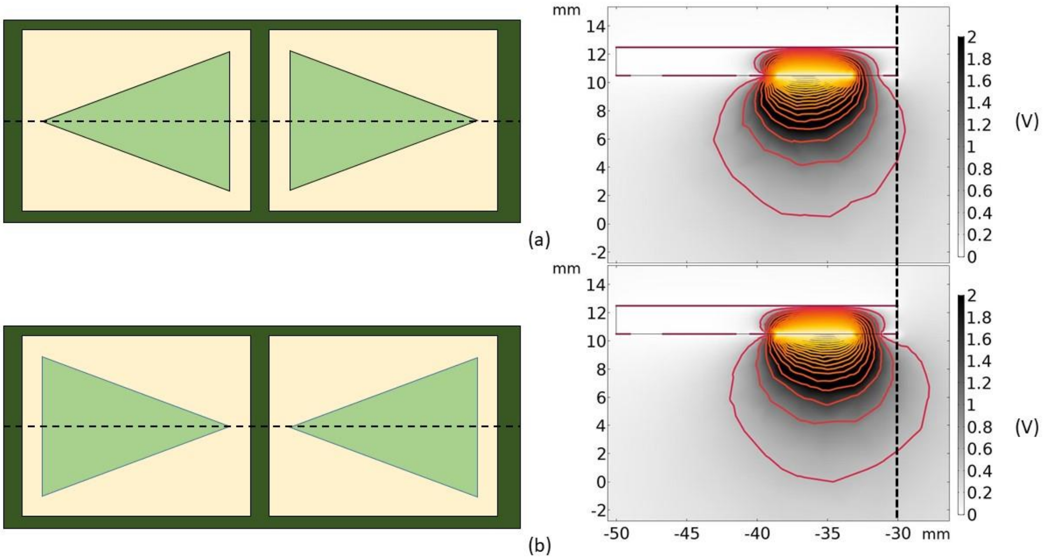

Figure 5.17 Electric field plots along the dotted lines for each probe: (a) back-to-back triangular electrodes and (b) point-to-point triangular electrodes. The electric field potential in air is depicted by a grey-scale from 0 to 2 (as shown in both colour bars) even though the source electrode is fired up with 10 V. The narrower scale is given for showing the electric potential in the area surrounding the CI probe. The "yellow-to-red" lines represent the electric field lines generated from the driving electrode. While the red lines depict the position of the sensing electrode, guard electrode and back of the CI probe. These lines give a better insight of the overall figure (position of driving and sensing electrode, and electric field converging (a) and diverging (b) with respect to the centre of the CI probe).

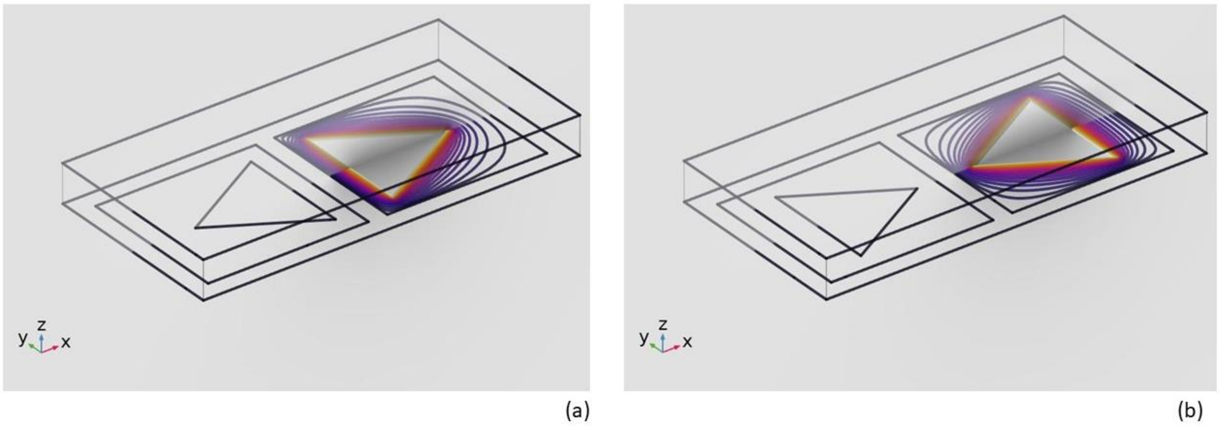

Figure 5. 18 Distribution of electric field lines for (a) back-to-back triangular electrodes and (b) point-to-point triangular electrodes. In (a) the electric field lines converges toward the centre, while in (b) toward the edge.

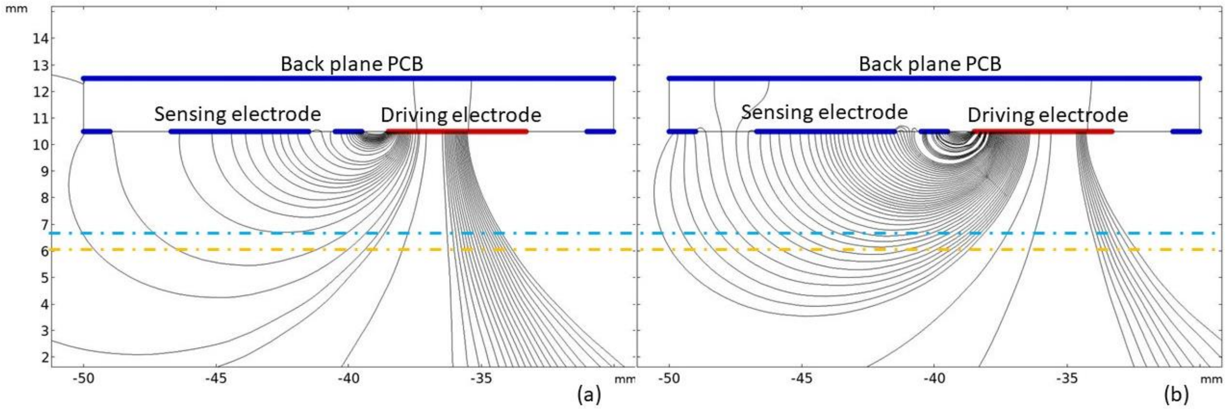

Figure 5.19 Electric field plots along the dotted lines as depicted in figure 5.17: (a) back-to-back triangular electrodes and (b) point-to-point triangular electrodes. The streamlines represent the electric lines generated by the driving electrode, those ones reaching the sensing electrode actively affect a measurement. The dashed lines, light blue and orange, represent the tangent to the farthest electric line to reach the sensing electrode in case (a) and (b), respectively.

When imaging a bulk feature in non-conducting samples using symmetric probes, the entire volume of the fringing electric field takes part. Hence, a back-to-back triangular probe, with a smaller volume of influence, provides a better image resolution and is capable of identifying smaller size defects. On the other hand, the point-to-point triangular probe, which has a bigger volume of influence, provides a deeper penetration depth being capable of detecting deeper buried defects.

When a surface feature on a conducting sample is being imaged, the fringing electric field between the nearest parts of the electrodes will dominate. In the case that point-to-point triangular electrodes are used, the volume of the fringing field between the two points of the two electrodes is relatively small which improves the sharpness of an image, adding a further advantage to this kind of probe. An additional advantage of the triangular electrode probes is that the sharper corners will gather more charges and generate more electric lines at the corners, which makes the signal stronger.

In a recent study, point-to-point triangular electrodes were compared to other shapes: rectangular (two orientations), square and circular [24], as shown in figure 5.20.

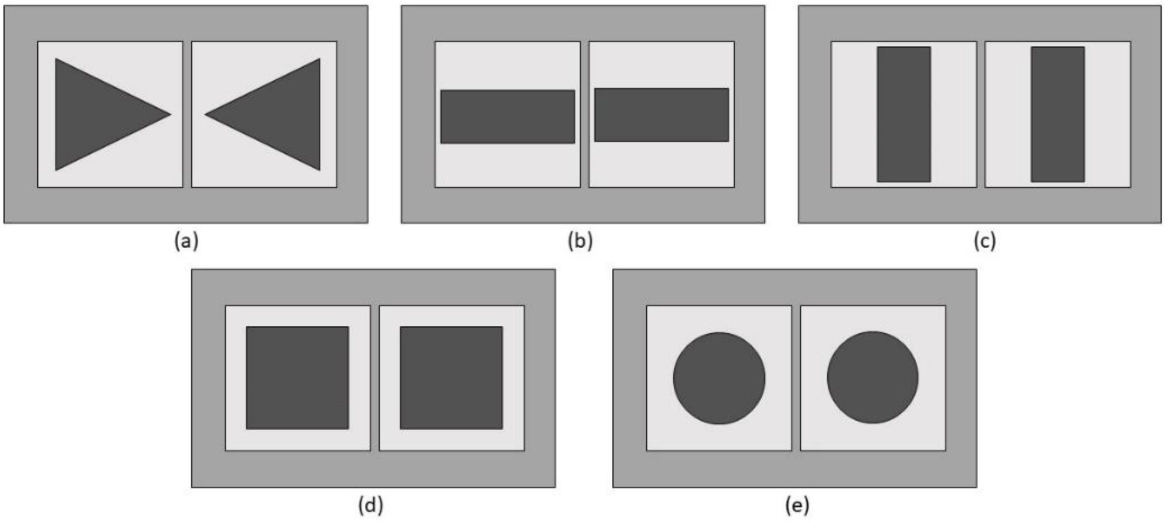

Figure 5.20 CI sensors with different geometries. (a) point-to-point triangular electrodes, (b) rectangular-I electrodes, (c) rectangular-II electrodes, (d) square electrodes, (e) circular electrodes (after [24]).

The parameters taken in account for making the comparison are: detection signal strength, dynamic change rate (namely an evaluation of the performance of sensors) and the best lift-off for detecting defects on conductive and non-conductive materials, as displayed in table 5.1.

Table 5.1 Outline of the advantages and limitations of different electrode geometries.

Electrode geometry	**Pros**	**Cons**
Triangular	Signal strength (conductors and dielectric materials). Dynamic change rate (dielectric materials).	Dynamic change rate (conductors).
Rectangular-I	Signal strength (conductors and dielectric materials).	Dynamic change rate (dielectric materials).
Rectangular-II		Signal strength (conductors and dielectric materials). Dynamic change rate (conductors and dielectric materials).
Square	Average performance	Average performance
Circular	Dynamic change rate (conductors and dielectric materials).	Signal strength (conductors and dielectric materials).

The results showed that the rectangular-I sensor is better than conventional triangular sensor in terms of detection signal strength, while the circular sensor is better in terms of dynamic change rate. For detecting defects on conductive materials (hence surface features), the optimal lift-off varies depending on the electrode geometry. Conversely, for detecting defects on non-conductive materials (therefore, surface and bulk features), the best lift-off is found to be 1 mm for all geometries.

4) Back plane:

The electrodes of CI probes are made of conductive material and usually a non-conducting substrate is present to support the electrodes mechanically. There is often a grounded back plane which is used for shielding undesired electric field and for guaranteeing the electric field is radiated predominantly in the direction towards the specimen. The CI probes used in this work were fabricated by etching a PCB substrate. Even the back surface of the PCB was coated in copper and connected to ground when the probe is in use. The effect of the grounded back plane reveals that the electric field decays more rapidly. This is due to the electric lines being drawn from the front surface, which results in a weaker signal level. On the other hand, without the grounded back plane, the penetration depth increases. Again, there exists a trade-off between the penetration depth and signal strength.

5.7.2 Concentric electrodes

Another geometry for CI probes is the use concentric electrodes, which could give better results under some circumstances [10]. The typical arrangement consists of two active electrodes separated by a thinner guard ring, as shown in figure 5.21.

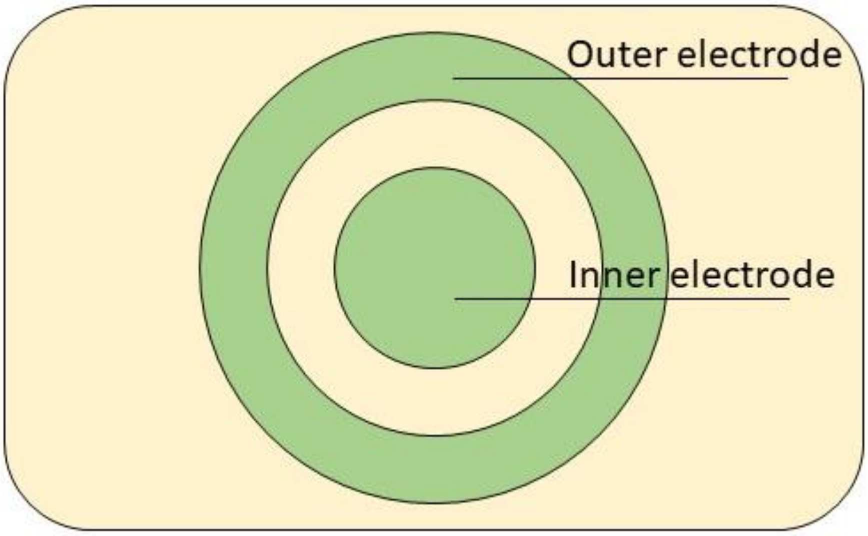

Figure 5.21 Schematic diagram of a concentric probe.

This probe geometry offers two modes of operation: either the central disc can be driven or the outer annulus can be a source. The excitation of the inner disc provides a more suitable electric field distribution and a decay of electric field amplitude fairly uniform unlike when the outer annulus is driven, whose field drops off far more rapidly, as shown in figure 5.22. Nonetheless the two modes of operation produce identical images for the same sample due to the reciprocity theorem [25]. This will be explained later in the Chapter.

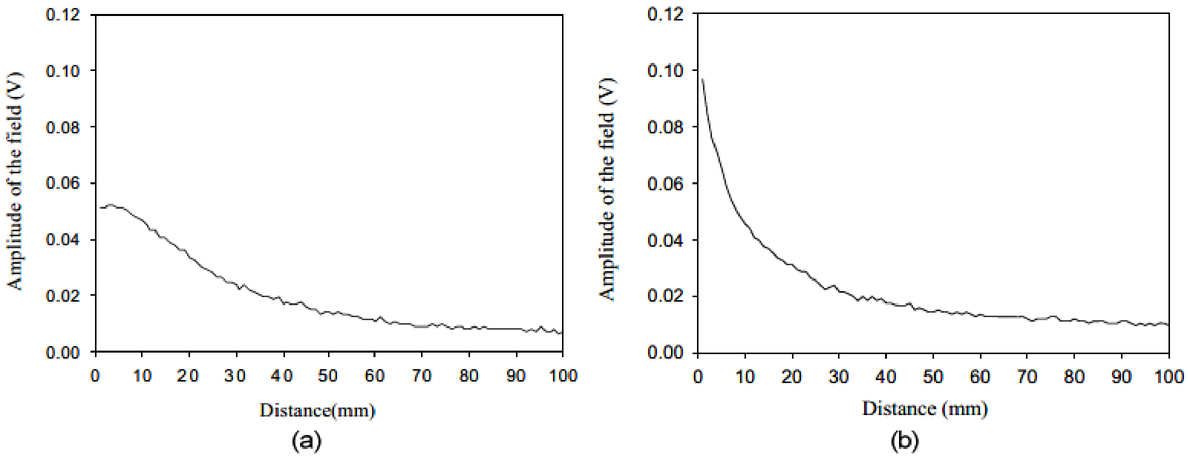

Figure 5.22 The decay of electric field amplitude as a probe is scanned in a transverse direction away from the PCB surface, starting from (a) the centre of the inner disc and (b) from within the outer electrode (from [22]).

The parameters which affect the performance of this geometry are: the width of the surrounding ring, the size of the inner disc and the gap between them.

5.8 Method of modelling/experiment (COMSOL)

As discussed in the previous sections, finite element modelling (FEM) is essential to achieve the optimal probe design and, moreover, to better understand the mechanism of interaction of CI probes with different types of samples (conductive and non-conductive ones). The analytical simulations are performed by modelling both 2D and 3D models: the former are to get a better insight of the capacitive coupling and the interaction of electric fields, while the latter are for validating the experimental results, basically a comparison. Before giving some examples of the model used, an explanation of the physics behind the measurement is necessary in order to let the reader understand the way the models are set up.

Unlike EMAT modelling, where the generation and propagation of guided waves are performed in two separate simulation software packages (COMSOL and PZFlex), CI modelling has been performed using COMSOL only.

5.8.1 Finite element modelling of CI probes

The application of FEM to the CI probes follows the governing equations previously mentioned, namely Maxwell's equations. Generally, materials present both dielectric and conductive properties, hence the Maxwell-Ampere equation is adopted.

$$\nabla \times \vec{H} = \vec{J} + \frac{\partial \vec{D}}{\partial t}. \tag{2.4}$$

In order to eliminate the magnetic field intensity ($\vec{H}$), the divergence of both sides of Equation (2.4) needs to be taken, as:

$$\nabla \cdot (\vec{J} + \frac{\partial \vec{D}}{\partial t}) = 0 \tag{5.14}$$

As the frequencies used for capacitive imaging probes are between 10 kHz and 1 MHz, the inductive phenomena, which would occur at the surface (within the skin depth), can be neglected and the electromagnetic field can be accounted as a quasi-static electric field. Furthermore, the time-derivative of the magnetic flux density ($\vec{B}$) can be assumed to be negligible, and according to Faraday's law the electric field ($\vec{E}$) is curl free,

$$\nabla \times \vec{E} = -\frac{\partial \vec{B}}{\partial t} = 0 \tag{5.15}$$

Referring to equation (5.15), the electric field ($\vec{E}$) can be expressed by an electric scalar potential distribution $\varphi(x, y, z)$, which can be introduced as:

$$\vec{E} = -\nabla\varphi(x,y,z) \tag{5.16}$$

And using the constitutive relationships (equation 2.8 and 2.9) which the form as follows:

$$\vec{J} = \sigma(x,y,z)\vec{E} \tag{5.17}$$

$$\vec{D} = \varepsilon(x,y,z)\vec{E} \tag{5.18}$$

Equation 5.14 can assume the form:

$$\nabla \cdot [\sigma(x,y,z)\nabla\varphi(x,y,z)] + \nabla \cdot \left\{\frac{\partial}{\partial t}[\varepsilon(x,y,z)\nabla\varphi(x,y,z)]\right\} = 0 \tag{5.19}$$

where $\sigma(x,y,z)$ is the conductivity distribution and $\varepsilon(x,y,z)$ is the permittivity distribution. If both distributions within the area contained by the electric field are known, the electric potential can be obtained by solving equation (5.19). However, in practice, because of the time-derivative coupling between the dielectric and conductive properties, the resolution of equation (5.19) is computationally prohibitive [27]. The practical resolution of this problem is to consider the system either “predominantly dielectric” or “predominantly conductive” [27]. In the former case, equation (5.19) can be simplified to be a Laplace’s equation:

$$\nabla \cdot [\varepsilon(x,y,z)\nabla\varphi(x,y,z)] = 0 \tag{5.20}$$

The previous equation is valid, for instance, for Electrical Capacitance Tomography (ECT) applications [28,29] and dielectrometry sensors [30]. In latter case, on the other hand, the equations assume the following form:

$$\nabla \cdot [\sigma(x,y,z)\nabla\varphi(x,y,z)] = 0 \tag{5.21}$$

which can be used for Electrical Resistance Tomography (ERT) applications [31-33] and potential drop methods [34,35]. Adopting the quasi-static assumption, FE can be used to solve the above equations, and to predict the potential distribution due to capacitive electrodes in a specific medium and geometry.

5.8.2 2D FE models

2D models were built in COMSOL and the model geometry with the finite elements (meshes) is presented in figure 5.23.

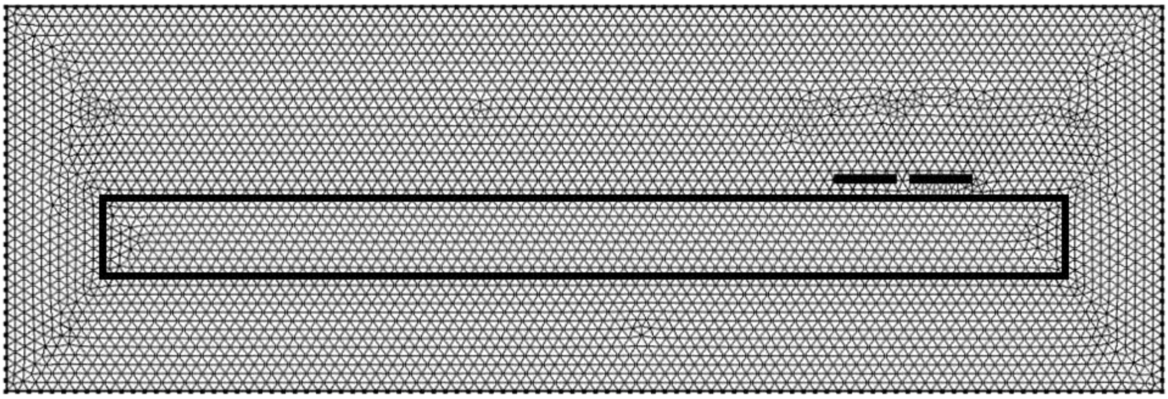

Figure 5.23 2D model geometry with elements (meshes).

The simplest CI probe geometry (two rectangular shape electrodes) was considered in the 2D models. The assumption is that the length of the electrode (transverse to the page) is much bigger than the width, so that the electric field distributions along the length can be thought to be constant and not affected by end fields. According to this assumption, the 3D geometry of the probe can be reduced to a 2D model, which, in turn, can be adopted to describe the entire probe. Furthermore, the electrodes are considered to have zero thickness (ideal electrodes). The electrodes length is 9 mm with a separation between them of 5 mm. The mesh has been selected to be triangular shaped. The triangular mesh is here adopted because it is a quick and simple way to achieve the high element quality which covers the entire geometry, therefore the convergence can be obtained more easily. The size of the mesh has been chosen to “extremely fine” for achieve a good level of accuracy.

5.8.2.1 Field interaction with non-conducting materials

Figure 5.24 depicts the electric field distribution predicted by the FE model for a non-conductive material for a uniform sample (a) and two faulty ones (surface defect (b) and internal defect (c)). The internal defect is an air-filled circular void. The non-conductive material selected is Perspex, whose dimensions are 100 mm x 8 mm. The surface defect, square shaped, has a side of 4 mm, alike the diameter of the internal defect. The assumption made for the electrode shape and size is the same mentioned in the previous section. It can be noted that the presence of both air-filled defects distort the electric field leading to a detectable change in signal. This is due to the discrepancy in values of the relative permittivity, ε_r, supposed for the solid medium (Perspex, relative permittivity $\varepsilon_r = 3.3$) and air (relative permittivity $\varepsilon_r = 1$). Thus, the model presents how the CI probe detects surface and sub-surface defects because of the permittivity difference between the two media.

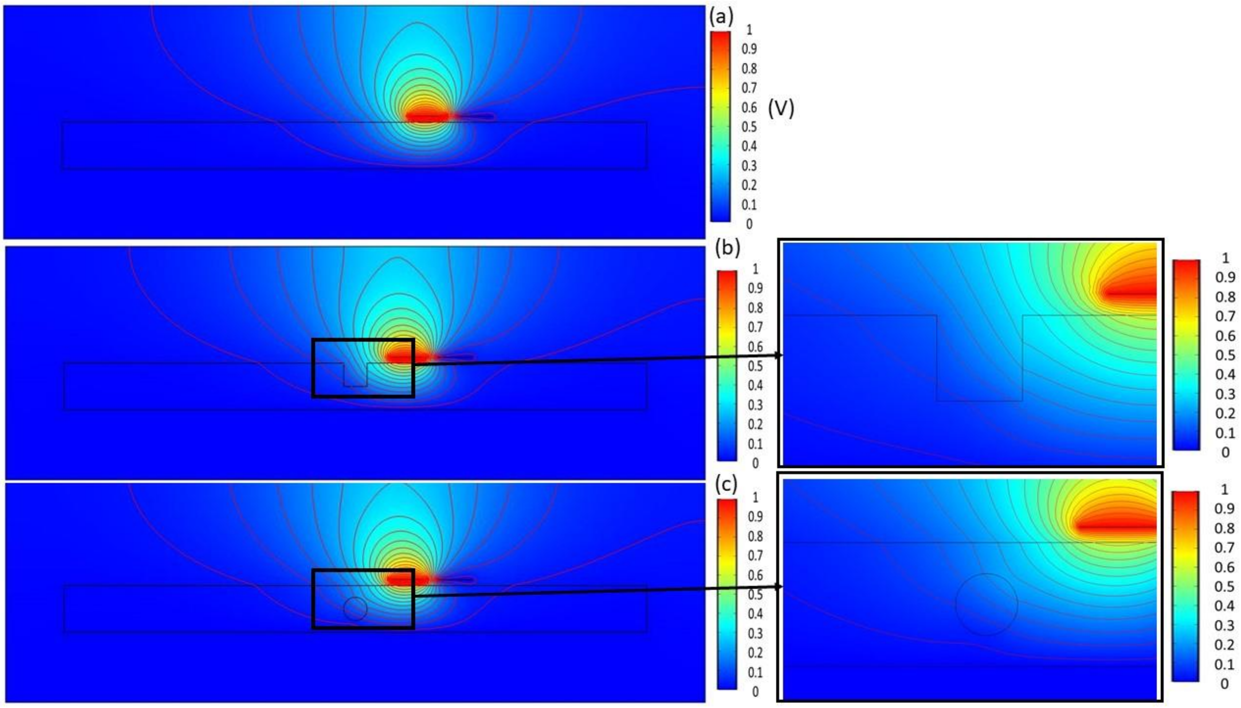

Figure 5.24 The electric field distribution inside an non-conducting specimen: (a) uniform sample, (b) with a surface defect and (c) with an internal defect (filled with air). The driving electrode is on the left. The colour bars at the right hand side of each figures represent the intensity of the electric potential (V). The driving electrode was powered by 1 V.

5.8.2.2 Field interaction with conducting materials

Figure 5.25 shows the prediction of the electric field distribution for a conductive material. Even in this case, three geometries are taken into account: (a) a uniform sample, (b) one with a surface defect (b) and (c) one with a sub-surface defect. The sub-surface defect is an air-filled circular void. The dimensions of the sample and defects are the same of the 2D model presented in the previous section. In this case the material is aluminium.

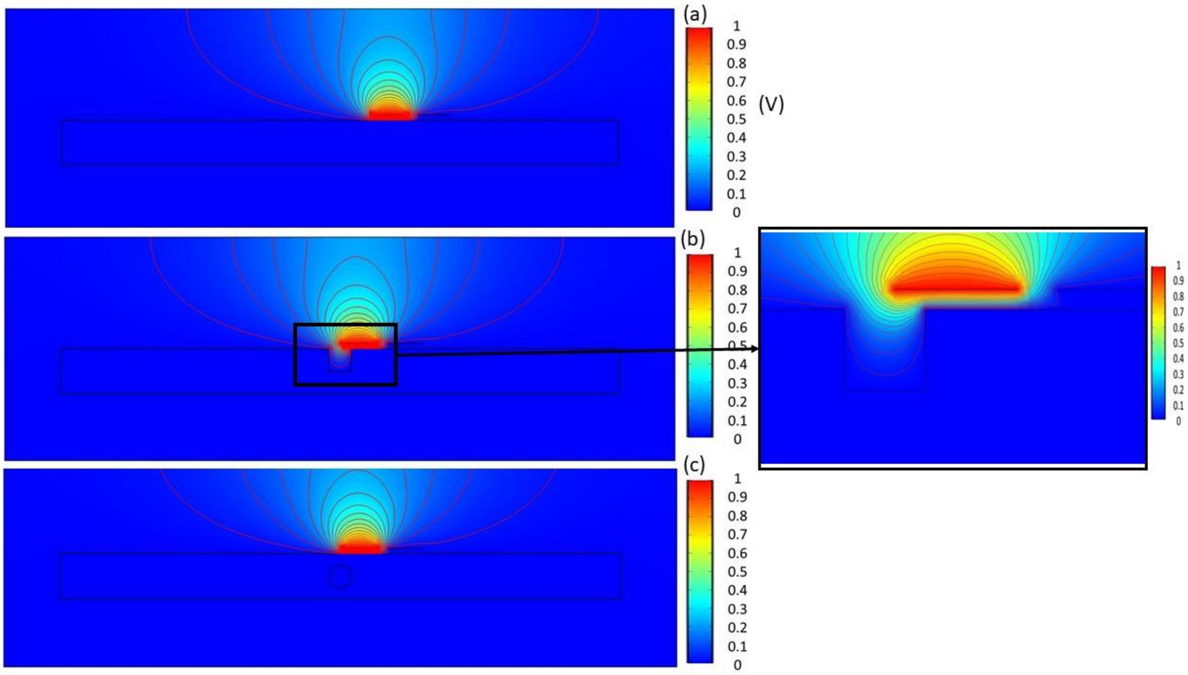

Figure 5.25 The electric field distribution inside an electrically conducting specimen: (a) uniform sample, (b) with a surface defect and (c) with an internal defect (filled with air). The driving electrode is on the left. The colour bar at the right hand side of each figures represent the intensity of the electric potential (V).

It can be seen that in cases of no defect or a sub-surface defect, the electric field is not affected, and the internal defect is not detected, in accordance to the theory explained earlier in this chapter. On the other hand, surface features, like the one shown in figure 5.25(b), are detected as the electric field is distorted by its presence.

5.8.3 3D FE models

3D models are used to compare numerical predictions to actual experiment data, and to study the sensitivity distribution of the CI probe used. Unlike the 2D models, where the shape of the electrodes is neglected, the 3D models are carefully designed following the actual dimensions, separation and shape of the electrodes used for conducting the measurement. The following example aims to compare the results obtained on a Perspex sample having 4 flat bottom holes.

5.8.3.1 Set-up 3D simulation – CI probe

The CI probe considered and modelled is a back-to-back triangular probe and can be identified by the base (b) and height (h) of each triangle and the separation distance (s) between the parallel sides of the two triangles. In this case, the CI probe considered has b = 16 mm, h = 19 mm and s = 4 mm. The details of the model for a back-to-back triangular probe are as follows. An 80 mm x 80 mm cubic block centred at (0, 0, 0) in a Cartesian system (xyz) was defined to be the computational domain. A 46 mm x 20 mm x 2 mm block also centred at (0, 0, 0) designed to be the dielectric substrate of the CI probe and an additional block (50 mm x 40 mm x 30 mm) as the plastic case where the dielectric substrate is placed within. The 3D model is presented in figure 5.26(a).

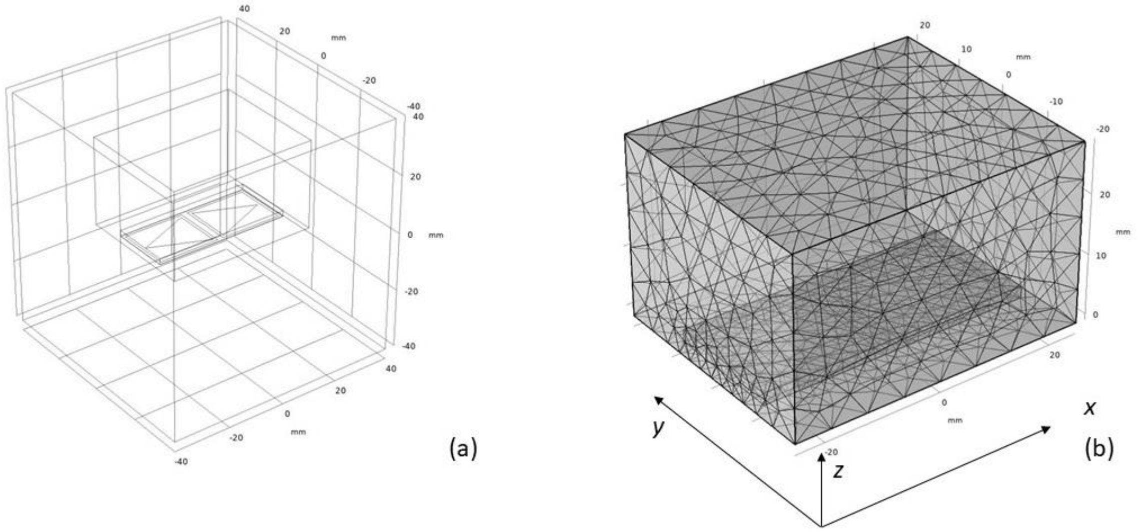

Figure 5.26 3D model: (a) the computational domain (80 mm x 80 mm x 80 mm) with a CI probe; (b) example of FE meshing of the CI probe (plastic case included) and relative coordinate system.

In the coordinate system shown in figure 5.26(b) the probe surface is centred at (0, 0, 0). In order to give an extensive overview of the CI probe and to clarify the results shown later, the plane coordinate systems for the three cross-sections are depicted in figure 5.27.

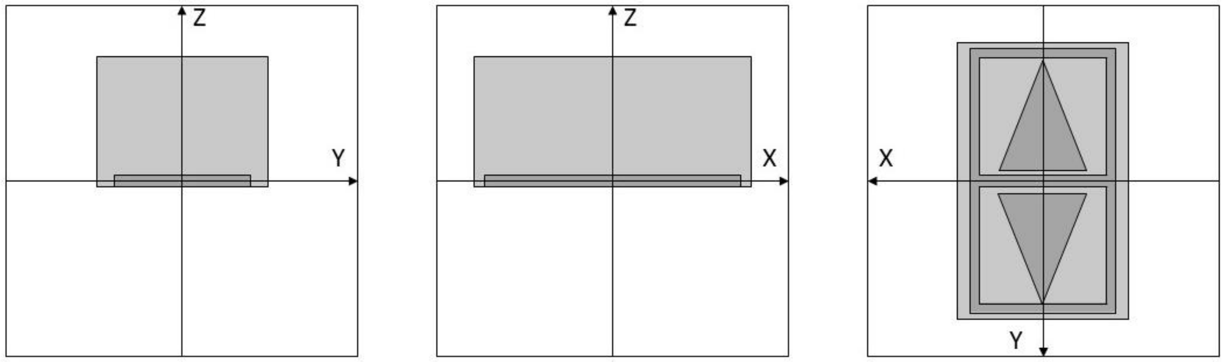

X = 0 plane Y = 0 plane Z= -1 plane

Figure 5.27 Plane coordinate systems for the 3 types of cross sections.

The computational domain (the cube mentioned earlier) is filled with air only whose dielectric constant is set to be unity. The material of the insulating substrate of the PCB is flame retardant woven glass reinforced epoxy resin (FR-4) and its relative dielectric is 4.5. Since the thickness of the electrodes is around 35μm, they can then be treated as boundaries rather than sub-domains. As consequence the computation complexity will be reduced, as very thin sub-domains require a very fine mesh element, which increases the total number of elements. The plastic case material is set to be acrylic, whose relative dielectric is 3.

All faces of the computational domain but the bottom side (z = -40 plane set to be 'ground') have a Neumann boundary condition which can be represented by:

$$\frac{\partial \Phi}{\partial \vec{n}} = 0 \tag{5.22}$$

where $\vec{n}$ is the normal to the surfaces. The driving electrode was set to have an electric potential equal to 1 V, whereas the sensing electrode was set to be 0 V (Dirichlet boundary condition). Guard electrodes and backplane of the probe were set to 'ground'. The electric field expected from the 3D models can be presented in two ways: either as electric field lines as shown in figure 5.17, 5.24 and 5.25, or as electric potential. Figure 5.29 shows the outcome of the 3D model for electric potential in the planes (a) y = 0, (b) x = 0, (c) z = -1, (d) z = -2 (plane parallel and below the probe surface at a distance of 1 cm) and (e) z = -3 (plane parallel and below the probe surface at a distance of 2 cm). The planes are depicted in figure 5.28. The driving electrode is on the left in figure 5.29(a) and on top in figure 5.29(c-e). Figure 5.29(a-b) gives a panoramic view of the electric field distribution. On the other hand, figure 5.29(c-e) shows the attenuation of the electric field with distance away from the plane containing the electrodes.

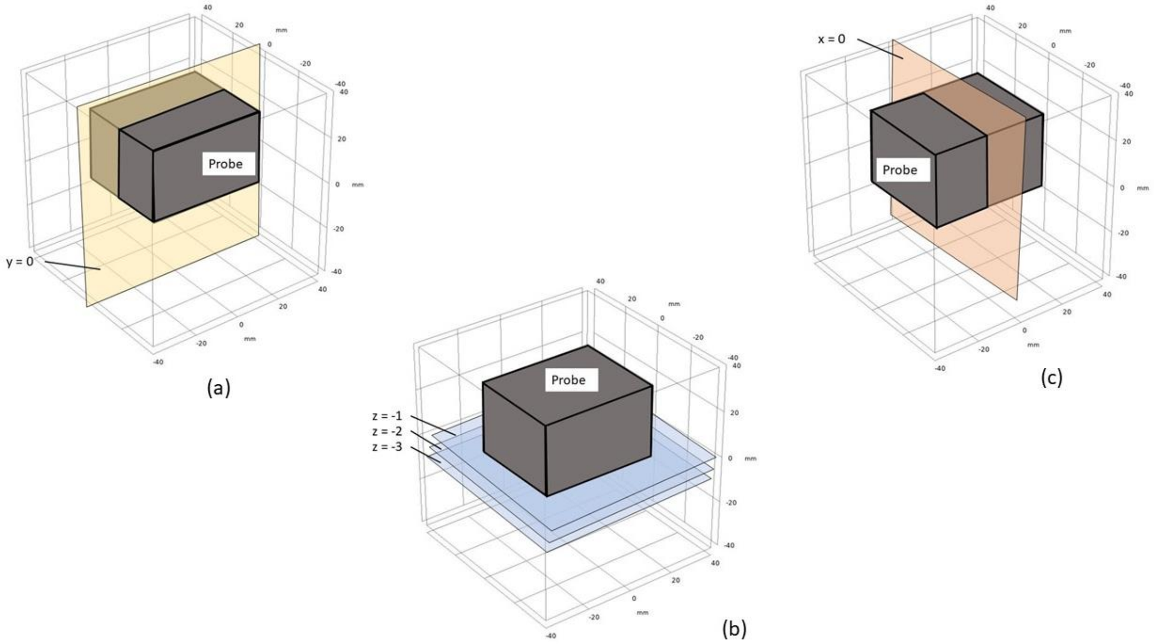

Figure 5. 28 Sketches of the planes: (a) y=0, (b) z=-1, -2, -3, and (c) x=0.

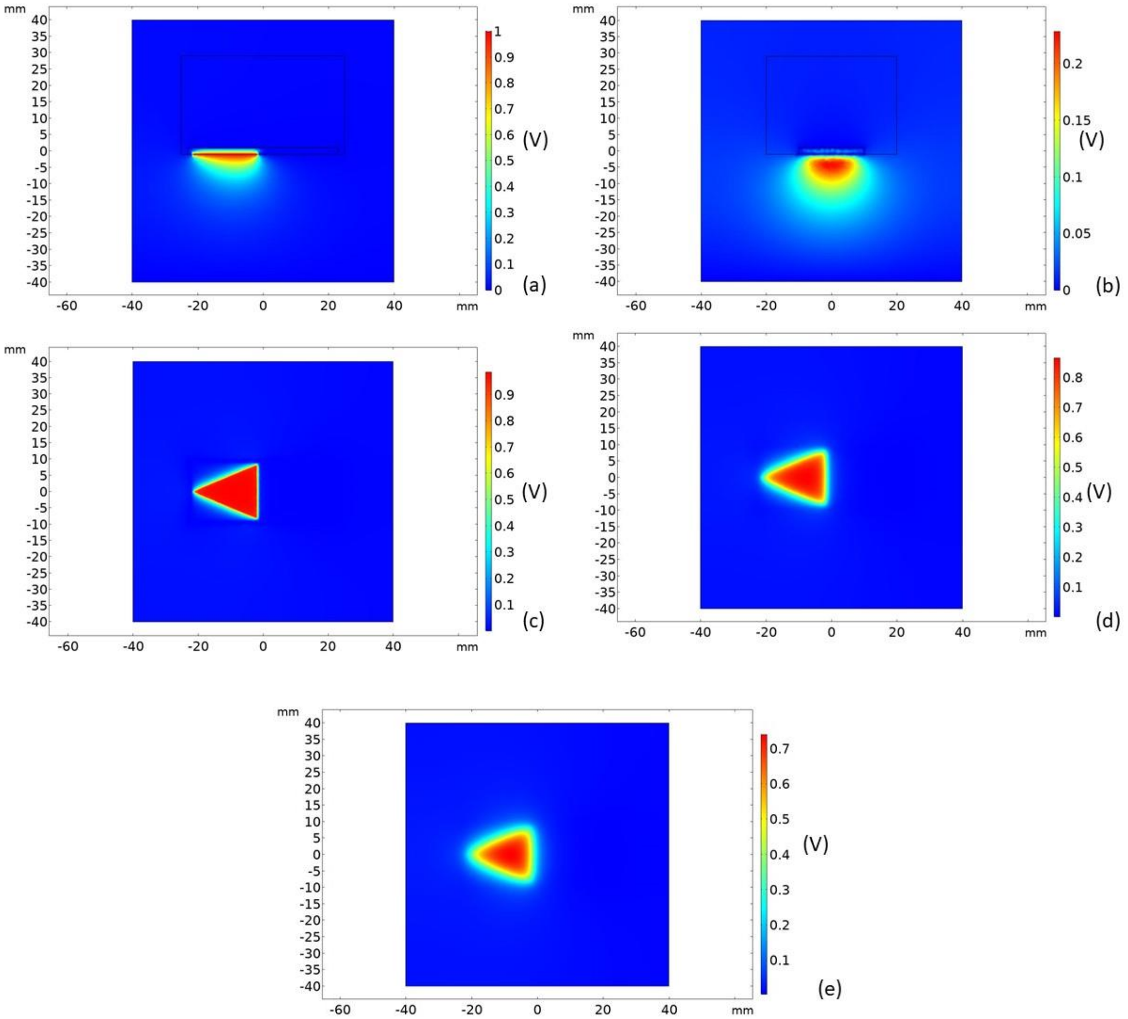

Figure 5.29 Electric field potentials for (a) y=0 plane, (b) x=0 plane, (c) z=-1 plane, (d) z=-2 plane and (e) z=-3 plane obtained from analytical simulation.

5.8.3.2 Sensitivity distribution – CI probe

As anticipated in the section 5.7.2, the measurement sensitivity distribution indicates how each region in the sensing area is effectively contributing to the measurement. For coplanar CI probes, the sensitivity distribution is crucial for retrieving the actual shape of the targeted feature and, additionally, is useful for giving insights into the CI performance improvement and hints to the optimal probe design. An extensive explanation of the measurement sensitivity distribution is given by Yin et al. [36] where methods for obtaining the distribution from both analytical calculation and experiment are also presented. The mathematical model relies, for convenience, on the reciprocity theorem, introduced by Helmholtz, which can be briefly summarized as follows: the source and the detector can be swapped without modifying the detected signal [25]. The expression for defining the sensitivity distribution is:

$$S = -\overrightarrow{E_D} \cdot \overrightarrow{E_S} \tag{5.23}$$

where $\overrightarrow{E_D}$ and $\overrightarrow{E_S}$ are the electric fields in a particular position when the driving and sensing electrodes are powered with a unit voltage respectively. As eq. 5.23 is a dot product, the sensitivity distribution can be, depending on the angle between the two electric fields, zero, positive or negative. In figure 5.30 this situation is shown.

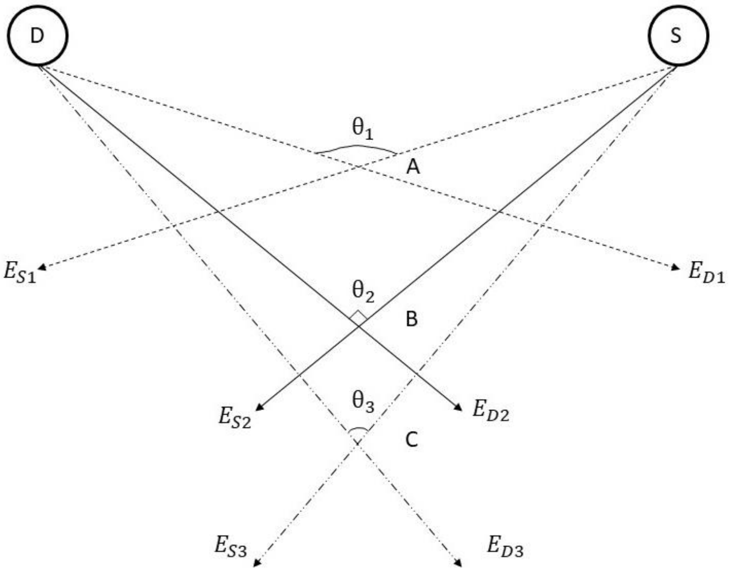

Figure 5.30 Distribution of positive, zero and negative sensitivity values (after [36]). At point A, the sensitivity is positive as the angle is greater than 90 degrees. At point B, the sensitivity is zero as the angle is 90 degrees. At point C, the sensitivity is negative as the angle is less than 90 degrees.

Below, an analytical calculation for the probe used in this thesis work is presented, using the same 3D model as described in the previous section. In figure 5.31 the sensitivity distributions obtained from eq. 5.23 for different planes: (a) $x = 0$, (b) $y = 0$, (c) $z = -1$ and (d) $z = -3$. It can be noted from figure 5.31 that the high sensitivity values are mostly concentrated at the boundaries between driving and sensing electrode, and the sensitivity values drop along the negative z-axis.

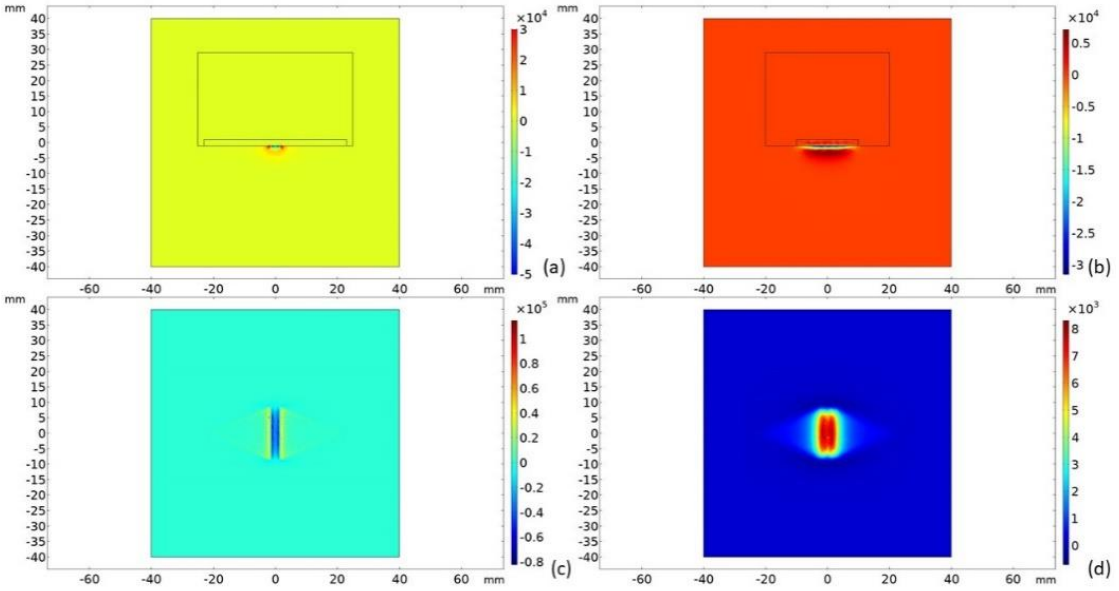

Figure 5.31 Sensitivity distribution for (a) x=0 plane , (b) y=0 plane, (c) z=-1 plane and (d) z=-3 plane. The colour bar at the right hand side of each figure represents the magnitude of the sensitivity.

5.9 Comparison to an experiment – Perspex sample

In this section, a test measurement will be presented in order to show the CI technique in action and validate the results of the analytical model. This used a Perspex sample containing four defects in the form of flat bottom holes. Figure 5.32 shows the dimensions of the specimen.

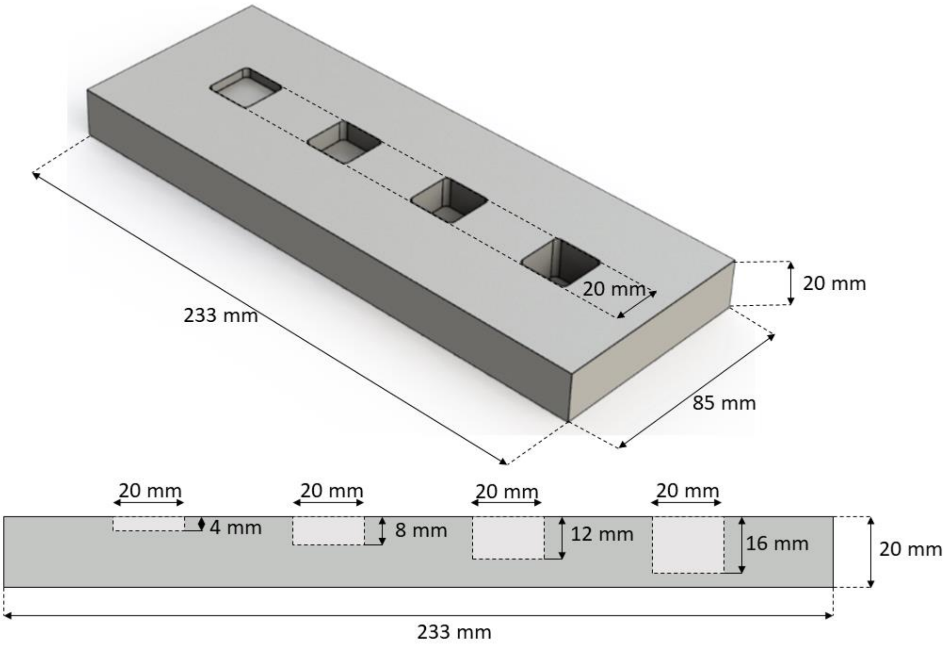

Figure 5.32 Schematic diagram of the Perspex sample.

5.9.1 Experimental set-up

The apparatus, shown in figure 5.33, consisted of a Function generator (Wavetek 191) which generates a sinewave within the frequency range where the assumption of quasi-static electrostatic field is valid. For the purpose of the following results, the sinewave frequency (f_{in}) is 15 kHz. The signal goes to the driving electrode and to the lock-in amplifier as reference signal ($V_{ref}(t)$). The amount of charge over the sensing electrode are converted into a voltage and amplified by the charge amplifier (Cooknell CA/6C). The output of the Cooknell is input into the low-noise preamplifier (Stanford Research, model SR560) where is bandpass-filtered between 10 and 30 kHz. Then the signal (referred as $V_{out}(t)$) goes into a lock-in amplifier (Stanford Research, model SR850) which gives the measured amplitude (or phase). The amplitude (or phase) of each point is saved and stored in a computer where can be used at will of the operator. The following diagram aims to give a clearer idea of the system just explained, see figure 5.33.

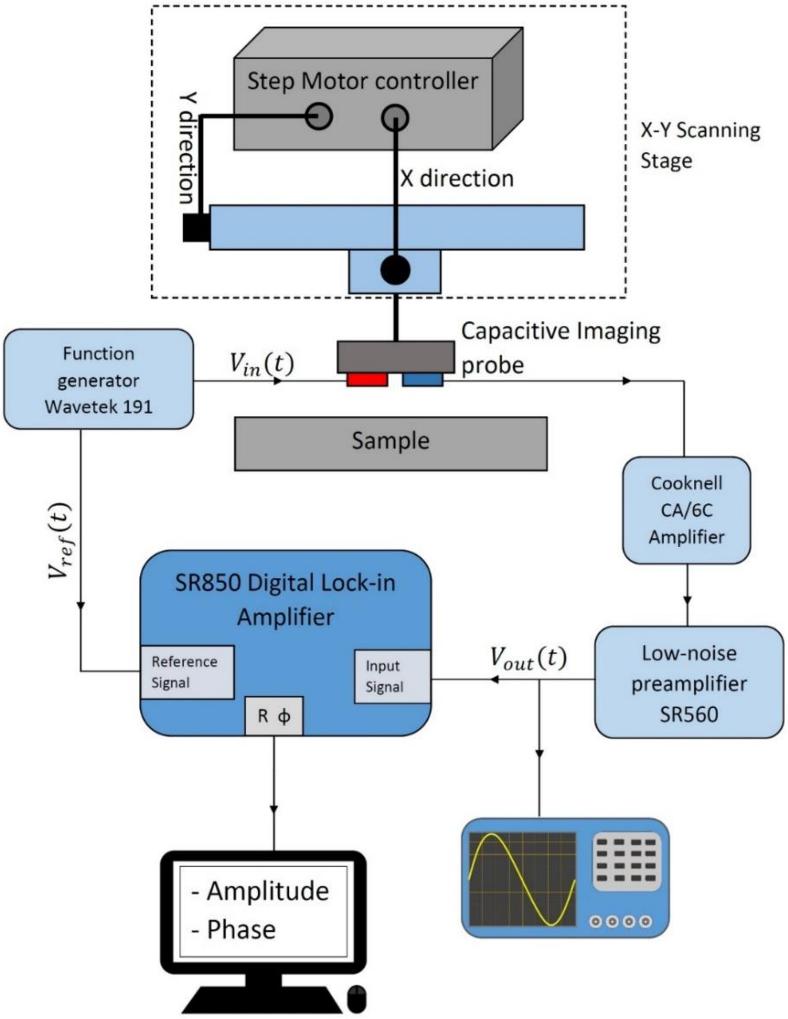

Figure 5.33 Schematic diagram CI laboratory set-up.

The lock-in amplifier is a phase-sensitive detection system, which allows a high degree of noise suppression in small signal measurements. In the lock-in amplifier the manipulation of the signals occurs as follows. The signal $V_{out}(t)$ in the form of a sinusoidal wave, with noise $N(t)$, can be expressed as:

$$V_{out}(t) = V_{out}\sin(\omega t + \Phi_{out}) + N(t), \tag{5.24}$$

with Φ_{out} being the phase of $V_{out}(t)$, and $\omega = 2\pi f_{in}$.

The lock-in amplifier is fed with the reference signal $V_{ref}(t) = V_{ref}\sin(\omega t + \Phi_{ref})$, which is exploited to calculate both the in-phase X and out-of-phase Y contributions. As an example, the in-phase X feature is obtained as follows:

$$\begin{aligned} V_{out}(t)\cdot V_{ref}(t) &= V_{out}V_{ref}\sin(\omega t + \Phi_{out})\sin(\omega t + \Phi_{ref}) + \\ &\quad N(t)\,V_{ref}\sin(\omega t + \Phi_{ref}) \\ &= {}^{1}\!/_{2}\,V_{out}V_{ref}\left[\cos(\Phi_{out} - \Phi_{ref}) - \cos(2\omega t + \Phi_{out} - \Phi_{ref})\right] + \\ &\quad N(t)V_{ref}\sin(\omega t + \Phi_{ref}). \end{aligned} \tag{5.25}$$

Thus, when using a low-pass filter, the in-phase feature X can be written as:

$$X = \frac{1}{2}V_{out}V_{ref}\cos(\Phi_{out} - \Phi_{ref}). \tag{5.26}$$

The out-of-phase contribution Y can be calculated by shifting V_{ref} of 90°, *i.e.* using $V'_{ref}(t) = V_{ref}\cos(\omega t + \Phi_{ref})$ in equation (5.25), yielding to:

$$Y = \frac{1}{2}V_{out}V_{ref}\sin(\Phi_{out} - \Phi_{ref}) \tag{5.27}$$

The amplitude R and phase ϕ of the signal can be then obtained:

$$R = \sqrt{X^2 + Y^2} \tag{5.28}$$

$$\phi = \tan^{-1}\left(\frac{Y}{X}\right) = \Phi_{out} - \Phi_{ref} \tag{5.29}$$

Both output can be used as parameters to construct images. Nonetheless, phase-based images are usually discarded as showing lower signal-to-noise ratios than amplitude-based images [19]. For demonstrative purposes, only the amplitude-based image is shown in this Chapter.

The CI probe used was a back-to-back triangular probe, whose parameters *s*, *b* and *h* are equal to 4, 16 and 19 mm, respectively. Figure 5.34 depicts the CI probe and its parameters (s, b and h).

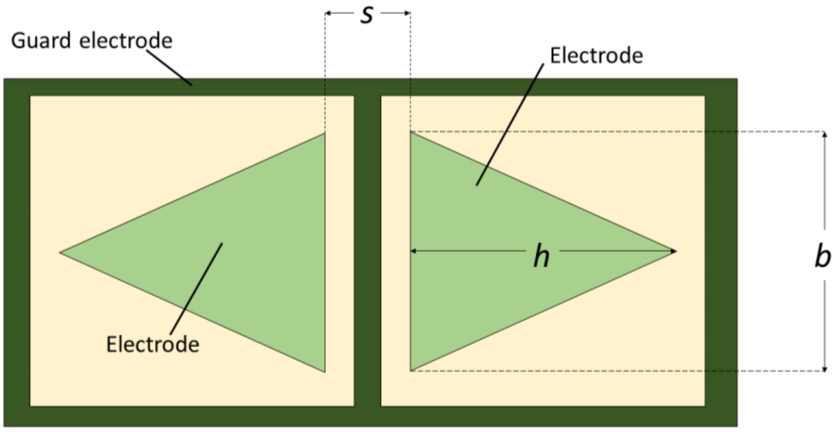

Figure 5. 34 Sketch of the employed CI probe electrodes' arrangement and geometry.

The measurement was performed by placing the flat side of the sample on a grounded platform. The probe was positioned at 1 mm lift-off from the surface of the specimen, which was scanned over an area 200 mm by 80 mm with a step of 1 mm.

5.9.2 Results

The data were stored and handed in MATLAB. The resultant image is depicted in figure 5.35, with the darker areas corresponding to lower values. It can be noted from the intensity variations of the image that the holes in the Perspex sample affected the measured signal to a different extent depending on the depths of the defect.

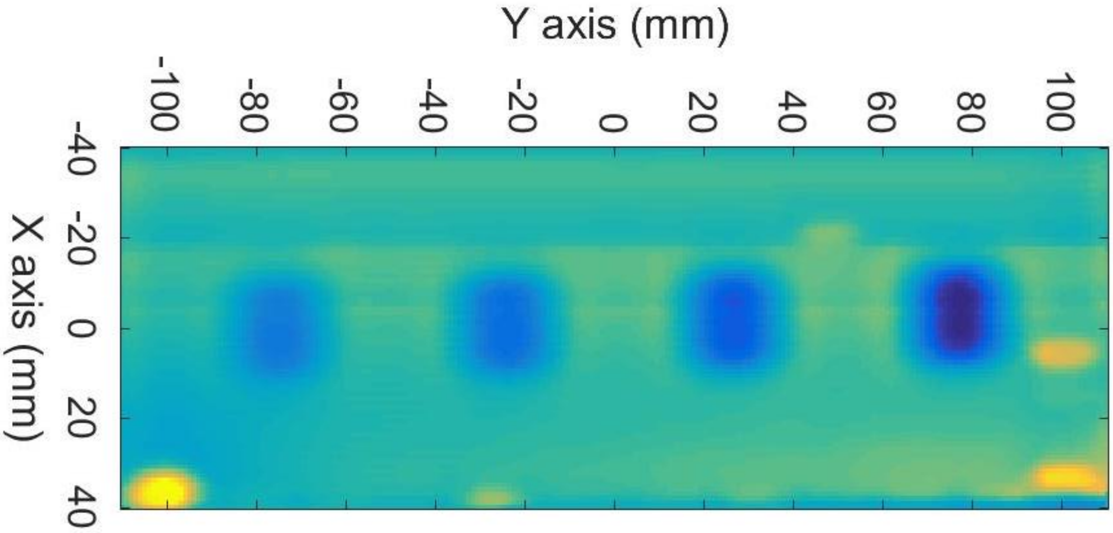

Figure 5. 35 Resultant image of the Perspex sample.

5.9.3 Comparison to a FE model

For this simulation the computational domain has been enlarged (250 mm x 250 mm x 250 mm) in order to introduce, inside the domain filled with air, the abovementioned sample. In figure 5.36 it can be seen the 3D model.

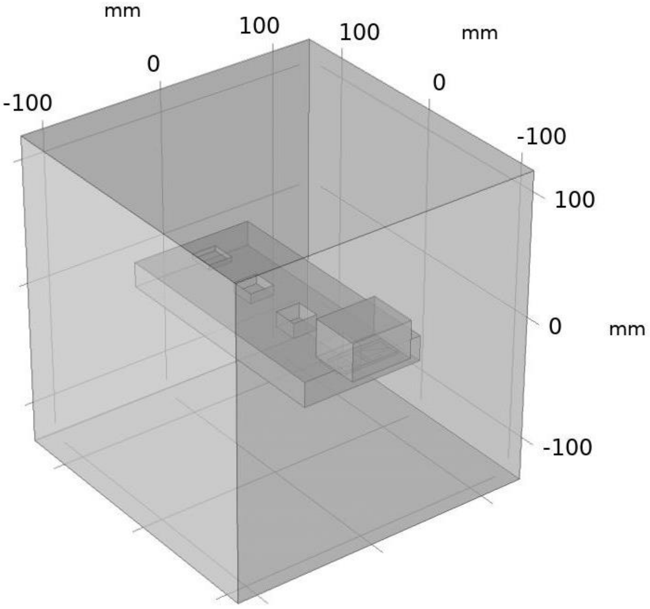

Figure 5. 36 3D model of the CI probe with the Perspex sample.

A 200 mm x 100 mm x 20 mm block represents the Perspex sample. The defects are designed as blocks having same width and depth, (20 mm x 20 mm) with different height: 4 mm, 8 mm, 12 mm and 16 mm. Two types of simulations were set up. The first simulates a linear scan made along the central axis of the sample. Figure 5.37 shows a comparison between the results obtained from an experiment (top) and a simulation (bottom). It can be noted that there is good match between the two plots.

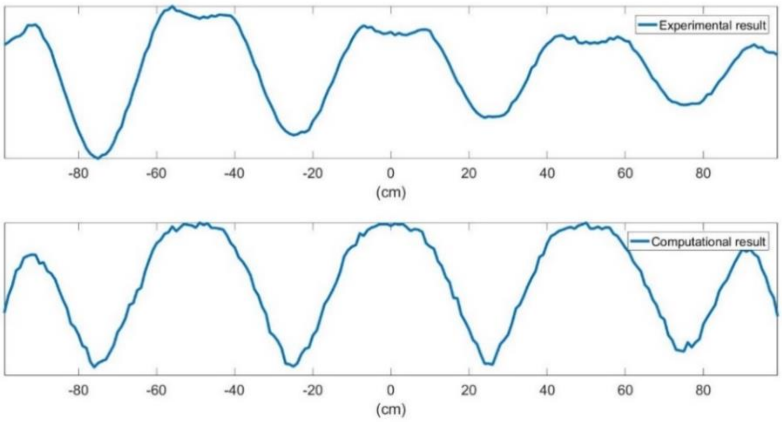

Figure 5. 37 Comparison between an analytical and experimental output.

On the other hand, the second simulates the acquisition as described experimentally. Due to excessive memory requirements, instead of scanning 200 mm by 80 mm, four scans were performed. Each scan was centred on the centre of a defect, scanning an area 30 mm by 30 mm. Then, all images obtained were combined into one in MATLAB. The results depicted in figure 5.38 show a good match between the analytical and experimental results.

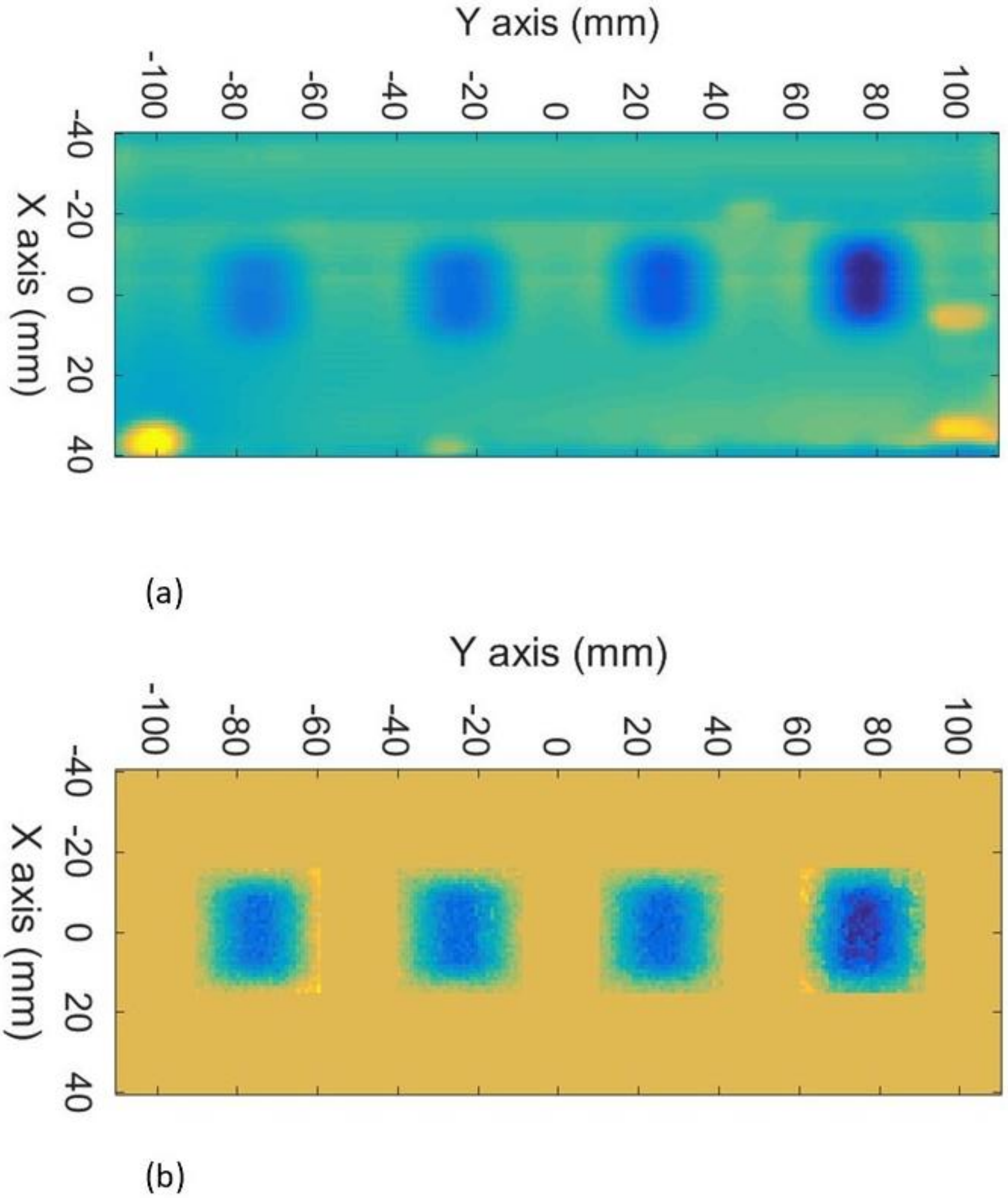

Figure 5. 38 Comparison between an (a) experimental and (b) analytical result.

5.10 Conclusions

CI probes can be used for inspecting different kind of materials (both conducting and insulating ones) without the need to be in contact to the sample surface. Depending on the sample material, that is its electrical properties, different features can be evaluated: surface, for conducting materials, and internal, for insulating ones. CI probes are governed by their geometry, which plays a crucial role for establishing their performance and, consequently, achieving the optimal design for the testing purpose. A means to achieve the best design is the use of finite element modelling, as 2D or 3D models. The former were constructed to show the interaction of the electric field with both kind of sample materials, with or without a defect. Then, 3D models were built to acquire the sensitivity distribution of the CI probe in use in actual experiments in order to determine the VOI and evaluate the imaging ability. Furthermore, the 3D models have been used to compare the outcome to experimental results demonstrating the reliability.

Throughout this thesis, back-to-back triangular electrodes have been mainly used, offering a better versatility in terms of penetration depth. The samples tested were plate-like whose thickness was within the mm range, and where the image resolution (dependent on the VOI) was relatively small (if compared to point-to-point design) which allows the identification of smaller defects.

The aim of this chapter was to give the reader a clear understanding of the CI technique from a physical to a practical point of view, showing advantages and limitations of this method. This gives the background to the results shown in the next chapter, where measurements are made on composite samples containing a range of defects.

References Chapter 5

[1] J. Garcia-Martin, J. Gomez-Gil, E. Vazquez-Sanchez, "Non-Destructive Techniques Based on Eddy Current Testing," *Sensors,* vol. 11, no. 3, pp. 252-2565, 2011.

[2] M.P. De Goeje, K.E.D. Wapenaar, "Non-destructive inspection of carbon fibre-reinforced plastics using eddy current methods," *Composites,* vol. 23, no. 3, pp. 147-157, 1992.

[3] D. Jiles, "Review of magnetic methods for nondestructive evaluation (Part 2)," *NDT International,* vol. 23, no. 2, pp. 83-92, 1990.

[4] Y. Shi, C. Zhang, R. Li, M. Cai and G. Jia, "Theory and Application of Magnetic Flux Leakage Pipelin Detection," *Sensors,* vol. 15, pp. 31036-31055, 2015.

[5] A. Mamishev, Interdigital dielectrometry sensor design and parameter estimation algorithms for non-destructive materials evaluation, 1992.

[6] E. Bozzi, M. Bramanti, "A planar applicator for measuring surface dielectric constant of materials," *IEEE Transactions on Instrumentation and Measurement,* vol. 49, no. 4, pp. 773-775, 2000.

[7] P.A. von Guggenberg, M.C. Zaretsky, "Estimation of one-dimensional complex-permittivity profiles: a feasibility study," *Journal of Electrostatics,* vol. 34, no. 2-3, pp. 263-277, 1995.

[8] A.V. Mamishev, A.R. Takahashi, Y. Du, B.C. Lesieutre, M. Zahn, "Parameter estimation in dielectrometry measurements," *Journal of electrostatics,* vol. 56, no. 4, pp. 465-492, 2002.

[9] G. Diamond, D.A. Hutchins, "A new capacitive imaging technique for NDT," in *ECNDT,* Berlin, 2006.

[10] X.B. Li, S.D. , A.S. Zyuzin, A.V. Mamishev, "Design principles for multichannel fringing electric field sensors," *IEEE Sensors Journal,* vol. 6, no. 2, pp. 434-440, 2006.

[11] J. Jackson, Classical Electrodynamics, New York: Wiley, 1999.

[12] J. Larsson, "Electromagnetics from a quasistatic perspective," *American journal of physics,* vol. 75, no. 3, pp. 230-239, 2007.

[13] A. J. Schwab, in *Field Theory Concepts,* Berlin, Springer, 1988, p. 176.

[14] A. Jonscher, Dielectric relaxation in solids, London: Chelsea dielectric press, 1983.

[15] C. Böttcher, Theory of electric polarization, Amsterdam: Elsevier, 1993.

[16] G. Raju, Dielectrics in electric fields, New York: CRC press, 2003.

[17] W. McCarter, G. Starrs, T. Chrisp, and P. Banfill, "Activation energy and conduction in carbon fibre reinforced cement matrices," *Journal of Materials Science,* vol. 42, pp. 2200-2203, 2007.

[18] X. Yin, D.A. Hutchins, G. Chen, W. Li, Z. Xu, "Studies of the factors influencing the imaging performance of the capacitive imaging technique," *NDT & E International,* vol. 60, pp. 1-10, 2013.

[19] X. Yin, D.A. Hutchins, G. Chen, W. Li, "Detecting surface features on conducting specimens through an insulator layer using a capacitive imaging technique," *NDT& E International,* vol. 52, pp. 157-166, 2012.

[20] J. Zoethout, A. Boletis, H. Bleuler, "High performance capacitive position sensing device for compact active magnetic bearing spindles," *JSME International Journal Series C,* vol. 46, no. 3, pp. 900-907, 2003.

[21] A.V. Bugrov, N.I. Dudkin, I.M. Maslennikov, "One-sided capacitance transducer with a guard electrode," *Measurement techniques,* vol. 18, no. 7, pp. 967-969, 1976.

[22] D. Hordern, D. Liu, G. Dissanayake, N. Kirchner, "Capacitive sensor for object ranging and material type identification," *Sensors and Actuators A: Physical,* vol. 148, no. 1, pp. 96-104, 2008.

[23] K. Sundara-Rajan, A.V. Mamishev, M. Zahn, "Fringing electric and magnetic field sensors," *Encyclopedia of sensors,* vol. 4, pp. 89-100, 2005.

[24] Z. Li, G. Chen, C. Li, J. Fu, Y.Gu, W. Li, X. Yin, "Performance evaluation of capacitive imaging sensors with different geometries," *Insight - Non-Destructive Testing and Condition Monitoring,* vol. 60, no. 12, pp. 676-684, 2018.

[25] J. Malmivuo, "Principle of reciprocity solves the most important problems in bioimpedance and in general bioelectromagnetism," *Journal of Physics: Conference Series,* vol. 224, no. 1, p. 012001, 2011.

[26] X. Yin, Capacitive imaging technique for non-destructive evaluation (NDE) (PhD dissertation), Coventry: University of Warwick, 2011.

[27] G. Meng, A.J. Jaworski, J.C.S. Kimber, "A multi-electrode capacitance probe for phase detection in oil-water separation process: design, modelling and validation," *Measurement science and technology,* vol. 17, no. 4, pp. 881-894, 2006.

[28] A.J. Jarwoski, G.T. Bolton, "The design of electrical capacitance thermograpy sensor for use with media of high dielectric permittivity," *Measurement science and technology,* vol. 11, no. 6, pp. 743-757, 2000.

[29] F. Jiang, S. Liu, J. Liu, X. Wang, "Measurement of ice movement in water using electrical capacitance thermography," *Journal of thermal science,* vol. 18, no. 1, pp. 8-12, 2009.

[30] A.A. Nassr, W.W. El-Dakhakhni, "Non-destructive evaluation of laminated composite plates using dielectrometry sensors," *Smart Materials and Structures,* vol. 18, no. 5, p. 055014, 2009.

[31] R. Nimmer, J. Osiensky, A. Binley, K. Sprenke, B. Williams, "Electrical resistivity imaging of conductive plume dilution in fractured rock," *Hydrogeology journal,* vol. 15, no. 5, pp. 877-890, 2007.

[32] G.M. Maillet, E. Rizzo, A. Revil, C. Vella, "High resolution electrical resistivity tomography (ERT) in a transition zone environment: application for detailed internal architecture and infilling processes study of a Rhône river paleo-channel," *Marine Geophysical researches,* vol. 26, pp. 317-328, 2005.

[33] K. Karhunen, A. Seppänen, A. Lehikoinen, P.J.M. Monteiro, J.P. Kaipio, "Electrical resistance tomography imaging of concrete," *Cement and concrete research,* vol. 40, no. 1, pp. 137-145, 2010.

[34] V. Spitas, P. Michelis, "The potential drop technique for measuring crack growth in shear," in *Fracture of nano and engineering materials and structures*, 2006, pp. 463-464.

[35] M. Saka, M. Nakayama, T. Kaneko, H. Abé, "Measurement of stress-intensity factor by means of a-c potential drop technique," *Experimental mechanics,* vol. 31, no. 3, pp. 209-212, 1991.

[36] X. Yin, D.A. Hutchins, G. Chen, W. Li, "Investigations into the measurement sensitivity distribution of coplanar capacitive imaging probes," *NDT&E International,* vol. 58, pp. 1-9, 2013.

Chapter 6

Application of the CI technique for inspecting GFRP samples

6.1 Introduction

The previous chapter provided an extensive explanation of the fundamentals of this technique, the analytical models required for probe designing, and a measurement example. In this Chapter, results obtained on several GFRP composite samples will be presented. First, the specimens and the damage they contain will be described, together with the resulting conventional amplitude-based images. For the first time, data fusion techniques have been applied to images produced by CI technique. The novel approach will then be introduced for generating images based on the fusion of amplitude and phase data. This will be achieved by means of two types of algorithms, which experimentally revealed an improvement in the characterisation and localisation of defects. Finally, the results will be compared with those obtained using air-coupled ultrasonic testing of the same defects.

6.2 CI probes

Two configurations of CI probes were used: a symmetric, triangular back-to-back design, as described earlier in section 5.9.1 and shown in figure 6.1, and a concentric probe, described in section 5.7.2 and shown in figure 6.2. The parameters for the concentric probe R1, R2 and R3 are equal to 8, 16 and 24 cm, respectively.

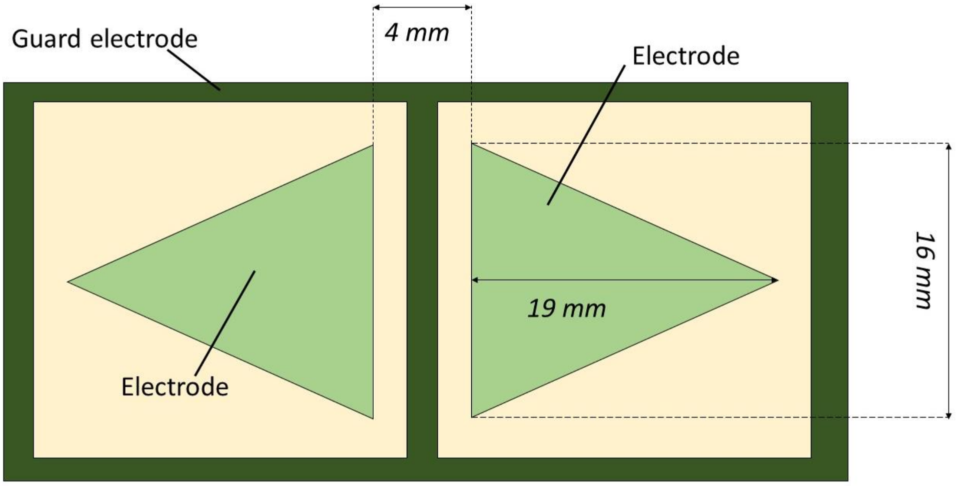

Figure 6.1 Sketch of the employed symmetric CI probe electrodes' arrangement and geometry and its parameters (s, b and h).

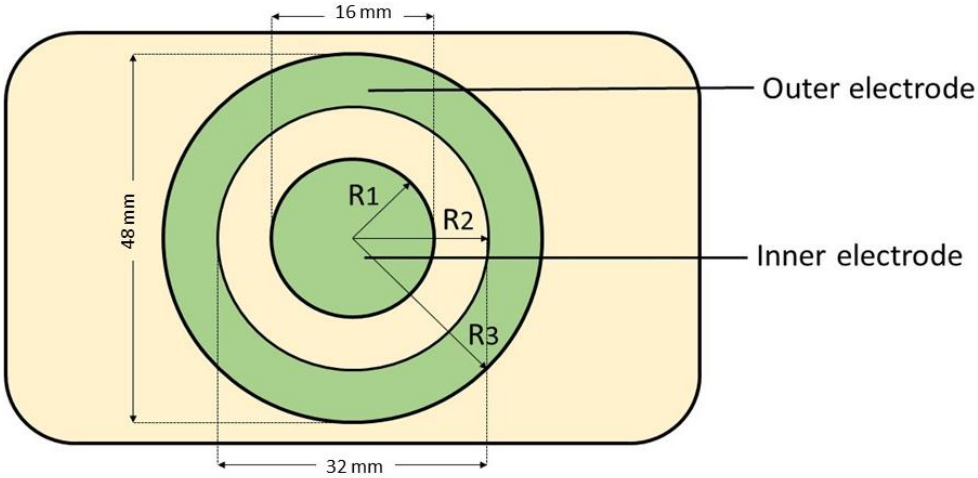

Figure 6.2 Sketch of the employed concentric CI probe electrodes' arrangement and geometry.

Due to their geometry, the two probes present different volumes of influence (VOIs), which will result in different images for the same samples. It is also worth mentioning that the concentric probe would likely produce lower-resolution images due to both the overall diameter of the concentric design and the fact that the electric field distribution is not contained principally along one axis but it is created radially from the central electrode to the outer annulus. Figure 6.3 illustrates the electric field distribution on planes parallel to the electrodes' surface at various lift-off for both designs from a plane 1 to 11 mm distant from the probe surface.

It can be seen from the predicted electric field distributions that the concentric probe presents an electric field distribution (and hence a VOI) that is bigger than that of the back-to-back probe. Thus, while it would be able to inspect a larger area, it is likely to be less sensitive to a small defect.

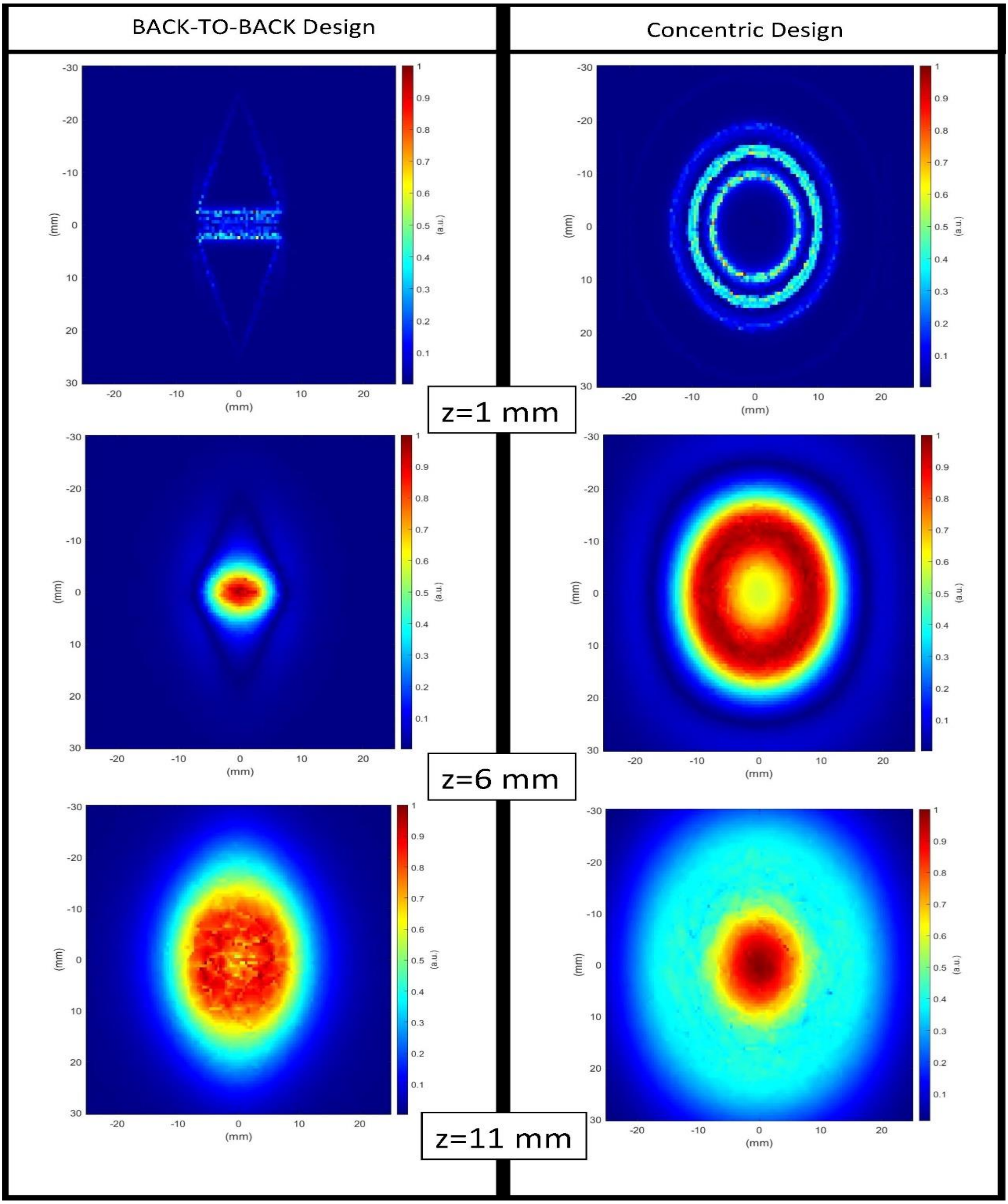

Figure 6.3 Calculated electric field distribution of the employed CI probes on a plane parallel to the electrodes' surface at various distances (1, 6 and 11 mm).

6.3 Inspection of pultruded GFRP plates

The laboratory set-up that was used is the same as that described in section 5.9.1, and the GFRP specimens investigated are similar to those described in section 4.6.4 but now contained defects. These were in the form of impact damage caused by a hemispherical head impactor with various impact energies of 14, 16 and 18 J. The surfaces of the three samples on which the impacts were applied are shown in figure 6.4.

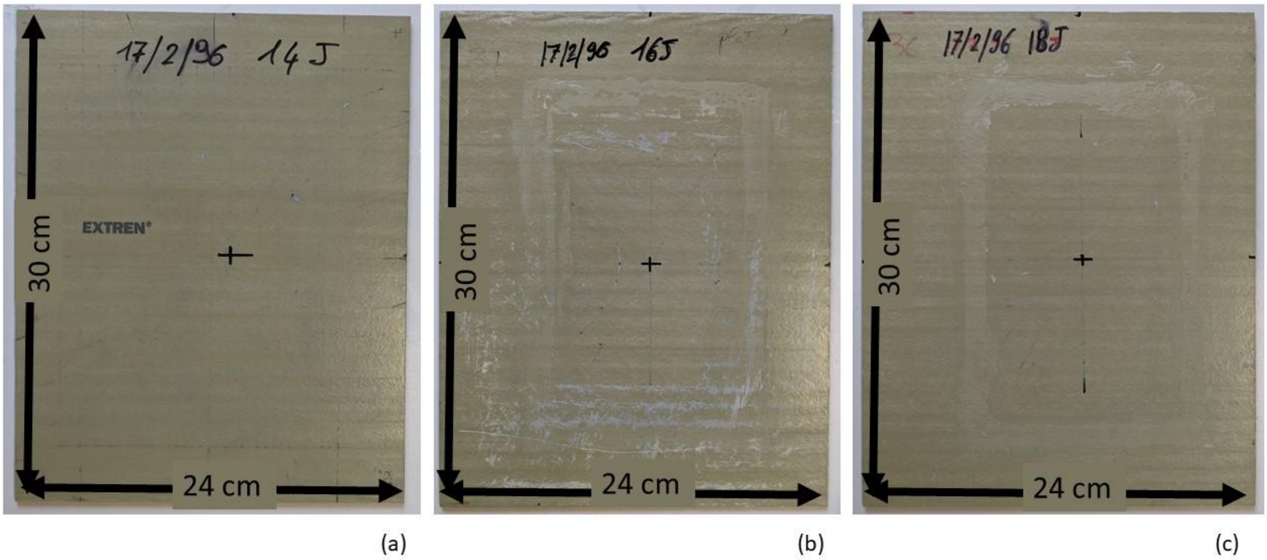

Figure 6.4 Impacted side of pultruded GFRP samples with damage caused by (a) 14 J, (b) 16 J and (c) 18 J impact energies at their centres (black cross mark).

The side on which the impact took place, which in a real scenario would be the external side, shows no visible sign of impact. However, the opposite surfaces (shown in figure 6.5) show signs of matrix and fibre breakage. This type of localised defect is called Barely Visible Impact Damage (BVID), the most frequent type of defect found in composite structures [1], and a potential cause of mechanical weakness, particularly if the structure is subjected to subsequent compressive loads [2].

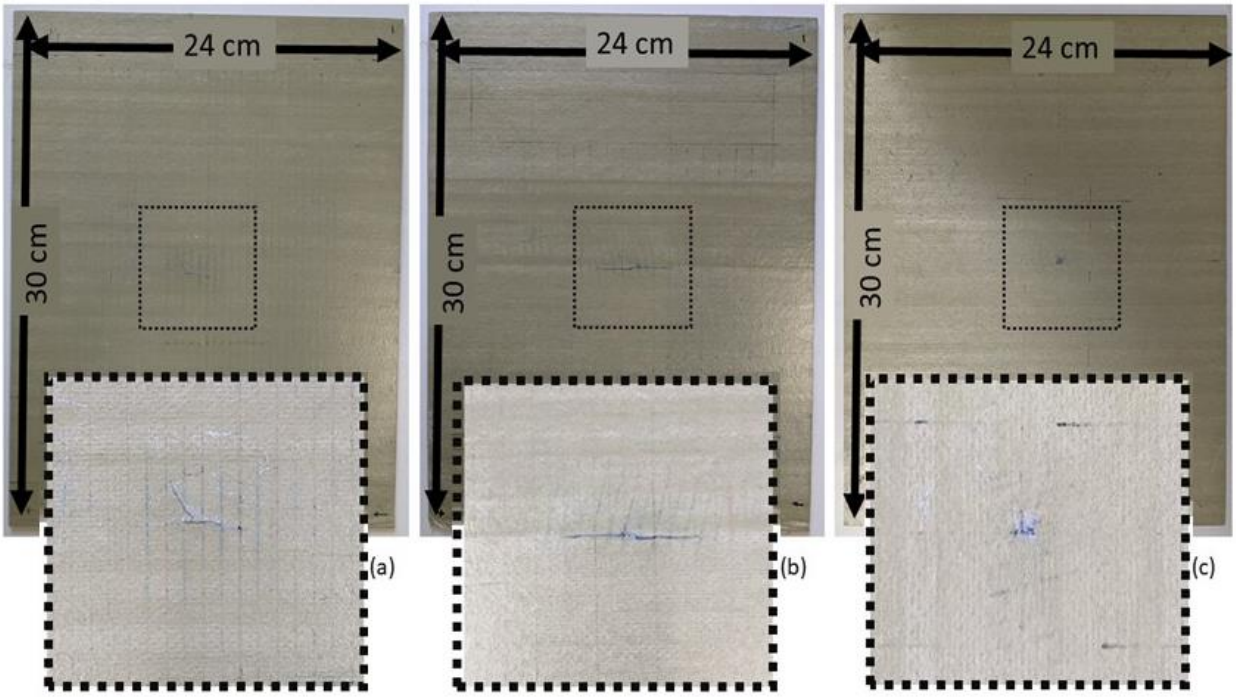

Figure 6.5 Damaged sides of pultruded GFRP samples with damage caused by (a) 14 J, (b) 16 J and (c) 18 J impact energies and detail of the damaged area.

The measurements were conducted from the impact side shown in figure 6.3 in order to simulate actual inspections. The CI probes were scanned over an area 60 x 60 mm centred at the spot of the impact (the black cross marks visible in figure 6.4), as indicated by the dashed line in figure 6.5, with a measurement taken at 1 mm intervals. The lift-off of each probe was 2 mm from the sample surface.

6.3.1 Conventional images

Figures 6.6(a-c) show the CI amplitude-based images obtained for the three GFRP pultruded samples, with defects caused by impact energies of 14 J, 16 J and 18 J. These were taken with the back-to-back triangular probe design. It is noted that the damage seems to have spread under the surface, and was detected as the darker areas as located in the negative sensitivity area. Furthermore, the CI probe is sensitive to regular surface features created during manufacture in the form of parallel lines. This is because lift-off effects will detect variations in the surface waviness. This is typical of samples made by the pultrusion process [2], and can be seen as vertical stripes (these are most visible in figure 6.6(c)).

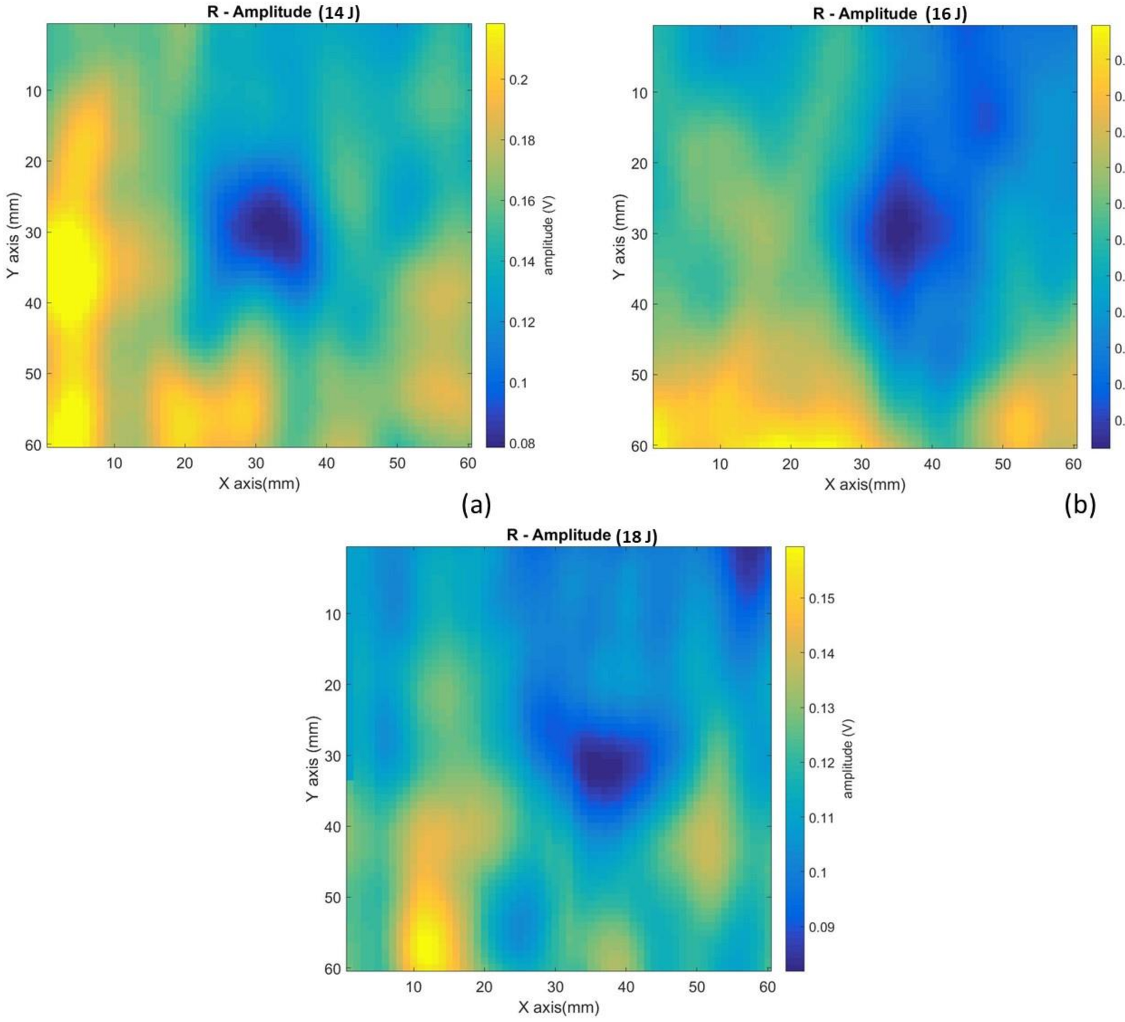

(a) (b)

(c)

Figure 6.6 Capacitive amplitude-feature images for the GFRP samples for impact energies of (a) 14 J, (b) 16 J, and (c) 18 J using the back-to-back electrodes. The defect is detected as the darker area.

The size of the defect can be estimated by simply considering the radius of the darker area in the image. An additional way can be by plotting the values of two perpendicular lines crossing around the centre of the detected damage. Once extracted and plotted the two lines, the width of the depression, assumed to be the width of the defect, can be measured adopting the concept of full width at half maximum (FWHM). However, in this case, the height of the “bell curve”, rather than being measured from zero to the maximum, was measured from the mean value to the minimum value. The mean value was previously calculated from the whole image. Figure 6.7 shows how the defect size was estimated.

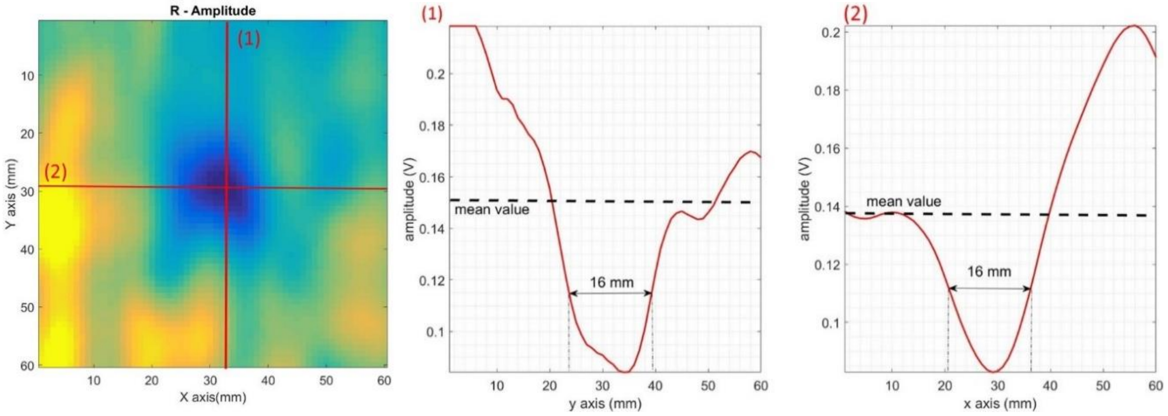

Figure 6.7 Estimation of the defect size by plotting the two pixel lines (1) and (2) shown, which cross the centre of the darker area, assumed to be the impact damage.

The samples were then tested by using the concentric probe design. The resultant images are shown in figures 6.8(a-c).

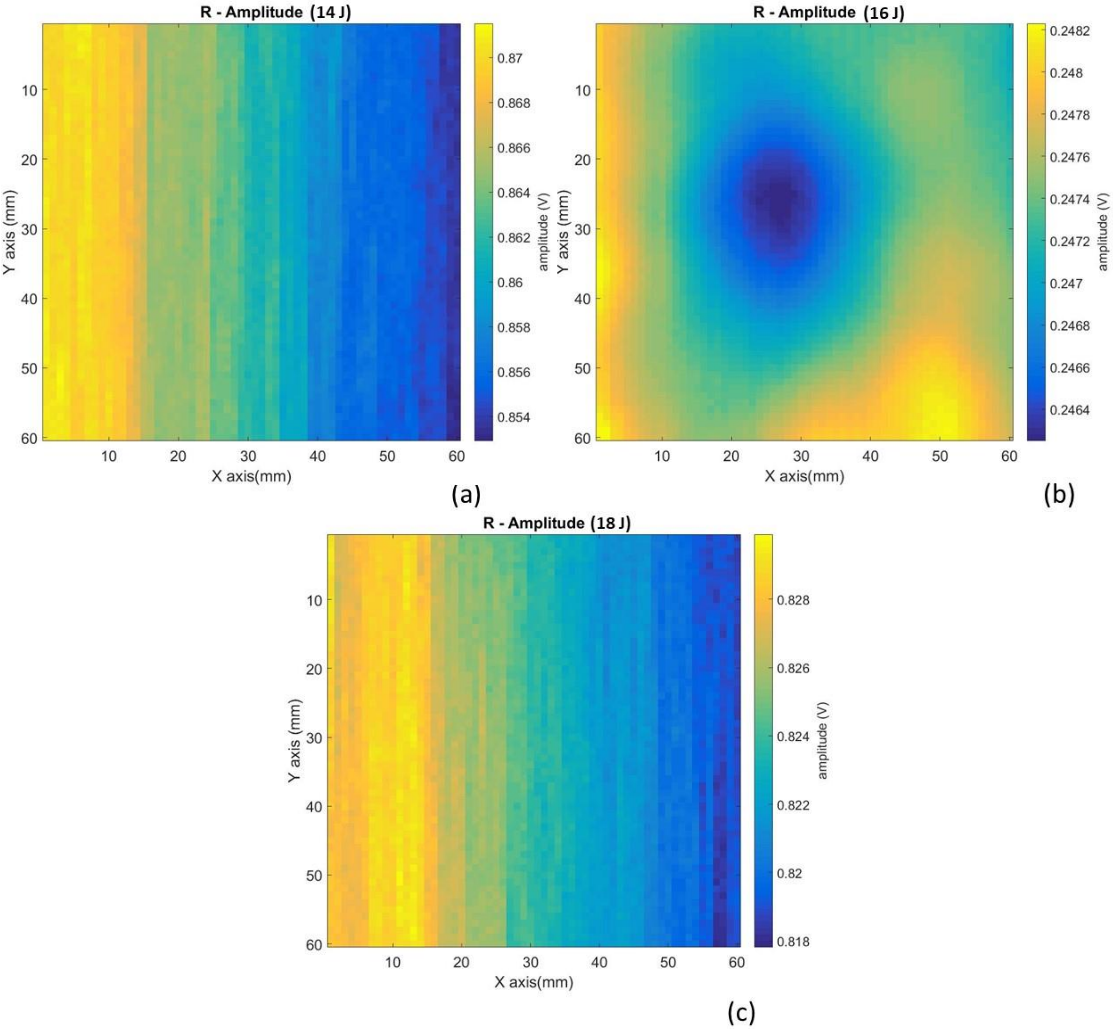

Figure 6.8 Capacitive amplitude-feature images for the GFRP samples (a) 14 J, (b) 16 J, (c) 18 J using the concentric electrodes. The system detects the impact daamge in only one case due to electric field distribution of the probe, and the position, size and geometry of the defect.

It can be seen that the inspections using the concentric electrode probe detect the presence of impact damage in only one of the images in Fig. 6.8(b). This is due to the position, and size, of the defect within the VOI of the probe. As explained in Chapter 5, defects can be better detected if closer to the probe surface where electric field lines are more densely spaced and the inspections were conducted at the face further from the matrix/fibre breakage, shown in figure 6.4.

6.3.2 Data fusion approach

Data fusion is the synergistic combination of information (or data) that results in more accurate and reliable information; this can be obtained, for example, from different measurement sensors, information sources or decision makers [4-6], as figure 6.9 illustrates. The two input images, (I) and (II), showing certain features (A, B and C) can be obtained from two NDE methods or same NDE method but plotting different physical properties (like amplitude and phase). The images are then combined by feeding a proper fusion algorithm in order to produce an image (III) where the detection of those features is improved.

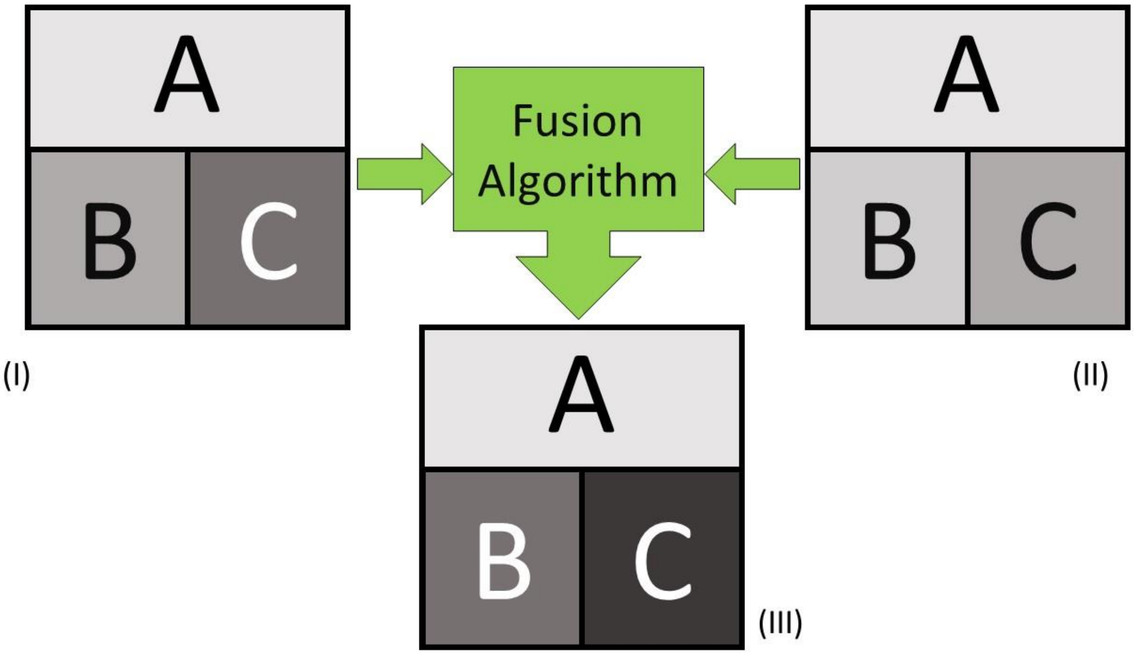

Figure 6.9 Schematic diagram of data fusion approach (after [1]).

Several NDE methods, such as eddy current [7], ultrasound [8], thermography [9] and radiography [10], employ data fusion algorithms in order to reduce uncertainty and thus achieve enhanced detection robustness and accuracy.

Generally, NDE data fusion problems can be categorised into either feature integration and classification or characterization [11]. The former integrates two sets of data into a new data set, achieving more information about the specimen through the fusion at the signal or pixel level. The latter, on the other hand, combines information obtained from sensors which discriminate different features. For instance, two data sets obtained from eddy current measurement, which detects a near-surface defect in conductive materials, and ultrasonic measurements, which yields volumetric information, can be combined in order to generate a unified representation which describes different aspects of the specimen. This could help in identifying the type of defect present [12].

Pixel-level data fusion involves combining images from multiple NDT systems with different physical properties to enhance the raw input images, thereby disclosing complementary or redundant information about the physical and mechanical properties of a specimen [13]. The input images can be combined together by means of addition, subtraction, multiplication, division or a combination of them. Such a form of data fusion is adopted in this work. Although data fusion has been used for several years, the CI technique has never exploited the two sets of data obtained at the output of the lock-in amplifier, which are amplitude (R) and phase (ϕ).

The procedure relies on the fusion of R and ϕ to enhance both defect identification and the selection of a proper threshold for imaging, as well as a more accurate visualization of the features of interest. This is achieved by carried out the following steps:

1. Normalising both R and ϕ matrixes to [0,1] by min-max normalisation.
2. Fusing R_{norm} and ϕ_{norm} in the following two ways:

$$\Delta = \phi_{norm} \times (1 - R_{norm}), \tag{6.29}$$

$$\Xi = \phi_{norm} R_{norm}^{-1}. \tag{6.30}$$

As will be shown below, the data fusion approach can be used for unique feature detection, *e.g.* defect localisation by imaging via Ξ, whilst a better defect evaluation can be achieved by imaging after calculating Δ.

6.3.3 Example application (Perspex)

In order to demonstrate the data fusion method, the same Perspex sample that was described earlier in Section 5.9 was used as benchmark as it contained visible defects whose geometries were known.

Figure 6.10 shows the CI results obtained by imaging R and ϕ with the back-to-back probe. Unlike previous images, the colour mapping has been changed in order to highlight the presence of discontinuities. Figures 6.10 (a-c) are scans of the whole sample, whereas figures 6.10(b-d) show the improved images that were obtained by both limiting the results to areas not close to the sample edges and by choosing a correct thresholding value for the image. As stated in Chapter 5 and noticeable especially in figure 6.10(c), the phase-based images present lower signal to noise values than amplitude-based ones [14,15], resulting in a difficult interpretation and, therefore, worse discrimination of the defects.

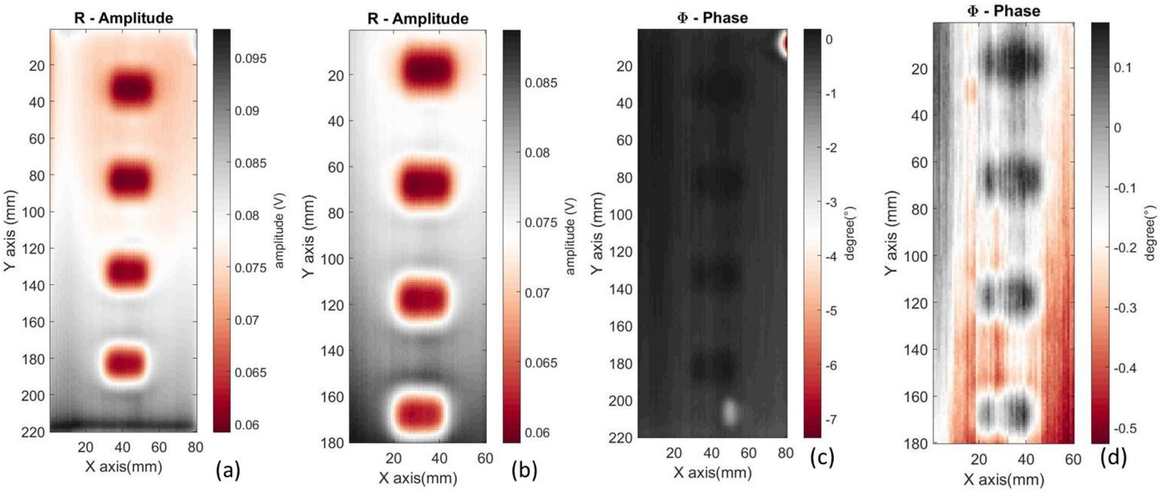

Figure 6.10 Capacitive images for the Perspex sample shown earlier in Fig. 3 using the back-to-back electrodes of Fig. 5(a). (a) Amplitude (R) image; (b) R image for a smaller region away from the sample edges; (c) Phase-based (ϕ) image; (d) ϕ image for a smaller region away from the sample edges.

Even though the careful selection of the scan and thresholding values improves the images, rapid inspections are often highly desirable when evaluating real samples over their whole area, especially in an industrial environment. For this reason, a method like the one proposed, which does not need any selection, is preferable.

As shown in figure 6.11, improvements can be achieved through the proposed data fusion approach by making use of both R and ϕ values. Two series of images are presented. These two sets are obtained by using both of the electrode designs and by imaging the whole sample without any area selection to remove edge effects. It can be noted that the use of the proposed fusion approach can lead to enhanced imaging for both algorithms, Δ (equation 6.1) and Ξ (equation 6.2). The properties of the Ξ variable allow all the Perspex defects to be visualised by both the back-to-back probe and the circular probe.

The R and ϕ images from the back-to-back probe (figure 6.11 (a)) present a higher resolution than that from the concentric probe (figure 6.11 (b)), as expected from the argument above. For both electrode types, it can be seen that the ϕ images have lower signal to noise values than those for R, as already mentioned; however, the data fusion results leading to images based on Ξ and Δ produce improvements over the standard R and ϕ images. In the concentric electrode case, especially, the defects are more easily detected, even though the phase image does not show the defect clearly. The lack of visible phase information for the concentric probe is understandable — in this case the electric field is radial, and the phase information would be an overall result over a 360° angular range. The back-to-back design concentrates the field in one direction only, producing better phase information.

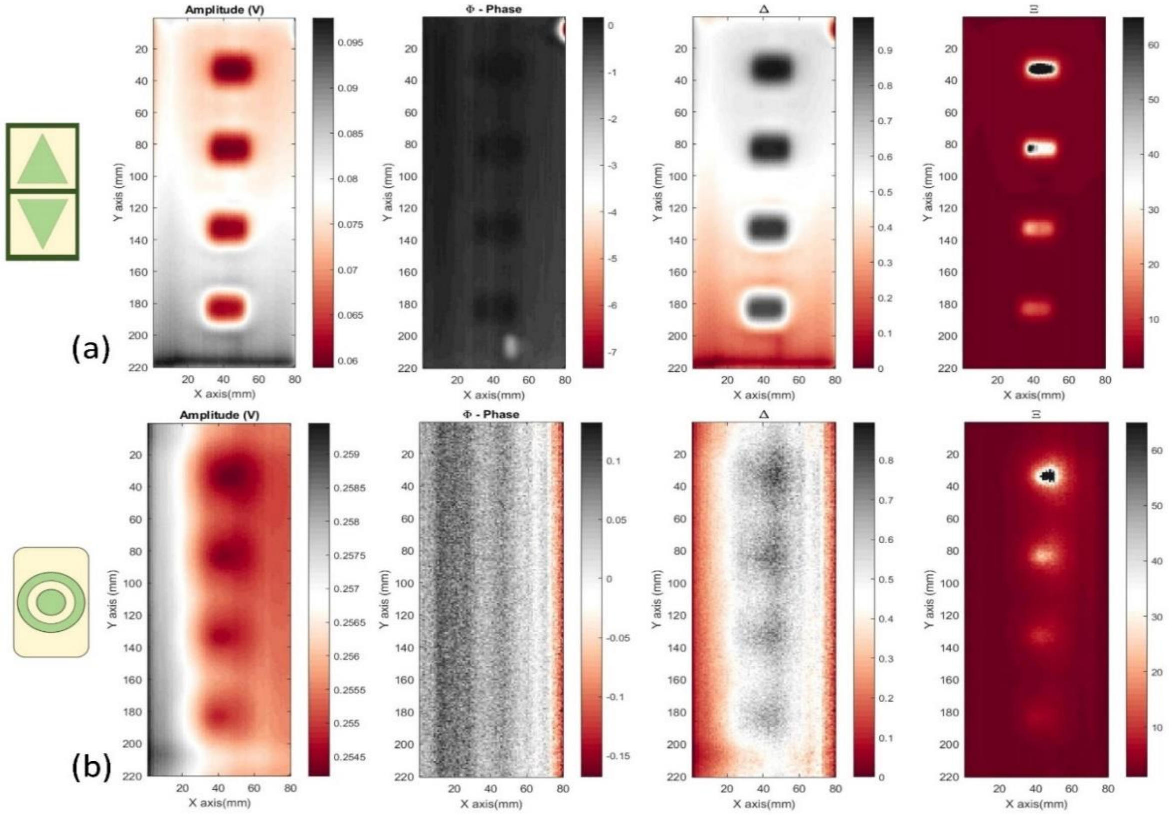

Figure 6.11 Experimental results for scans on the Perspex sample using (a) the back-to back probe, and (b) the concentric design.

In order to demonstrate the contribution of Δ to the defect characterization, the normalized values of R and Δ along the same line of pixels crossing all the defects are taken for comparison in figure 6.12(a). At first glance, both the trends are very similar. As the Perspex defects have a depth values increasing linearly, from the deepest one (Number 1), 16 mm, to the shallowest one (Number 4), 4 mm, obtaining a feature showing a linear relation with those defects in order to illustrate the effectiveness of the imaging procedure. In figure 6.12(b) the comparison between the normalized amplitude peak values for both R and Δ at the location of maximum sensitivity to a given defect is shown. The linear fits and their root mean square errors (RMSE) values, quoted in the figure, demonstrate that Δ is better than the standard R-based estimation, for which a higher order polynomial fitting would be more accurate. This means that the phase information is perhaps more beneficial for inferring defects features such as depths. Finally, it can be noted that the images obtained with the concentric electrodes show poor SNR values — this is due to the electrodes dimension which are bigger than that of the defect.

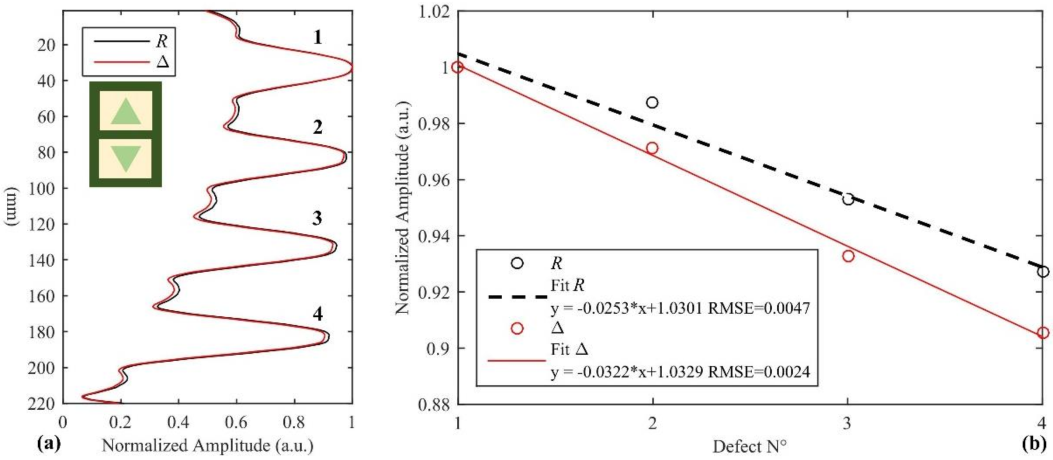

Figure 6.12 (a) Normalized amplitude of R and Δ along a line crossing the centre of the defects (b) maximum values of R and Δ for each defect to demonstrate linearity.

6.4 GFRP results

Figure 6.13 shows CI results for both R (already shown in figure 6.6, with a different colour mapping) and ϕ for the three GFRP samples. These were taken with the back-to-back probe design.

The result of fusing data to obtain Δ and Ξ for the damaged area is shown in figure 6.14, where now the defects are more clearly visible in both sets of images. It can be seen that the Δ and Ξ images gave a better estimate of the defect size and much better idea of the location of the defect than was available from the raw amplitude (R) and phase (ϕ) data before the fusion process.

Figure 6.15 shows the results obtained using the concentric probe design on the 16 J GFRP impact-damaged sample, as the inspections on the other two samples did not detect the presence of discontinuities. Again, the poor SNR achieved with the phase (ϕ) image was due to the dimensions and radial geometry of the probe, although this became somewhat more visible in the Δ image after data fusion. However, the Ξ image, as in the previous cases described here, demonstrated a very good retrieval of the image location. This is interesting, as it would allow the larger concentric probe to be used for rapid scanning of large objects without having to consider alignment of the probe geometry (as would be needed for the back-to-back design). More detailed scanning via the back-to-back probe could then get a better idea of its lateral dimensions.

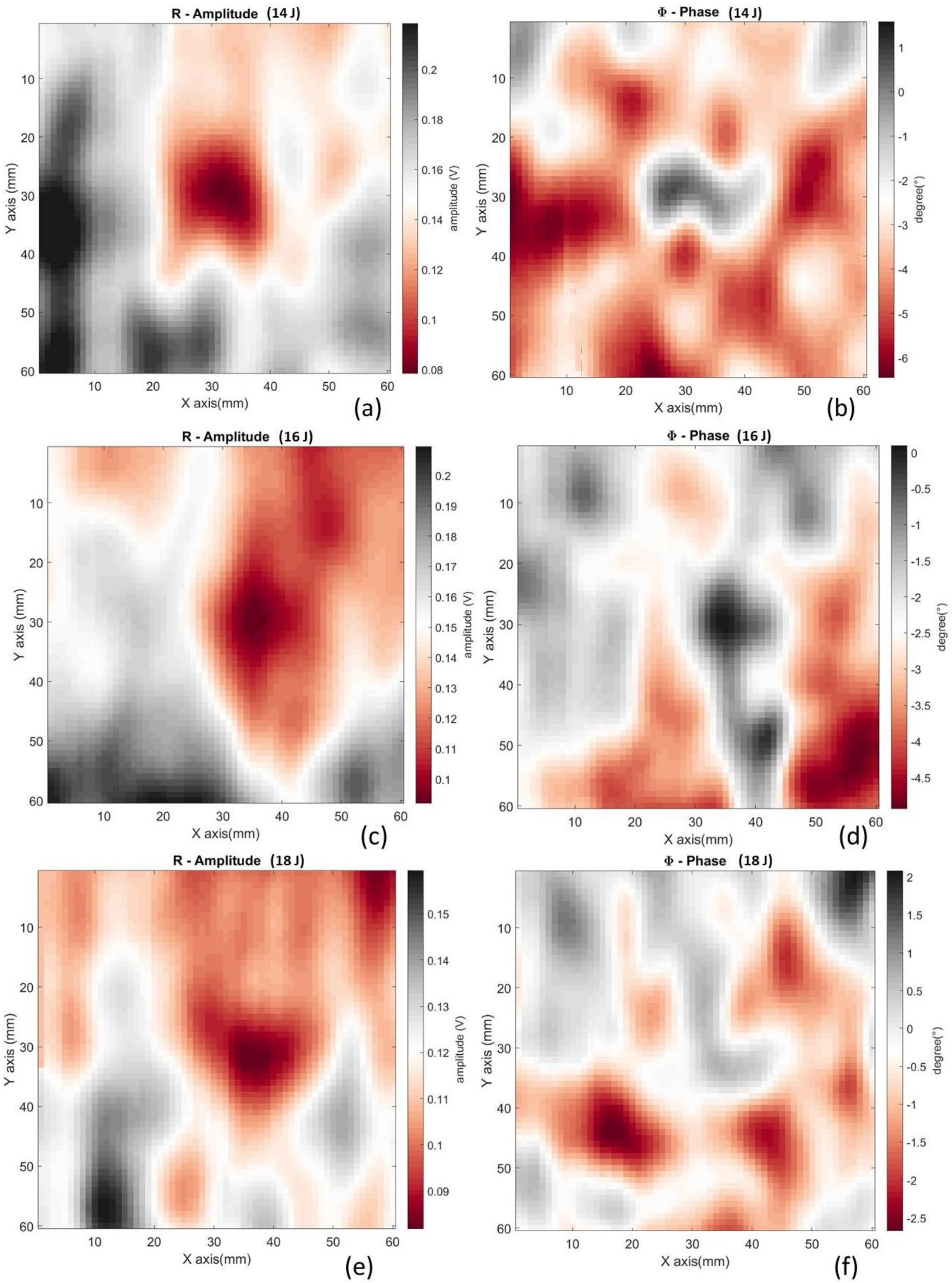

Figure 6.13 Experimental scan results for GFRP samples with impact damage caused by impact energies of (a-b) 14 J, (c-d) 16 J, (e-f)18 J. The images (a), (c) and (e) are amplitude-based. The images (b), (d) and (f) are phase-based.

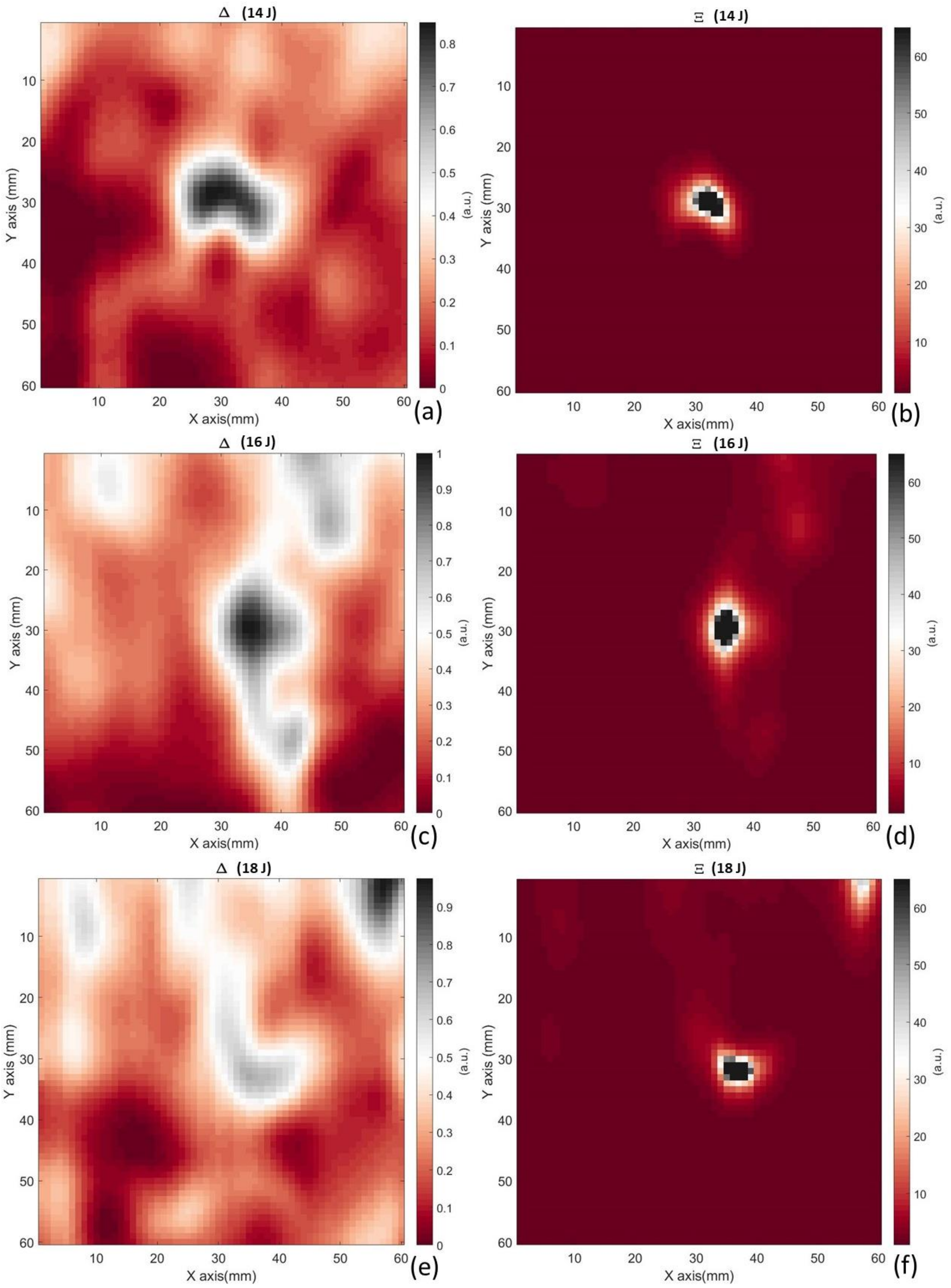

Figure 6.14 Experimental scan results for Δ and Ξ for the three samples with impact damage caused by impact energies of (a-b) 14 J, (c-d) 16 J and (e-f) 18 J.

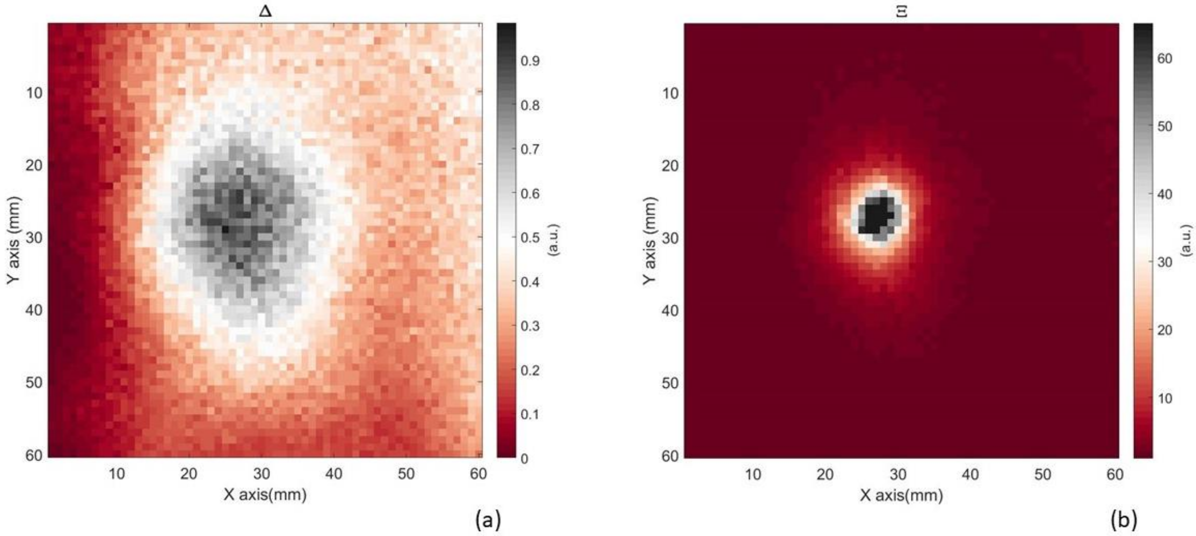

Figure 6.15 Experimental scan results with concentric probe for Δ and Ξ for the sample with impact damage caused by impact energy of 16 J.

6.5 Comparison with an air-coupled ultrasonic measurement

In this section, images produced from air-coupled ultrasonic (ACU) testing are compared to those obtained from CI. These measurements were taken in collaboration with Jaishree Vyas, who was a visitor from Kaunas University of Technology, as part of the NDTonAIR EU program. The results were presented in the QNDE2019 conference [16]. My contribution was to help to collect experimental data using the air-coupled ultrasonic system already available at the University of Warwick and, consequently, to produce the images. The laboratory set-up of ACU system is illustrated in figure 6.14 where a pair of capacitive ultrasonic transducers was used in a through-transmission configuration.

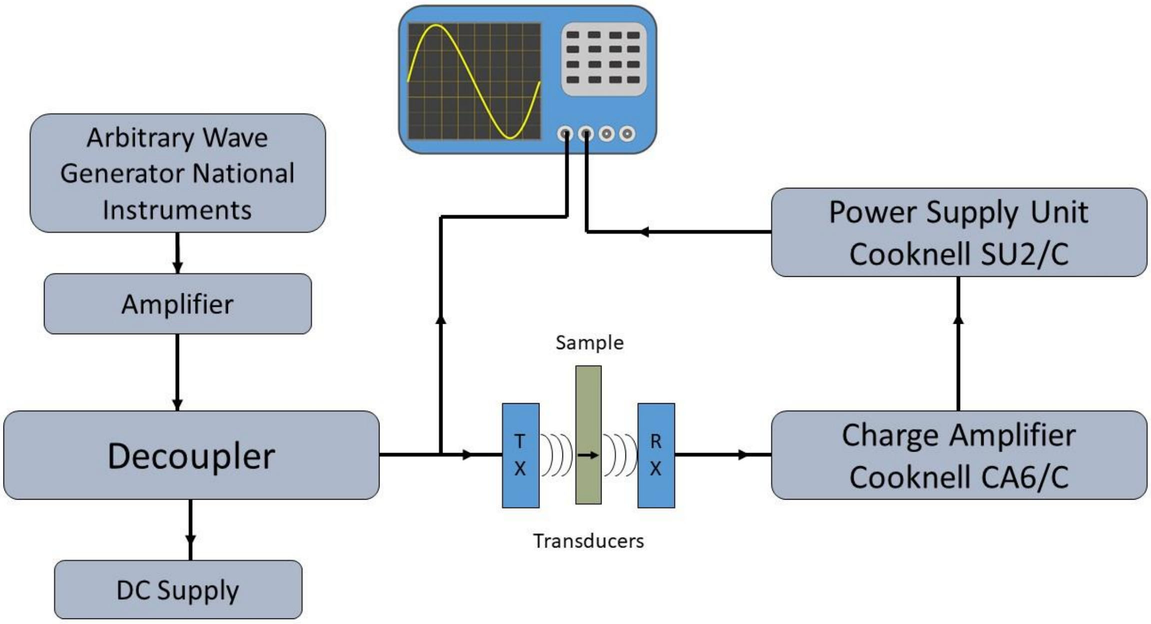

Figure 6.16 Schematic diagram of the laboratory set-up of the ACU sytem.

In order to overcome the low SNR in air-coupled measurements the pulse-compression approach was used [17]. To achieve this, the source was connected to an arbitrary wave generator within a National Instruments PXI system, which fed the source via a power amplifier and a DC de-coupler. The air-coupled ultrasonic detector was connected to the Cooknell CA6/C, which provides both DC bias to apply to the transducer and a charge amplifier, and to the Cooknell SU2/C, which is a power supply providing DC bias voltages, for detecting the changes in charge induced by the movement of the membrane, when acting as a detector. The output from the charge amplifier was then fed into a digital oscilloscope within the PXI system for recording and cross-correlation. The driving signal was a chirp waveform centred at a frequency of 450 kHz. The transducers were scanned over an area of 60 x 60 mm with data being acquired at 1 mm intervals, same as capacitive imaging. A comparison of the resulting air-coupled images with CI data for the same samples is shown in figure 6.15, 6.16 and 6.17. It can be seen that the Δ and Ξ images indicate that the defects were smaller than they appear in the ACU images. This is due to the larger 10 mm diameter of the air-coupled ultrasonic transducers, resulting in an image where the defect is visible over a larger area. It can be seen that the CI images are in the same location, indicating that both methods have correctly identified the defect location, with the CI method perhaps giving a better indication of the defect size from the Δ image.

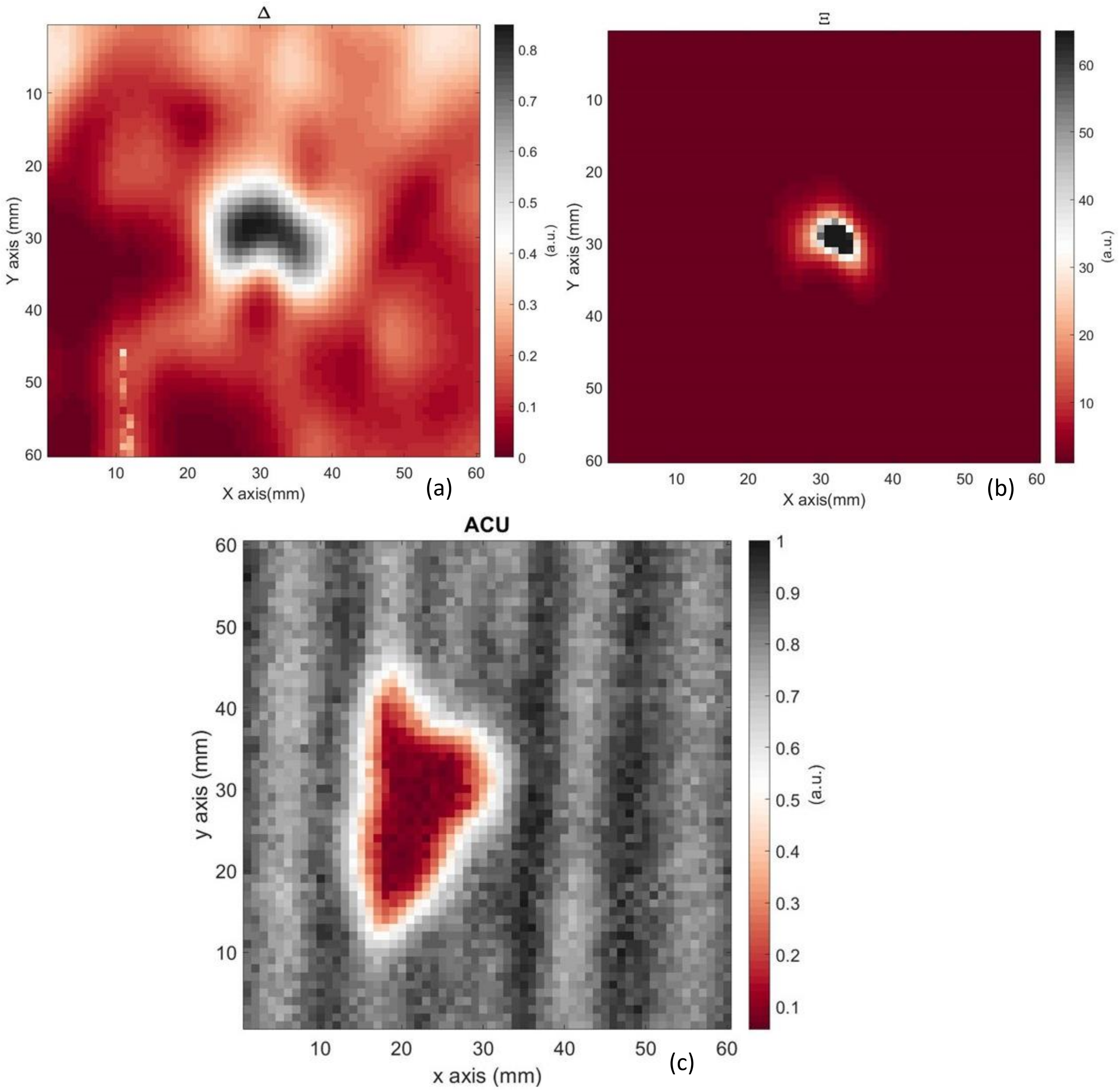

Figure 6.17 Comparison between (a)-(b) CI and (c) ACU scan results for the sample with impact damage caused by impact energy of 14 J.

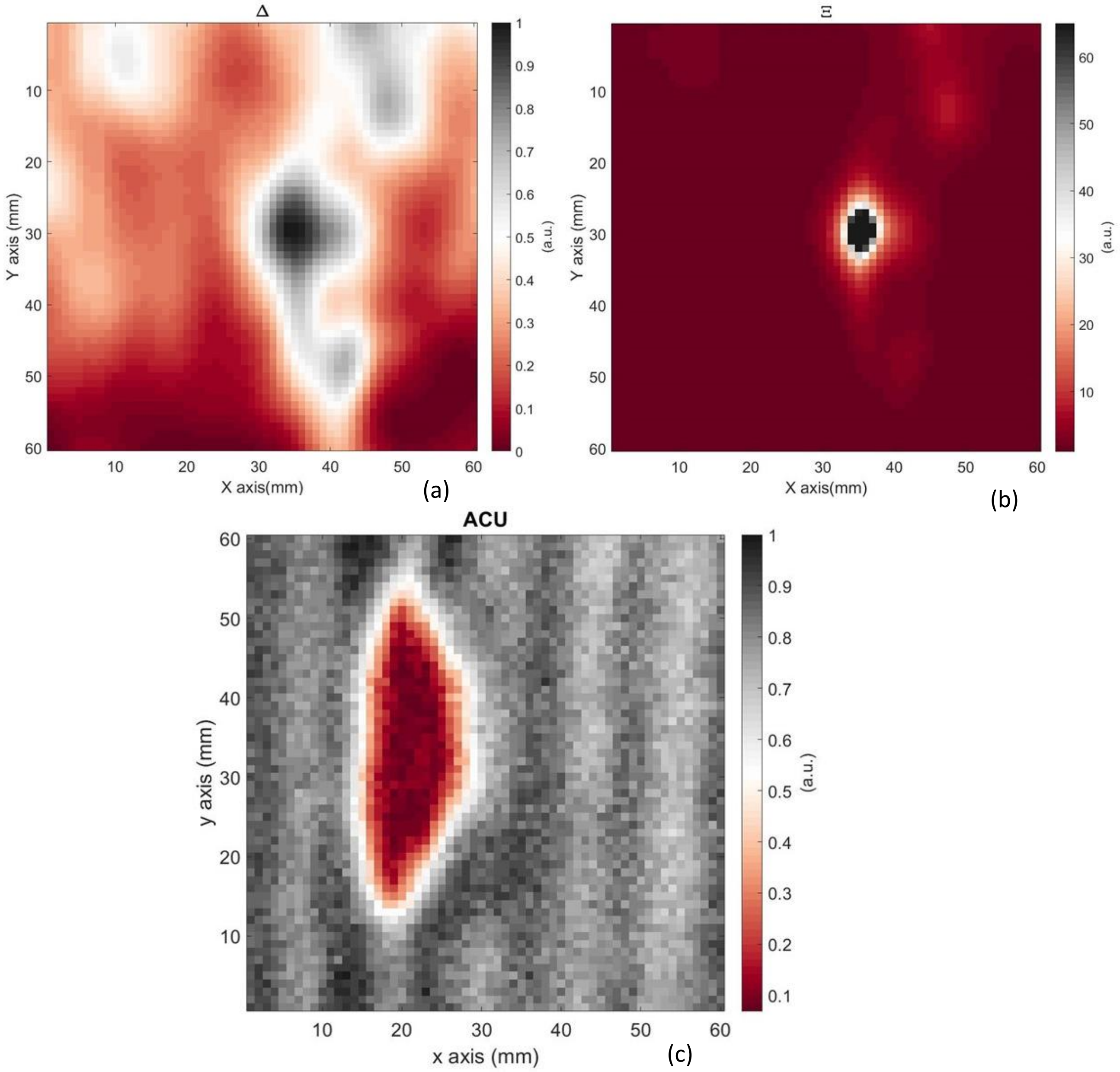

Figure 6.18 Comparison between (a)-(b) CI and (c) ACU scan results for the sample with impact damage caused by impact energy of 16 J.

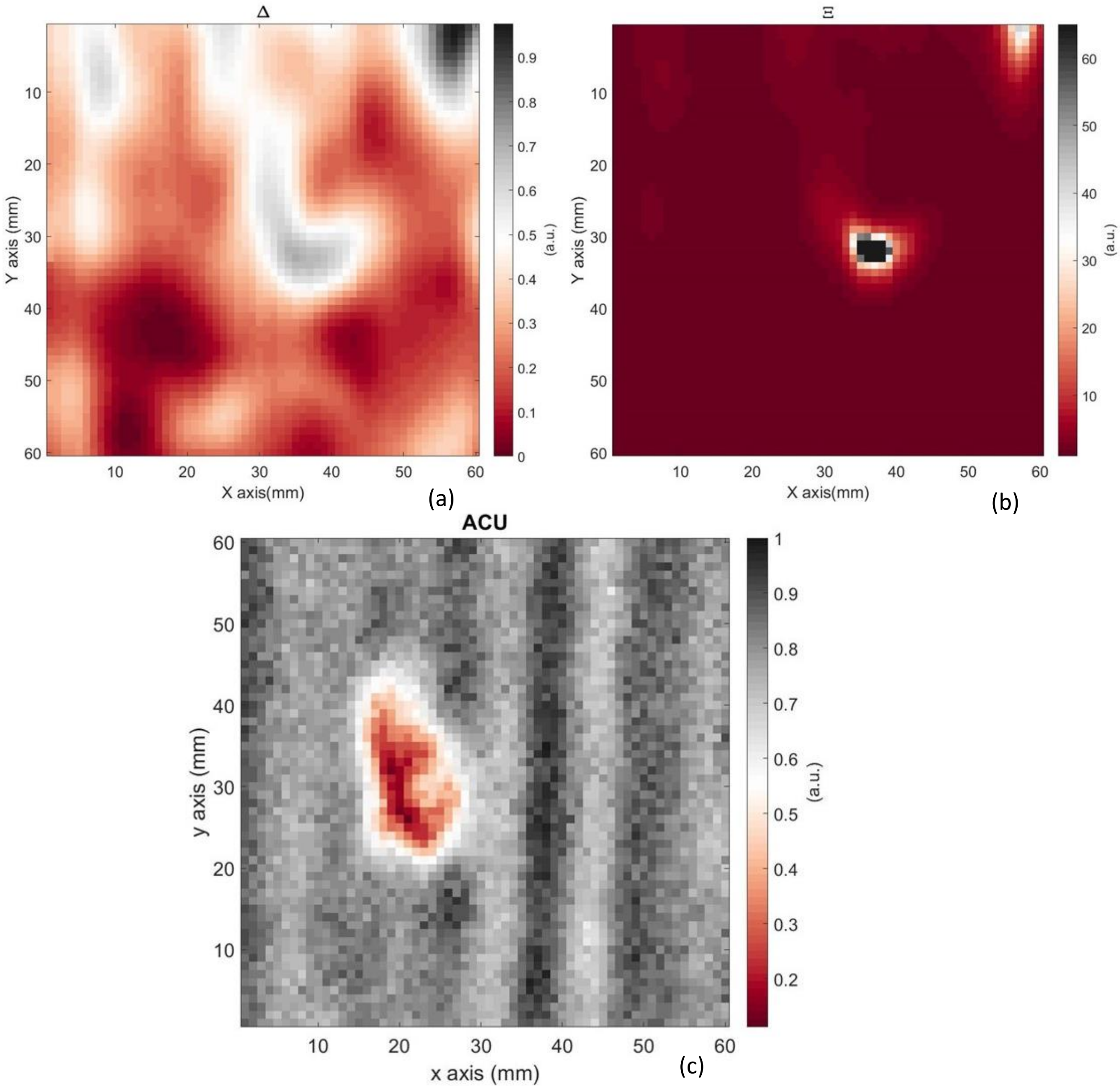

Figure 6.19 Comparison between (a)-(b) CI and (c) ACU scan results for the sample with impact damage caused by impact energy of 18 J.

6.6 Conclusions

In this chapter, the CI technique has been tested on GFRP samples. The inspections were conducted using two probe designs: symmetrical and concentric. The samples investigated contained impact damage, a type of defect that can lead to potential failures if not detected. In the first instance, conventional images resulting from the lock-in output amplitude (which tends to be used over phase information) were displayed, as the phase-based images show a high noise level. A data fusion method was then introduced. The present method is based on amplitude and phase fusion in order to mitigate events such as edge effects, lift variations and geometric complexities, which can affect the resulting images by hiding features of interest. Preliminary tests to demonstrate and optimise image processing were conducted on a sample of Perspex with flat-bottomed holes. The results showed that the fusion of amplitude and phase information provides both a unique localisation of defects and a better assessment of them. The data fusion approach was then used successfully to image GFRP samples containing impact damage. This indicated that two metrics (Δ and Ξ) could lead to better estimation of defect size and location respectively. In conclusion, the results on GFRP samples were compared with images obtained from a pulse-compression air coupled ultrasonic measurement, illustrating the robust nature of the imaging approach in terms of successfully identifying barely-visible impact damage in CFRP plates.

References Chapter 6

[1] H. Mei, R. James, and V. Giurgiutiu, "Damage detection in laminated composites using pure SH guided wave excited by angle beam transducer," 2020, no. April, p. 28.

[2] S. A. Hitchen and R. M. J. Kemp, "The effect of stacking sequence on impact damage in a carbon fibre/epoxy composite," *Composites*, vol. 26, no. 3, pp. 207–214, 1995.

[3] M. Thor, M. G. R. Sause, and R. M. Hinterhölzl, "Mechanisms of Origin and Classification of Out-of-Plane Fiber Waviness in Composite Materials—A Review," *J. Compos. Sci.*, vol. 4, no. 3, p. 130, 2020.

[4] X. E. Gros, J. Bousigue, and K. Takahashi, "NDT data fusion at pixel level," *NDT E Int.*, vol. 32, no. 5, pp. 283–292, 1999.

[5] J. Esteban, A. Starr, R. Willetts, P. Hannah, and P. Bryanston-Cross, "A review of data fusion models and architectures: Towards engineering guidelines," *Neural Comput. Appl.*, vol. 14, no. 4, pp. 273–281, 2005.

[6] O. Sidek and S. A. Quadri, "A review of data fusion models and systems," *Int. J. Image Data Fusion*, vol. 3, no. 1, pp. 3–21, 2012.

[7] M. Mina, S. S. Udpa, L. Udpa, and J. Yim, "A New Approach For Practical Two Dimensional Data Fusion utilizing a single eddy current probe," *Rev. Prog. Quant. Nondestruct. Eval.*, vol. 16, pp. 749–755, 1997.

[8] A. Salazar, J. Gosalbez, G. Safont, and L. Vergara, "Data fusion of ultrasound and GPR signals for analysis of historic walls," *IOP Conf. Ser. Mater. Sci. Eng.*, vol. 42, no. 1, pp. 3–7, 2012.

[9] M. Streza, B. Belean, I. Hodisan, and C. Prejmerean, "Improving lock-in thermography detection of microgaps located at the tooth-filling interface using a phase versus amplitude image signal extraction approach," *Meas. J. Int. Meas. Confed.*, vol. 104, pp. 21–28, 2017.

[10] A. Mohammad-Djafari, “Fusion of X-ray and geometrical data in computed tomography for nondestructive testing applications,” *Proc. 5th Int. Conf. Inf. Fusion, FUSION 2002*, vol. 1, no. February 2002, pp. 309–316, 2002.

[11] Z. Liu, D. S. Forsyth, J. P. Komorowski, K. Hanasaki, and T. Kirubarajan, “Survey: State of the art in NDE data fusion techniques,” *IEEE Trans. Instrum. Meas.*, vol. 56, no. 6, pp. 2435–2451, 2007.

[12] R. Heideklang and P. Shokouhi, “Application of data fusion in nondestructive testing (NDT),” *Proc. 16th Int. Conf. Inf. Fusion, FUSION 2013*, pp. 835–841, 2013.

[13] X. E. Gros, Ed., *Applications of NDT Data Fusion*. Kluwer Academic Publishers, 2001.

[14] Z. Liu and H. Liu, “Experimenting capacitive sensing technique for structural integrity assessment,” *Proc. IEEE Int. Conf. Ind. Technol.*, vol. 2, no. 1, pp. 922–927, 2017.

[15] X. Yin, D. A. Hutchins, G. Chen, W. Li, and Z. Xu, “Studies of the factors influencing the imaging performance of the capacitive imaging technique,” *NDT E Int.*, vol. 60, pp. 1–10, 2013.

[16] J. Vyas, E. Jasiuniene, R. Kažys, S. Amato, S. Dixon, and D. A. Hutchins, “The NDE of pultruded GRP composites using air-coupled ultrasound and EMAT-based guided wave inspection,” *Rev. Prog. Quant. Nondestruct. Eval.*, vol. 0, no. 0, pp. 1–3, 2019.

[17] D.A. Hutchins, P. Burrascano, L. Davis, S. Laureti, and M. Ricci, “Coded waveforms for optimised air-coupled ultrasonic nondestructive evaluation,” *Ultrasonics*, vol. 54, no. 7, pp. 1745–1759, 2014.

Chapter 7

Imaging of defects in composites

7.1 Introduction

The basic operation principles of EMATs, the analytical models and their applications to composite materials were explained in Chapters 2-4. This chapter aims to demonstrate the detectability of defects in composite samples with SH_0 guided waves generated by PPM EMATs. Furthermore, images will be generated by a Synthetic Aperture Focusing Technique (SAFT) algorithm, for better characterisation of defects. Firstly, the composite specimens investigated will be introduced as well as the defects within them. The SAFT algorithm and the Phase Shift Migration (PSM) method will be explained. The experimental set-up for taking the measurements and the relative results will be presented, and results for GFRP samples will be compared with those obtained with CI presented earlier in Chapter 6, demonstrating how guided waves and CI could be combined to make a dual mode NDE strategy for composites.

7.2 Samples and defects

The samples inspected are CFRP and GFRP composites, described in Chapter 4. In this Chapter, however, the samples have various internal defects including impact damage, a lightning strike and a delamination. The GFRP plates investigated here were the same as those already introduced in Section 6.3. All CFRP samples were 3 mm quasi-isotropic plates having a stacking sequence as illustrated in figure 4.37, and with the stiffness matrix shown in table 7.1.

Table 7. 1 Stiffness matrix for the quasi-isotropic CFRP plate with the copper mesh.

50.08 (GPa)	15.97	15.97	0	0	0
15.97	49.26	15.775	0	0	0
15.97	15.97	49.26	0	0	0
0	0	0	16.74	0	0
0	0	0	0	11.53	0
0	0	0	0	0	11.53

Different types of defects within CFRP plates were tested, as described below.

7.2.1 Impact damage

The 3 mm quasi-isotropic CFRP plate, whose dimensions were 350 x 160 mm, was damaged by a hemispherical head impactor mounted on a horizontal sleigh, as shown in figure 7.1.

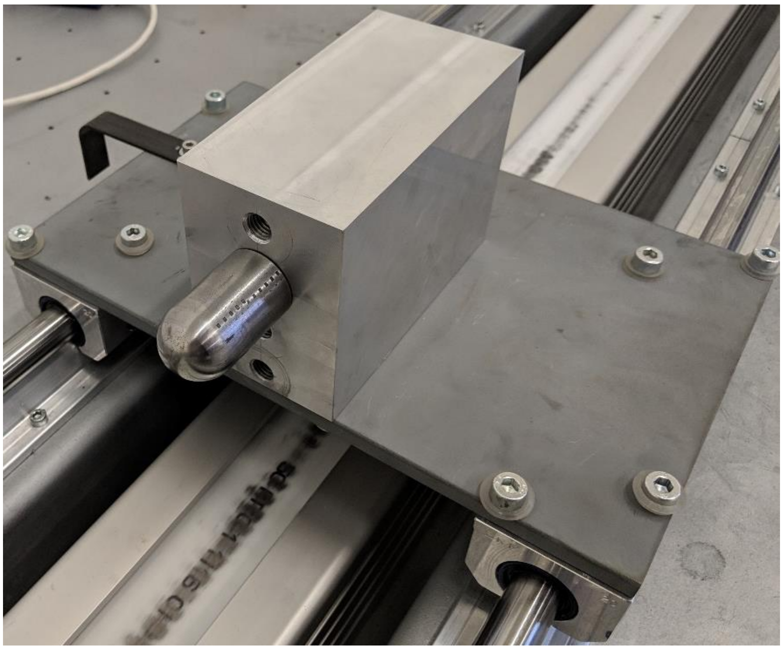

Figure 7.1 Photo of the sleigh and the hemispherical head of the impactor.

The impact was designed to replicate the damage caused by an object (such as a 0.8 kg hammer) dropped from approximately waist height (1.20 m) of an average worker on an aircraft wing. The impact energy, calculated by using the gravitational potential energy ($U = mgh$), was 10 J. The settings of the sleigh, velocity and acceleration, were established by converting the potential energy into kinetic energy. The speed of the sleigh was 1.5 m/s, while the acceleration 10 N/s^2 (approximately the gravitational acceleration). Figure 7.2 shows the two sides of the plate after impact, and is an examples of Barely Visible Impact Damage (BVID) [1]. Indeed, the surface where the impact took place, figure 7.2(a), does not show signs of impact, whereas, on the opposite side, figure 7.2(b), a cross-shaped mark where the matrix and fibre failed after impact can be seen.

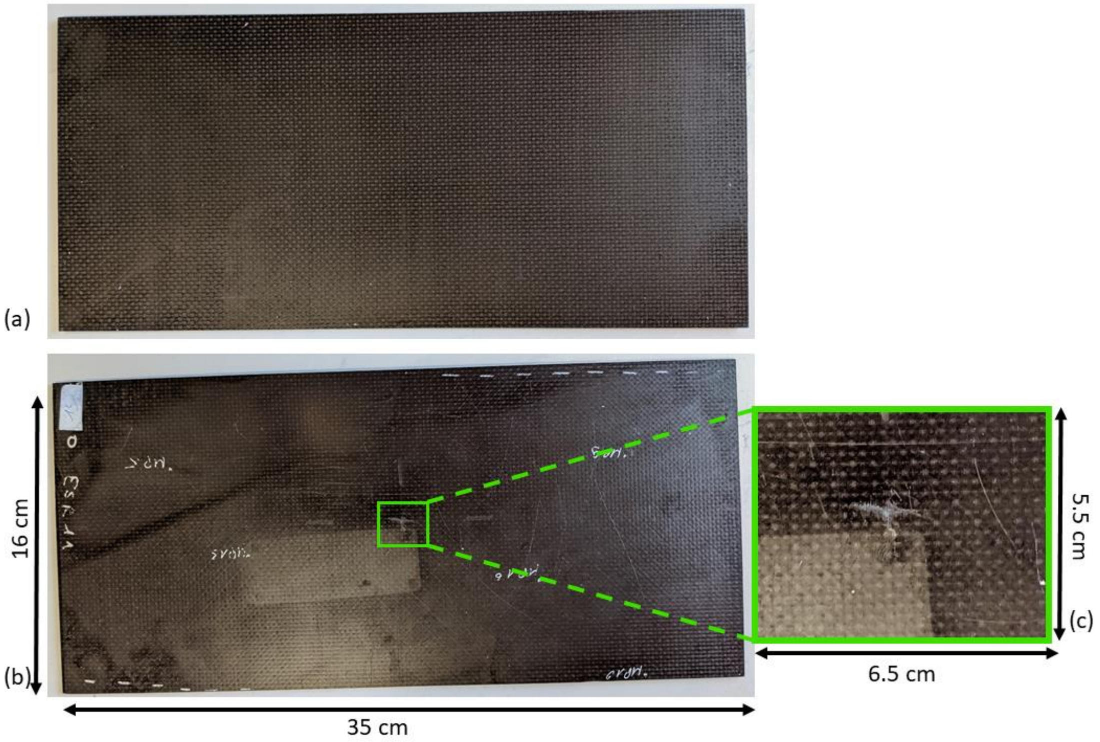

Figure 7.2 Photo of a quasi-isotropic CFRP plate after being damage. (a) Impact side, (b) damage side, (c) detail of the damage.

The defect was inspected with a commercial phase array system revealing the extension of the damage and its dimensions. Figure 7.3 shows the image produced from the evaluation.

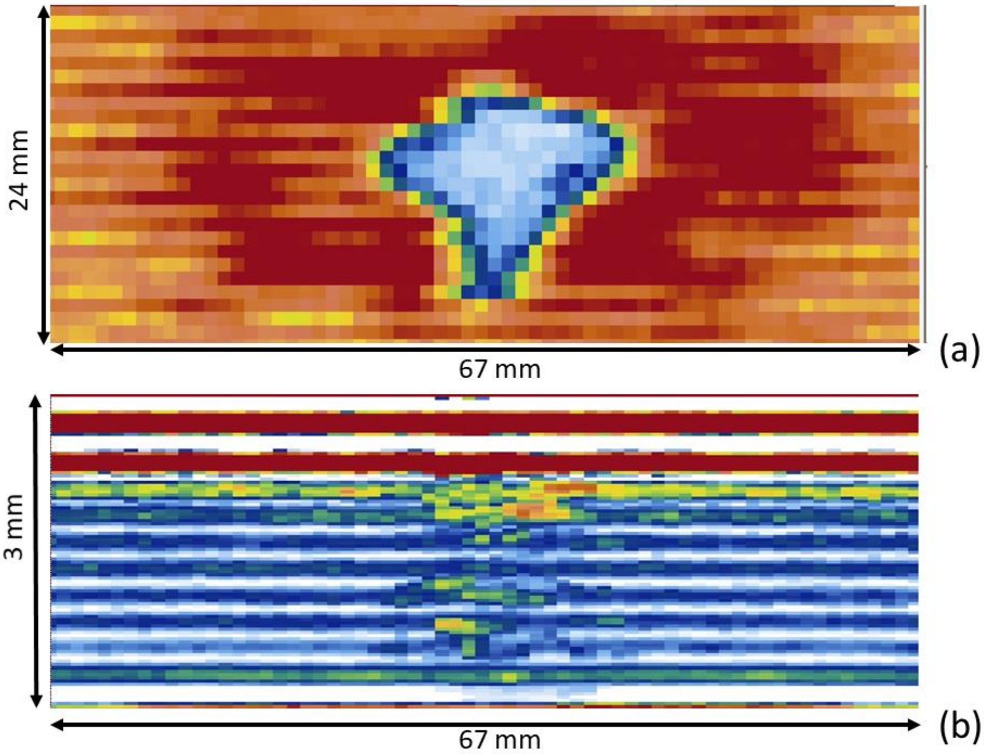

Figure 7.3 Image of the impact-damaged CFRP plate produced from a phase array commercial system. (a) Front view, (b) through thickness.

7.2.2 Delamination defect

Delamination is a critical failure appearing as a separation of adjacent layers in composite laminates. This kind of defect can be due to several reasons occurring during both the manufacturing process and in service. In the former case, delaminations can occur due to improper laying of laminae, air pockets and inclusions, and errors while curing. In the latter case, on the other hand, interlaminar stresses (e.g. caused by impact) in combination with the commonly low through-thickness strength can caused such a defect [2].

This CFRP plate, whose dimensions are 350 x 480 mm, contained 6 artificial delaminations. These were arranged in pairs at three different depths during the hand-built lay-up. Each defect was in the form of 100 nm thick PTFE (Teflon) tape and plastic film which covers the wet side of the prepreg, thinner than the Teflon tape. The artificial delaminations were placed at the following positions within the thickness of each plate:

(1) Between second and third plies, starting from the top surface;
(2) Mid-thickness;
(3) Between second and third plies, starting from the bottom surface.

The pairs placed at positions (1) and (2) were 25 x 25 mm in size, whereas the pair located at position (3) was 10 x 10 mm. Figure 7.4 shows the delaminations at position (1) during the hand lay-up process.

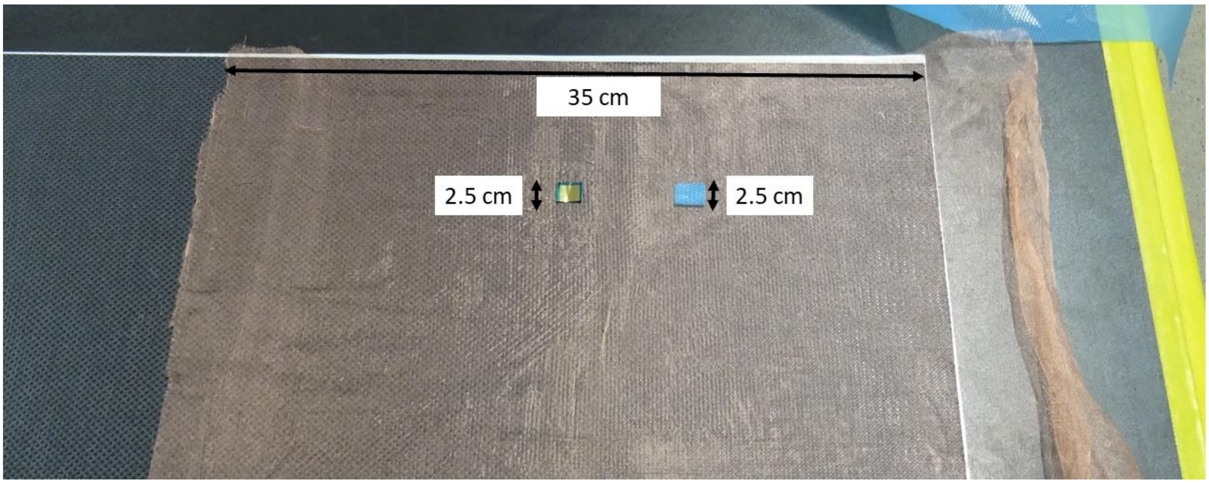

Figure 7.4 Photo of on pair of the artificial delaminations placed during the hand lay-up.

This sample was also inspected with an ultrasonic commercial system, and figure 7.5 shows the result.

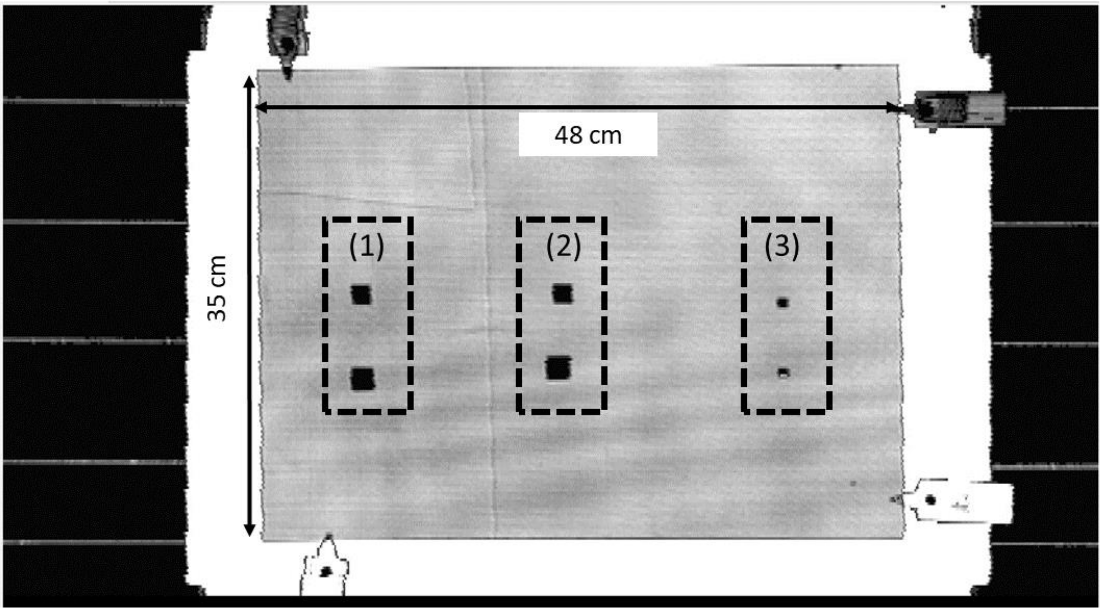

Figure 7.5 Image produced from a standard ultrasonic system depicting the 3 pairs of delamination within a 3mm quasi-isotropic CFRP plate.

7.2.3 Sample affected by a lightning strike

Lightning strike damage can occur after an aircraft is struck by lightning while in service. Several factors affect the frequency of such events, such as geographic area and how often the airplane passes through take-off and landing altitudes [3].

Modern radar systems have reduced the chances of encountering lightning strikes by detecting, in advance, dangerous areas where the odds are higher. Nonetheless, the aviation industry has developed methods for coping with this issue by introducing several lightning protection measures for composite materials. Composite components are not as electrically or as thermally conductive as metals, so lightning strikes can seriously degrade the integrity of the structure. The lightning protection adopted for the sample investigated is “metallic expanded foils” [4]. This consist of inserting a copper mesh within the laminate structure, close to the outer surface. The metallic layer dissipates the high current, shielding the structure below [5].

The sample’s dimensions were 355 x 160 x 3 mm. The damage was induced by an artificial “lightning” strike created in the lab, whose current and voltage were, 100 kA and 100 kV respectively. Figure 7.6 shows the sample before and after the experiment. In figure 7.6(b), it can be seen two heat-affected areas, the attachment and the exit point. The former, figure 7.6(c), is where the “lightning” made contact to the surface, while the latter, figure 7.6(d), is where it exited the sample after spreading across the metallic layer.

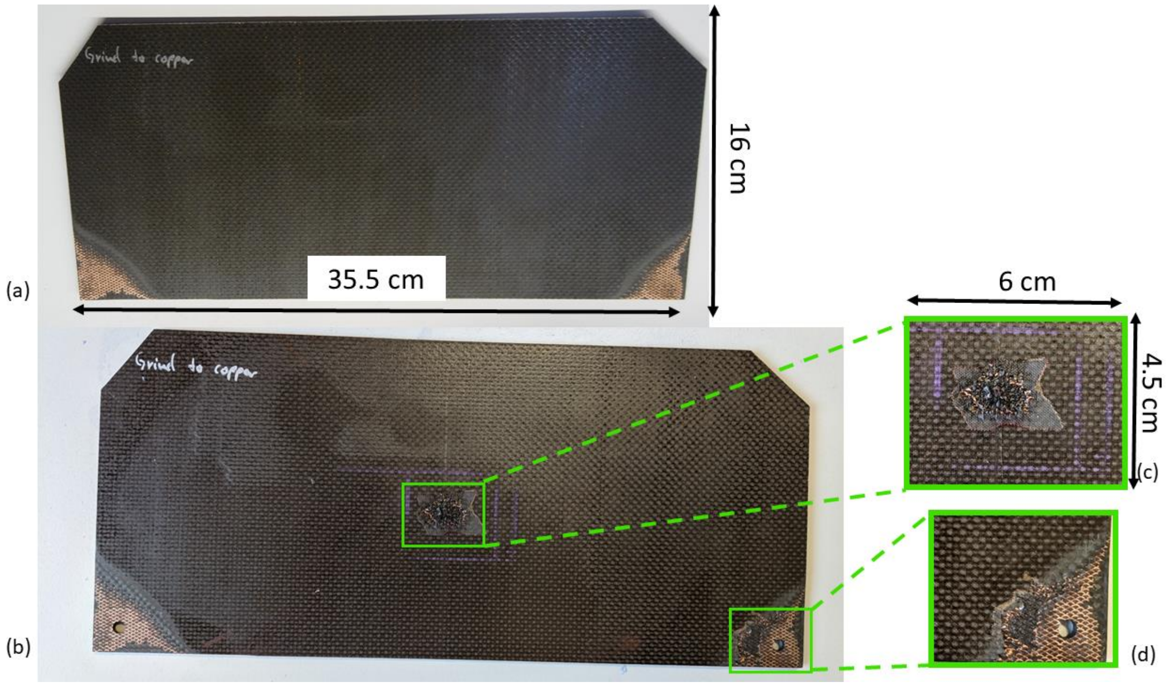

Figure 7.6 Photo of a quasi-isotropic CFRP plate (a) before and (b) after a "lightning" strike. (c) Attachment point and (d) exit point.

7.3 Methods used for ultrasonic imaging

Multiple ultrasonic acquisitions, typically taken along straight lines, can be presented typically as an ultrasonic B-scan. The resulting image which can be displayed in several ways, such as the amplitude of the raw data, the envelope of the waveform, on a logarithmic scale etc. Such images identify any reflector or scatterer, due to the different time of travel of the wave [6]. Furthermore, the ultrasonic beam tends to diverge, causing a decrease of the lateral resolution as the range of inspection increases [7].

A technique which significantly enhances the lateral resolution by focusing the acoustic field in post-processing is the Synthetic Aperture Focusing Technique (SAFT). There exist several SAFT algorithms which can be performed in both time and frequency domain [8]. The algorithm adopted for this case work performs in the frequency domain and is called the Phase Shift Migration (PSM) method.

7.3.1 The phase shift migration (PSM) method

The PSM method is a frequency domain approach developed in seismology for dealing with the scenario of horizontal homogenous layers [9,10]. The approach is based on the "exploding reflector model" [11,12]. The model assumes that all targets (reflectors and scatterers) "explode" at the time t=0 and the resultant field propagates at half of the wave propagation velocity toward the receiver. The algorithm is thus explained considering an object consisting of one homogenous layer.

The arrangement of a standard ultrasonic measurement with separate transmitter (TX) and receiver (RX) is shown in figure 7.7.

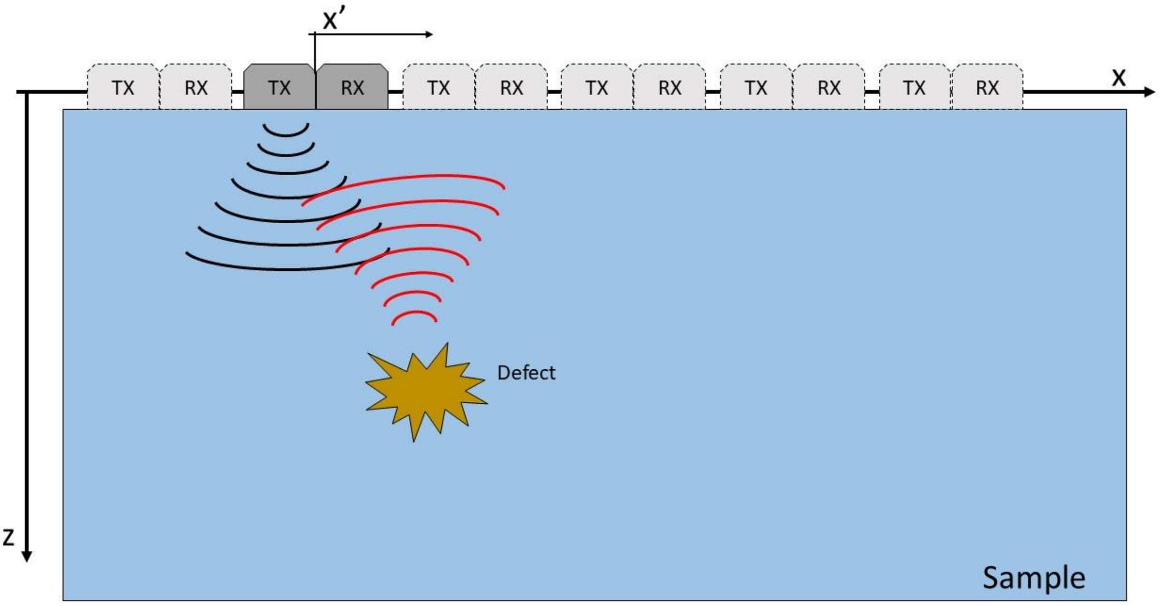

Figure 7.7 Schematic diagram of a standard ultrasonic measurement for a bulk material.

A typical pitch-catch measurement using longitudinal waves consists of a pair of transducers that are moved along the x-axis to known positions and the transmitted and reflected waves are in the $x - z$ plane. The resultant wave field observed at $z = 0$ can be expressed as $p(t, x, Z)$, where t is the time, x the horizontal position and Z is the z coordinate at 0. The wave field is then Fourier transformed and in the frequency domain is extrapolated to other depths, every Δz (i.e. $z - Z$), iteratively multiplying by the phase shift factor ($e^{ik_z(z-Z)}$). The extrapolation of wave field in the Fourier domain is based on the assumption that all scatterers are located in the half-space $z > Z$ [8]. The following step is the application of the so-called “imaging condition” to the extrapolated wave field. This condition evaluates the wave field at $t = 0$. Finally, the data is inverse Fourier transformed yielding the focused image. The flowchart of the algorithm is illustrated in figure 7.8.

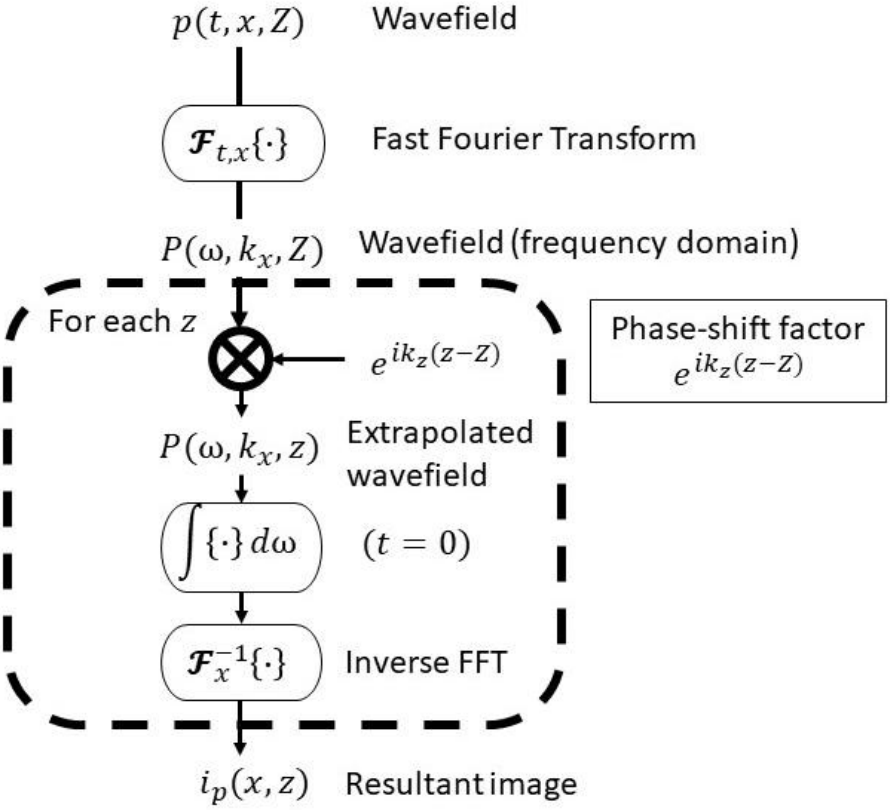

Figure 7. 8 Flow chart of the PSM algortihm (after [8]).

In the present work guided waves are used. Thus, the PSM algorithm is simply adjusted by "rotating" the system. The wave propagation now occurs in the x-y plane instead of x-z, as shown in figure 7.9.

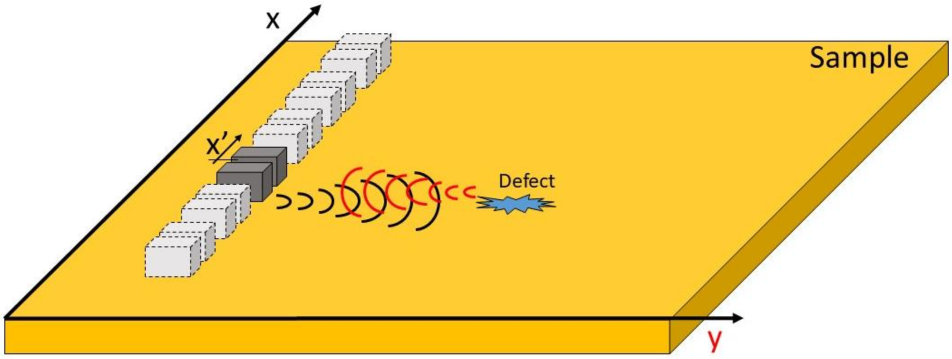

Figure 7. 9 Schematic diagram of guided wave inspections in plate-like structures.

7.4 Example measurement – CFRP Impact Damage

The laboratory set-up was as described in section 4.3 and illustrated in figure 4.3(b). The experiment consisted of inspecting the quasi-isotropic CFRP plate, described in section 7.2.1, by moving a pair of PPM EMATs fixed at 8 cm apart, along a given scan line, as depicted in figure 7.10. Note that there was no significant anisotropy in this quasi-isotropic plate (see figure 4.38). The two transducers had a nominal wavelength of 10 mm as defined by their geometry.

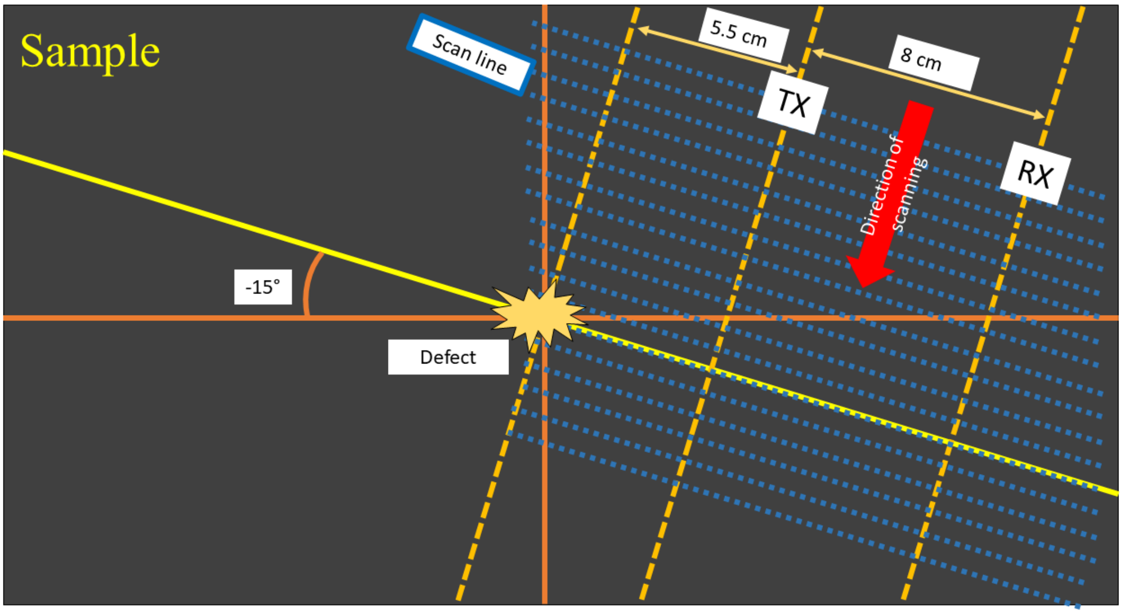

Figure 7.10 Schematic diagram of the experimental set-up for scanning samples with PPM EMATs. The orange lines represent the reference system centred at the defect location. The yellow line depicts the direction of the wave propagation. The blue dashed lines depict the scan lines.

As illustrated in figure 7.10, two perpendicular lines (orange) were drawn which crossed at the defect location and used as reference system. A series of lines (blue dashed) were then traced at -15° with respect to the horizontal line. Such a direction was chosen to reduce reflections coming from the edges of the sample. The following step was to establish the position of the probes with respect to the defect: the distance of the defect to the source and the receiver were 5.5 and 13.5 cm, respectively. The measurement was taken by starting from a line 8 cm above the centre of the defect down, to a line 4 cm below, in 5 mm steps.

The driving current was a 4-cycle sine wave signal at a frequency of 250 kHz, windowed with a Gaussian function. The acquired signals were bandpass-filtered between the lower and upper frequencies of the driving frequency bandwidth (187 kHz and 312 kHz respectively), to reduce noise. Two recorded signals are plotted in figure 7.11 for comparison.

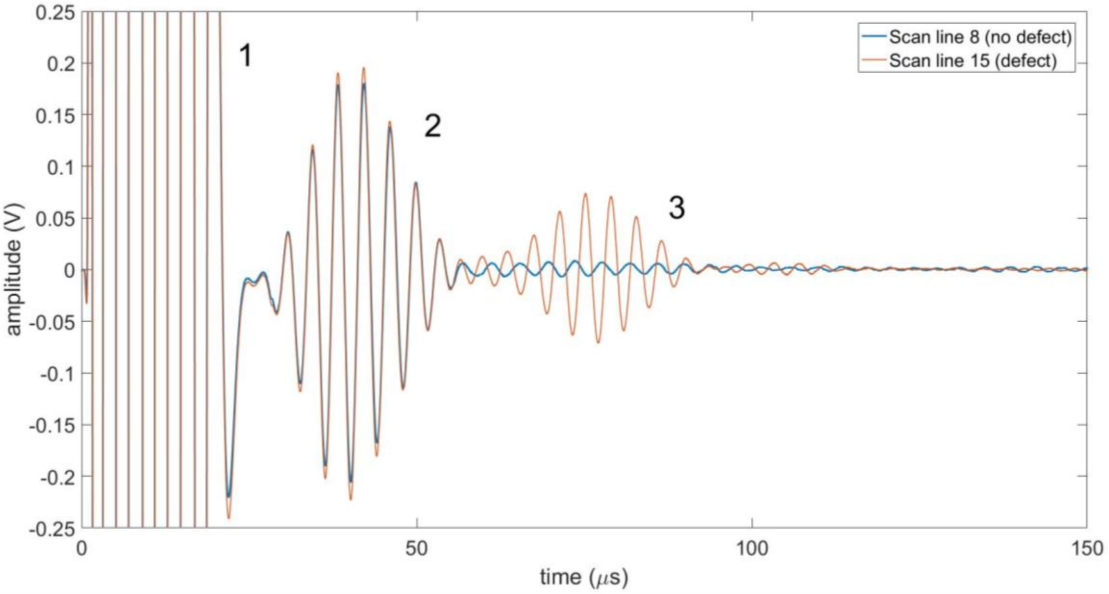

Figure 7.11 Comparison between two acquisitions. The blue line shows a wave travelling in an undamaged area, while the red line of a wave travelling across the defect. (1) Electrical pick-up, (2) direct signal and (3) defect reflection.

The two signals were taken on two different scan lines, whose one across the defect (scan line 15). In both cases, the electrical pick-up (1) and the direct signal (2) can be noted. In only one case, when the wave was travelling across the impact damage region, a third signal can be seen (3), as shown more clearly in figure 7.12.

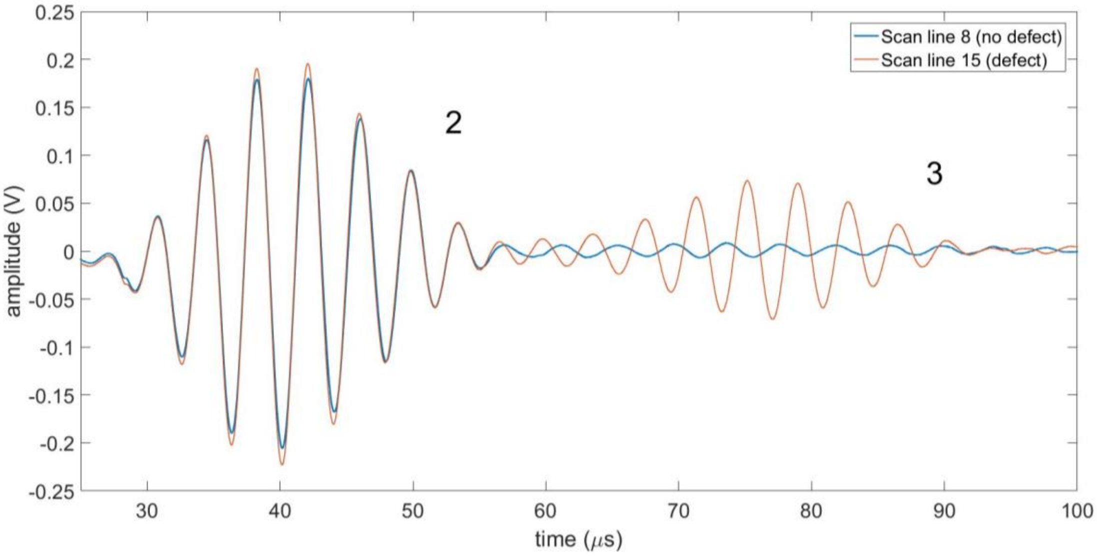

Figure 7.12 Detail of the two signals acquired on two scan lines. The blue line shows a wave travelling in an undamaged area, while the red line of a wave travelling across the defect. (2) Direct signal and (3) defect reflection.

Even though the amplitudes of the direct signals were slightly different, their time profiles matched, showing good consistency of the measurement at different scan lines. A further test as a demonstration of the defect detection capability is the evaluation of the time of flight (ToF) of the two signals (2) and (3). The evaluation was performed by using a cross-correlation. Figure 7.13 shows the cross-correlation of all the signals recorded.

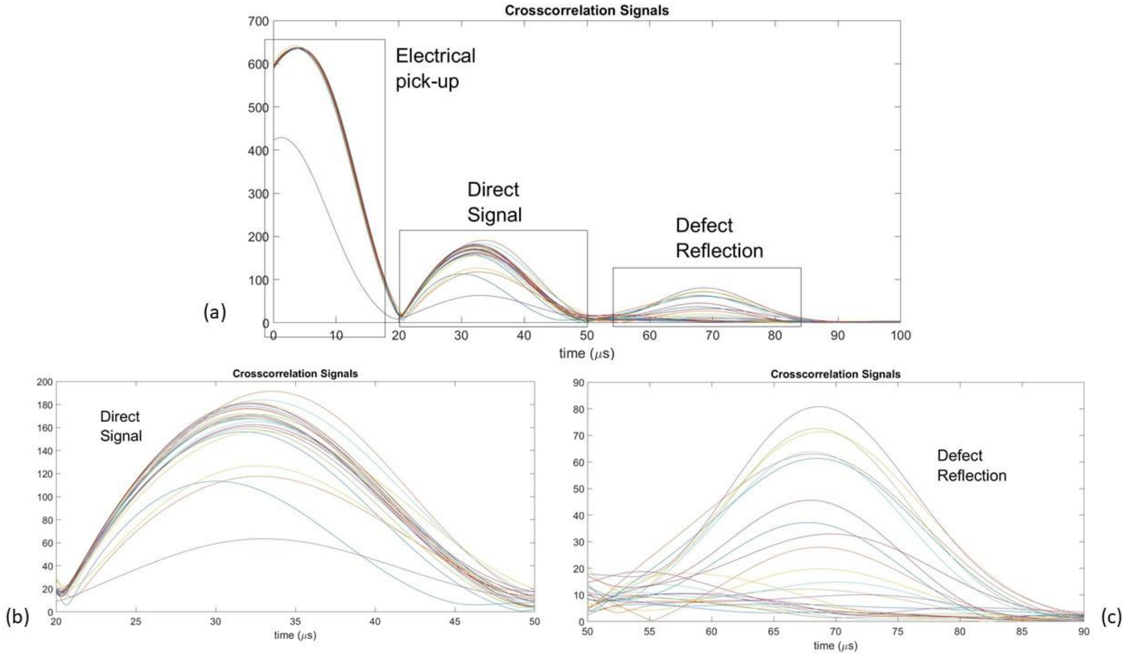

Figure 7.13 (a) Cross-correlation of all acquired signals with the driving waveform. (b) Cross-correlation of the direct signal with the driving waveform. (c) Cross-correlation of the defect reflection with the driving waveform.

It can be observed that the envelopes of the direct signals were concentrated around 34 µs which corresponded to 8.8 ± 1 cm in space, as the propagation velocity for SH_0 mode was 2600 m/s (see section 4.6.3.2). Conversely, the second set of curves were centred on 68 µs, which corresponds to 18 ± 1 cm. This distance corresponds to the path of the wave travelling from the source to the defect, 5.5 cm, and bouncing back to the receiver, 13.5 cm. In conclusion, it can be stated that the SH_0 wave successfully detected the impact damage.

In order to characterise the defect and give an evaluation of its dimensions, the next step was to produce images. These were obtained by performing the PSM algorithm. Figure 7.14 shows the wave-field after each scan line was cross-correlated to the driving waveform.

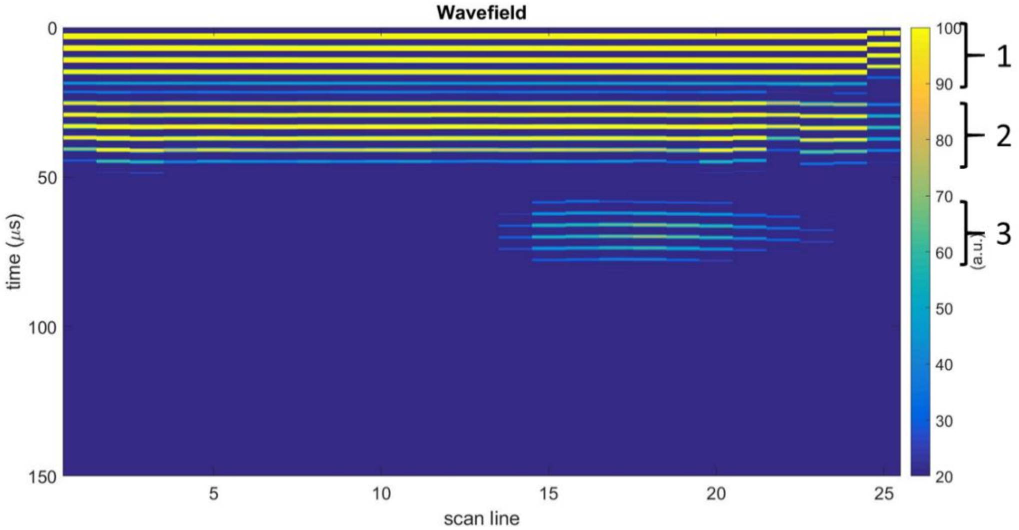

Figure 7.14 Wavefield of the a quasi-isotropic CFRP plate having an impact damage. (1) Electrical pick-up, (2) direct signal, (3) impact damage.

In figure 7.15, the B-scan is shown. The B-scan was obtained by performing the envelope of each scan line. In the B-scan two stripes can be seen representing the electrical pick-ups and direct signals, together with a lighter, more localised area where the defect was located.

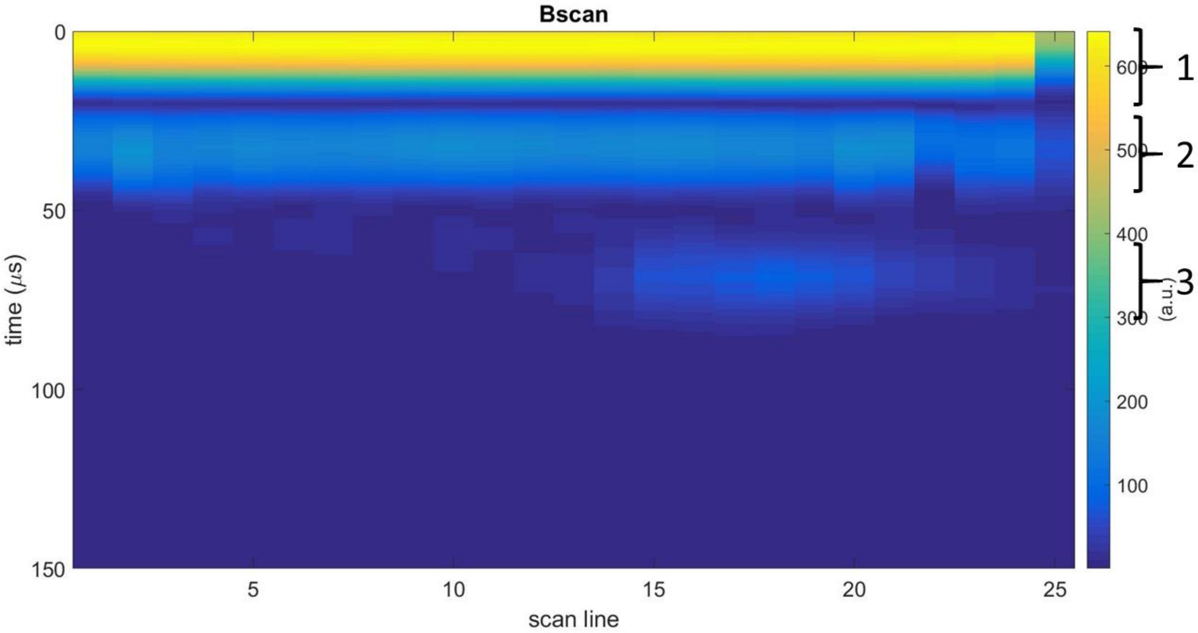

Figure 7.15 B-scan of a quasi-isotropic CFRP plate having an impact damage. (1) Electrical pick-up, (2) direct signal and (3) impact damage.

Such a representation does not provide a good resolution for characterising the defect [13]. The different time travels affect the resolution producing a distorted image of the defect.

Therefore, for the reasons already stated, the PSM algorithm has been used. Before performing the actual algorithm, further pre-processing was needed. The electrical pick-up and direct signal presented a higher signal-to-noise ratios than the defect reflection, so they have been neglected, as meaningless for imaging, and discarded by substituting them with zeros. Furthermore, usually the PSM algorithm has been performed with source and receiver at the same spot, as illustrated in figure 7.7. Therefore, source and receiver were moved on the same position by adding zeros to each scan line in order to cover the time delay of the wave travelling the distance between the probes. Figure 7.16 shows the input image after being fully pre-processed.

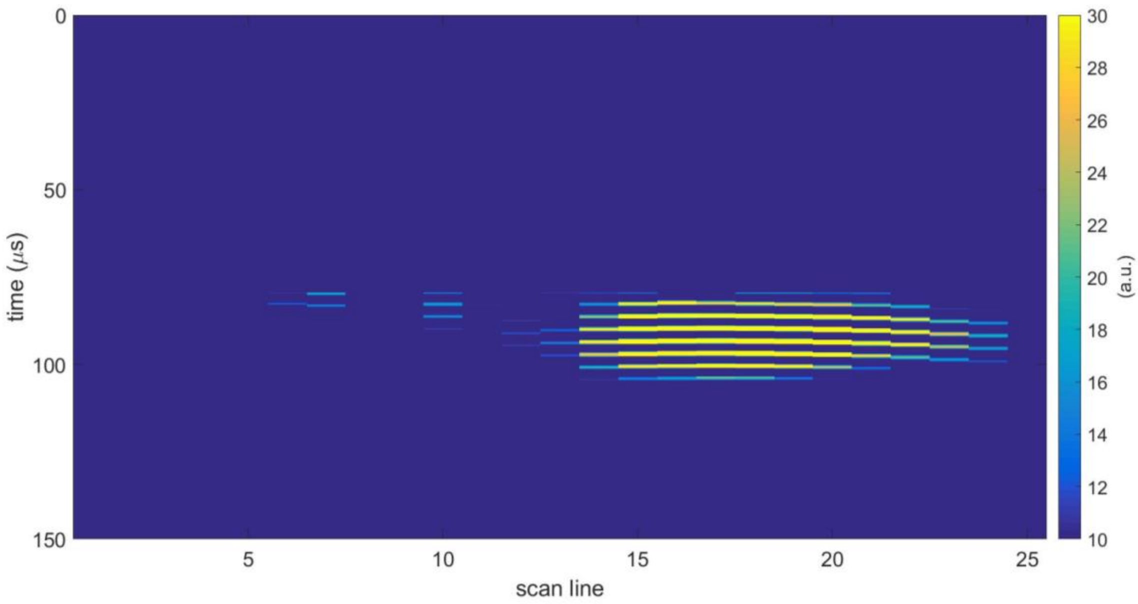

Figure 7.16 Input of the PSM algorithm.

Due to the limited number of scan lines (25), in order to increase the number of pixels and, hence, improve the resolution, the input image (figure 7.16) was resampled. The number of scan lines was increased of 30 times by performing a nearest neighbour interpolation. The output of the PSM algorithm is depicted in figure 7.17.

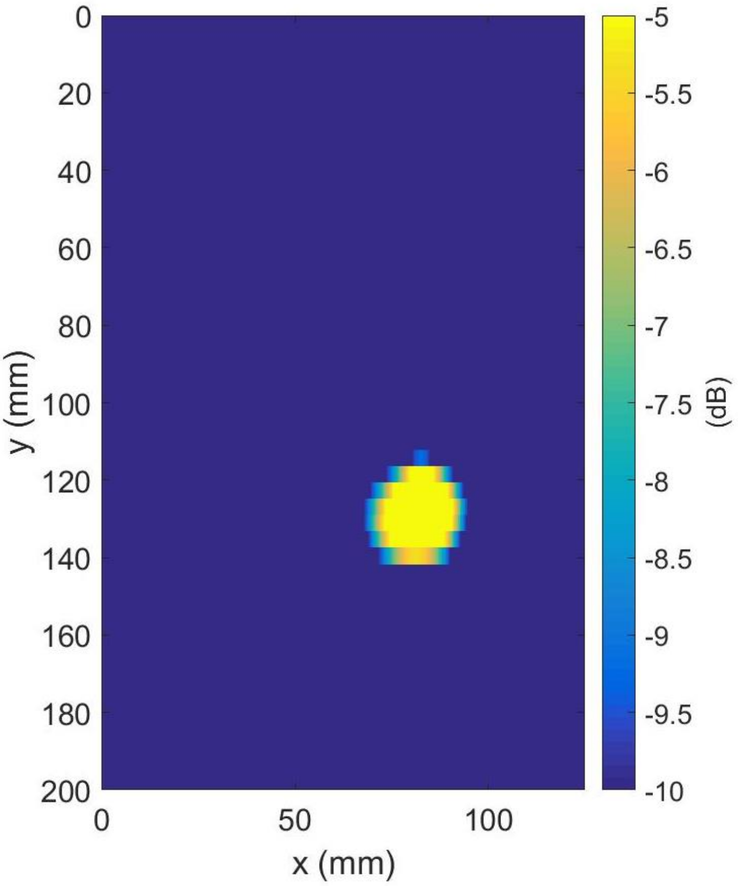

Figure 7.17 Image of a quasi-isotropic CFRP plate having an impact damage. The defect is detected as a lighter area.

The impact damage is displayed as a lighter yellow area. Confining the evaluation around that area, as in figure 7.18, it can be seen that its location is (8, 13) cm, corresponding to where the impact damage was expected to be detected.

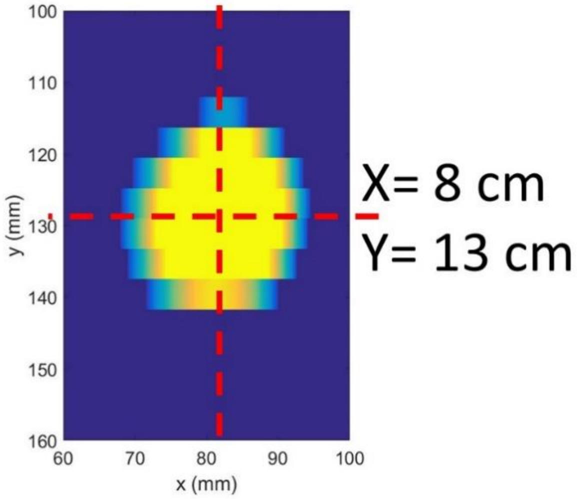

Figure 7.18 Detail of image representing the location of the impact damage.

As illustrated in figure 7.19, the dimensions of the yellow area representing the defect was approximately 2 x 2 cm, showing good agreement with those obtained from a phased array commercial system. Nonetheless, it can be noted that the resultant defect shape looks different. The lower resolution in figure 7.19(a) was due to the step taken between each scan line (5 mm) and the size of the transducers, whose width is comparable to the width of the defect. The width of the active surface of the PPM EMATs was 20 mm.

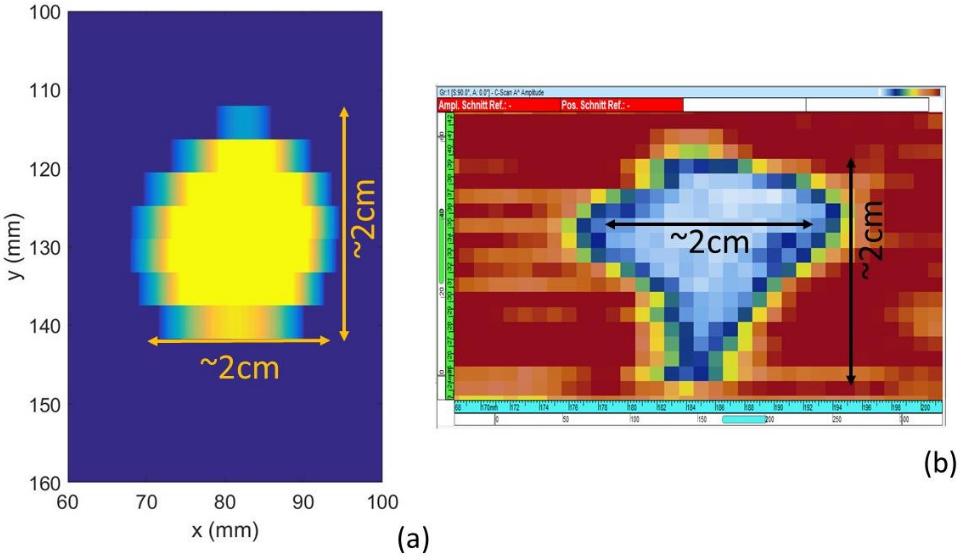

(a)

(b)

Figure 7.19 Detail of image representing the impact damage produced from (a) guided waves inspections and (b) commercial phased array sycstem.

7.5 Results

In this section, the final images are presented and were produced following the process described in Section 7.4.

7.5.1 CFRP

7.5.1.1 Delamination

The results were obtained only for the delaminations placed between the second and third plies, starting from the top surface. The fixed distance between source and receiver was 8 cm. The two EMATs were then scanned at 15° with respect to the direction of the fibres (0°). The receiver was placed at 25.5 and 27.5 cm from the two delaminations, whereas the generation source was placed at 17.5 and 19.5 cm from the two delaminations. Figure 7.20 illustrates the geometry used.

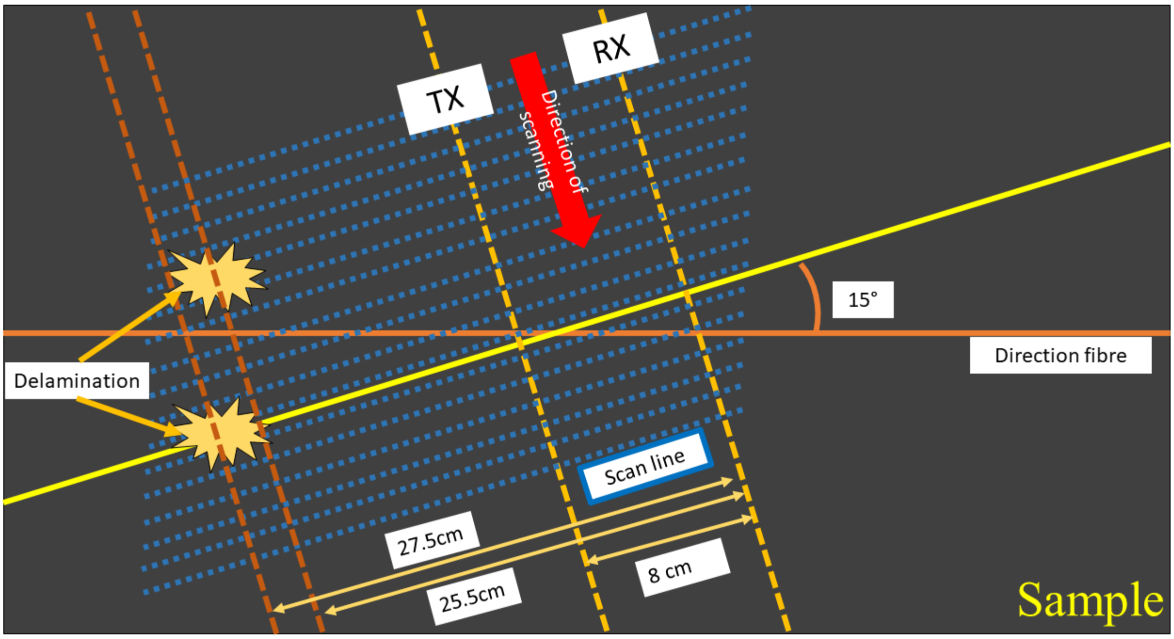

Figure 7.20 Schematic diagram of the experimental set-up for inspecting a quasi-isotropic CFRP plate. The orange line represents the reference line parallel to the 0° direction of the fibre. The yellow line depicts the direction of the wave propagation. The blue dashed lines depict the scan lines.

The data were then pre-processed and input to the PSM algorithm. The outcome is shown in figure 7.21.

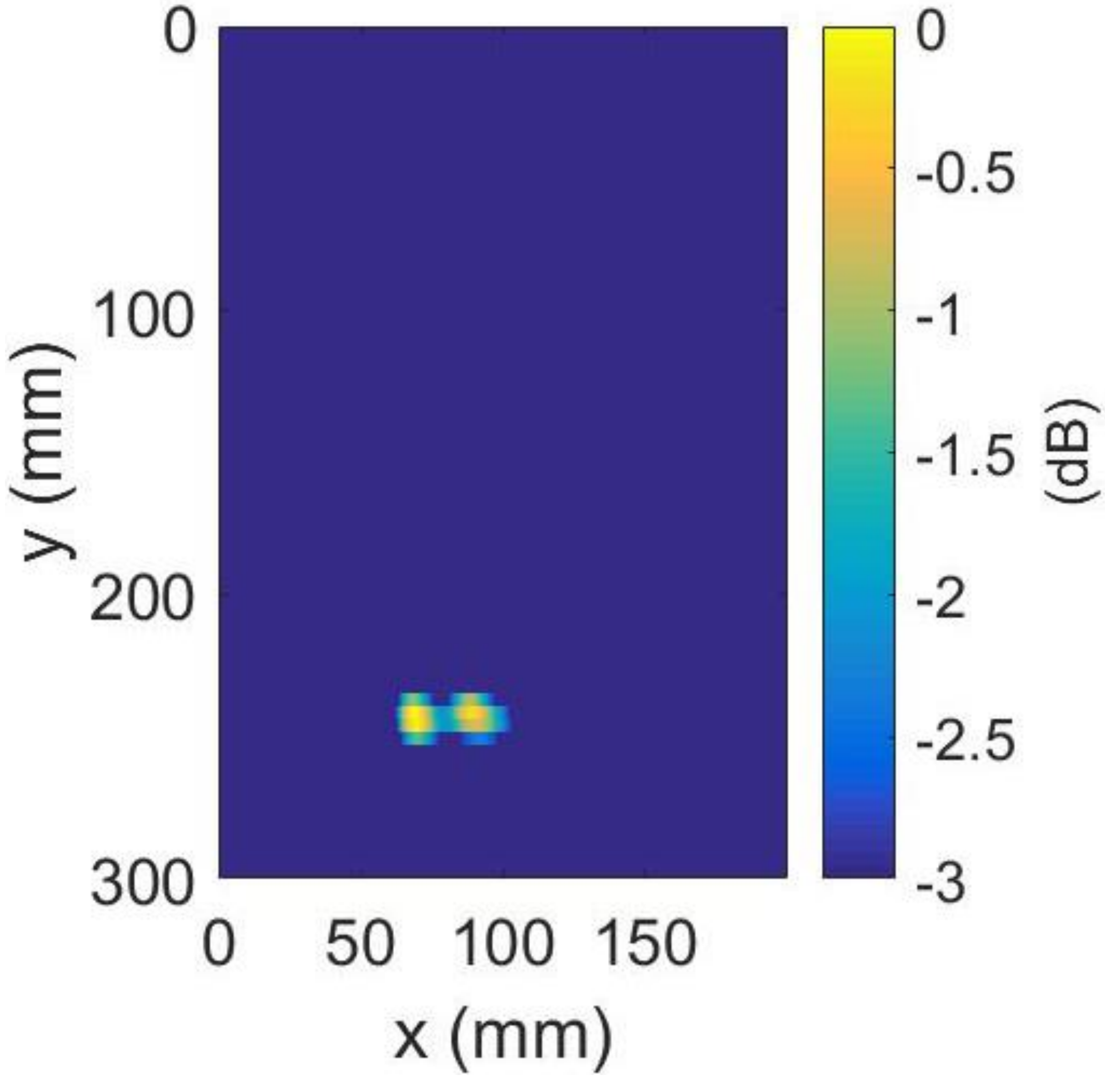

Figure 7.21 Image of a quasi-isotropic CFRP plate having two delaminations. The defect is detected as a lighter area.

It can be seen that the delaminations are showing up as the lighter areas in figure 7.17. Their location is approximately where they were expected, but it can be observed that the two detects are not fully separated or resolved in the image. This is due to the finite width of the active surface of the transducers. Figure 7.22 shows a zoom in of the defect area in figure 7.21. It can be still noted that the two defects can be distinguished. In service, further evaluation would be necessary for full characterisation of each individual defect.

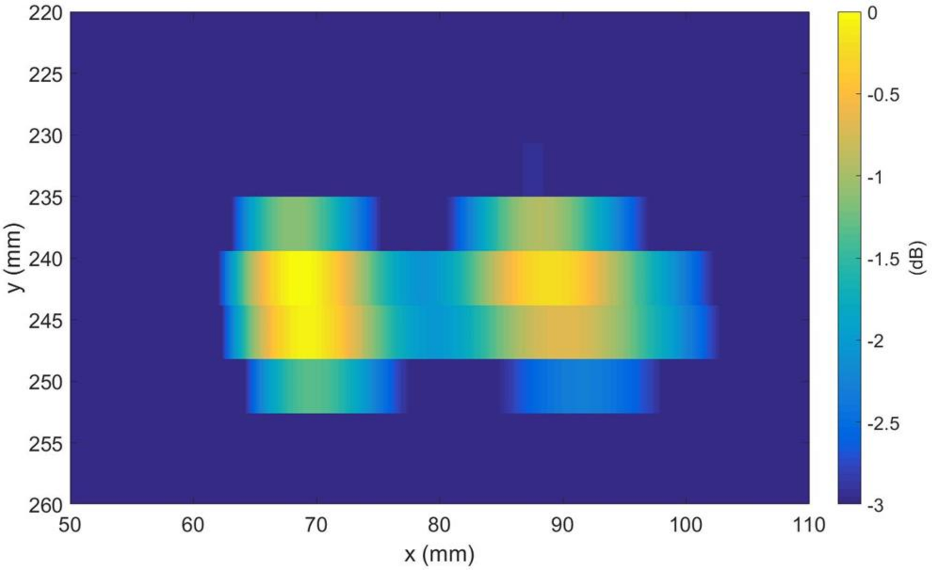

Figure 7.22 Detail of the two delaminations.

7.5.1.2 Lightning strike

Figure 7.23 shows the image resulting from the inspection of the CFRP plate damaged with a "lightning" strike. The investigation was conducted from the opposite side of the heat-damaged areas. Normally, this defect can be detected by visual inspection. The two transducers were fixed at 8 cm from each other. The distance between receiver and defect was 13 cm.

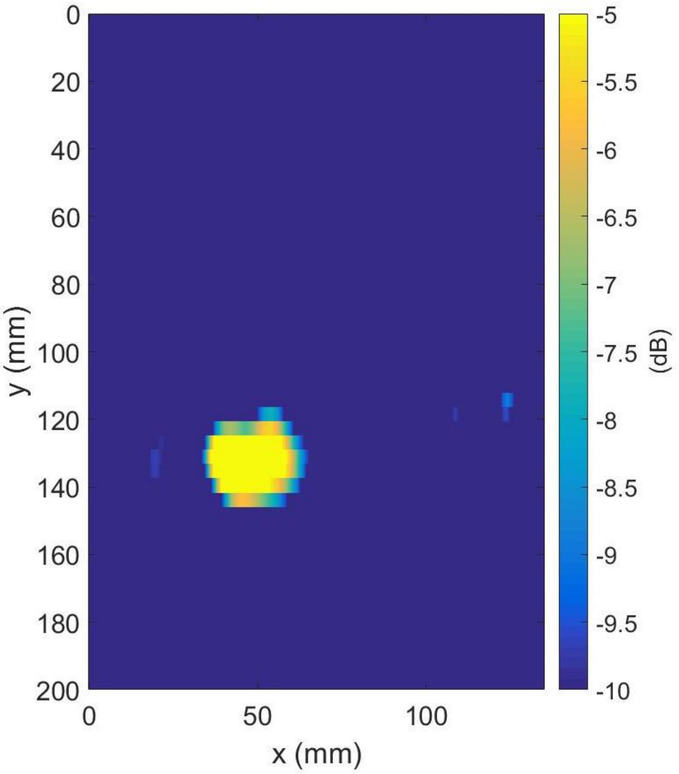

Figure 7.23 Image of the quasi-isotropic CFRP having a lightning strike. The defect is detected as a lighter area.

It can be clearly noted a lighter area at (5, 13) cm depicting the scorched area on the opposite side. The location and size of the defect can be easily yielded by zooming in on the interested area, as shown in figure 7.24. The position corresponds to where the defect was expected to be detected, and the estimated size matches the real dimensions.

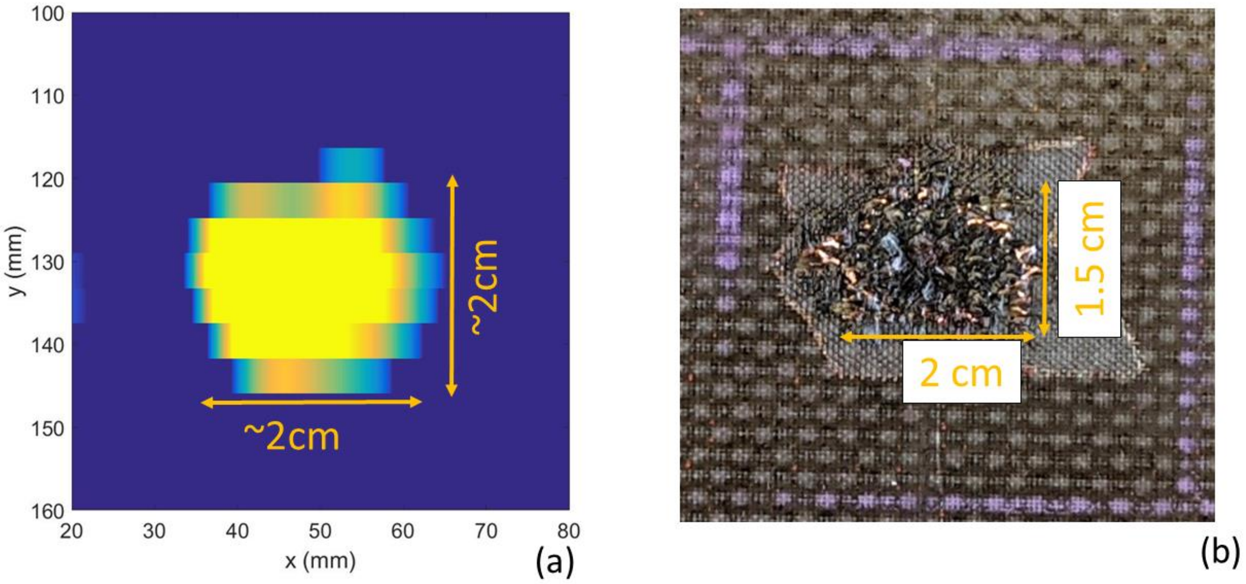

Figure 7.24 (a) Detail of image representing the impact damage produced from guided waves inspections. (b) Photo of the scorched area where the lightning hit the sample.

7.5.2 GFRP

Figure 7.25 show the results of inspecting the GFRP plates with PPM EMATs. The investigations have been conducted by placing the transducers, as for the previous experiments, at a fixed distance of 8 cm between each other. For all GFRP samples, the distance between receiver and the centre of the impact damage was 13 cm.

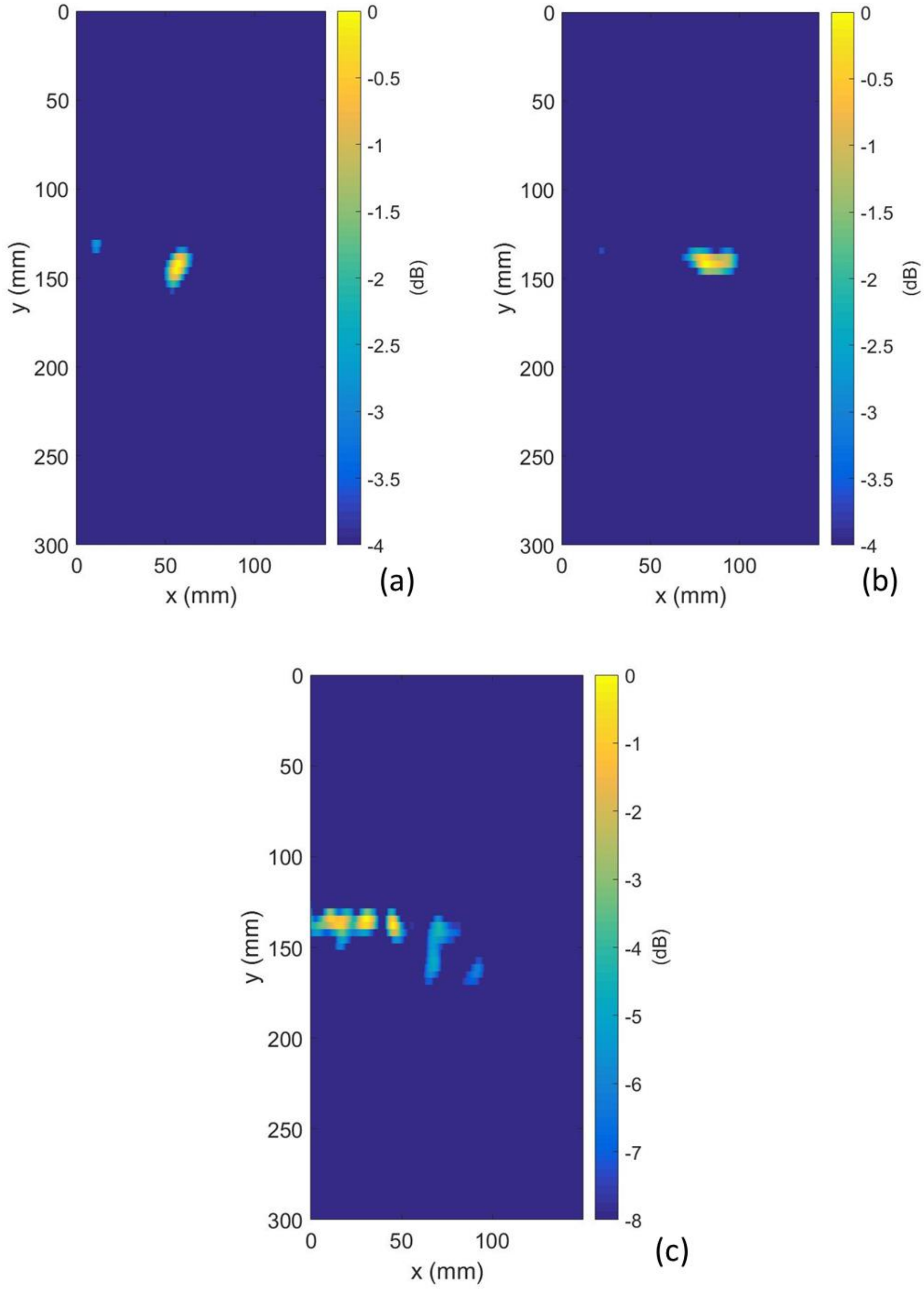

Figure 7.25 Images of the GFRP samples for impact energies of (a) 14 J, (b) 16 J and (c) 18 J. The defect is detected as a lighter area.

It can be seen that the impact damages have been detected as a lighter (yellow) area. In figure 7.25(c), it can be also noted a few additional lighter areas. These are artefacts from the ultrasonic guided wave reflections from the edges, which worsen the detection of the damage as the signal-to-noise ratios of these signals are higher than the reflection of defect. Nonetheless, the defects were detected in all cases.

7.6 Dual guided wave inspection and capacitive imaging

In this section, the images of the GFRP plates produced from guided waves testing and capacitive imaging are compared. A comparison for three difference samples of Section 7.5 is shown in figure 7.26. The colour mapping has been changed in order to ease the comparison.

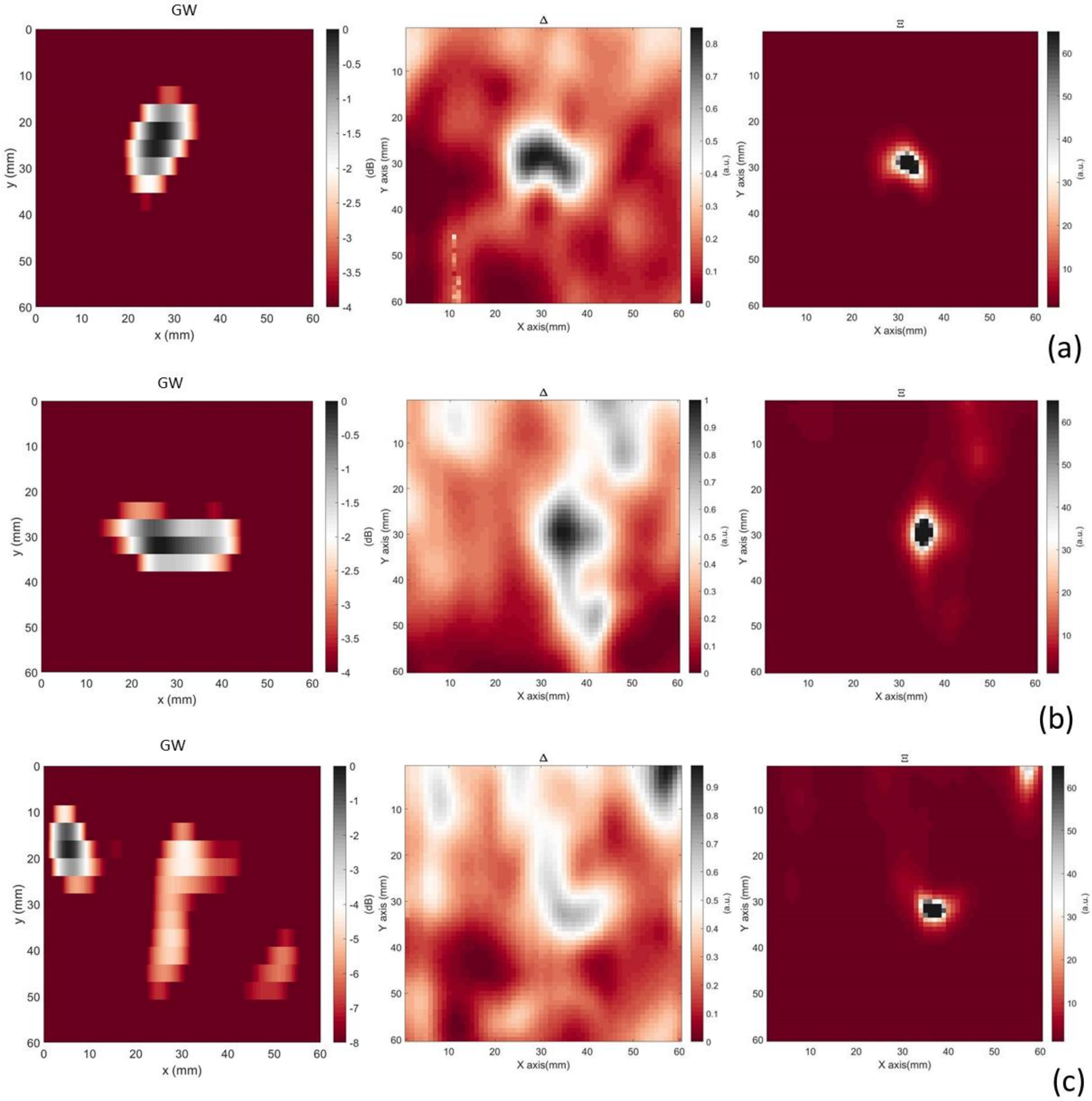

Figure 7.26 Comparison between the images produced from guided wave inspections (GW) and capacitive imaging (Δ and Ξ) for the GFRP samples for impact energies of (a) 14, (b) 16 and (c) 18 J.

It can be noted that the results produced from the guided wave inspections present shapes and dimensions that are closer to Ξ, which depicts the defect localisation, than to Δ, which leads to the evaluation of the defect size (see section 6.3.2). It should be also noted that CI inspections have a higher resolution due to a finer scanning step (1 mm for CI and 5mm for EMATs). It is also worth mentioning that guided wave inspections (GW) covered a larger area than the CI technique. The GW scanned the sample from a line 15 cm long covering the whole possible length, while the CI locally scanned the damaged area yielding a higher image resolution of the damage. Thus, these two techniques can be used together for fully characterising defects. For non-conductive materials, such as GFRP composite, guided wave inspections can be adopted for detecting discontinuities over large areas, and capacitive imaging then used for evaluating them in more detail over a much smaller region [14]. The techniques can thus be considered complementary, as the former can be used over distances as long as 150 m [15], while the latter can be used locally for characterising the defect once guided waves have identified an anomaly in the structure.

7.7 Conclusions

In this chapter, PPM EMATs have been used for generating SH_0 guided waves in order to detect defects within CFRP and GFRP composite samples. The defects were typical of the types of flaw of interest in the aerospace field, such as impact damage, lightning strikes and delaminations. The experiment consisted of scanning the samples by moving the source and receiver together at a fixed distance apart. The inspections have been conducted by placing the transducers on one side only. These tests simulated real testing conditions, where typically only one side (the outer side) is accessible. The results demonstrated that defects can be detected and, moreover, the data can be used for generating images. The imaging process has been performed by means of a SAFT technique using the PSM algorithm. Images of defects in CFRP samples (including impact damage and lightning strikes) gave information for characterising the flaws. In addition, the results obtained for GFRP samples were compared with those of CI from Chapter 6, showing the reliability of the imaging process. This demonstrates that a dual scanning strategy using guided waves for large area scanning and CI for more local (higher resolution) imaging is an interesting concept that will be of interest in the aerospace industry.

References Chapter 7

[1] H. Mei, R. James, V. Giurgiutiu, "Damage detection in laminated composites using pure SH guided wave excited by angle beam transducer," in *SPIE*, 2020.

[2] M. R. Wisnom, "The role of delamination in failure of fibre-reinforced composites," *Philosophical Transactions of the Royal Society A: Mathematical, Physical and Engineering Sciences,* vol. 370, no. 1965, pp. 1850-1870, 2012.

[3] G. Sweers, B. Birch, J. Gokcen, "Boeing," 2012. [Online]. Available: https://www.boeing.com/commercial/aeromagazine/articles/2012_q4/pdfs/AERO_2012q4_article4.pdf. [Accessed 17 April 2021].

[4] C. Karch, C. Metzner, "Lightning protection of carbon fibre reinforced plastics - An Overview," in *33rd International Conference on Lightning Protection, ICLP 2016*, 2016.

[5] T.M. Dhanya, C.S. Yerramalli, "Lightning strike effect on carbon fiber reinforced composites - effect of copper mesh protection," *Material today communications,* vol. 16, pp. 124-134, 2018.

[6] A. Akbari, M. Meshinchi-Asl, M. Riyahi, "An Improved Hyperbolic Summation Imaging Algorithm for Detection of the Subsurface Targets," *Journal of Geophysics & Remote Sensing,* no. 04, p. 03, 2014.

[7] W. Müller, V. Schmitz, G. Schäfer, "Reconstruction by the synthetic aperture focussing technique (SAFT)," *Nuclear Engineering and Design,* vol. 94, no. 3, pp. 393-404, 1986.

[8] M. Skjelvareid, T. Olofsson, Y. Birkelund, Y. Larsen, "Synthetic aperture focusing of ultrasonic data from multilayered media using an omega-K algorithm," *IEEE Transactions on Ultrasonics, Ferroelectrics, and Frequency Control,* vol. 58, no. 5, pp. 1037-1048, 2011.

[9] J. Gazdag, "Wave Equation Migration With the Phase-Shift Method," *Geophysics,* vol. 43, no. 7, pp. 134-1351, 1978.

[10] T. Olofsson, "Phase shift migration for imaging layered objects and objects immersed in water," *IEEE Transactions on Ultrasonics, Ferroelectrics, and Frequency Control,* vol. 57, no. 11, pp. 2522-2530, 2010.

[11] J. Claerbout, Imaging the Earth's Interior, Cambridge: MA: Blackwell Scientific, 1985.

[12] D. Loewenthal, L. Lu, R. Roberson, J. Sherwood, "The wave equation applied to migration," *Geophysical Prospecting,* vol. 24, no. 2, pp. 380-399, 1976.

[13] C.B. Burckhardt, PA. Grandchamp, H. Hoffmann, "Methods for Increasing the Lateral Resolution of B-Scan," *Acoustical Holography,* vol. 5, pp. 391-413, 1973.

[14] A. Cobb, J. Fisher, "Flaw depth sizing using guided waves," in *AIP Conference Proceedings*, 2016.

[15] H. Kwun, A. E. Crouch, "Guided wave fills inspection gap," *Pipelin and Gas Technology,* vol. 7, pp. 28-31, 2006.

Chapter 8

Conclusions

8.1 Contributions to knowledge

The research reported in this thesis has demonstrated a possible new path in the future of NDE in the aerospace industry. Two reliable methods have been introduced for the detection of impact damage and evaluation of aerospace composite materials in order to reduce inspection time, and therefore costs, while ensuring the high safety standards required in the field. The two techniques can be used in a complementary manner. The first technique described is the use of guided waves for inspecting large areas and detecting possible defects, such as impact damage. In the case of glass fibre composites, capacitive imaging could then be used to perform a localised analysis at higher spatial resolutions.

8.1.1 EMATs and patches

The research on Electromagnetic Acoustic Transducers (EMATs) has demonstrated that EMATs can be used to generate or detect ultrasonic guided SH waves on aerospace composite plates with the use of thin removable metallic patches. These waves have been used for detecting defects in both non-conductive and low electrical conductivity materials. The removable metallic patches are simply fabricated from readily available, self-adhesive metallic foils that are attached onto the surface of the sample. The electrical conductivity of the metallic layer allows the induction of eddy currents in the patch, which interacting with the static magnetic field of the EMAT, facilitates generation and detection of the elastic waves. The resulting elastic strains are transmitted to or from the sample by mechanical coupling via the adhesive layer. The usefulness of this technique has been demonstrated on different types of samples, both with and without defects. The materials tested included isotropic, non-conductive materials, such as glass plates, and various glass and carbon fibre composite materials with varying amounts of anisotropy. The results showed that the correct excitation of certain guided waves depends predominantly on the mechanical properties of the plates, and no significant influence of the patches on the plates' mechanical properties was observed. Given the mechanical properties of the sample it is possible to select of the desired wave mode.

Throughout the thesis the ultrasonic guided wave mode used in experiments was the SH_0, fundamental non-dispersive mode of the SH guided waves. A 3-step method for predicting the generation of this mode was developed, that consisted of calculating the quantities involved in generating the Lorentz forces, eddy currents and the magnetic flux density. The calculations were carried out in two separate 3D COMSOL models to reduce the computational time. Each model included the metal patch placed under one of the two main components of the PPM EMAT, a racetrack coil and a set of magnets (with alternating polarity). For both models, a grid of points was formed on the patch, and at each point the components of the calculated quantities were evaluated. The data was then extracted and imported into MATLAB for the calculation of the resulting Lorentz forces at each point. These forces were determined by means of a cross product between the components of the eddy currents and the magnetic flux density in a matrix form. At each point, the resulting Lorentz force magnitudes and direction cosines were calculated. The last step of the method was the construction of an analytical model in PZFlex, in which the propagation of the SH wave within the specimen was simulated. The results were then compared to actual measurements by extracting the velocity component of the wave along the direction perpendicular to the direction of propagation, since EMATs are actually velocity sensors.

This thesis reports the inspection of various composite samples containing different types of defects with PPM EMATs. Importantly, it was observed that the patch did not observably affect the surfaces of the composites tested. Removal of the patch did not damage the surface of either carbon fibre or glass fibre composites. Measurements using these patches demonstrated that defects could be detected and images produced in the form of B-scans. Better results were obtained using a variation of the SAFT technique based on the phase-shift migration method, which operated in the frequency domain. This methodology has demonstrated the possibility of producing images to make a preliminary evaluation of defects, illustrating their position and size. The method thus represents a way of scanning large areas, as would be encountered for example in the aerospace industry (wings, fuselage etc).

8.1.2 Capacitive imaging

In the research on capacitive imaging (CI), the possibility of using a combination of CI and guided waves to investigate non-conductive or low electrically conductive materials was explored. As stated already, SH guided waves could be used to scan a large portion of the sample in order to detect possible spatial discontinuities in the mechanical properties of the sample. Once the component was scanned, a low resolution image could be obtained which revealed the location and size of the damaged area. Once the defect has been identified and the area of inspection restricted, the CI technique can be used for a localised, higher resolution analysis, to characterise the defects and study their shape and size in detail.

A data fusion method was also introduced in this thesis to improve the localisation and resolution of the CI technique images. Generally, this technique tends to utilise amplitude-based images, while discarding the phase-based data, due to lower SNR of phase based data. The novel method reported in the thesis relies on the fusion of phase and amplitude in order to mitigate various influences on the sensor and measurement, such as edge effects, lift-off variations and possible geometric complexities. The influence of such effects can affect image resolution by hiding features of interest. Preliminary tests were first carried out on a sample whose defects (Perspex with flat bottom holes) were clearly visible on the opposite defect free side to where the sensor was scanned to demonstrate the imaging process. The results showed that the images generated provide both a unique localisation of the defect and a better assessment of its dimensions. It is thought that this will enable CI to be more widely used in the NDE of glass fibre composites and other non-conducting samples.

8.2 Future work

The results reported in this thesis have significant potential in various NDT and NDE applications. EMATs are already widely used for the inspection of metallic pipelines. Recently, several market analyses have predicted an upsurge in the use of plastic, hence non-conductive, materials for pipe production. EMATs may be used for generating and receiving guided waves in plastic pipelines via metallic patches. In addition, it would be possible to combine the use of CI for localised defect analysis, and thus improve the quality of inspections.

Defect detection and image processing with EMAT can be further improved and studied. In fact, the resolution of the images produced could be improved by making some modifications to the metal patch, the transducers or the scanning method. In this thesis, the influence of the size and shape of the metal patch in the generation of the guided waves has not been investigated in depth. For example, the use of a curved patch could introduce a change in directivity for a particular application if needed. In addition, it might be possible to replace a periodic PPM EMAT with a conventional EMAT and a periodic patch in the form of parallel strips. Many other shapes are possible, and this would be a good subject for further study.

The ultrasonic transducers used in this thesis work were PPM EMATs having a wavelength of 10 mm. The use of smaller transducers or transducers with a shorter wavelength increases the discrimination of defects such as in section 7.5.1.1, where the two delaminations could not be distinguished clearly, due to a low lateral resolution. It is suggested that the use of higher ultrasonic frequencies be investigated, so as to determine whether there is an upper limit to the use of such patches on these composite materials, which will probably be limited by the ultrasonic properties of the samples themselves. It would also be interesting to look at EMATs and patches for use on curved surfaces such as pipes. This may need modification to the EMAT face acting at the surface to increase efficiency by the coil conforming to the curved surface, but the patch would easily conform to the surface of a pipe.

Finally, the scanning method can be modified by reducing the step side of the scans, increasing the number of measurements, and therefore the lateral resolution. Thus, for example, it might be possible to obtain linear scans along different angles, thereby obtaining data in the form of projections (data obtained along a linear scan at a certain angle). This data could then be used to reconstruct tomographic images, using the ability of the EMAT to be scanned across patches in the form of long strips.

Recently, dual-mode sensors have been developed to perform defect imaging in conductive and non-conductive components by means inductive (eddy current) and capacitive mechanisms, respectively. These devices are used as CI probes, so scanning a surface yields representative images of the defects contained in the sample. For future research, it would be interesting to study these devices by trying to add one or more magnets. This addition could allow the development of sensors that can be used as EMATs or CI probes at necessity.